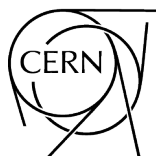


**ICFA Mini-Workshop on
Impedances and Beam Instabilities in Particle Accelerators**

Benevento, Italy, 18–22 September 2017

Editors: V. Brancolini, G. Rumolo, M. R. Masullo and S. Petracca



CERN Yellow Reports: Conference Proceedings
Published by CERN, CH-1211 Geneva 23, Switzerland

ISBN 978-92-9083-496-0 (paperback)

ISBN 978-92-9083-497-7 (PDF)

ISSN 2519-8084 (Print)

ISSN 2519-8092 (Online)

DOI <https://doi.org/10.23732/CYRCP-2018-001>

Accepted for publication by the CERN Report Editorial Board (CREB) on 27 September 2018

Available online at <http://publishing.cern.ch/> and <http://cds.cern.ch/>

Copyright © CERN, 2018

© Creative Commons Attribution 4.0

Knowledge transfer is an integral part of CERN's mission.

CERN publishes this volume Open Access under the Creative Commons Attribution 4.0 license (<http://creativecommons.org/licenses/by/4.0/>) in order to permit its wide dissemination and use.

The submission of a contribution to a CERN Yellow Report series shall be deemed to constitute the contributor's agreement to this copyright and license statement. Contributors are requested to obtain any clearances that may be necessary for this purpose.

This volume is indexed in: CERN Document Server (CDS), INSPIRE.

This volume should be cited as:

Proceedings of the ICFA Mini-Workshop on Impedances and Beam Instabilities, Benevento, Italy, 18–22 September 2017, edited by V. Brancolini, G. Rumolo, M. R. Masullo and S. Petracca, CERN Yellow Reports: Conference Proceedings, Vol. 1/2018, CERN-2018-003-CP (CERN, Geneva, 2018), <https://doi.org/10.23732/CYRCP-2018-001>

A contribution in this volume should be cited as:

[Author name(s)], in Proceedings of the ICFA Mini-Workshop on Impedances and Beam Instabilities, Benevento, Italy, 18–22 September 2017, edited by V. Brancolini, G. Rumolo, M. R. Masullo and S. Petracca, CERN Yellow Reports: Conference Proceedings, Vol. 1/2018, CERN-2018-003-CP (CERN, Geneva, 2018), pp. [first page]–[lastpage], <https://doi.org/10.23732/CYRCP-2018-001>. [first page]

Abstract

The ICFA Mini-Workshop on Beam Coupling Impedances and Beam Instabilities in Particle Accelerators was held in Benevento (Italy) from 18 to 22 September, 2017.

The workshop was intended initially to continue the tradition of dedicated conferences on beam coupling impedances in particle accelerators, initiated with the 2014 ICFA mini-Workshop on “Electromagnetic Wake Fields and Impedances in Particle Accelerators” held in Erice (organised by Vittorio Vaccaro, Maria Rosaria Masullo and Elias Métral). Therefore, the aim of the event was first of all to provide an up-to-date review of the subject of beam coupling impedances (theory & modelling, simulation tools, bench measurements, beam based measurements). Besides, it was decided to widen its scope to include recent advances on theory and simulations of beam instabilities.

The workshop was hosted by the University of Sannio in Benevento (Italy). Benevento is a world heritage city in Southern Italy, with remarkable monuments and fine pieces of arts, in a unique cultural and natural environment.

Preface

The ICFA Mini-Workshop on Impedances and Beam Instabilities in Particle Accelerators, was held in Benevento, Italy, from 18 to 22 September, 2017. The rich scientific program of the workshop was defined and shaped by a strongly motivated International Advisory Committee, composed of worldwide experts who actively provided their inputs. The conference venue was the San Vittorino complex, located in the very center of the historical town of Benevento. The workshop was supported and sponsored by the University of Sannio, three ongoing large accelerator projects (High Luminosity LHC, LHC Injectors Upgrade, LHC Collimation), the European network ARIES and the INFN section of Naples. Moreover, it was held under the auspices of the Italian Physical Society (SIF). The main goal was to summon the accelerator community actively working in the field of impedances and beam instabilities, and discuss together recent advancements and breakthroughs while defining future directions. Eighty-four participants from different laboratories all around the world attended the workshop, with a strong representation of young accelerator physicists with little experience and plenty of enthusiasm. That's why all the speakers made their best effort to provide a solid educational background into their subjects, before highlighting novelties, challenges and open questions.

The workshop chairs also had the great pleasure to celebrate Prof. Vittorio G. Vaccaro on the occasion of the 50 years since the birth of the concepts of beam coupling impedance and stability charts, to which he gave fundamental contributions unanimously recognised by the whole community. The workshop also provided the opportunity to remember dearly Dr. Francesco Ruggiero, who passed away 10 years ago, by highlighting in the opening speech his amazing foresight into all the beam dynamics issues of LHC and all future machines.

The web sites of the CFA Mini-Workshop on Impedances and Beam Instabilities in Particle Accelerators are:
<http://prewww.unisannio.it/workshopwakefields2017/>
<https://agenda.infn.it/conferenceDisplay.py?ovw=True&confId=12603>

Contents

Preface

..... iv

Proceeding Papers

A general overview on the 2017 ICFA Mini-Workshop on impedances and beam instabilities in particle accelerators

M. R. Masullo, S. Petracca, G. Rumolo 1

The impedance of flat metallic plates with small corrugations

K. Bane 5

New longitudinal beam impedance formula with 8 terms

O. Berrig, F. Paciolla 11

2D and 3D collimator impedance modeling and experimental measurements

N. Biancacci, D. Amorim, S. Antipov, G. Mazzacano, B. Salvant, E. Mètral, O. Frasciello, M. Zobov, A. Mostacci 17

The circulant matrix model and the role of beam-beam effects in coherent instabilities

X. Buffat 25

Observation and damping of longitudinal coupled-bunch oscillations in the CERN PS

H. Damerau, A. Lasheen, M. Migliorati 33

Feedback systems for multibunch beam diagnostics and instabilities suppression

A. Drago 39

The future of the e-p instability in the SNS accumulator ring

N. Evans, M. Plum 45

Electron cloud effects

G. Iadarola, G. Rumolo 49

Studies for the SPS travelling wave cavities upgrade

P. Kramer, C. Vollinger 57

Modeling of fast beam-ion instabilities

L. Mether, A. Oeftiger, G. Rumolo 63

Impedance theory and modeling

E. Mètral 69

Vlasov solvers and macroparticle simulations

N. Mounet 77

A rectangular waveguide with dielectric coatings as a dedicated wakefield dechirper at ELBE

F. Reimann, U. van Rienen, P. Michel, U. Lehnert 87

Effect of HOM frequency shift on bunch train stability

J. Repond, E. Shaposhnikova 93

Impedances and instabilities in hadron machines

B. Salvant 99

Beam Transfer Function measurements and transverse stability in presence of beam-beam

C. Tambasco, J. Barranco, T. Pieloni, L. Rivkin, X. Buffat, E. Mètral 105

Design of low-impact impedance devices: the new Proton Synchrotron Booster absorber scraper (PSBAS)

ML. Teofili, I. Lamas, T. L. Rijoff, M. Migliorati 111

The birth and childhood of a couple of twin brothers <i>V. G. Vaccaro</i>	117
Needs and solutions for machine impedance reduction <i>C. Vollinger, A. Farricker, T. Kaltenbacher, P. Kramer, B. Popovic</i>	125
Analytical impedance models for very short bunches <i>I. Zagorodnov</i>	133
Multi-physics simulations of impedance effects in accelerators <i>C. Zannini</i>	141
Acknowledgements	145
International Advisory Committee	146

A GENERAL OVERVIEW ON THE 2017 ICFA MINI-WORKSHOP ON IMPEDANCES AND BEAM INSTABILITIES IN PARTICLE ACCELERATORS

M.R. Masullo, INFN section of Naples, Naples, Italy
S. Petracca, University of Sannio, Benevento, Italy
G. Rumolo*, CERN, Geneva, Switzerland

Abstract

The ICFA mini-Workshop on impedances and beam instabilities in particle accelerators, which took place in Benevento (Italy) from 18 to 22 September 2017, was intended to continue the tradition of dedicated conferences on the subject of beam coupling Impedances in particle accelerators, initiated with the 2014 ICFA mini-Workshop on “Electromagnetic Wake Fields and Impedances in Particle Accelerators” held in Erice (organized by Vittorio Vaccaro, Maria Rosaria Masullo and Elias Métral). The aim of the event was therefore to provide an up-to-date review of the subject, while widening its scope to include recent advances on beam instabilities and different instability sources.

The workshop was hosted by the University of Sannio at Benevento, under the auspices of the Italian Institute for Nuclear Physics (INFN), the Italian Physical Society (SIF) and CERN - and with the sponsorship of the European network ARIES, as well as the running projects for LHC Injectors Upgrade (LIU), Collimation and High Luminosity LHC (HL-LHC).

INTRODUCTION

The ICFA Mini-Workshop on Impedances and Beam Instabilities in Particle Accelerators, was held in Benevento, Italy, from 18 to 22 September, 2017. The workshop was backed by a well assorted International Advisory Committee, who actively provided their inputs to define and shape the varied scientific program. The conference venue, the San Vittorino complex, is at the heart of the old town of Benevento. The workshop was supported and sponsored by several projects and networks (High Luminosity LHC, LHC Injectors Upgrade, LHC Collimation, ARIES), INFN (Napoli) and University of Sannio, and it was held under the auspices of the Italian Physical Society (SIF).

The main goal was to review relevant material in the field of impedances and beam instabilities and address recent advancements and breakthroughs. The workshop was attended by 84 participants from different laboratories all around the world (see Fig. 1), and more than a half were young accelerator physicists at the beginning of their careers. To best suit the young audience as well as the academic environment of the University of Sannio, speakers were requested to present their work providing an educational background of their subjects, before highlighting also the novelties, challenges and open questions.

* Giovanni.Rumolo@cern.ch

WORKSHOP ANNIVERSARIES, STRUCTURE AND TOPICS

Given the timing, the workshop also provided an excellent setting to mark the occasion of two round anniversaries.

- 50 years of the Beam Coupling Impedance concept, introduced by Prof. Vittorio Vaccaro to describe the electromagnetic interaction of a particle beam with the external environment. Prof. Vaccaro entertained the audience with a historical talk describing the birth of the concepts of beam coupling impedance and stability charts. He specially stressed how the two concepts of impedance and representation of beam stability in complex stability diagrams were logically linked and were born together. He was warmly thanked by the workshop participants and awarded a memorial plaque for his important achievements.
- 10 years of Francesco Ruggiero’s passing away. F. Ruggiero was an outstanding accelerator physicist, who gave enormous contributions to the fields of impedances and instabilities, in particular by fostering the necessity of building detailed impedance models of machines and by working on the improvement of the models to describe beam instabilities. Applied to LHC, his vision led to the implementation of a strict impedance budget control during the phase of LHC design, the identification of collimators as major impedance source as well as of octupole magnets as fundamental means of stabilisation, and the recognition of the relevance of electron cloud in the LHC beam parameter range. His foresight has been instrumental to both guide the understanding of the current LHC operation and lay the ground for the general design strategy of all future machines with challenging beam parameters.

The workshop featured plenary sessions with 48 talks and 5 final summary reports. A Poster Session was also organised, during which 22 posters were displayed in the Santa Sofia Cloister. The general impression was that, although the subjects of beam coupling impedance and instabilities are 50 years old, they remain fashionable and up-to-date, because

- Old concepts need to be adapted and extended to new types of accelerators (e.g. FELs, plasma wake-field accelerators);



Figure 1: Workshop participants, group picture.

- Observations (or diagnostics) of new phenomena are made in running machines and need to be interpreted;
 - Exploring new parameter regimes for upgrades or future machines requires original approaches and studies;
 - Modeling and understanding of the phenomena related to impedance and instabilities are still making a steady progress benefiting from the advancement of technology;
 - Open theoretical questions are still being intensively studied and widely debated.
- New regimes are being explored (e.g. frequencies beyond 100 GHz, small structures).

DISCUSSIONS AND OUTCOME

In the field of beam coupling impedance, a few main points emerged from the various discussions.

- When a new device for either old or new accelerators is designed to its performance specifications, it is crucial to include impedance reduction at the design stage, possibly also including all considerations coming from multi-physics simulations associated to the impedance effects.
- The evaluation of beam coupling impedances of accelerator devices becomes increasingly challenging due to several factors:
 - Devices become more and more complicated and require accurate electromagnetic descriptions;
 - Accelerators have more and more demanding performance requirements, which requires special attention to their impedance budgets. This leads to the necessity of enacting a strictly low impedance design policy;
- Electromagnetic codes to calculate numerically beam coupling impedances and wake functions are becoming ever more powerful and new ones are being produced using more advanced computational techniques (e.g. the moving window). This allows the detailed analysis of structures that could not be efficiently simulated before.
- Beam based measurements of beam coupling impedances are of fundamental importance to understand and pinpoint the limitations of running machines, in particular to identify:
 - Missing impedances in the global impedance model of a certain machine;
 - Impedance contributions of newly installed hardware through comparative measurements over successive machine runs;
 - Non-conformities, malfunctioning or ageing equipment leading to a degradation of impedance and possibly undesired effects on the beam;
 - Main contributors to the global impedance and relative mitigation techniques to reduce them in view of upgrades.

Establishing detailed impedance models of machines would be useless if this information could not be fed in beam dynamics calculations capable of assessing beam stability under the effect of the impedance.

Therefore, the techniques of modeling of beam instabilities were discussed at length and reviewed in detail.

- Two-particle models are still being used and extended to new cases (to include space charge, feedback systems, chromaticity). They are fairly simple, didactic and capable of unveiling the basic physics mechanisms behind coherent instabilities. An interesting generalization of these models is the circulant matrix formalism (Bim-Bim code), which is based on a radial and azimuthal slicing of the longitudinal phase space making it effectively an N-particle model that takes into account the full complexity of the longitudinal phase space structure of the beam in the study of the transverse stability.
- Vlasov solvers are widely used (e.g. MOSES, NHTS, DELPHI) to explore stability areas of complex machines in multi-dimensional parameter spaces. Their advantages and disadvantages were highlighted. Solvers of this type are:
 - Fast and suited to parameter scans;
 - Able to reveal slow growing modes;
 - Usually based on approximations/simplifications that need to be kept in mind before drawing strong conclusions from their results.
- Macroparticle simulations are also widely used (e.g. PyHEADTAIL, Elegant, COMBI, BLonD) and benefit from the increasing computing power that makes this approach more and more attractive. They:
 - Are relatively simple to implement and to be extended to include several effects (e.g. active loops, feedforward);
 - Provide full 6D monitoring of the beam evolution and their outputs can be used to make direct comparisons with beam measurements (e.g. pick up signals, emittance evolution, Schottky, BTF);
 - Need an appropriate choice of the numerical parameters (based on physics as well as numerical considerations) and convergence studies;
 - Are limited by computational times (memory, CPU time) and have a limited observation window, which may conceal slow growing modes.

It was underlined how, while the main driver for beam instabilities is usually the machine beam coupling impedance, many other mechanisms then come into play and affect instability thresholds.

- Space charge: Models suggest it acts against the onset of Transverse Mode Coupling Instability, although some machine observations do not confirm this (e.g. the SPS TMCI thresholds). Besides, its influence on the loss of decoherence could play a detrimental role by helping coherent signals to remain long-lived.
- Beam-beam, electron cloud, ions: They have been clearly described as, and proved to be, exciters of coherent motion that couples not only different bunches but

also head and tail of single bunches. On the other hand they also introduce important betatron tune spreads that should counteract the onset of beam instabilities. Including these mechanisms in the wake/impedance formalism is not straightforward, and maybe not even possible. However, the dynamics of these effects, together with the interplay between them and with the machine impedance, is in many cases fundamental to build a global picture of beam stability.

Finally, several mechanisms to suppress beam instabilities and potentially extend the performance reach of present and future machines were reviewed and illustrated, covering in particular the items listed below.

- Optimise machine optics, both linear and nonlinear, for collective effects. This has been shown to be the key to several knobs to reduce sensitivity to coherent motion, in particular:
 - Setting of tunes and linear chromaticities;
 - Control of nonlinear chromaticity, for instance its second order term Q'' ;
 - Use of octupoles to generate transverse amplitude detuning;
 - Control of linear coupling, which can be beneficial, when transferring more stability from one transverse plane to the other, or detrimental, when it moves the coherent tunes out of the range for Landau damping;
 - Change of the transition energy.
- Rely on Landau damping by using conventional methods like octupole detuning or by exploring the efficiency of novel sources of betatron tune spread like Radio Frequency Quadrupole (RFQ) or electron lenses, which have not been yet used for this purpose in running machines but hold promise for upgrades and future machines.
- Employ feedback systems to damp coherent instabilities. Typically, the bandwidth of these systems have made them suitable to suppress coupled bunch instabilities of dipolar type, but they have remained inefficient against single bunch instabilities with strong head-tail coupling. However, in their most cutting edge development, these systems have been demonstrated to be capable of damping transverse intra-bunch modes for short bunches (which requires high bandwidth and a complex electronics chain) or quadrupolar type oscillations in the longitudinal plane (which requires special configuration of the hardware and could be of uttermost interest for machines like the CERN PS).

CONCLUSIONS AND FUTURE

To conclude, the workshop provided a great platform to expose and debate all the scientific questions above, while at the same time it gave the participants a chance to enjoy the atmosphere and the sense of community fostered by the intense social program, which included a tour of the archaeological site of Pompeii and a concert performed by Trio Pragma, at the Museum of Sannio.

The subject of beam instabilities and instability sources in particle accelerators (e.g., impedance, electron cloud, ions) is far from being exhausted and the community is motivated to exchange experience and join efforts to advance further. The amount of open questions, the continuing progress recorded on different fronts and the promising outlook of many studies in terms of development and search for solutions fully legitimate the quest to pursue this series of workshops and to envisage a continuation in two or three years time.

More information on this workshop, including program and slides of the single talks, can be found on the [web site](#) and [Indico page](#) of the workshop.

ACKNOWLEDGMENTS

We would like to thank all the workshop participants, in particular all the speakers, the session chairs and the scientific secretaries, who gave their active contributions to the success of the event. Concerning these proceedings, we also would like to give special thanks to all those who took their time to contribute both as authors and as internal referees. Finally, we would like to express our gratefulness to the local organising committee, composed by G. Barbati, M. Caldora, E. Carideo and A. Pepiciello.

THE IMPEDANCE OF FLAT METALLIC PLATES WITH SMALL CORRUGATIONS[§]

K. Bane[¶], SLAC National Accelerator Laboratory, Menlo Park, CA, USA

Abstract

This report summarizes recent work on using a device composed of two flat, metallic plates with small corrugations (sometimes called a dechirper) at the end of linac-based, X-ray free electron lasers (FELs) for energy chirp control and as a passive fast kicker. We present an analytical theory of the wakefields/impedances of such dechirpers, followed by comparisons with numerical simulations, and comparisons with measurements at the Linac Coherent Light Source (LCLS). We show that agreement in all cases was found to be excellent. The theoretical and simulation work presented includes work originally performed in collaboration with, in particular, G. Stupakov, I. Zagorodnov, and E. Gjonaj.

INTRODUCTION

The RadiaBeam/SLAC dechirper has been installed and commissioned at the Linac Coherent Light Source (LCLS) [1]. It consists of two pairs of flat plates with small corrugations, with the beam passing in between. The purpose of a dechirper is to compensate residual energy chirp—energy to longitudinal position correlation—just upstream of the undulator in a linac-based, free electron laser (FEL). The flat geometry allows for adjustment of strength of the dechirper; having both a horizontal and vertical module allows for cancellation of unavoidable quad wake effects. The LCLS, however, doesn't generally need extra chirp control; the installed dechirper has, instead, been used more as a fast kicker, to facilitate a two-color mode of operation [2].

Analytical formulas for the longitudinal and transverse wakes of a dechirper have been developed to make it easier to do parameter studies and to plan the effective use of the device [3]. These formulas are more accurate than results of perturbation calculations of the past [4]. Note that we are here interested in very short-range wakes/high frequency impedances: the typical rms bunch length $\sigma_z \sim 10 \mu\text{m}$, which implies that the typical frequency of interest is $f \sim c/(2\pi\sigma_z) = 5 \text{ THz}$ (c is the speed of light).

In this report we begin by introducing the concepts of wakefield and impedance, particularly in periodic structures and in flat geometry. Then we discuss the corrugated structure as a dechirper, the surface impedance approach to wake calculation, and how explicit analytical formulas for the wakes of the dechirper are obtained. This is followed by comparisons with numerical simulations and with measurements at the LCLS, and finally by a summary.

This report summarizes much of the theoretical work on the dechirper done together with G. Stupakov, I. Zagorodnov,

and E. Gjonaj. The comparison with measurements are taken from Ref. [5], [6]. The formulas of this report are given in Gaussian units; to change a wake or impedance to MKS units, one merely multiplies by $Z_0 c/(4\pi)$, with $Z_0 = 377 \Omega$.

WAKEFIELDS AND IMPEDANCES

Let us here limit consideration to periodic structures with boundaries made of metal or dielectrics; *e.g.* resistive pipes, dielectric tubes, periodic cavities. A driving charge Q passes at the speed of light c through such a structure. A test charge moves on a parallel trajectory, also at speed c , but at distance s behind. The longitudinal (point charge) wake, $w(s)$, is the (longitudinal) voltage loss of the test particle per unit charge Q per unit length of structure. Thus, the point charge wake, for structure period p , is

$$w(s) = -\frac{1}{Qp} \int_0^p E_z(z, t) \Big|_{t=(s+z)/c} dz, \quad (1)$$

with E_z the longitudinal electric field, z the longitudinal position, and t the time of the test particle.

The *bunch wake* is given by the convolution of the point charge wake and the (longitudinal) bunch distribution $\lambda(s)$:

$$W_\lambda(s) = -\int_0^\infty w(s')\lambda(s-s') ds'; \quad (2)$$

note that a value of $W_\lambda < 0$ means energy loss by the beam. The impedance, for wavenumber $k = 2\pi f/c$, is given by the Fourier transform of the wake, $\tilde{w}(k)$:

$$Z(k) = \tilde{w}(k) = \frac{1}{c} \int_0^\infty w(s)e^{iks} ds. \quad (3)$$

The transverse wakes and impedances, $w_y(s)$, $Z_y(k)$, which are concerned with the transverse force on the test particle, are defined analogously to the longitudinal ones.

Case of Flat Geometry

Typically we are interested in wakes of *pencil beams*, *i.e.* of beams with small transverse extent. In round (cylindrically symmetric) geometry it is known that, for particles near the axis, the longitudinal wake is (nearly) independent of their transverse positions, and the dominant transverse wake—the dipole wake—depends linearly on the offset of the driving particle. Consider, however, the flat geometry of two (longitudinally) corrugated infinite plates, with the aperture defined by $y = \pm a$. The transverse wakes and impedances, for particles near the axis, are of the form: [7]

$$w_y(s) = y_0 w_d(s) + y w_q(s), \quad w_x(s) = w_q(s)(x_0 - x), \quad (4)$$

with (x_0, y_0) the transverse offset of the driving charge, (x, y) that of the test charge.

[§] Work supported by the U.S. Department of Energy, Office of Science, Office of Basic Energy Sciences, under Contract No. DE-AC02-76SF00515.

[¶] kbane@slac.stanford.edu

Wakes at the Origin, at $s = 0^+$

For a periodic structure, the wake approaches a finite constant as $s \rightarrow 0$, $w_0 \equiv w(0^+)$, one that is independent of the properties of the boundary material. This has been shown to be true if the boundary is a resistive metal, a (metallic) disk-loaded structure, or a dielectric tube. It is probably generally true for boundaries made of metal or dielectric (see [8]; but not if the boundary is a plasma [9]). The constant w_0 depends only on the shape and size of the aperture (e.g. iris radius in disk-loaded RF structure) and on the (transverse) location of the particles. The same statement can be made about the slope of the transverse wakes at the origin w'_{y0} —for both the dipole and quad wakes discussed above.

For example, in a round structure, with the particles moving on axis, $w_0 = 4/a^2$, with a the radius of the aperture. However, for particles on axis in flat geometry, $w_0 = \pi^2/(4a^2)$, where here a represents the half-aperture of the structure.

One can see that, if one knows the impedance $Z(k)$, then w_0 is given by (c/π) times the area under $\text{Re}[Z(k)]$. However, one can obtain w_0 also from the asymptotic behavior of $Z(k)$ at high frequencies [10, 11]. The asymptotic impedance $Z_a(k)$ is related to the wake at the origin w_0 . By letting the wake $w(s) \approx H(s)w_0$, we find the asymptotic form

$$Z_a(k) = \frac{w_0}{c} \int_0^\infty ds e^{iks} = i \frac{w_0}{kc}, \quad (5)$$

where we have neglected the contribution to the integral at the upper limit. Thus if we know $Z(k)$, we can obtain w_0 by the relation [11]

$$w_0 = -ikcZ_a(k) = -ic \lim_{k \rightarrow \infty} kZ(k); \quad (6)$$

this procedure will yield a positive constant.

In the transverse case the wake starts at the origin linearly:

$$w_y(s) = H(s)w'_{y0}s, \quad (7)$$

with w'_{y0} the value of the slope of the wake at the origin. Substituting into the impedance formula, we find the form of the asymptotic impedance

$$Z_{ya}(k) = -i \frac{w'_{y0}}{c} \int_0^\infty ds s e^{iks} = i \frac{w'_{y0}}{ck^2}, \quad (8)$$

(where again we have neglected the contribution to the integral at the upper limit). Thus, from the high frequency impedance we obtain [11]

$$w'_{y0} = -ik^2 c Z_{ya}(k) = -ic \lim_{k \rightarrow \infty} k^2 Z_y(k), \quad (9)$$

which is a positive constant.

THE CONCEPT OF A DECHIRPER

In a linac-based, X-ray FEL, by the use of accelerating structures and chicanes, a low energy, low (peak) current beam (~ 10 MeV, ~ 100 A) is converted to one with high

energy and high current (~ 5 – 10 GeV, ~ 1 kA). After the last bunch compressor the beam is typically left with an energy–longitudinal position correlation (an energy “chirp”), with the bunch tail at higher energy than the head (see Fig. 1, the blue curve).

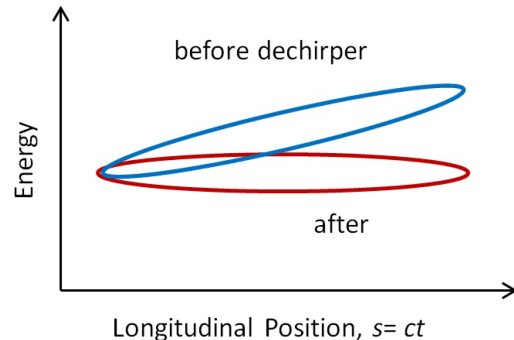


Figure 1: Sketch of typical longitudinal phase space of beam at the end of acceleration in a linac-based FEL, before the dechirper (blue), and after passing through the dechirper (red). The front of the bunch is to the left.

A typical value of chirp might be $\nu = 40$ MeV/mm. To cancel the chirp, one can run the beam off crest in downstream RF cavities. Running the beam on the zero crossing of the wave, we would need length $L_{rf} = \nu/(G_{rf}k_{rf})$ of extra RF. Or with peak RF gradient $G_{rf} = 20$ MeV/m, wave number $k_{rf} = 27/\text{m}$ (for frequency $f = 1.3$ GHz), we would need $L_{rf} = 74$ m of extra active RF. A dechirper is a passive way to achieve the same result in a few meters of structure.

An ideal dechirper would have the wake: $w(s) = w_0H(s)$, with $H(s) = 0$ (1) for $s < 0$ ($s > 0$). This is because at the end of an X-ray FEL the bunch distribution is (approximately) uniform: $\lambda(s) = H(s + \ell/2)H(\ell/2 - s)/\ell$, with ℓ the full bunch length. For an ideal dechirper and a uniform bunch distribution we find that Eq. 2 yields, $W_\lambda(s) = -w_0s/\ell$, which is linear in s , with the tail losing the most energy. The induced chirp is $\nu = -QLw_0/\ell$, with Q bunch charge and L the length of structure. Note that a resistive beam pipe or periodic (passive) RF cavities do not work well as dechirpers, since the wake $w(s)$ drops quickly as s moves away from the origin.

Corrugated Structure as Dechirper

A metallic pipe with small corrugations (see Fig. 2) can function as a good dechirper for an X-ray FEL [12]. Ideally we would like $h, p \ll a$, and it is important that $h \gtrsim p$. If $h, p \ll a$, then perturbation solutions exist; in the case of round geometry, the wake is dominated by a single mode: $w(s) \approx H(s)w_0 \cos ks$, with $w_0 = 4/a^2$ and $k = \sqrt{2p/ah}$ [13].

As an example calculation we consider the beam properties of the NGLS project [14], where $Q = 300$ pC and $\ell = 150$ μm . We performed a time-domain wake calculation using I. Zagorodnov’s ECHO code [15] for (round) dechirper parameters $a = 3$ mm, $h = 0.45$ mm, $p = 1$ mm, $t = p/2$,

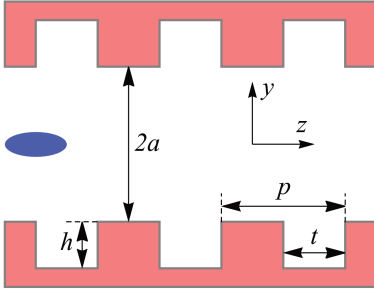


Figure 2: Geometry of a dechirper showing three corrugations. The blue ellipse represents an electron beam propagating along the z axis. For the RadiaBeam/SLAC dechirper, (typical) half-gap $a = 0.7$ mm, $h = 0.5$ mm, $p = 0.5$ mm, and $t = 0.25$ mm.

and $L = 8.2$ m. In Fig. 3 we show the numerical result (the blue curve), the analytical result (the dashed red line), and the bunch shape (in black, with the head to the left). We see that the numerical result, over the core of the beam, agrees well with the analytical one.

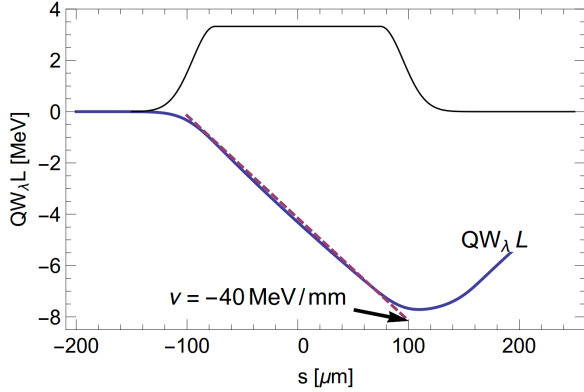


Figure 3: Dechirper for NGLS [12]: wake of model of NGLS bunch distribution (blue). The dashed, red line gives the linear chirp approximation. The bunch shape λ , with the head to the left, is given in black.

Using a corrugated structure with flat geometry as dechirper has the advantage over round geometry in that the strength of interaction can be changed by simply changing the gap between the two plates. However, as we saw above, w_0 becomes weaker (for the same aperture). In addition, an unavoidable quad wake is excited, even when the beam is on axis; its effect, however, can simply be canceled by having half the dechirper oriented horizontally and half vertically. This, in fact, is the configuration of the RadiaBeam/SLAC dechirper that is installed in the LCLS.

SURFACE IMPEDANCE APPROACH

To find the impedance of a structure like the dechirper one can use the method of field matching (see *e.g.* [16]). However, if the corrugations are small ($h \ll a$), the fields

excited by the driving particle can typically be solved using a simpler method, a surface impedance approach [7]. According to this method, on the walls we let

$$\tilde{E}_z(k) = \zeta(k)\tilde{H}_x(k), \quad (10)$$

with $\zeta(k)$ the surface impedance; and E, H , are the electric and magnetic fields. We solve Maxwell's equations (in the frequency domain) for the fields excited by the point driving charge. For flat geometry calculation we perform also the Fourier transform in x of the fields, *e.g.* for the magnetic field we use

$$\hat{H}_x(q) = \int_{-\infty}^{\infty} dx \tilde{H}_x e^{iqx}. \quad (11)$$

We finally obtain the flat geometry *generalized impedances*, *i.e.* impedances where the transverse positions of driving and test particle can be located anywhere within the aperture. The longitudinal generalized impedance can be written in the form: [3]

$$Z(x_0, y_0, x, y, k) = \int_0^{\infty} dq f(q, y, y_0, k, \zeta) e^{-iq(x-x_0)}, \quad (12)$$

where f is an explicit, analytical function of its arguments. The transverse generalized impedance is given in the same form, with a different (explicit analytical) function in the integral, $f_y(q, y, y_0, k, \zeta)$. Finally, the wake is obtained by numerically performing the inverse Fourier transform. Thus, by performing two numerical integrals, we obtain an estimate of the generalized longitudinal and transverse wakes. A subset of these results, one in which we are normally interested, is the special case of pencil beams, *i.e.* the case where $x \approx x_0, y \approx y_0$.

For the case of a beam passing near a single plate, we begin with the impedance for two plates separated by distance $2a$. In the expression for $f(q, y, y_0, k, \zeta)$ described above we let $y = a - b$ and then $a \rightarrow \infty$. Using the new version of f and performing the same integrals as before, we obtain the wakes of a beam passing by a single dechirper jaw at distance b .

The only problem with using the surface impedance approach for the calculation of the RadiaBeam/SLAC dechirper is that it normally is valid only if $(h/a) \ll 1$, whereas here nominally $(h/a) = (0.5/0.7) = 0.7 \not\ll 1$ (and similarly for the single jaw case). However, for the short, LCLS-type bunches—with rms length of 10's of microns—we demonstrate below that this approach still works when used with a surface impedance that represents the wall corrugations at high frequencies.

EXPLICIT ANALYTICAL APPROXIMATIONS OF WAKES

We have further simplified the results by extracting (analytical) parameters and using simplified formulas for cases of pencil beams. In the *zeroth order* approximation [11], we let $w(s) = H(s)w_0$, where w_0 is obtained using Eqs. 6, 12 (longitudinal case), and $w_y(s) = H(s)w'_{y0}s$, where w'_{y0} is obtained using Eqs. 9, 12 (using f_y ; transverse case).

For better agreement with results obtained directly from Eq. 12 and with numerical simulations, we use the *first order* approximation [3], which in the longitudinal case is of form

$$w(s) = H(s)w_0e^{-\sqrt{s/s_0}}. \quad (13)$$

Parameter s_0 can also be derived in analytical form from the structure of the impedance at high frequencies. Equation 13 corresponds to the two-term, Taylor expansion:

$$Z(k) \approx i \frac{w_0}{kc} \left[1 - \frac{(1+i)}{\sqrt{2ks_0}} \right] \quad (k \rightarrow \infty). \quad (14)$$

Thus, to obtain parameter s_0 , we begin with general form of the impedance (Eq. 12), and substitute in the high frequency surface impedance for the corrugated structure [3, 17]

$$\zeta(k) = \frac{1}{\alpha p} \left(\frac{2it}{\pi k} \right)^{1/2}, \quad (15)$$

with $\alpha \approx 1 - 0.465\sqrt{t/p} - 0.070(t/p)$. We then expand to two terms in Taylor series (at high k), integrate over dq , and find s_0 by comparing with the form of Eq. 14. A similar procedure is followed for the transverse (dipole and quad) wakes; in this case, the wake is of the form

$$w_y(s) = 2H(s)w'_{0y}s_{0y} \left[1 - \left(1 + \sqrt{\frac{s}{s_{0y}}} \right) e^{-\sqrt{s/s_{0y}}} \right], \quad (16)$$

with parameters w'_{0y} and s_{0y} . Note that the analytical forms for the longitudinal and transverse, short-range wakes (Eqs. 13, 16) have been used before, for the case of periodic, disk-loaded accelerating structures [18, 19]; a major difference, however, was that the parameters s_0 and s_{0y} were there obtained through fitting to numerical results.

We now give results for two specific example calculations. In the first example we consider a short beam on the axis of a two-plate dechirper and find the quad wake, where the two analytical wake parameters are given by [3]

$$w'_{0q} = \frac{\pi^4}{32a^4}, \quad s_{0q} = \frac{a^2t}{2\pi\alpha^2p^2} \left(\frac{15}{16} \right)^2. \quad (17)$$

We consider the RadiaBeam/SLAC dechirper parameters with half-gap $a = 0.7$ mm, and a Gaussian driving bunch with $\sigma_z = 10$ μm . We obtain the zeroth and first order analytical bunch wakes by performing the convolution Eq. 2. The analytical and numerical results of ECHO(2D) [20] are shown in Fig. 4. We see that the agreement of the 1st order analytical result and the numerical one is quite good.

Our second example considers the dipole wake of a beam offset by distance b from one plate. For this case the wake parameters are given by [21]

$$w'_{0d} = \frac{1}{b^3}, \quad s_{0d} = \frac{8b^2t}{9\pi\alpha^2p^2}. \quad (18)$$

In Fig. 5 we plot, as functions of b , the analytically obtained (1st order) kick factor κ_{yd} —the average of the bunch

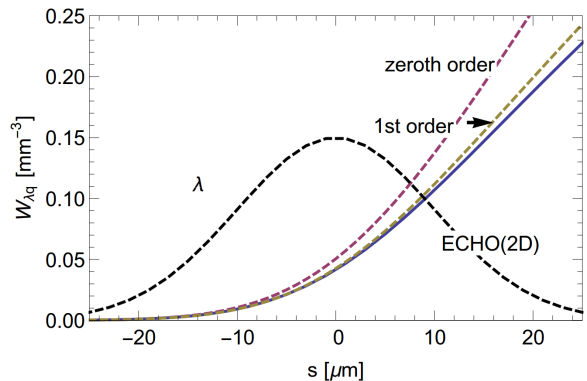


Figure 4: Quad bunch wake for a Gaussian beam on axis, with $\sigma_z = 10$ μm , $a = 0.7$ mm, in the RadiaBeam/SLAC dechirper [3]. Given are the numerical results of ECHO(2D) (blue), and the analytical zeroth order (magenta) and 1st order results (olive). The bunch shape $\lambda(s)$ is shown in black.

wake $W_{\lambda d}(s)$ —and the numerical result obtained using CST Studio [22]. The bunch here is Gaussian with length $\sigma_z = 100$ μm . We see from the figure that the agreement of the analytical and numerical calculations is very good.

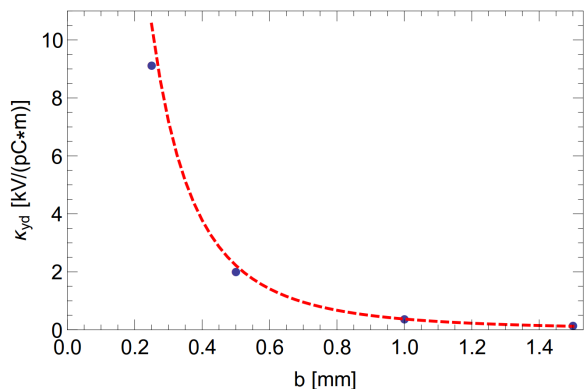


Figure 5: Single plate dipole kick factor κ_{yd} as function of distance of the beam from the wall b , showing the CST results (blue symbols) and those of the 1st order analytical model (red dashes) [23]. The bunch is Gaussian with length $\sigma_z = 100$ μm .

MEASUREMENTS

One example measurement of the longitudinal effect of the beam on axis between the jaws of both dechirper modules is shown in Fig. 6. Here $Q = 190$ pC, energy $E = 4.4$ GeV, and dechirper half gap $a = 1.2$ mm. The X-band, deflecting cavity diagnostic, XTCAV, measures longitudinal phase space of the bunch after the undulator in the LCLS. From it, we obtain the longitudinal bunch distribution $\lambda(s)$ and the induced energy chirp $\Delta E(s)$ due to the dechirper, by taking the average energy at position s minus that when the dechirper jaws are wide open. Here the bunch shape is ap-

proximately uniform, with peak current $I = cQ\lambda = 1.0$ kA. For the calculation we convolve the measured $\lambda(s)$ with the analytical $w(s)$ (see Eq 2), noting that $w_0 = \pi^2/(4a^2)$ and $s_0 = 9a^2t/(8\pi\alpha^2p^2)$; then $\Delta E = eQW_\lambda L$, with $L = 4$ m, the length of dechirper. In Fig. 6 the measured chirp using XTCAV (with arbitrary horizontal and vertical offsets) is given in blue, the calculation (with the head of the bunch at $t \equiv s/c = -85$ fs) is given in red dashes. We see that the agreement in induced chirp is good.

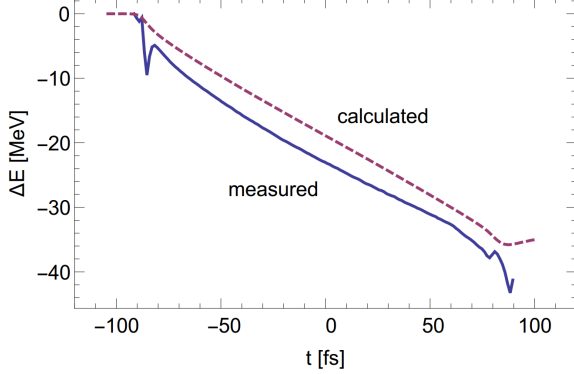


Figure 6: Chirp induced in beam passing on axis between the jaws of both dechirper modules, according to measurement (blue) and calculation (red dashes) [5]. Here $Q = 190$ pC, $I = 1.0$ kA, $E = 4.4$ GeV. The bunch head is to the left.

In the next example the beam was kept fixed, half the dechirper (the horizontal half) was scanned across the beam (keeping the half-gap a fixed), while the other half (the vertical half) was opened wide, and the transverse kick was measured. The parameters are half gap $a = 1$ mm, bunch charge $Q = 152$ pC, and energy $E = 6.6$ GeV. The results are given in Fig. 7, where we plot the offset at a downstream BPM, Δx_w vs. offset of the beam from the axis in the dechirper, x . The figure shows the data (plotting symbols) and the calculations (the curves). The bunch shape as obtained by measurement (with head to the left), is given in the inset plot. For the scale of the wake effect, note that a value of $\Delta x_w = 0.4$ mm corresponds to an average kick of $V_x = 160$ kV.

For the comparison calculations, we first numerically performed the convolution of Eq. 2 to obtain the bunch wake; then the result is given by $\Delta x_w = eQW_{\lambda x}L_{BPM}/E$, with L_{BPM} ($= 16.26$ m) the distance between dechirper and measuring BPM (the dashed curve in the figure). For the analytic curves, the gap parameter was reduced by 11% to fit the experimental data. The agreement between theory and measurements is good; the discrepancy in scale is small. In aligning the structure, the ends of the plates are independently adjusted; one possible cause of the discrepancy is that, during measurement, the jaws have an unknown residual tilt.

The final example is a single jaw measurement of downstream offset due to transverse kick, Δx_w vs. beam offset in dechirper, b (see Fig. 8). Note that $\Delta x_w > 0$ indicates a kick toward the jaw, and a value of $\Delta x_m = 0.6$ mm cor-

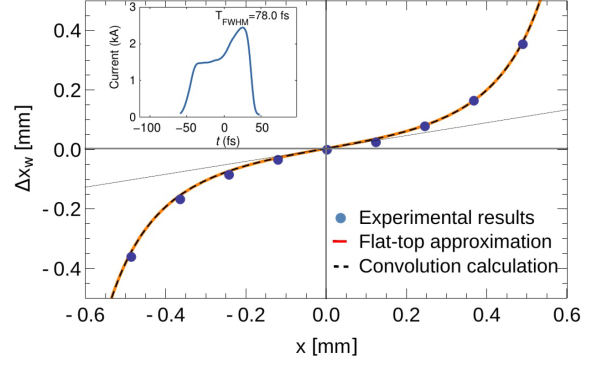


Figure 7: Downstream deflection, Δx_w , as function of offset in the (horizontal) dechirper, x , for half-gap $a = 1$ mm [6]. Here $Q = 152$ pC, $E = 6.6$ GeV. For the analytic curves, the gap parameter was reduced by 11% to fit the experimental data. The bunch current, with head to the left, is shown in the inset.

responds to a kick of $V_x = 480$ kV. The beam parameters were charge $Q = 180$ pC, peak current $I = 3.5$ kA, and energy $E = 13$ GeV. The absolute offset of the beam from the dechirper plate is not well known. Therefore, a fit of the model to the measurement was performed, where an overall shift in beam offset Δb was allowed. We see that the fit of the theory (the curve) to the data (the plotting symbols) is good. The fit gives an overall shift of $\Delta b = -161$ μm , and the data in the plot has been shifted by this amount. During this measurement, the longitudinal wake effect was simultaneously recorded, using a downstream BPM at a location of dispersion. The agreement between the longitudinal theory and measurement was again good, when an overall shift of $\Delta b = -138$ μm was assumed in the theory. The fact that, in both cases, the theory and measurement curves agree well, and that the fitted shifts are close to each other, is confirmation of our wake models and of our analysis.

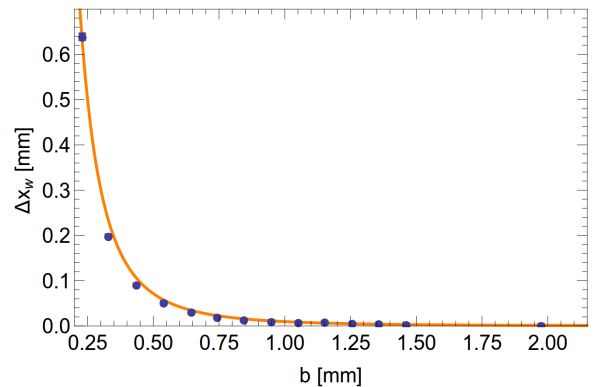


Figure 8: Downstream deflection, Δx_w as functions of beam offset from a single dechirper plate, b [6]. Here $Q = 180$ pC, $I = 3.5$ kA, $E = 13$ GeV. The symbols give the data points, with their b values shifted by -161 μm ; the curves give the analytical theory.

SUMMARY

The corrugated, metallic structure can be used for passive chirp control at the end of a linac-based, X-ray FEL. It can also be used as a fast kicker, to facilitate two-color, fresh-slice operation of an FEL such as the Linac Coherent Light Source (where it is regularly being used for this purpose). Using the surface impedance approach, we are able to obtain analytical solutions for the wakes of the structure: longitudinal, dipole, quad wakes; two-plate case, on axis and off; and single plate case. These wakes agree well with numerical simulations for LCLS-type beam parameters, in spite of the fact that the corrugation perturbation is often not small. They also agree quite well with measurements performed using the RadiaBeam/SLAC dechirper at the LCLS.

More comparisons with numerical simulations can be found in [3, 23], with measurements in [5, 6].

REFERENCES

- [1] P. Emma et al, “First lasing and operation of an angstrom-wavelength free-electron laser,” *Nat. Photon* **4** 641–647 (2010).
- [2] A. Lutman et al, “Fresh-slice multi-colour x-ray free-electron lasers,” *Nat. Photon.* **10**, 745–750 (2016).
- [3] K. Bane, G. Stupakov, I. Zagorodnov, “Analytical formulas for short bunch wakes in a flat dechirper,” *Phys. Rev. Accel. Beams* **19**, 084401 (2016).
- [4] K. Bane and G. Stupakov, “Impedance of a rectangular beam tube with small corrugations,” *Phys. Rev. Accel. Beams* **6**, 024401 (2003).
- [5] M. Guetg et al, “Commissioning of the RadiaBeam/SLAC dechirper,” in *Proc. IPAC’16*, Busan, Korea, May 2016, pp. 824–826.
- [6] J. Zemella et al, “Measurement of wake-induced electron beam deflection in a dechirper at the Linac Coherent Light Source,” *Phys. Rev. Accel. Beams* **20**, 104403 (2017).
- [7] K. Bane and G. Stupakov, “Using surface impedance for calculating wakefields in flat geometry,” *Phys. Rev. ST Accel. Beams* **18**, 034401 (2015).
- [8] S. Baturin and A. Kanareykin, “Cherenkov Radiation from Short Relativistic Bunches: General Approach,” *Phys. Rev. Lett.* **113**, 214801 (2014).
- [9] G. Stupakov, “Short-range wakefields generated in the blowout regime of plasma-wakefield acceleration,” arXiv:1710.07371 [physics.acc-ph], October 2017.
- [10] R. Gluckstern, “Longitudinal impedance of a periodic structure at high frequency,” *Phys. Rev. D* **39**, No. 9, 2780–2783 (1989).
- [11] K. Bane and G. Stupakov, “Dechirper wakefields for short bunches,” *Nucl. Instrum. Meth. A* **820**, 156–163 (2016).
- [12] K. Bane and G. Stupakov, “Corrugated pipe as a beam dechirper,” *Nucl. Instrum. Meth. A* **690**, 106–110 (2012).
- [13] K. Bane and A. Novokhatski, “The Resonator impedance model of surface roughness applied to the LCLS parameters,” LCLS-TN-99-1, March 1999.
- [14] J.N. Corlett et al, “Design Studies for a VUV-Soft X-ray FEL Facility at LBNL,” in *Proc. IPAC’10*, Kyoto, Japan, May 2010, pp. 2639–2641.
- [15] I. Zagorodnov and T. Weiland, “TE/TM field solver for particle beam simulations without numerical Cherenkov radiation,” *Phys. Rev. ST Accel. Beams* **8**, 042001 (2005).
- [16] Z. Zhang et al, “Electron beam energy chirp control with a rectangular corrugated structure at the Linac Coherent Light Source,” *Phys. Rev. ST Accel. Beams* **18**, 010702 (2015).
- [17] G. Stupakov, “Coupling impedance of a periodic array of diaphragms,” in *Proc. PAC’95*, Dallas, TX, May 1995, p. 3303.
- [18] K. Bane, A. Mosnier, and A. Novokhatskii, “Calculations of the Short-Range Longitudinal Wakefields in the NLC Linac,” SLAC-PUB-7862 (Revised), November 1998.
- [19] K. Bane, “Short range dipole wakefields in accelerating structures for the NLC,” SLAC-PUB-9663, March 2003.
- [20] I. Zagorodnov, K. Bane, and G. Stupakov, “Calculation of wakefields in 2D rectangular structures,” *Phys. Rev. ST Accel. Beams* **18**, 104401 (2015).
- [21] K. Bane, G. Stupakov, and I. Zagorodnov, “Wakefields of a Beam near a Single Plate in a Flat Dechirper,” SLAC-PUB-16881, November 28, 2016.
- [22] CST-Computer Simulation Technology, CST Particle Studio, <http://www.cst.com>.
- [23] K. Bane, G. Stupakov, and E. Gjonaj, “Joule heating in a flat dechirper,” SLAC-PUB-16922, February 2017.

NEW LONGITUDINAL BEAM IMPEDANCE FORMULA WITH 8 TERMS

O. Berrig, F. Paciolla
 CERN, CH-1211 Geneva, Switzerland

Abstract

A previous formula for longitudinal beam impedance was developed by S. Heifets, A. Wagner and B. Zotter and consists of 13 terms. The formula by Heifets, Wagner and Zotter is developed up to terms of second order in the transverse offsets. In this report we develop a new formula, which use symmetries from the Lorentz reciprocity principle and the multipolar decomposition of transverse fields to reduce the number of terms from 13 to 8. This new formula is also developed up to second order, but could of course be developed up to any higher order. The transverse beam impedances (for horizontal and vertical planes) can be by obtained by differentiation of this new formula.

INTRODUCTION

The previous formula for the longitudinal impedance by S. Heifets, A. Wagner and B. Zotter in Ref. [1] (See also Ref. [2]) and it gives the longitudinal beam coupling impedance as a function of the position of the transverse positions of the drive and test particles (See Ref. [3] for a definition of the drive and test particles). The new formula shown in this paper is based on additional constrains to Heifets, Wagner and Zotter's formula. These constraints comes from two physical principles: *The Lorentz reciprocity principle* and the *Multipolar expansion of 2D fields*. It is important to note that both the Heifets, Wagner and Zotter formula and the new formula gives the beam coupling impedance only - neither includes direct nor indirect space charge impedance.

The Lorentz reciprocity principle

The Lorentz reciprocity principle says that the longitudinal beam impedance must stays unchanged if the drive and test particles are interchanged. The principle can be illustrated with two antenna. Injecting a current in the first antenna will give a voltage on the second antenna. Reversing the situation, and now injecting the same current in the second antenna, we will get exactly the same voltage in the first antenna as we had in the second antenna (see Fig. 1):

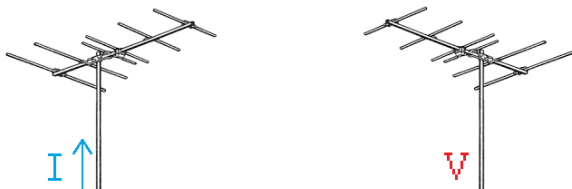


Figure 1: Injecting a current in the antenna to the left, will induce a voltage in the antenna to the right. The Lorentz reciprocity principle says that injecting the same current in the antenna to the right will produce exactly the same voltage in the antenna to the left.

The Lorentz reciprocity principle describes what is also called the mutual impedance. Mutual impedance is best illustrated by transformers. (see Fig. 2). In this example a current I_1 (this is an oscillating current) is injected on the primary winding. This current will induce a flux $\vec{I}\vec{E}$ in the iron core: $\phi = B \cdot A$, where ϕ is the flux, B is the B-field and A is the area of the transformer core. Using Amperes law: $\oint_C B dl = \mu_0 \mu_r I_1 \cdot N_1$, where C is the circumference of the transformer; μ_0 and μ_r are the permeability of free space and the relative permeability of the iron in the transformer; I_1 is the current in the primary winding and N_1 is the number of windings on the primary side. Making the approximation that the circumference is everywhere the same, then the flux will be: $\phi = A \cdot \mu_0 \mu_r \cdot \frac{N_1}{C} \cdot I_1$. The induced voltage on the secondary windings from this flux is: $V_2 = -N_2 \cdot \frac{d\phi}{dt} = -A \cdot \mu_0 \mu_r \cdot \frac{N_1 \cdot N_2}{C} \cdot \frac{dI_1}{dt}$. With a similar argument, the voltage on the primary winding can be calculated as a function of the secondary current: $V_1 = -A \cdot \mu_0 \mu_r \cdot \frac{N_1 \cdot N_2}{C} \cdot \frac{dI_2}{dt}$. If I_1 is identical to I_2 then the voltages V_1 and V_2 will also be identical and the Lorentz reciprocity principle is shown for a transformer.

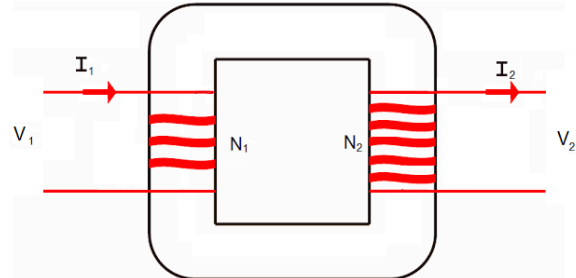


Figure 2: Injecting the current “ I_1 ” in the primary winding, will give a voltage “ V_2 ” on the secondary winding. In the same way, if we would inject the same current in the secondary winding, the voltage on the primary winding would be exactly the same. The Lorentz reciprocity principle is clear if the number of windings would have been the same on both the primary and secondary sides, because then currents and voltages would also be the same on both sides.

It is interesting to note that the beam impedance coming from the wall currents is more precisely called the beam coupling impedance. The reason is that a beam going through a vacuum chamber represents a current. This current will induce currents on the chamber walls, because just like a transformer they are coupled like the currents in the primary (i.e. the the beam current) and secondary windings (i.e. the wall currents) of a transformer.

Whether the path of the drive particle works as the transmitting antenna while the path of the test particle works as

the receiving antenna or vice-versa i.e. The longitudinal beam coupling impedance is the same when the drive and test particle positions are interchanged: $Z_{||}(x_d, x_t, y_d, y_t) = Z_{||}(x_t, x_d, y_t, y_d)$. This feature was already documented by S.Heifets and B.Zotter in Ref. [4].

Multipolar expansion in 2D

Multipolar expansion is described in Ref. [5] and the expansion in cartesian coordinates is detailed in Ref. [6]. Multipolar expansion is well known for accelerator magnets, where e.g. dipole magnet bends the beam in circular trajectories, and quadrupolar magnets (i.e. 4 poles, 2 North and 2 South) acts as special bending magnets that bends the beam more the further the beam is from the center. Fig. 3 shows the shape of the fields. For each order of multipole there are two types of fields, called Normal and Skew fields. The Normal or Skew types of field depends on the azimuthal angle of the magnet:

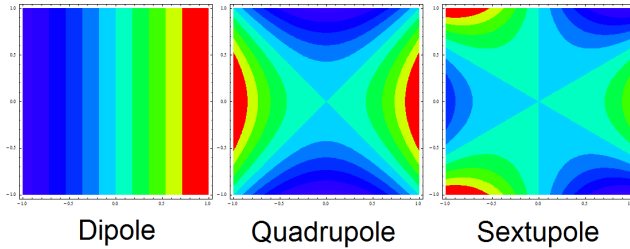


Figure 3: **Normal** field patterns up to third order for respectively a dipole, quadrupole and sextupole magnet. The potentials are:

$$\text{Dipole: } x \quad \text{Quadrupole: } \frac{x^2}{2} - \frac{y^2}{2} \quad \text{Sextupole: } \frac{x^3}{3} - xy^2$$

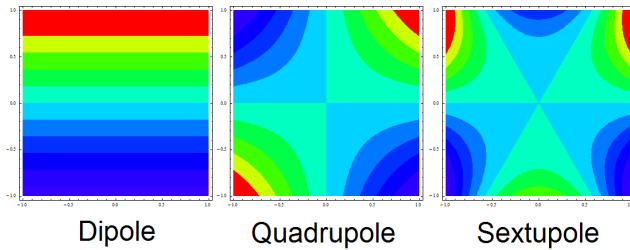


Figure 4: **Skew** field patterns up to third order for respectively a dipole, quadrupole and sextupole magnet. The potentials are:

$$\text{Dipole: } y \quad \text{Quadrupole: } x \cdot y \quad \text{Sextupole: } x^2 y - \frac{y^3}{3}$$

There is no limit to how high the order can be. In LHC there are correction magnets up to 12th order (Dodecapole). The idea of multipolar decomposition is the same as in Fourier Transforms, where a function is decomposed into a sum of Sin[] and Cos[] functions. The new formula for longitudinal beam coupling impedance has only terms up to second order i.e. only terms up to quadrupolar order are included. Please note that multipolar decomposition only works for realistic field patterns i.e. field patterns that occurs in nature. In this sense the decomposition is an analytical function (See Ref. [7]).

DERIVATION OF THE NEW FORMULA

Standard Taylor series evaluation, up to second order, gives the longitudinal beam coupling impedance with 15 terms. Each term consist of a function of frequency multiplied with a combination of transverse positions of the drive and test particles:

$$Z[x_d, x_t, y_d, y_t] = Z_1[w] + Z_2[w]x_d + Z_3[w]x_t + Z_4[w]y_d + Z_5[w]y_t + Z_6[w]x_d^2 + Z_7[w]x_t^2 + Z_8[w]y_d^2 + Z_9[w]y_t^2 + Z_{10}[w]x_dx_t + Z_{11}[w]x_dy_d + Z_{12}[w]x_dy_t + Z_{13}[w]x_t y_d + Z_{14}[w]x_t y_t + Z_{15}[w]y_d y_t$$

Using the multipolar decomposition, the following relations are obtained: $Z_6[w] = Z_7[w] = -Z_8[w] = -Z_9[w]$

The formula for the longitudinal beam coupling impedance is now reduced to 13 terms and these terms are identical to the terms in Heifets, Wagner and Zotter's formula (See Ref. [1] equation (24)). By using the Lorentz reciprocity principle i.e. that the longitudinal beam coupling impedance is the same when the drive and test particle positions are interchanged: $Z_{||}[x_d, x_t, y_d, y_t] = Z_{||}[x_t, x_d, y_t, y_d]$ the number of terms in the formula is reduced from 13 to 8 terms and the new formula is obtained:

$$\begin{aligned} Z_{||}[x_d, x_t, y_d, y_t] = & Z_0 \\ & + Z_{1,x}(x_d + x_t) + Z_{1,y}(y_d + y_t) \\ & + Z_{2,A}(x_d^2 + x_t^2 - y_d^2 - y_t^2) \\ & + Z_{2,B}(x_d y_d + x_t y_t) + Z_{2,C}(x_d y_t + x_t y_d) \\ & + Z_{2,D}(x_d x_t) + Z_{2,E}(y_d y_t) \end{aligned} \quad (1)$$

where x_d and y_d are the transverse positions of the drive particle i.e. generally the beam moves along the this path. x_t and y_t are the transverse positions of the test particle i.e. the induced voltage is measured along this path.

To illustrate the Lorentz reciprocity principle, a simulation with CST (See Ref. [8]) was done on a collimator type structure, see Fig. 5:

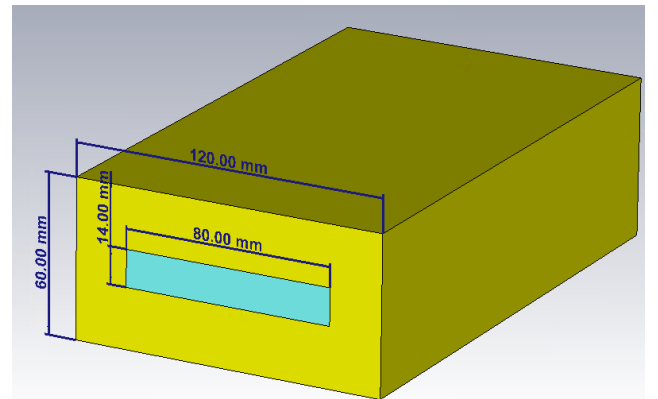


Figure 5: CST simulation of a collimator type structure. The jaws (yellow) have a conductivity of 10^5 [S/m]

where the jaws are made of lossy metal with a conductivity of 10^5 [S/m]. The result is shown in Fig. 6 and clearly demonstrates that the Longitudinal beam coupling impedance is

identical when the path of the drive and test particles are interchanged:

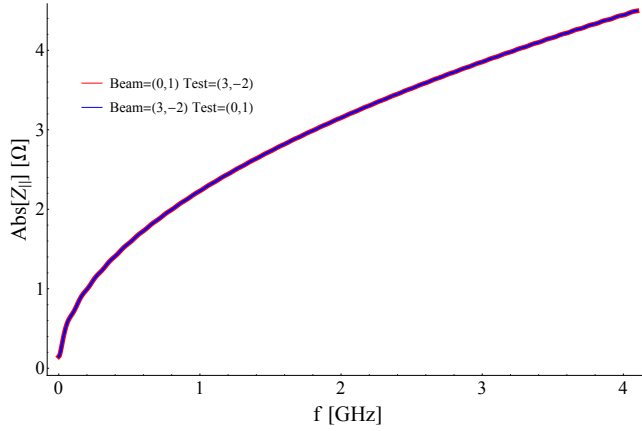


Figure 6: Result of the CST simulations of the collimator in Fig. 5. The longitudinal beam coupling impedance is identical when the path of the drive and test particles are interchanged. Red curve: The drive particle have the transverse coordinates: $(x,y)=(0,1)$ and the test particle has the coordinates: $(x,y)=(3,-2)$. Blue curve: The drive particle have the transverse coordinates: $(x,y)=(3,-2)$ and the test particle has the coordinates: $(x,y)=(0,1)$.

The new formula in equation (1) make several predictions, one of which is that changing the product $x_d y_d$ should give the same effect on the $Z_{||}$ as changing the product $x_t y_t$, i.e. both these product have the same coefficient $Z_{2,B}$. This is again illustrated with a CST simulation of the structure in Fig. 5, but this time the conductivity of the jaws is 10^2 [S/m]. This is done to avoid the classical thick wall regime, where the real and imaginary parts of $Z_{||}$ are always equal to each other. Using a conductivity in the jaws equal to 10^2 [S/m] ensures that the real and imaginary parts are different. The simulation result is shown in Figure 7:

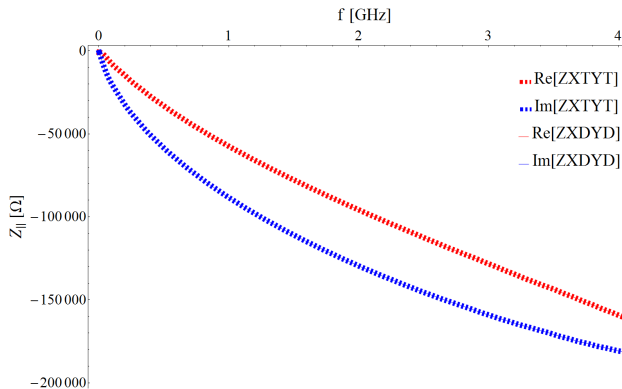


Figure 7: Result of the CST simulations of the collimator in Fig. 5 illustrating that the coefficient $Z_{2,B}$ is the same for both the product of XTYT as the product of XDYD.

The new formula in equation (1) for the longitudinal beam coupling impedance can, in combination with the

Panofsky-Wenzel theorem, be used to calculate the transverse impedances: $Z_{\perp,x} = \frac{\beta c}{\omega} \frac{dZ_{||}}{dx_t}$ and $Z_{\perp,y} = \frac{\beta c}{\omega} \frac{dZ_{||}}{dy_t}$.

Looking at the horizontal transverse beam impedance terms: $Z_{\perp,x} = Z_{1,x} + 2\frac{\beta c}{\omega} Z_{2,A} x_t + \frac{\beta c}{\omega} Z_{2,B} y_t + \frac{\beta c}{\omega} Z_{2,C} y_d + \frac{\beta c}{\omega} Z_{2,D} x_d$ we see the two well known transverse impedance terms, the dipolar impedance: $\frac{\beta c}{\omega} Z_{2,D}$ and the quadrupolar impedance: $2\frac{\beta c}{\omega} Z_{2,A}$.

Conventionally an equipment is characterized by only five parameters: Z_0 = Longitudinal impedance; $2\frac{\beta c}{\omega} Z_{2,D}$ = Dipolar impedance (horizontal plane); $2\frac{\beta c}{\omega} Z_{2,A}$ = Quadrupolar impedance (horizontal plane); $\frac{\beta c}{\omega} Z_{2,E}$ = Dipolar impedance (vertical plane) and finally $-2\frac{\beta c}{\omega} Z_{2,A}$ = Quadrupolar impedance (vertical plane). However, since the quadrupolar impedances for horizontal and vertical planes have the same amplitude, but opposite signs, there are in fact only four distinct parameters. To characterize an equipment with the above four parameters neglects the additional four other parameters: $Z_{1,x}$; $Z_{1,y}$; $Z_{2,B}$ and $Z_{2,C}$. Even though the parameters $Z_{1,x}$; $Z_{1,y}$; $Z_{2,B}$ and $Z_{2,C}$ are often zero because of symmetries (see next chapter SYMMETRIC VACUUM CHAMBERS AND THEIR EFFECT ON BEAM IMPEDANCE), they should not be forgotten in asymmetric structures.

SYMMETRIC VACUUM CHAMBERS AND THEIR EFFECT ON BEAM IMPEDANCE

Vacuum chamber symmetries will reduce the number of parameters in the longitudinal beam coupling impedance formula (1). A Left/right symmetric vacuum chamber gives $Z_{1,x} = 0$, $Z_{2,B} = 0$ and $Z_{2,C} = 0$. (this results from solving the equation: $Z_{||}[x_d, x_t, y_d, y_t] = Z_{||}[-x_d, -x_t, y_d, y_t]$) Similarly an up/down symmetric structure, see Figure 8, gives $Z_{1,y} = 0$, $Z_{2,B} = 0$ and $Z_{2,C} = 0$:

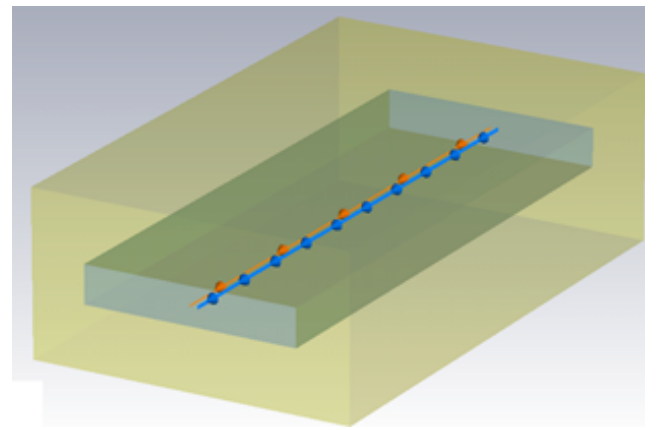


Figure 8: Up/Down symmetric structure. The transverse wake potentials of this structure is simulated with CST and the result of these simulations are shown in Fig. 9 and 10

For the Up/Down symmetric structure in Fig. 8 above, the transverse horizontal beam impedance is:

$$Z_{\perp,x} = Z_{1,x} + 2\frac{\beta c}{\omega} Z_{2,A} x_t + \frac{\beta c}{\omega} Z_{2,B} y_t + \frac{\beta c}{\omega} Z_{2,C} y_d + \frac{\beta c}{\omega} Z_{2,D} x_d$$

If $Z_{2,B}$ and $Z_{2,C}$ are zero, then the transverse horizontal wake potential should stay constant when the vertical position of either the drive- or the test particles are changed. This is illustrated in Fig. 9 and 10.

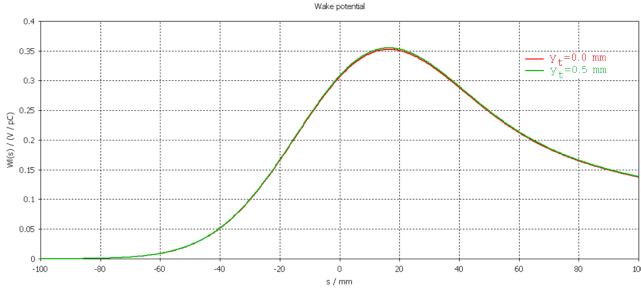


Figure 9: CST simulation of the transverse horizontal wake potential for the Up/Down symmetric structure in Fig. 8. The red curve is the transverse wake potential for $y_t = 0.0$ mm. The green curve is the transverse wake potential for $y_t = 0.5$ mm. Since the two curves are identical, $Z_{2,B}$ must be zero.

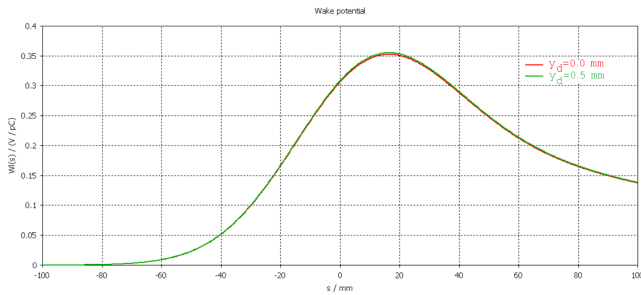


Figure 10: CST simulation of the transverse horizontal wake potential for the Up/Down symmetric structure in Fig. 8. as a function of the vertical position of the drive particle. The red curve is the transverse wake potential for $y_d = 0.0$ mm. The green curve is the transverse wake potential for $y_d = 0.5$ mm. Since the two curves are identical, $Z_{2,C}$ must be zero.

A 90 degrees symmetric structure, i.e. a structure which is unchanged when rotated by 90 degrees (see Fig. 11), only have dipolar transverse impedance.

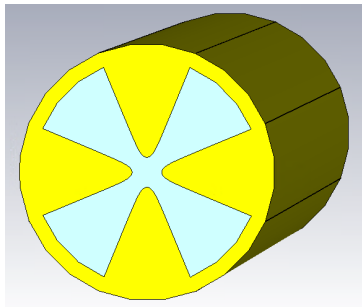


Figure 11: Structure with 90 degrees symmetry. Because of the 90 degrees symmetry, this structure only have dipolar beam impedance.

This means that only the horizontal dipolar term $Z_{2,D}$ and the vertical dipolar term $Z_{2,E}$ are different from zero while all the other transverse parameters:

$Z_{1,x}, Z_{1,y}, Z_{2,A}, Z_{2,B}$ and $Z_{2,C}$ are all zero (See Ref. [9]).

is interesting to note also that the horizontal and vertical dipolar terms are equal for 90 degrees symmetric structures $Z_{2,D} = Z_{2,E}$ - in fact the dipolar impedence is the same in any direction - i.e. independent of the angle that it is measured - see Fig. 12:

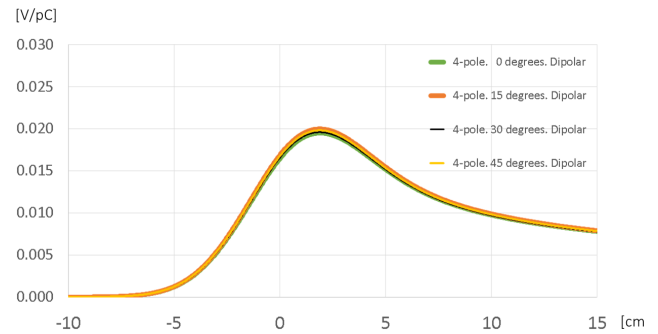


Figure 12: PBCI (See Ref. [10]) simulation of the 90 degrees symmetric structure in Fig. 11. The dipolar wakefields are identical for any rotation angle of the structure in Fig. 11, confirming that structures with 90 degrees symmetry have the same dipolar beam impedance in any direction. *Simulation courtesy of Dr. E. Gjonaj TU Darmstadt*

MORE WORK TO BE DONE

More work needs to be done to better understand the new formula for the longitudinal beam coupling impedance. The formula is presently developed to second order, but should be developed to third order, so that feed-down analysis can be done. Feed-down analysis will show the beam impedance if the beam does not go through the center, but is offset from the center. The principle of feed-down analysis is best known from accelerator magnets and is shown in Ref. [11].

It was shown recently that the quadrupolar beam impedance for circular vacuum chambers is only zero if the beam moves at ultra-relativistic speeds i.e. $\gamma = \infty$ (See Ref. [12]). The formula for the quadrupolar beam impedance per unit length, was gives as:
$$\frac{dZ_Y(quad)}{dz} = \frac{k_0 Z_s}{4\pi b \beta \gamma^2 I_0^2 \left(\frac{k_0 b}{\beta \gamma}\right)}$$
 and we can indeed see that it will only be zero if $\gamma \rightarrow \infty$. However, this formula looks very much like it describes a space charge beam impedance, and if this is indeed the case, then the new formula for the beam coupling impedance in (1) could still be true for $\gamma < \infty$, as it only describes beam coupling impedance and not space charge impedance.

Another *very interesting prospect* for multipolar expansion is that possibly one could eliminate all transverse beam impedance in collimators (and other structures) by shaping the collimator as a very high order multipole (See Ref. [13])

ACKNOWLEDGEMENTS

We are very grateful for Elias Metral to push for the publication of this research into multipolar decomposition. Great thanks to Christian Berrig, who explained the theory of analytic functions, and to Erion Gjonaj who spent quite some time simulating the 4-pole structure with PBCI as we could not get the simulation with CST to get precise results.

REFERENCES

- [1] S.Heifets(SLAC), A.Wagner(CERN), and B.Zotter(CERN), “Generalized impedances and wakes in asymmetric asymmetric structures,” SLAC, Tech. Rep. SLAC-AP-110, 1998. [Online]. Available: <http://inspirehep.net/record/466605/files/slac-ap-110.pdf>
- [2] H. Tsutsui, “On single wire technique for transverse coupling impedance measurement,” CERN, Tech. Rep. sl-note-2002-034. [Online]. Available: <https://cds.cern.ch/record/702715/files/sl-note-2002-034.pdf>
- [3] B. Salvant. (2010) Impedance model of the cern sps and aspects of lhc single-bunch stability. (See page 37 for definition of drive and test particles.). [Online]. Available: <https://cds.cern.ch/record/1274254/files/CERN-THESIS-2010-087.pdf>
- [4] S.Heifets(SLAC/CERN) and B.Zotter(CERN). (1999) On the symmetry of the impedance. [Online]. Available: <https://cds.cern.ch/record/410755/files/tua20.pdf>
- [5] (2018) Multipole expansion — Wikipedia, the free encyclopedia. [Online]. Available: https://en.wikipedia.org/wiki/Multipole_expansion
- [6] J. Jowett. (2012) Holomorphic decomposition. [Online]. Available: [\\cern.ch\dfs\Projects\LHC\MathematicaExamples\Accelerator\MultipoleFields.nb](https://cern.ch/dfs/Projects/LHC/MathematicaExamples/Accelerator/MultipoleFields.nb)
- [7] (2018) Analytical function — Wikipedia, the free encyclopedia. [Online]. Available: https://en.wikipedia.org/wiki/Analytic_function
- [8] CST. (2018) Computer Simulation Technology. [Online]. Available: <https://www.cst.com/>
- [9] O. Berrig. (2017) New research strongly indicates the elimination of transverse beam impedance by making beam equipment in the shape of higher order multipoles - continued. [Online]. Available: https://indico.cern.ch/event/677919/contributions/2776188/attachments/1561064/2457603/Higher_Order_BeamImpedance_OB_2.pptx
- [10] E. Gjonaj. (2017) Longitudinal and quadrupolar rw impedance in elliptic pipe. [Online]. Available: <https://agenda.infn.it/getFile.py/access?contribId=10&sessionId=1&resId=0&materialId=slides&confId=12603>
- [11] A. K. Jain. (1998) Basic theory of magnets. [Online]. Available: https://www.bnl.gov/magnets/staff/gupta/scmag-course/Talk1_manuscript.pdf
- [12] M. Migliorati. (2018) Longitudinal and quadrupolar rw impedance in elliptic pipe. [Online]. Available: https://indico.cern.ch/event/705550/contributions/2936076/attachments/1618400/2573379/20180316_RW_elliptic.pptx
- [13] O. Berrig. (2017) New research leading to possible elimination of transverse beam impedance by making beam equipment in the shape of higher order multipoles. [Online]. Available: https://indico.cern.ch/event/669352/contributions/2741966/attachments/1533263/2400784/Higher_Order_BeamImpedance_OB.pptx

2D AND 3D COLLIMATOR IMPEDANCE MODELING AND EXPERIMENTAL MEASUREMENTS

N. Biancacci, D. Amorim, S. Antipov, G. Mazzacano, B. Salvant, E. Métral,
CERN, Geneva, Switzerland

O. Frasciello, M. Zobov, INFN-LNF, Frascati, Italy

A. Mostacci, University of Rome “La Sapienza”, Rome, Italy

Abstract

In order to safely operate high energy particle accelerators, an advanced collimation system in terms of absorber material choice, alignment precision and low impedance impact is often required.

In this work we will summarize the recent advancement on collimator impedance modeling starting from simple 2D structures, involving resistive jaws and transition tapers, to complex 3D structures, involving multilayer coatings, embedded beam position monitors, contact fingers, and jaw segmentation.

Measurements techniques based on the stretched and resonant wire methods will be presented in order to support simulations, together with DC and RF resistivity measurements of the jaw material samples. Recent single collimator beam based measurements will be presented as well.

INTRODUCTION

Collimators are one of the most critical equipment in high energy particle accelerators: among several requirements [1], they are used to protect the sensitive machine elements from unavoidable regular and irregular beam losses (e.g. unforeseen beam loss on the superconducting magnets in the LHC); to remove high amplitude/momentum particles; to reduce beam-induced backgrounds in the experimental areas.

Modern collimators, as the one shown in Fig. 1, are constituted by two absorbing jaws of composite materials, RF fingers to ensure good electrical contact for any jaw gap aperture, tapered sections before the main jaws for beam coupling impedance reduction, embedded BPM buttons for fast alignment relative to the beam.

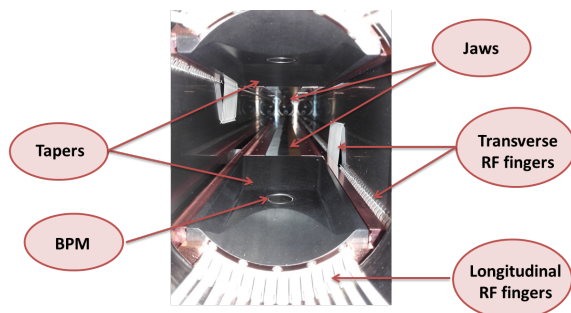


Figure 1: Example of a vertical collimator used for low impedance tests in the LHC: RF fingers, tapered transitions with embedded BPM buttons and main jaws are highlighted.

In the LHC, the collimation system is conceived in order to protect the machine from the 360 MJ circulating beams [1–3]. Two main cleaning points are present: IR3 for momentum and IR7 for betatron cleaning. Collimators are sequenced in a staged approach: primaries (TCP) intercept particles in the primary beam halo, secondaries (TCS) intercept particle scattered from the TCPs, shower absorbers (TCL) clean out remaining leakages from the previous stages. Together with these, additional collimators are installed to protect the machine against injection (TDI) and extraction (TCDQ) failures, and to protect the experiments (TCT) from remnant not cleaned particles.

Due to the proximity to the beam, the material resistivity and to the number of collimators, the LHC collimation system represents one of the major contributions to the total machine impedance budget [4] and contribute to a large fraction of the total octupole strength necessary to stabilize the beam against impedance related instabilities [5].

Due to the large impact on the LHC impedance budget, a careful estimation of the collimator impedance is mandatory in order to correctly predict the limits of stability in the context of the future HL-LHC project [6] when the beam intensity will be doubled with respect to the present LHC operational scenario [7]. This is also essential in order to quantify the possible gain in impedance reduction using different jaw materials or tapering geometry.

In the frame of impedance simulations, two approaches can be followed: a 2D or a 3D approach. In the following sections we will describe the approximations behind the two approaches together with comparisons with bench and beam measurements.

2D COLLIMATOR IMPEDANCE MODELING

A collimator can be approximated as a sequence of a tapered section, the main jaw and again a tapered section. This approach, of course, neglects any coupling between the elements, the possibility to develop resonant modes in the whole structure or the effect of the finite width and length of the collimator jaw. Nevertheless it has been proven to be sufficient for reproducing the impedance of the single device [8, 9] in dedicated LHC machine development sessions, and for quickly building the full LHC collimator impedance model for different settings scenarios. Moreover, it can be used to validate benchmark studies with 3D numerical solvers.

Taper impedance

The impedance of taper structures with arbitrary cross section was calculated by G. Stupakov in [10]. The dipolar impedance for a vertical taper with rectangular cross section is given by

$$Z_y^{dip} = \frac{jwZ_0}{4} \int_{-\infty}^{+\infty} \frac{(g')^2}{g^3} dz, \quad (1)$$

with w the width in the horizontal direction, $g = g(z)$ the gap of the taper in the vertical direction, $Z_0 = 120\pi$ the characteristic impedance of vacuum. The expression in Eq. (1) is valid for $g \ll w \ll l$ with l length of the tapered transition, and for relatively low frequencies. An extensive work of benchmark and optimization of the taper geometry for the LHC collimators was done in [11, 12]. Figure 2 shows the comparison of GdfidL [13] simulations against the formula of Eq. (1) for a flat tapered collimator transition: the agreement is very good. For reference, the simulations are also compared with the impedance computed with Yokoya's [14] model for a taper with circular cross-section as used in the early LHC impedance model: the impedance is seen to be drastically underestimated with respect to the flat taper model.

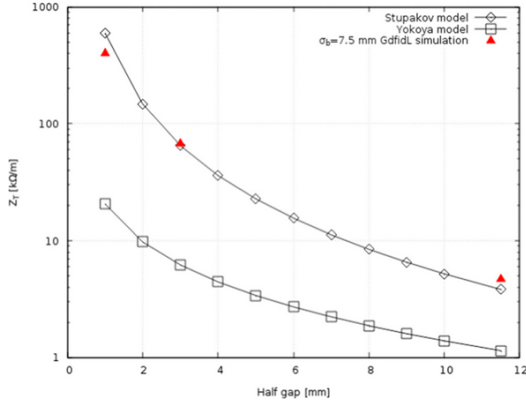


Figure 2: Effective vertical dipolar impedance for a flat tapered collimator transition: comparison of GdfidL simulations against Stupakov's and Yokoya's (round taper) models.

The impact on the overall impedance of the LHC collimators is shown in Fig. 3: below 10 mm half gap, the geometrical impedance starts contributing significantly with respect to the resistive wall impedance of the LHC secondary collimators whose jaw is made of Carbon Fiber Reinforced Carbon (CFC) composite. The contribution is also significant with respect to the tungsten (W) resistive wall impedance of the TCTs starting from 4 mm half gap.

Jaw resistive wall impedance

The jaw transverse resistive wall impedance is proportional to $\sqrt{\rho}/g^3$ with ρ the jaw resistivity [15] and it can be computed in detail considering a two parallel plates geometry with the IW2D code [16]: the code is based on field matching techniques and allows impedance calculation for an arbitrary number of layers with different material properties. The validity of the model has been checked against

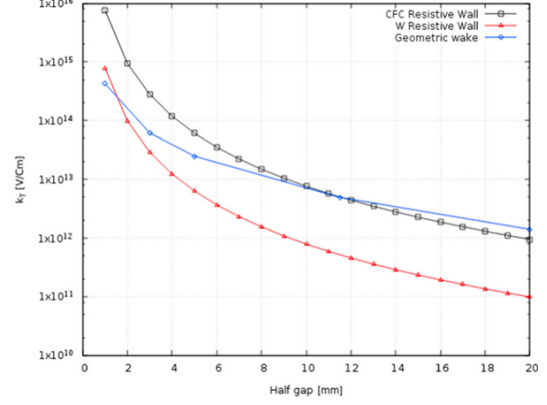


Figure 3: Impact of the geometrical impedance of the LHC taper transitions with respect to the jaw resistive wall impedance.

CST [17] simulations for the TCSPM collimator of Fig. 1. The TCSPM is a test collimator which hosts three different materials on the main jaws as shown in Fig. 4: Molybdenum (Mo), Molybdenum-graphite (MoGr) and Titanium nitride (TiN).

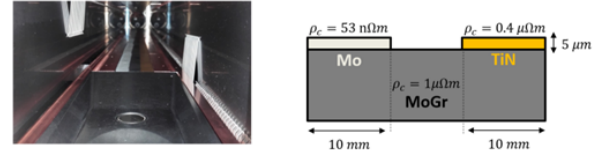


Figure 4: TCSPM jaw materials: three 10 mm wide stripes of Molybdenum (Mo), Molybdenum-graphite (MoGr) and Titanium Nitride (TiN) are present. Mo and TiN stripes are deposited with coating techniques to achieve 5 μm thickness.

Figure 5 shows the impedance computed with CST once the beam is simulated on top of each of the stripes together with comparisons with the IW2D code computation. The agreement is very good demonstrating the validity of a 2D approximation especially for low gaps. One limitation of a two parallel plates flat model is that it does not account for the width of the stripes. Figure 6 shows the impedance variation versus beam position at 1 GHz: the impedance agrees with the value corresponding to the center of the stripes within a ± 2 mm displacement which is well within the operationally achievable orbit precision.

Resonant wire impedance measurements

Bench impedance measurements were performed on the TCSPM collimator to verify its compatibility with respect to the LHC impedance requirements. As an additional value, longitudinal resonant wire impedance measurements [18] were performed in order to probe the expected impedance reduction from each of the different stripes: the wire has been horizontally shifted on top of each stripe and the corresponding impedance computed. The resonant wire method was chosen in place of the classic matched wire one thanks

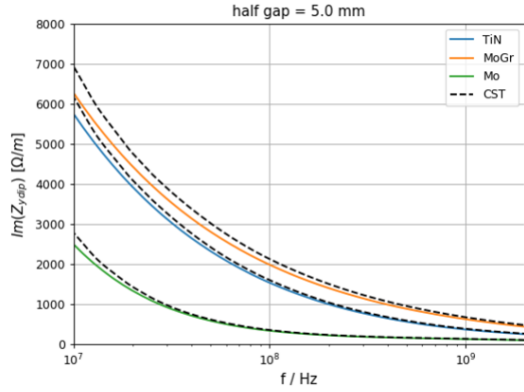


Figure 5: TCSPM resistive wall impedance computed with CST and the IW2D code. Each CST simulation curve corresponds to the beam position on the middle of the corresponding stripe.

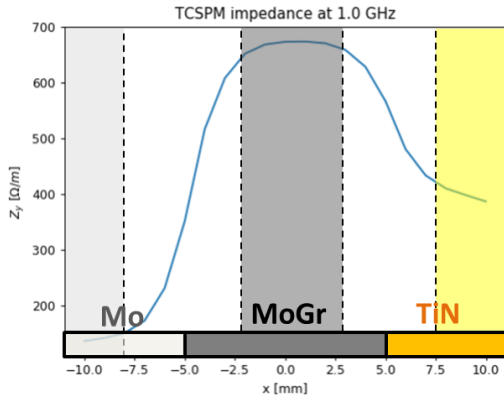


Figure 6: Resistive wall impedance versus horizontal position on the TCSPM collimator.

to the enhanced accuracy and perfect match at the resonant frequencies (see Fig. 7 for a schematic representation). We point out that the method, as applied in the TCSPM measurements, only allows the deduction of the real part of the impedance, as this is related to the change in the Q factor of the self-resonances in the DUT.

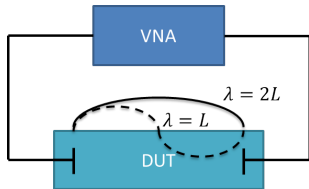


Figure 7: Resonant wire method setup: capacitors are placed at the matching sections before/after the DUT in order to produce DUT resonances at multiples of its half length.

Figure 8 shows the measured longitudinal impedance versus gap and frequency: the sampling due to the discrete number of resonances is visible as well as the presence of few higher order modes (HOMs). If, on the one hand the impedance cannot be correctly evaluated if HOMs are

present due to the discrete sampling intrinsic to the method, on the other the broadband impedance can be accurately determined outside of the resonances.

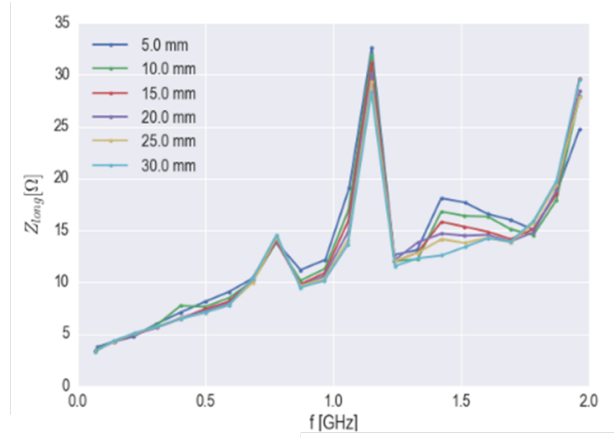


Figure 8: Longitudinal impedance versus half gap reconstructed from S21 parameters measured with the resonant wire technique. The sampling is determined by the device length.

Figure 9 shows the dependence of the longitudinal impedance on the half gap for different wire displacements: once outside of a HOMs the broadband impedance shows the characteristic $1/g$ behavior of a resistive wall longitudinal impedance. Nevertheless, the asymptotic value is determined by the parasitic resistances due to the contacts between the device parts. The contact resistance Z_c contribution is supposed to be constant and it is removed fitting the measurement data with a fitting function $f(g) = \Delta Z_{long}/g + Z_c$, from which the longitudinal impedance ΔZ_{long} is obtained.

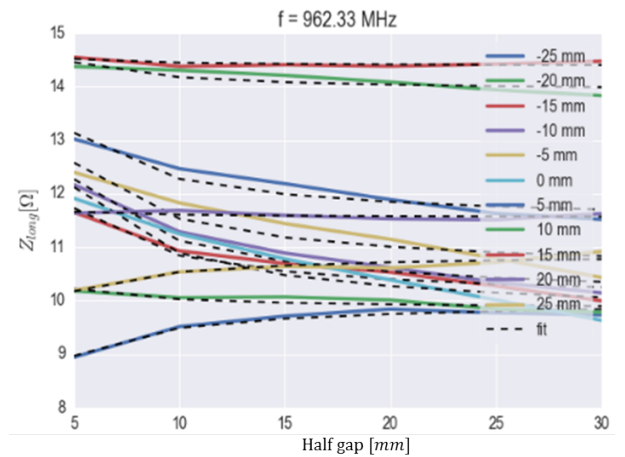


Figure 9: Longitudinal impedance versus gap and wire displacement at 962 MHz together with $1/g$ line fits: the coefficient of the fit determines the impedance.

The result of the fitting procedure is shown in Fig. 10. Few observations can be made:

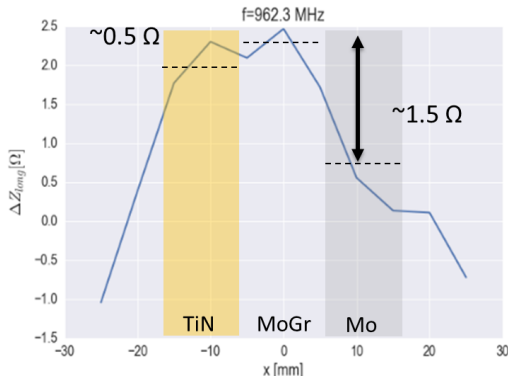


Figure 10: Longitudinal impedance versus horizontal position: a clear reduction is observed for the impedance measured on the Mo and TiN stripe. The largest reduction corresponds to the Mo stripe.

1. For very large displacements the impedance coefficient ΔZ_{long} is found to be negative, or, in other words, the impedance increases versus gap. These positions correspond to the far end of the displacement scan, when the wire is placed on the Glidcop support: enlarging the gap the stainless steel frame is showing more and more, dominating the impedance otherwise negligible.
2. The impedance simulated with IW2D, as shown in Fig. 11, is smaller than measured: this is probably due to the constant additional resistive wall due to the tapered sections made of MoGr. Nevertheless the relative difference is found in very good agreement with measurements.

These two observations will be addressed in more detail in the future with the help of dedicated CST simulations.

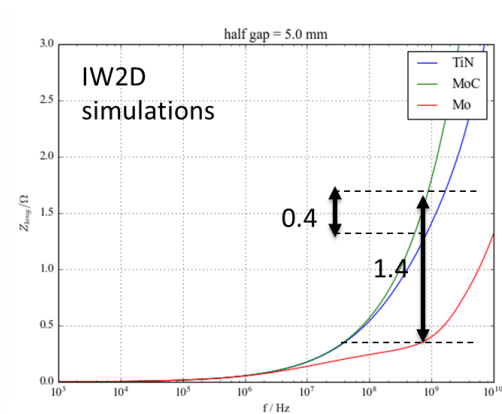


Figure 11: Longitudinal impedance versus horizontal position: IW2D simulations.

Resistivity measurements

In order to correctly model the collimator resistive wall contribution, it is important to evaluate the resistivity of the absorber material. This can be done at DC with standard

4 wires techniques [19], or at RF frequency using a loop antenna [20]. The latter is based on the measurement of the magnetic field induced by the presence of a good conductor in front of a loop antenna as shown in Fig. 12. Comparison of the measured input impedance to the value expected with IW2D simulations allows to deduce the resistivity at each measured frequency. The method has been used to estimate the MoGr resistivity versus frequency as shown in Fig. 13.

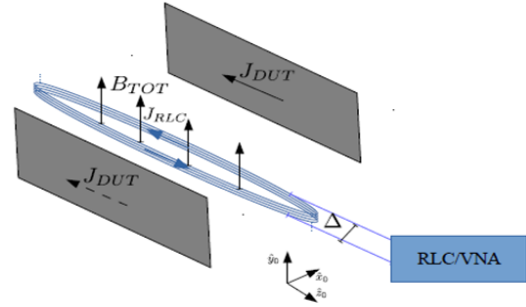


Figure 12: Setup for low frequency resistivity measurements.

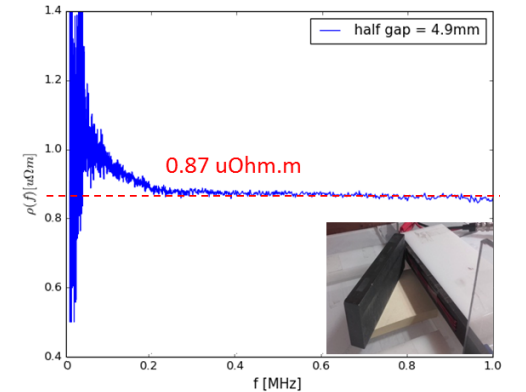


Figure 13: MoGr resistivity versus frequency measured with a loop. The average measurement is close to expected resistivity of 1 uΩm.

The method allows to measure the resistivity of thin films/coatings as well. The application to Mo coating on MoGr is presently under study [21].

Beam based impedance measurements

The quality of an impedance model is subject to the final crosscheck with beam based impedance measurements. One of the standard techniques to measure the transverse impedance of a collimator is the observation of the tune shift induced by the movement of the collimator gap (the impedance is strongly defocussing for small gaps inducing a negative tune shift). CERN collimators have been extensively measured by means of this technique already in the past [22,23], but only recently the method has been improved in a way to boost its resolution down to the 10^{-5} tune shift resolution [8, 24], opening the road for the measurement of the impedance of a single collimator.

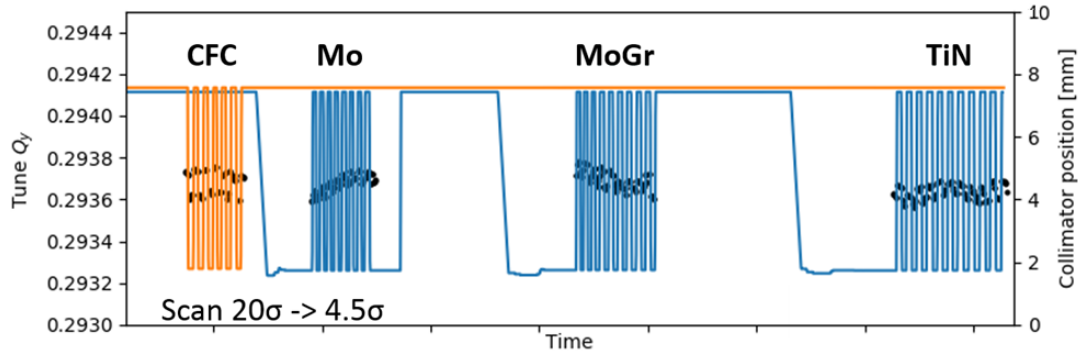


Figure 14: Vertical tune shift measurement versus gap opening for the TCSPM (blue curve) and TCSG.D4R7 (orange curve): the width of the band of dots during the scan is correlated to the collimator transverse reactive impedance.

One of the most interesting applications of the method was the measurement of the impedance of each of the single stripes of the TCSPM collimator. The test is of vital importance as one of the key ingredients for the HL-LHC project is the upgrade of the present collimation system to the new low-impedance collimators featuring (at least for the IR7 collimators) Mo coated MoGr jaws. Figure 14 shows the measured tune while moving the gap of the TCSPM and the adjacent TCSG.D4R7 whose jaw is made of CFC: already by visual inspection it is clear that the Mo stripe presents the least tune shift, i.e. the smallest impedance among the 4 tested materials. Plotting the tune shift versus gap for each of the stripes as shown in Fig. 15, the agreement with the simple 2D model can be appreciated, in particular for the CFC, MoGr and TiN materials. A discrepancy is found for the Mo stripe which is apparently contradicting the longitudinal wire measurements. One of the possible causes is related to the Mo coating surface roughness [25]: the roughness, in first approximation, would mainly affect the inductive impedance, i.e. the tune shift measurements, with negligible impact on the real part of the transverse (and longitudinal) real part of the impedance. This aspect is still presently under investigation.

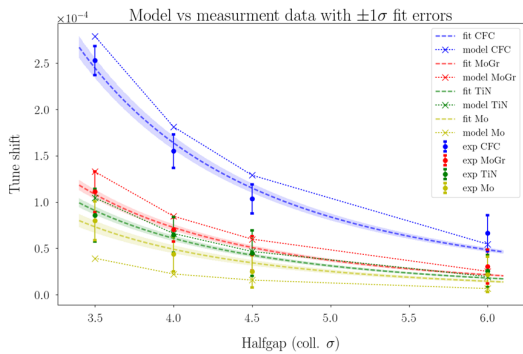


Figure 15: TCSPM and TCSG.D4R7 tune shift versus gap opening. The Mo stripes clearly shows the maximum impedance reduction.

3D COLLIMATOR IMPEDANCE MODELING

Even though it has been proven to be a good approximation, the 2D modeling of a collimator has of course many limitations. When coming to the details of the HOMs modeling, for example, only a complete 3D description of the device allows to obtain precise estimation of the device resonance parameters (frequency, shunt impedance and Q factor). This is the case of the TCTP collimator [26], subject of recent intense studies both with GdfidL and CST: the removal of lateral RF fingers to allow for the space needed by the embedded BPMs, introduced a large cavity volume producing a large number of HOMs. Of these, only part could be suppressed using ferrite tiles as in Fig. 16 and a campaign of simulations and device bench impedance measurements was launched in order to characterize the HOMs and ensure their negligible impact on machine stability.

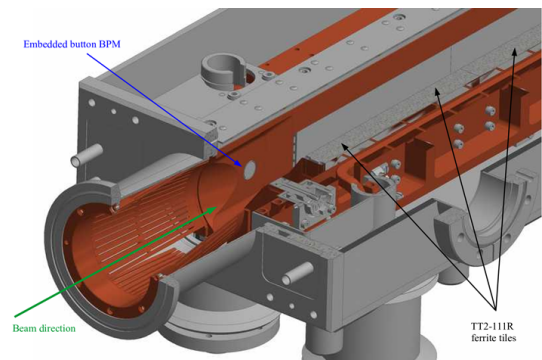


Figure 16: 3D model of the TCTP collimator: ferrite tiles are placed in order to damp the HOMs present in the structure.

Figure 17 shows the effect of the ferrite tiles on the longitudinal impedance: a clear damping effect above 500 MHz can be appreciated. On the other hand, few transverse modes at 82 MHz and 167 MHz are present as shown in Fig. 18.

Bench impedance measurements were performed on the TCTP in order to crosscheck these observations. Indeed, using a probe terminated with a loop, the low frequency

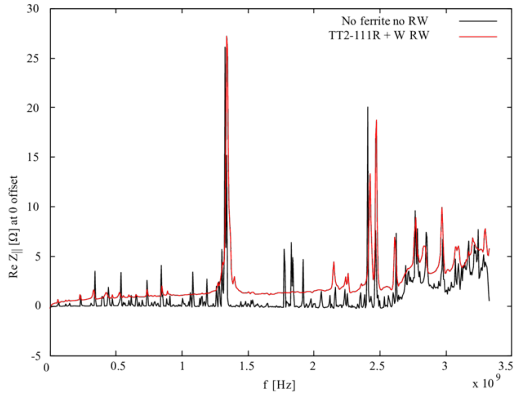


Figure 17: Longitudinal impedance for the new collimator as computed by GdfidL, with (red curve) and without (black curve) TT2-111R ferrite and tungsten resistive wall (W). No offset is applied.

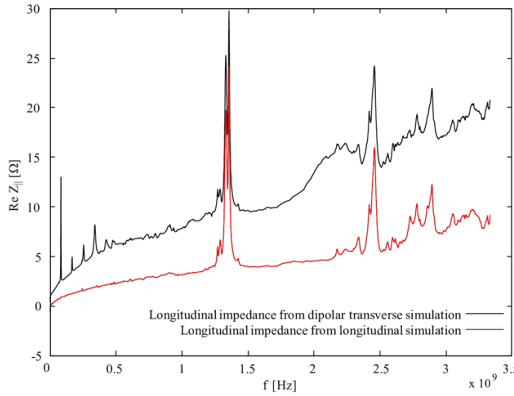


Figure 18: Longitudinal impedances computed for a beam with zero transverse beam offset (red curve) and with a transverse beam offset as done in transverse dipolar impedance simulations (black curve). The computed low frequency HOMs correspond to transverse modes.

HOMs could be detected as shown in Fig. 19 and were found in close agreement with the expected frequency and Q factor.

The shunt impedance was measured with the stretched wire method [27]. The setup was substantially different from the one shown in Fig. 7 as the equivalent coaxial line made by the stretched wire and the device was matched to the characteristic impedance of the device itself. This is done to have finer frequency resolution to localize the HOMs. Unfortunately, the characteristic impedance of a collimator is well defined only for a fixed gap value introducing a mismatch pattern in the measured S21 parameter. This issue can be overcome fitting the baseline mismatch pattern around the HOMs and extracting the information about the shunt impedance. A remarkably good agreement, within a factor of 2, is obtained comparing the measured shunt impedance of the 87 MHz transverse HOMs against GdfidL and CST simulations, as shown in Fig. 20. The discrepancy may depend on several collimator design constraints, namely the gap between the plate where ferrite blocks are installed, the

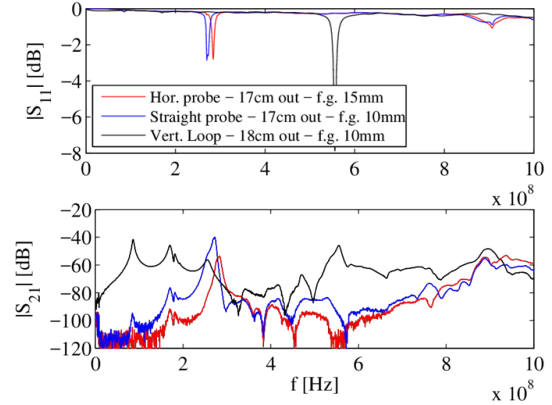


Figure 19: S11 (top) and S21 (bottom) measured with a straight and horizontal probe and with a loop: the low frequency resonant modes exhibit higher coupling through the magnetic field. The first length in the legend refers to the portion of probe outside the device, the second (“f.g.”) to the full gap of the collimator.

gap between collimator jaws and external tank and, also, on the mesh and computed wake length [12].

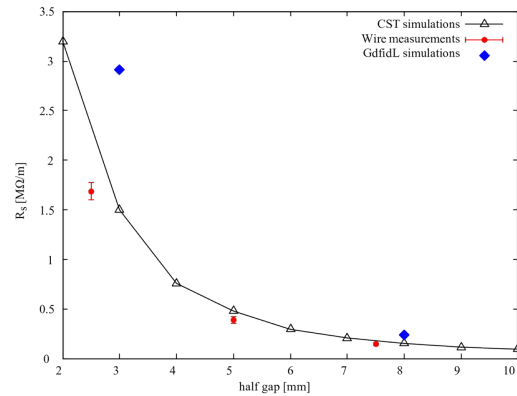


Figure 20: Shunt impedance R_s of the 87 MHz mode versus half gap as measured with wire and simulated in CST and GdfidL.

CONCLUSIONS

In this work we have summarized the most common techniques to model the collimator impedance resorting to simple 2D models. In its simplest form a collimator can be assumed to be approximated by two parallel plates of resistive materials. Adding the impedance of the tapers further refines the computed reactive part of the impedance. The modeling is in good agreement both with bench measurement and with beam based tune shift measurements for single collimators in the LHC, where unprecedented accuracy has been recently reached. More complex simulations based on 3D electromagnetic solvers like CST and GdfidL, are needed when, for example, the presence of HOMs in the collimator structure need to be assessed. Bench impedance measurements are in this case of high importance, especially if simplifications

on the mechanical model or on the material properties of dispersive materials (like ferrites) were needed in the simulation phase. Equally important, even though not treated here, are the simulations of the bench impedance measurements and beam based measurements like synchronous phase shift and threshold in octupole strength which give respectively a measurement of the longitudinal real part for the impedance and its impact on transverse stability.

REFERENCES

- [1] S. Redaelli. “Beam Cleaning and Collimation Systems”. In *Proceedings, 2014 Joint International Accelerator School: Beam Loss and Accelerator Protection: Newport Beach, CA, USA, November 5-14, 2014*, pages 403–437, 2016.
- [2] O. Brüning et al. “*LHC Design Report*”. CERN Yellow Reports: Monographs. CERN, Geneva, 2004.
- [3] R. Assmann et al. “The final collimation system for the LHC”. In *Particle accelerator. Proceedings, 10th European Conference, EPAC 2006, Edinburgh, UK, June 26-30, 2006*, volume C060626, pages 986–988, 2006.
- [4] N. Mounet. “*The LHC Transverse Coupled-Bunch Instability*”. PhD thesis, EPFL University, Lausanne, Mar 2012. Presented 2012.
- [5] S. Antipov et al. “Machine impedance and HOM power update”. 7th HL-LHC collaboration meeting, Madrid, Spain, 2017.
- [6] G. Apollinari et al. “*High-Luminosity Large Hadron Collider (HL-LHC): Technical Design Report V. 0.1*”. CERN Yellow Reports: Monographs. CERN, Geneva, 2017.
- [7] E. Métral et al. “Update of the HL-LHC operational scenarios for proton operation”. Technical Report CERN-ACC-NOTE-2018-0002, CERN, Geneva, Switzerland, Jan 2018.
- [8] D. Valuch et al. “Update on single-collimator impedance measurements”. COLUSM 75, CERN, Geneva, Switzerland, 19-08-2016.
- [9] D. Amorim et al. “Tune shifts: measurements and predictions”. COLUSM 91, CERN, Geneva, Switzerland, 11-08-2017.
- [10] G. Stupakov. “Low frequency impedance of tapered transitions with arbitrary cross sections”. *Phys. Rev. ST Accel. Beams*, 10:094401, Sep 2007.
- [11] O. Frasciello et al. “Geometric beam coupling impedance of LHC secondary collimators”. *Nuclear Instruments and Methods in Physics Research Section A: Accelerators, Spectrometers, Detectors and Associated Equipment*, 810:68 – 73, 2016.
- [12] O. Frasciello. *Wake fields and impedance calculations of LHC collimators’ real structures*. PhD thesis, Università degli Studi di Roma “La Sapienza”, Feb 2016. Presented 2016.
- [13] W. Bruns. <http://www.gdfidl.de>.
- [14] K. Yokoya. “Impedance of slowly tapered structures”. Technical Report CERN-SL-90-88-AP, CERN, Geneva, Jul 1990.
- [15] A. W. Chao and M. Tigner. “*Handbook of Accelerator Physics and Engineering*”. World Scientific, Singapore, 1999.
- [16] N. Mounet and E. Métral. “Electromagnetic fields and beam coupling impedances in a multilayer flat chamber”. Technical Report CERN-ATS-Note-2010-056 TECH., CERN, Geneva, Switzerland, 2010.
- [17] CST Studio Suite®. <http://www.cst.com>.
- [18] T. Kroyer, F. Caspers, and E. Gaxiola. “Longitudinal and transverse wire measurements for the evaluation of impedance reduction measures on the MKE extraction kickers”. Technical Report AB-Note-2007-028, CERN, Geneva, Switzerland, Jul 2007.
- [19] E. Bonanno et al. “Update on conductivity measurements of TDI blocks”. Impedance meeting, CERN, Geneva, Switzerland, 25-04-2016.
- [20] N. Biancacci et al. “LF impedance measurements on TDI blocks”. Impedance meeting, CERN, Geneva, Switzerland, 02-03-2015.
- [21] G. Mazzacano et al. “Resistivity measurements on Molybdenum coated CFC and MoGr blocks”. Impedance meeting, CERN, Geneva, Switzerland, 08-12-2017.
- [22] N. Mounet et al. “Collimator Impedance Measurements in the LHC”. Proc. IPAC’13, Shanghai, China, May 2013.
- [23] L. Carver et al. “MD 755: Instability threshold and tune shift study with reduced retraction between primary and secondary collimators in IR7”. Jan 2016. Rep. CERN-ACC-NOTE-2016-0005.
- [24] N. Biancacci et al. “Outcome of TCSG single collimator impedance and instability measurements”. LHC Collimation Working Group n.207, CERN, Geneva, Switzerland, 22-08-2016.
- [25] J. Guardia Valenzuela et al. “SEM observation of coatings for TCSPM blocks”. Impedance meeting, CERN, Geneva, Switzerland, 06-10-2017.
- [26] N. Biancacci et al. “Impedance simulations and measurements on the LHC collimators with embedded beam position monitors”. *Phys. Rev. Accel. Beams*, 20:011003, Jan 2017.
- [27] V. G. Vaccaro. “Coupling impedance measurements: An Improved wire method”. Technical Report INFN-TC-94-23, INFN, Naples, Italy, Nov 1994.

THE CIRCULANT MATRIX FORMALISM AND THE ROLE OF BEAM-BEAM EFFECTS IN COHERENT INSTABILITIES

X. Buffat, Geneva, Switzerland

Abstract

The role of beam-beam interactions in coherent instabilities in high energy colliders is discussed with a particular emphasis on the circulant matrix model. This model, based on the development of a one-turn matrix including all linearised coherent forces, is particularly suited for the study of the stability of complex configurations involving different forces. Thus it allows for the study of interplays, e.g. between the effect of the beam-beam interactions and the beam coupling impedance. Experimental evidence compatible with this model is reported.

INTRODUCTION

In a high energy collider, the stability of both beams needs to be considered in a common framework due to the electromagnetic interaction between the beams, that strongly couple their dynamics. In some configurations, the coherent beam-beam modes can be neglected and the effect of the beam-beam interaction on the beam stability is limited to its impact on the amplitude detuning and consequently on Landau damping [1, 2]. Here we focus on regimes where the models that consider the dynamic of the two beams separately, so-called weak-strong regimes, do not represent accurately the dynamics of the two beams. This applies to colliders where both beams feature a high brightness, i.e. most electron-positron or proton-proton colliders.

We start by deriving the coherent force between the two beams. Based on this force, we introduce the rigid bunch model to obtain the coherent modes of oscillation in the most simplistic configuration and then extend this model to the circulant matrix model. Two methods used to make predictions beyond the linearised model are discussed. Finally, observations of coherent beam-beam modes showing the accuracy of the model are reported.

THE COHERENT BEAM-BEAM FORCE

The beam-beam kick on a point-like particle, called the incoherent beam-beam kick, can be obtained by integration of Poisson's equation [3]. Using a Gaussian distribution of particles, with r.m.s. transverse beam size $\sigma = \sigma_x = \sigma_y$, one obtains the kick felt by a test particle at a position (x, y) with respect to the other beam's centroid [4] :

$$\Delta x' = -\frac{2r_0 N}{\gamma} \frac{x}{r^2} \left(1 - e^{-\frac{r^2}{2\sigma^2}} \right), \quad (1)$$

where we have introduced N the number of charges in the beam, r_0 the classical radius, $r = \sqrt{x^2 + y^2}$ and the relativistic γ factor. Since the opposing beam is not point-like,

the total beam-beam kick, called coherent kick, is obtained by integration of the single particle kicks over the beam distribution $\Psi(x, y)$:

$$\Delta x'_{\text{coh}}(x, y) = \int_{-\infty}^{\infty} dX dY \Delta x'(X, Y) \Psi(X - x, Y - y). \quad (2)$$

Assuming a round Gaussian distribution and using Eqs. 1 and 2, we have [5] :

$$\Delta x'_{\text{coh}}(x, y) = -\frac{2r_0 N}{\gamma} \frac{x}{r^2} \left(1 - e^{-\frac{r^2}{4\sigma^2}} \right). \quad (3)$$

For $x, y \ll \sigma$, we find that the coherent kick is half the single particle kick, whereas for large separation, i.e. for long-range interactions, the difference between coherent and incoherent vanishes.

THE RIGID BUNCH MODEL

In order to obtain a description of the coherent beam-beam modes, we want to solve the equations of motion of the two beams self-consistently. We use as dynamical variables the average transverse positions and momenta (x_l, x'_l) of the two beams ($l = 1, 2$) with respect to their closed orbits assuming that their particle distribution remains Gaussian with fixed sizes in all degrees of freedom. By linearising all forces, we may derive the one-turn matrix of this periodic dynamical system and perform a normal mode analysis, including the beam-beam interactions self-consistently, thus describing the coherent modes of oscillation. Let us start by defining the one-turn matrix of a single beam with a transverse tune Q and using the optical β function at the interaction point β^* as M_{1B} giving its coordinate at turn $k + 1$ with respect to the ones at turn k :

$$\begin{aligned} \begin{pmatrix} x_{l,k+1} \\ x'_{l,k+1} \end{pmatrix} &= \begin{pmatrix} \cos(2\pi Q) & \beta^* \sin(2\pi Q) \\ -\frac{1}{\beta^*} \sin(2\pi Q) & \cos(2\pi Q) \end{pmatrix} \cdot \begin{pmatrix} x_{l,k} \\ x'_{l,k} \end{pmatrix} \\ &\equiv M_{1B} \cdot \begin{pmatrix} x_{l,k} \\ x'_{l,k} \end{pmatrix}. \end{aligned} \quad (4)$$

For the two identical beams, we may define M_{2B} as the two-beam one-turn matrix :

$$\begin{pmatrix} x_{1,k+1} \\ x'_{1,k+1} \\ x_{2,k+1} \\ x'_{2,k+1} \end{pmatrix} = \mathbb{I}_2 \cdot M_{1B} \cdot \begin{pmatrix} x_{1,k} \\ x'_{1,k} \\ x_{2,k} \\ x'_{2,k} \end{pmatrix} \equiv M_{2B} \cdot \begin{pmatrix} x_{1,k} \\ x'_{1,k} \\ x_{2,k} \\ x'_{2,k} \end{pmatrix}, \quad (5)$$

with \mathbb{I}_n the identity matrix of size n . Within this basis, the matrix for a beam-beam interaction may be derived by

linearising Eq. (3) around (x_0, y_0) the closed orbit difference between the two beams at the interaction point :

$$\Delta x'_{\text{coh}}(x, y) \approx \Delta x'_{\text{coh}}(x_0, y_0) + \frac{\partial \Delta x'_{\text{coh}}}{\partial x}(x_0, y_0) \Delta x, \quad (6)$$

with :

$$\begin{aligned} \frac{\partial \Delta x'_{\text{coh}}}{\partial x}(x, y) = & -\frac{2Nr_0}{\gamma} \left[\left(\frac{1}{r^2} - 2\frac{x^2}{r^4} \right) \left(1 - e^{-\frac{r^2}{4\sigma^2}} \right) \right. \\ & \left. + \frac{x^2}{2r^2\sigma^2} e^{-\frac{r^2}{4\sigma^2}} \right]. \end{aligned} \quad (7)$$

Defining $k_0 \equiv \frac{\partial \Delta x'_{\text{coh}}}{\partial x}(x_0, y_0)$, one can then write the coupling matrix between the two beams, due to the beam-beam interaction :

$$M_{\text{BB}} = \begin{pmatrix} 1 & 0 & 0 & 0 \\ -k_0 & 1 & k_0 & 0 \\ 0 & 0 & 1 & 0 \\ k_0 & 0 & -k_0 & 1 \end{pmatrix}. \quad (8)$$

Thus we can write the one-turn matrix of the two beams including a single beam-beam interaction :

$$\begin{pmatrix} x_{1,k+1} \\ x'_{1,k+1} \\ x_{2,k+1} \\ x'_{2,k+1} \end{pmatrix} = M_{\text{BB}} \cdot M_{2B} \cdot \begin{pmatrix} x_{1,k} \\ x'_{1,k} \\ x_{2,k} \\ x'_{2,k} \end{pmatrix}. \quad (9)$$

The normal mode analysis reveals two frequencies each corresponding to two degenerate modes. The first mode corresponds to in-phase oscillation of the two beams (σ -mode), its coherent tune is the unperturbed machine tune $Q_\sigma = Q$. The second mode of oscillation corresponds to out-of-phase oscillation of the two beams (π -mode), we have :

$$\cos(2\pi Q_\pi) = \cos(2\pi Q) - \beta^* k_0 \sin(2\pi Q). \quad (10)$$

The stability of the beam-beam modes is given by the imaginary part of the eigenvalues of the matrix given by Eq. (9), which is reported in Fig. 1. Comparing to Eq. (10), we see that the stability boundary is given by the resonance condition $2Q_\pi = n$. Since we have limited our description of the lattice and of the beam-beam interactions to first order, only the lowest order resonances are visible. In principle higher order resonances could also drive the coherent beam-beam modes [6]. It is therefore important to make sure there exist damping mechanisms for these modes, the description of which will be discussed when extending beyond the linearised model.

The circulant matrix model

The circulant matrix model [7–9] offers a convenient way to describe the transverse oscillation of the two beams, including not only the effect of beam-beam interactions, but

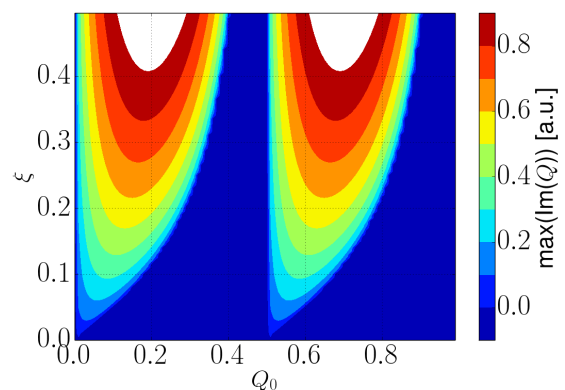


Figure 1: Largest imaginary part of the eigenvalues of Eq. (9), defining the stable area in terms of unperturbed tune Q_0 and beam-beam parameter ξ .

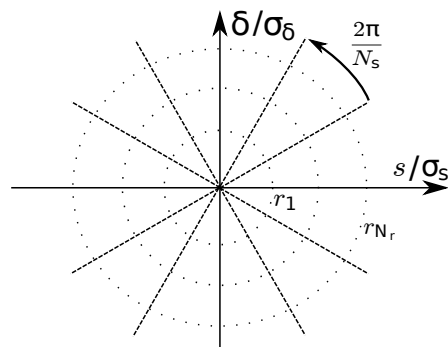


Figure 2: Discretisation of the longitudinal phase space into N_s slices and N_r rings.

also other important components of the coherent dynamic of the beam, in particular the effect of the transverse wake fields. This model is an extension of the rigid bunch model, allowing for different parts of the longitudinal phase space to oscillate independently, thus enabling the description of head-tail modes. The longitudinal phase space is discretised in polar coordinates using so-called slices and rings as illustrated in Fig. 2. The transverse motion of each discrete element can be treated as in the rigid bunch model, except that all the combinations of beam-beam interactions between the elements needs to be considered. Equation (6) becomes :

$$\Delta x_i = k_0 \left(\frac{\sum_{j=0}^{N_s N_r} Q_j x_j}{\sum_{j=0}^{N_s N_r} Q_j} - x_i \right). \quad (11)$$

As an example, let us use two slices and a single ring and start from Eq. (9) :

$$\begin{pmatrix} x_{1,1,k+1} \\ x'_{1,1,k+1} \\ x_{1,2,k+1} \\ x'_{1,2,k+1} \\ x_{2,1,k+1} \\ x'_{2,1,k+1} \\ x_{2,2,k+1} \\ x'_{2,2,k+1} \end{pmatrix} = M_{\text{BB}} \cdot M_{2B} \cdot \begin{pmatrix} x_{1,1,k} \\ x'_{1,1,k} \\ x_{1,2,k} \\ x'_{1,2,k} \\ x_{2,1,k} \\ x'_{2,1,k} \\ x_{2,2,k} \\ x'_{2,2,k} \end{pmatrix}, \quad (12)$$

where $x_{i,j,k}$ refer to the position of slice j from beam i at turn k . The lattice matrix M_{2B} can easily be extended since all slices go through the same lattice and the beam-beam coupling matrix becomes :

$$M_{\text{BB}} = \begin{pmatrix} 1 & 0 & 0 & 0 & 0 & 0 & 0 & 0 \\ -k_0 & 1 & 0 & 0 & k_0/2 & 0 & k_0/2 & 0 \\ 0 & 0 & 1 & 0 & 0 & 0 & 0 & 0 \\ 0 & 0 & -k_0 & 1 & k_0/2 & 0 & k_0/2 & 0 \\ 0 & 0 & 0 & 0 & 1 & 0 & 0 & 0 \\ k_0/2 & 0 & k_0/2 & 0 & -k_0 & 1 & 0 & 0 \\ 0 & 0 & 0 & 0 & 0 & 0 & 1 & 0 \\ k_0/2 & 0 & k_0/2 & 0 & 0 & 0 & -k_0 & 1 \end{pmatrix}. \quad (13)$$

Such a matrix can be built in a systematic way for an arbitrary number of slices and rings, and for complex configurations of beam-beam interactions involving multiple bunches and multiple interaction points, including the longitudinal variations of the beam-beam force due to a crossing angle or to the variation of the β function over the interaction [10]. In order to introduce the effect of the wake, we need to take

$$M_Z = \begin{pmatrix} 1 & 0 & 0 & 0 & 0 & 0 & 0 & 0 & 0 \\ W_{\text{quad}}(s_1 - s_0) & 1 & W_{\text{dip}}(s_1 - s_0) & 0 & 0 & 0 & 0 & 0 & 0 \\ 0 & 0 & 1 & 0 & 0 & 0 & 0 & 0 & 0 \\ W_{\text{dip}}(s_0 - s_1) & 0 & W_{\text{quad}}(s_0 - s_1) & 1 & 0 & 0 & 0 & 0 & 0 \\ 0 & 0 & 0 & 0 & 1 & 0 & 0 & 0 & 0 \\ 0 & 0 & 0 & 0 & 0 & W_{\text{quad}}(s_1 - s_0) & 1 & W_{\text{dip}}(s_1 - s_0) & 0 \\ 0 & 0 & 0 & 0 & 0 & 0 & 0 & 1 & 0 \\ 0 & 0 & 0 & 0 & 0 & W_{\text{dip}}(s_0 - s_1) & 0 & W_{\text{quad}}(s_0 - s_1) & 1 \end{pmatrix}, \quad (17)$$

such that the equation of motion becomes :

$$\begin{pmatrix} x_{1,1,k+1} \\ x'_{1,1,k+1} \\ x_{1,2,k+1} \\ x'_{1,2,k+1} \\ x_{2,1,k+1} \\ x'_{2,1,k+1} \\ x_{2,2,k+1} \\ x'_{2,2,k+1} \end{pmatrix} = M_Z \cdot M_{\text{BB}} \cdot M_{2B} \cdot \begin{pmatrix} x_{1,1,k} \\ x'_{1,1,k} \\ x_{1,2,k} \\ x'_{1,2,k} \\ x_{2,1,k} \\ x'_{2,1,k} \\ x_{2,2,k} \\ x'_{2,2,k} \end{pmatrix}. \quad (18)$$

We have written the transverse one-turn matrix for the longitudinal distribution, yet the longitudinal motion has been

a closer look at the discretisation of the longitudinal phase space, in particular the longitudinal position of the discrete elements needs to be defined. The definition of the discretisation is somewhat arbitrary, however it is convenient to split the phase space such that the charge contained in each element is identical, as was implicitly assumed when deriving Eq. (13). For a Gaussian distribution of particles, the slices are uniformly distributed, we have $\theta_i = 2\pi i/N_s$ and the radius of the rings set such that :

$$e^{-r_{j+1}} - e^{-r_j} = \frac{1}{N_r}, \quad (14)$$

where $r_j = \sqrt{(s_j/\sigma_s)^2 + (\delta_j/\sigma_\delta)^2}$ is the radius of the j^{th} ring in the normalised longitudinal phase space, i.e. σ_s and σ_δ are the bunch length and relative momentum spread. Therefore we obtain the longitudinal position $s_{i,j}$ and moment deviations $\delta_{i,j}$ of the i^{th} slice and j^{th} ring :

$$\begin{cases} s_{i,j} &= r_j \sigma_s \cos \theta_i \\ \delta_{i,j} &= r_j \sigma_\delta \sin \theta_i \end{cases}. \quad (15)$$

Thus we can write the interaction between the discrete elements of the distribution through the beam coupling by using the integrated dipolar and quadrupolar wake functions $W_{\text{dip}}(\Delta s)$ and $W_{\text{quad}}(\Delta s)$ [11]:

$$\Delta x'_i = \sum_{j=0}^{N_s N_r} W_{\text{dip}}(s_j - s_i) x_j + W_{\text{quad}}(s_j - s_i) x_i. \quad (16)$$

This can be written in a matrix form, in our two-slice model and assuming that the two beams experience identical impedances, we have :

put aside. Thanks to the choice of decomposition of the longitudinal phase space, the longitudinal motion can be introduced rather simply, as it consists of a rotation of the slices within each ring. The longitudinal one-turn matrix is given by the circulant matrix :

$$S_r = P_{N_s}^{N_s Q_s}, \quad (19)$$

where Q_s is the synchrotron tune and P_{N_s} is a permutation matrix :

$$P_{N_s} = \begin{pmatrix} 0 & 1 & & & \\ & 0 & 1 & & \\ & & \ddots & \ddots & \\ & & & 0 & 1 \\ 1 & & & & \end{pmatrix}. \quad (20)$$

Since the rotation is identical for all rings and for both beams and considering N_{B1} and N_{B2} number of bunches in the two beams, the matrix in the same basis can be built using the outer product with identity matrices :

$$M_s = \mathbb{I}_{N_{B1}+N_{B2}} \otimes \mathbb{I}_{N_r} \otimes S_r. \quad (21)$$

The full one-turn matrix, including the synchro-betatron motion, the beam coupling and beam-beam interactions is then given by :

$$M = M_Z \cdot M_{BB} \cdot M_s \otimes M_{1B}, \quad (22)$$

and its stability can be studied through normal mode analysis. Let us discuss a simple configuration of two identical bunches colliding at a single interaction point without crossing angle or variations of the β function over the interaction length and assuming that the lattice and the impedance experienced by both beams are identical. Figure 3a shows the frequency of the two normal modes obtained with a single slice and a single ring. As expected, we find back the solution of the rigid bunch model, where the σ -mode frequency stays unperturbed, while the π -mode frequency is shifted by $-\xi$. Figure 3b shows the same result with a single ring and 10 slices, allowing to see the frequency of azimuthal modes, appearing as sidebands of the betatron tune. Their frequencies are shifted by $-\xi/2$ due to the beam-beam interaction. This difference between the behaviour of the sidebands can be understood by looking at Eq. (11), where we observe that the sum over the positions of the slices is actually the dipolar moment of the oscillation. Since only the azimuthal mode 0 has a dipolar component, the other modes are only affected by the beam-beam interaction in an incoherent way. In other words, the frequency of the modes are shifted, however the corresponding sidebands of the two beams do not oscillate coherently. In the presence of wake fields, the situation is different, since the perturbed azimuthal modes may also have a dipolar component. Figure 4a illustrates the impact of a resistive wall impedance on the frequency of the normal mode in the same configuration. The perturbed modes have indeed acquired a dipolar moment, which allows them to interact through the beam-beam interaction. This effect manifests strongly as a mode coupling instability where the frequency of the π -mode reaches the one of the azimuthal mode -1 and where the frequency of the azimuthal mode 1 reaches the one of the σ -mode.

Moving towards more realistic configurations, the chromaticity also perturbs the head-tail modes, allowing them to couple through the beam-beam force at any beam-beam parameter, as shown by Fig. 4b. From this plot it is clear

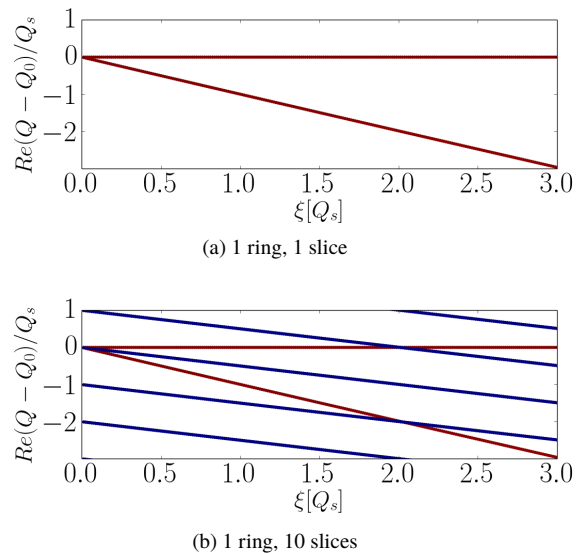


Figure 3: Eigenfrequencies of the coherent mode of oscillation of two round symmetric beams colliding head-on in one single interaction point for different beam-beam parameters. The points are colour coded according to their dipole moment, the σ and π modes are purely dipolar (red), while the synchrotron sidebands have no dipolar moment (blue). The eigenvalues are all real in absence of other mechanisms.

that an efficient damping mechanism is needed in order to maintain the stability of colliding beams. This point will be further discussed in the next section.

By construction the circulant matrix is well suited to study any linearised transverse force depending on the longitudinal position, such as the effect of an RF-quadrupole [12] or chromaticities of any order. The effect of a transverse feedback may also be considered [7].

As the model is based on the construction of a one-turn matrix, the modelling of multiturn effects, e.g. due to a long-range impedance source, is implicitly neglected. This limitation may be overcome by extending Eq. (16) such that the effect of previous turns is taken into account, assuming a given phase relation between the motion of the discretised element turn after turn. In other words, such a model would be based on an ad-hoc assumption on the mode of oscillation, which is not necessarily valid in complex configurations of beam-beam interactions.

Considering the one-turn matrix of multiple consecutive bunches in a given lattice, it is clear that it has several degenerate eigenvalues since every bunch has the same tune. The normal mode analysis of such a non-normal matrix is known to fail to describe its long term behaviour [13]. In accelerators, such effects were already observed as the beam breakup instability in a linear accelerator. Conceptually, the configuration of multiple bunches in a ring with a negligible multiturn wake is analogous to a linear accelerator. For

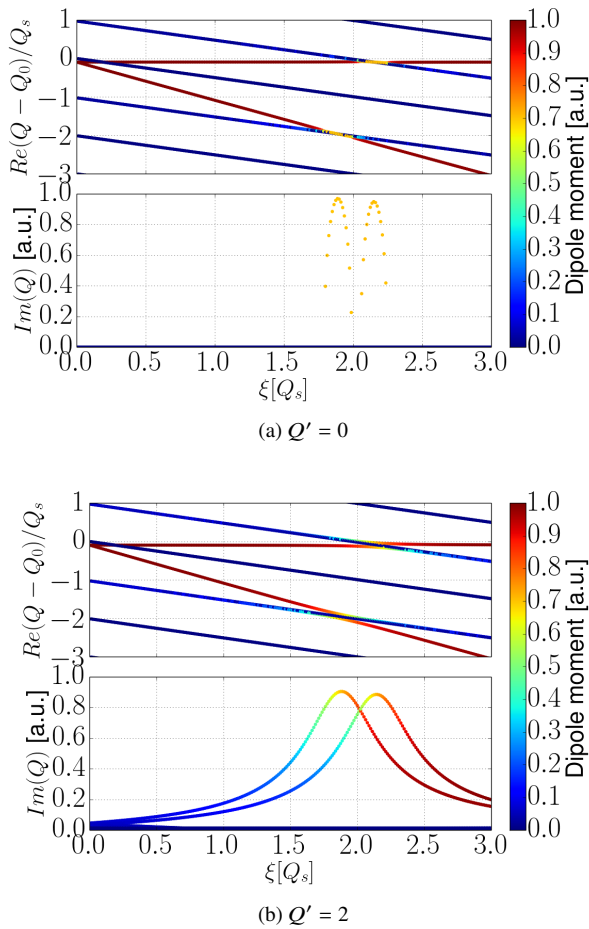


Figure 4: Eigenfrequencies of the coherent mode of oscillation of two round symmetric beams colliding head-on in one single interaction point for different beam-beam parameters in the presence of a resistive-wall type of impedance. In absence of chromaticity, a coupling instability appears when the frequencies of the coherent beam-beam modes reach the ones of the synchrotron sidebands. In the presence of chromaticity, the coherent interaction between the two beams has an impact on the stability of head-tail modes, at any beam-beam parameter.

example a short train of bunches in the LHC matches these assumptions, the circulant matrix model allows for a proper description of its behaviour, nevertheless the tools needed to analyse the stability of the one-turn matrix have to be adapted [10].

A major limitation of the circulant matrix lies in the linearisation of the forces which results in an inaccuracy of the frequency of the coherent modes [14] and prevents the study of transverse Landau damping.

BEYOND THE LINEARISED MODEL

Going beyond the linearised model is crucial to understand Landau damping. Analytically, this can be achieved by

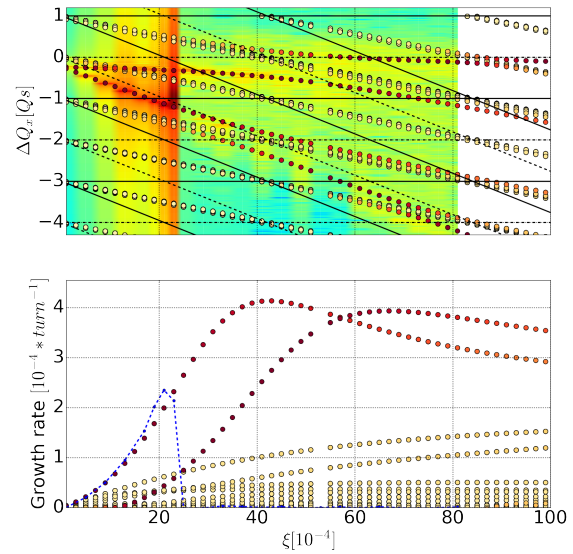


Figure 5: Estimation of the coherent modes of oscillation with the circulant matrix model using the code BimBim [10] for the nominal HL-LHC configuration [15] with a single interaction point based on the wake field of the HL-LHC model at top energy [16], which is largely dominated by the resistive wall impedance of the collimators. The dots are color coded with the dipolar component of the corresponding mode from yellow (min) to red (max). The spectrogram of the oscillation obtained with the macroparticle simulations (COMBI) is shown in the background of the upper plot, together with the exponential fit of the growth rate as a blue line in the lower plot. The dark lines represent the extension of the incoherent spectrum and its synchrotron side bands. Courtesy [17].

relaxing the constraint of the rigid bunch model and instead write the equation of motion of the particle distribution of both beams in a coupled system of Vlasov equations. Such a derivation can be found in [18], showing that in the simple configuration studied in the previous section of two identical beams colliding in a single interaction point, no Landau damping is expected for neither the σ nor the π modes due to the shift of the coherent mode frequencies that exceeds the shift of the frequency of oscillation of the single particles due to the non-linearity of the beam-beam force, constituting the so-called incoherent spectrum. The same model predicts qualitatively Landau damping for beam-beam tune shifts exceeding the synchrotron tune, due to an interplay of the coherent beam-beam modes with the synchrotron side bands of the incoherent spectrum. In order to quantify the strength of the Landau damping in the presence of a given impedance, self-consistent macro-particle simulations need to be performed. As an example, the result of an analysis of the stability of the two beams in the HL-LHC using the code COMBI [10] is shown in Fig. 5, using a 6 dimensional model

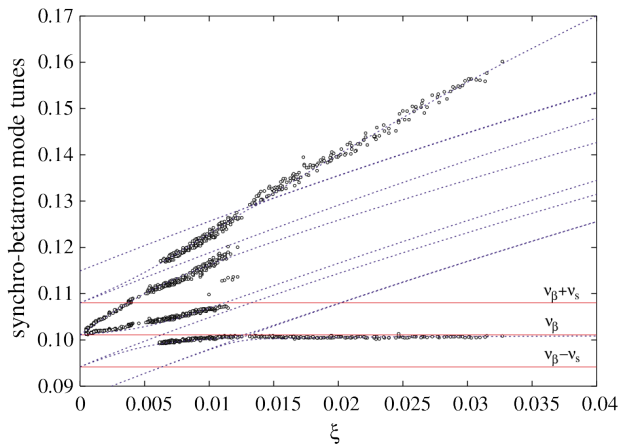


Figure 6: Measured (circles) and computed (lines) synchro-betatron coherent beam-beam mode tunes as a function of the beam-beam parameter ξ at BINP's VEPP-2M, with $Q_x = 0.101$, $Q_s = 0.0069$, $\beta^* = 6$ cm, $\sigma_s = 0.7 \cdot \beta^*$ and a beam energy of 440 MeV. Courtesy [19].

of the coherent kick taking into account the variation of the β function along the interaction length, the so-called hourglass effect [17]. Similarly to the chromaticity, the hourglass effect allows the beam-beam mode to couple and generate an instability at any beam-beam parameter, as shown by the prediction of the circulant matrix. As long as the frequencies of the coherent modes lie outside of the incoherent spectrum as well as its synchrotron side bands, the macro-particle simulations are consistent with the linearised model. As the π -mode frequency enters the lower sideband and the upper sideband overlaps with the σ -mode frequency, the instability predicted in the linearised model vanishes in the full model as predicted qualitatively by Vlasov perturbation theory. The remaining instability at low beam-beam parameter may be stabilised for example with a transverse feedback [9].

OBSERVATIONS

VEPP-2000

In absence of beam instabilities, the frequency of the head-tail coherent modes, or synchro-betatron coherent beam-beam modes, may still be investigated by exciting the beam and measuring its response in the frequency domain. This was tested at the VEPP-2M with a remarkable agreement between the circulant matrix model and the measurement (Fig. 6). Worth noting that since VEPP-2M is an electron-positron collider, the tune shift due to the beam-beam interaction is positive as opposed to the other examples discussed here from the (HL-)LHC which collides particles of identical charge.

LHC

As opposed to BINP's VEPP-2M, CERN's LHC features a strong impedance mainly due to the collimation system, which may excite the coherent beam-beam modes. A short

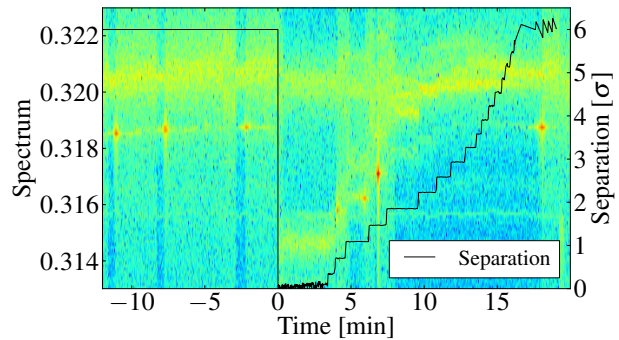


Figure 7: Spectrogram of the transverse beam oscillation during an experiment with two bunches per beam colliding with a varying transverse offset at the interaction point. The normalised separation between the beams at the IP (black line) is deduced from the measured luminosity reduction factor.

experiment was dedicated to the measurement of coupling instability with beams colliding with a transverse offset, at the end of a special fill with two bunches per beam [9]. Before $t = 0$, in Fig. 7, a series of spikes in the oscillation amplitude mark a few tests of the stability of separated beams without transverse feedback, by switching it off and on again when an instability was observed. At $t = 0$, the beams were brought into collision at one interaction point with the transverse feedback on. Once the beams were colliding HO, the transverse feedback was no longer required to maintain the beams stability. The beams were then re-separated transversally in steps, visible in Fig. 7. At each step, the stability without transverse feedback was tested, as previously. It was observed that the beams are stable without transverse feedback for separations below 0.7σ and from 1.8 to 6σ , whereas unstable from 0.7 to 1.8σ and at 6σ . Also, the instability at intermediate separations has different characteristics than for 6σ separation. The frequency of the mode with separated beams is consistent with a head-tail mode with $n_a = -1$, whereas the frequencies of the modes with intermediate separations are consistent with the ones of coherent beam-beam modes. Also, at intermediate separations both beams are unstable simultaneously, whereas at large separations, only one of the beams experienced instabilities. The small range of separations, and therefore of beam-beam tune shifts, are consistent with the circulant matrix model prediction, as well as the capacity of the transverse feedback to maintain the beam stability for any separation.

ACKNOWLEDGEMENT

I would like to thank L. Barraud, W. Herr, K. Li, A. Mailard, T. Pieloni, M. Schenk and S.M. White for their important contributions to this topic as well as for several fruitful discussions, as well as E. Métral for both the interesting discussions and for proofreading this document.

REFERENCES

- [1] X. Buffat et al. “Stability diagrams of colliding beams in the Large Hadron Collider.” In: *Phys. Rev. ST Accel. Beams* 17 (11 Nov. 2014), p. 111002.
- [2] C. Tambasco. “Beam Transfer Function (BTF) measurements and transverse stability in presence of beam-beam.” In: *these proceedings*. 2017.
- [3] W. Herr. “Beam-beam interactions.” In: *CAS - CERN Accelerator School: Intermediate Course on Accelerator Physics*. Ed. by D. Brandt. Zeuthen, Germany: CERN, 15-26 September 2003 2006, pp. 379–410.
- [4] M. Bassetti and G.A. Erskine. *Closed expression for the electrical field of a two-dimensional Gaussian charge*. Tech. rep. CERN-ISR-TH-80-06. Geneva: CERN, 1980.
- [5] K. Hirata. “Coherent betatron oscillation modes due to beam-beam interaction.” In: *Nucl. Instrum. Methods Phys. Res. A* 269.1 (1988), pp. 7–22. issn: 0168-9002.
- [6] Chao Alex. *Coherent Beam-Beam Effects*. Tech. rep. SSCL-346. Dallas: Superconducting Super Collider Laboratory, 1991.
- [7] V.V. Danilov and E.A. Perevedentsev. “Feedback system for the elimination of the transverse mode coupling instability.” In: *Nucl. Instrum. Methods Phys. Res. A* 391 (1997), pp. 77–92.
- [8] E. A. Perevedentsev and A. A. Valishev. “Simulation of the head-tail instability of colliding bunches.” In: *Phys. Rev. ST Accel. Beams* 4 (2 Feb. 2001), p. 024403.
- [9] S. White et al. “Transverse mode coupling instability of colliding beams.” In: *Phys. Rev. ST Accel. Beams* 17 (4 Apr. 2014), p. 041002.
- [10] X. Buffat. “Transverse beams instability studies at the Large Hadron Collider.” PhD thesis. EPFL, 2015.
- [11] B. W. Zotter and S. A. Kheifets. *Impedances and wakes in high-energy particle accelerators*. Singapore: World Scientific, 1998.
- [12] M. Schenk et al. “Analysis of transverse beam stabilization with radio frequency quadrupoles.” In: *Phys. Rev. Accel. Beams* 20 (10 Oct. 2017), p. 104402.
- [13] L. N. Trefethen and M. Embree. *Spectra and pseudospectra: The behavior of nonnormal matrices and operators*. Princeton: Princeton University Press, 2005.
- [14] K. Yokoya and H. Koiso. “Tune shift of coherent beam-beam oscillations.” In: *Part. Acc.* 27 (1990), pp. 181–186.
- [15] E. Métral et al. *Update of the HL-LHC operational scenarios for proton operation*. Tech. rep. CERN-ACC-NOTE-2018-0002. Geneva, Switzerland: CERN, Jan. 2018.
- [16] *CERN impedance webpage*. <http://impedance.web.cern.ch/impedance/>. Accessed: 2018-02-22.
- [17] Laurent Barrant and Xavier Buffat. *Mode coupling instability of colliding beams in the HL-LHC*. Tech. rep. Geneva: CERN, 2018.
- [18] Y. Alexahin. “A study of the coherent beam-beam effect in the framework of Vlasov perturbation theory.” In: *Nucl. Instrum. Methods Phys. Res. A* 480.2 (2002), pp. 253–288.
- [19] I. N. Nesterenko, E. A. Perevedentsev, and A. A. Valishev. “Coherent synchrotron beam-beam modes: Experiment and simulation.” In: *Phys. Rev. E* 65 (5 May 2002), p. 056502.

OBSERVATION AND DAMPING OF LONGITUDINAL COUPLED-BUNCH OSCILLATIONS IN THE CERN PS

H. Damerau, A. Lasheen, CERN, Geneva, Switzerland

M. Migliorati, Rome University and INFN Roma1, Rome, Italy and CERN, Geneva, Switzerland

Abstract

Longitudinal coupled-bunch instabilities pose a major limitation to the intensity and quality of LHC-type beams in the CERN Proton Synchrotron (PS). The oscillations are excited above transition energy and mainly driven by the impedance of the main accelerating cavities at around 10 MHz. When approaching the flat-top these cavities are partly short-circuited. However, due to the sweeping revolution frequency, the spectral components of the beam move towards the resonances of the high frequency cavities at 20 MHz, 40 MHz and 80 MHz. Hence different coupled-bunch oscillation mode patterns are observed during acceleration and at the flat-top. A dedicated frequency domain damping system has been installed. While dipole coupled-bunch instabilities are well suppressed, quadrupole oscillations remain, as well as longitudinal blow-up due to the impedance of the high frequency cavities. Recent results obtained with the coupled-bunch feedback are presented together with first studies using alternative mitigation techniques for the instabilities.

INTRODUCTION

In the framework of the LHC Injectors Upgrade (LIU) project the PS is being upgraded to deliver an intensity per bunch of $N_b = 2.6 \cdot 10^{11}$ ppb for a bunch spacing of 25 ns, twice the present nominal intensity of beams delivered to the Large Hadron Collider (LHC). Longitudinal coupled-bunch instabilities, both dipole and quadrupole, occur during acceleration and at the flat-top. They limit the achievable intensity and beam quality. For the dipole coupled-bunch instabilities a prototype feedback system is available for studies since 2016. It consists of a wide-band Finemet cavity [1] operated in the frequency range from the revolution frequency, f_{rev} to half the main RF frequency, $f_{RF}/2$, and a low-level signal processing covering all possible dipole oscillation modes [2]. Although a new intensity range, beyond $N_b \approx 1.4 \cdot 10^{11}$ ppb, has become accessible with the coupled-bunch feedback, dipole oscillations reappear above a bunch intensity of $N_b = 2.0 \cdot 10^{11}$ ppb. Additionally, quadrupole coupled-bunch instabilities are observed. Increasing the longitudinal emittance to stabilize the beam is not compatible with the tight constraints at transfer between PS and SPS.

The main harmonic of the RF system changes during the acceleration cycle. In total 6 bunches are injected into $h = 7$ and the principal RF harmonic is then brought to $h = 21$ by triple splitting [3] at a kinetic energy of 2.5 GeV [4]. Following acceleration of 18 bunches through transition to the flat-top at $h = 21$, each bunch is split in four parts by a sequence of two bunch splittings, $h = 21 \rightarrow 42 \rightarrow 84$.

The coupled-bunch oscillations occur during acceleration above transition energy and at the flat-top [5], hence before the quadruple splitting prior to extraction.

Since all bunch intensities in this contribution are given with reference to bunches at extraction from the PS to the SPS, held with $h = 84$, the bunch intensity at $h = 21$ during acceleration is four times that value.

DIPOLE COUPLED-BUNCH INSTABILITIES

In the frequency domain coupled-bunch oscillations manifest as synchrotron frequency, f_s , side-bands of the revolution frequency harmonics [6], which makes them difficult to observe directly in the PS. The side-bands are only about $f_s \approx 400$ Hz away from the strong spectral lines at multiples of f_{rev} . Additionally, the lower and upper f_s side-bands are driven by different oscillation modes. The phase motion of the bunches can be extracted from profiles measured in time domain instead. A discrete Fourier transform translates the oscillation amplitudes and phases per bunch to mode amplitude and phases [7]. The same analysis technique can also be applied to quadrupole coupled-bunch oscillations where the bunch length replaces the bunch phase.

Acceleration

Fig. 1 shows the mode spectrum of a dipole coupled-bunch instability during acceleration. The zero mode is suppressed

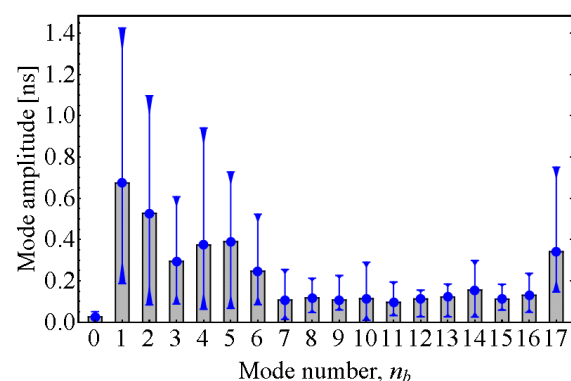


Figure 1: Mode spectrum of the dipole coupled-bunch oscillations during acceleration. The blue bars indicate the total spread of ten acceleration cycles (2011 data). The mode number, n_b , refers to modes within the batch of 18 bunches.

by the beam phase loop. Low and high mode numbers are strongest, which in the spectrum appear at frequencies close to f_{RF} . They are most likely excited by the impedance of the main accelerating cavities at 10 MHz [7].

Flat-top

The mode pattern changes at the flat-top, when the RF voltage is reduced in preparation of the RF manipulations and the gaps of the main cavities are sequentially short-circuited. The motion of bunches in time domain is illustrated in Fig. 2. The dipole mode spectrum (Fig. 3) at the flat-top differs

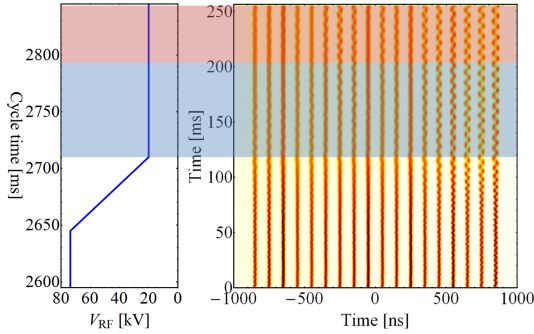


Figure 2: Dipole coupled-bunch instability at flat-top. The shaded areas indicate the time windows when the bunch splittings $h = 21 \rightarrow 42$ (blue) and $h = 42 \rightarrow 21$ (red) normally take place.

significantly from the one during acceleration (Fig. 1). In addition to the modified impedance of the accelerating cavities at the flat-top, the spectral components of the beam at the 84th and 168th harmonic of f_{rev} move to the resonance frequencies of the 40 MHz and 80 MHz cavities.

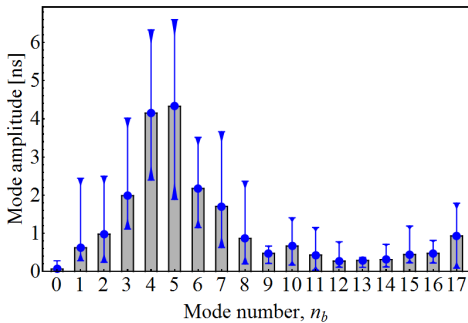


Figure 3: Mode spectrum of the dipole coupled-bunch oscillations at the end of the flat-top (Fig. 2).

COUPLED-BUNCH FEEDBACK

The coupled-bunch feedback extracts the f_s side-bands and reduces them by injecting a correction in opposite phase [6]. Out of the 21 possible dipole oscillation modes for LHC-type beams accelerated at $h = 21$, the zero mode is removed by the beam phase loop. The 20 other modes are covered by the coupled-bunch feedback as lower and upper side-bands at 10 revolution frequency harmonics. To avoid detecting the weak side-bands close to the much stronger f_{rev} harmonics at low frequencies, the band from $f_{\text{RF}}/2$ to f_{RF} has been chosen. However, due to higher shunt impedance of the Finemet cavity at low frequencies, the correction signals are translated to the frequency band from f_{rev} to $f_{\text{RF}}/2$ [2].

The benefit on longitudinal stability during acceleration is sketched in Fig. 4. The time domain evolution reveals a

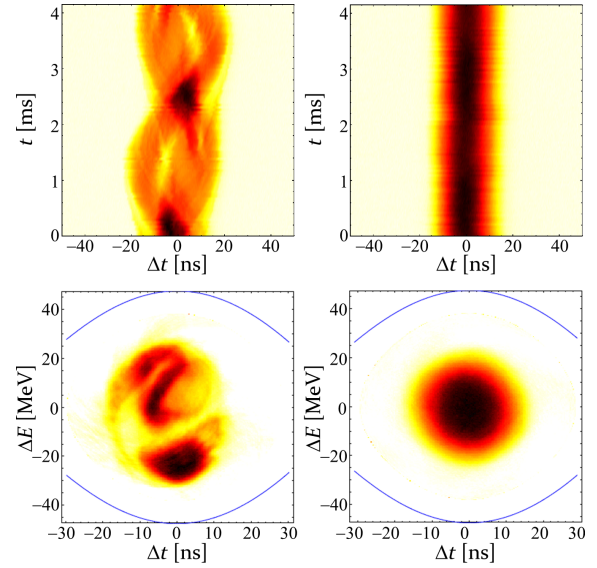


Figure 4: Instability (bunch number 12 of an 18-bunch batch) towards the end of acceleration without (left) and with (right) the coupled-bunch feedback. The intensity per bunch at extraction is $N_b = 2.0 \cdot 10^{11}$ ppb.

strong bunch oscillation, dipole and quadrupole, without the coupled-bunch feedback and the tomographic reconstruction illustrates the distorted bunch distribution. With the feedback system switched on the instability is fully suppressed. Although only an example measurement of one bunch is shown in Fig. 4, all bunches are reproducibly stabilized during each cycle with the feedback.

Thanks to the full mode coverage, stabilisation is also achieved at the flat-top, during the bunch splittings from $h = 21$ to $h = 84$ (Fig. 5). The significant beam quality im-

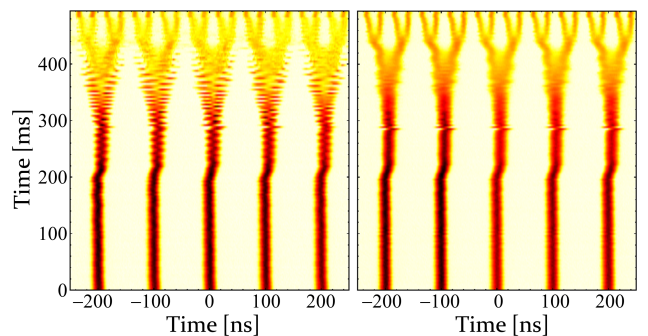


Figure 5: Bunch evolution during the flat-top splittings with the coupled-bunch feedback disabled (left) and enabled (right). The intensity per bunch at extraction is $N_b = 1.8 \cdot 10^{11}$ ppb.

provement is again clearly visible and reproducible from cycle to cycle. However, the coupled-bunch feedback designed for dipole oscillation modes has no effect on quadrupole-type instabilities which occur in the PS when pushing the intensity beyond an equivalent intensity of $N_b = 2 \cdot 10^{11}$ ppb.

QUADRUPOLE COUPLED-BUNCH OSCILLATIONS

With the feedback for dipole instabilities in place, coupled-bunch quadrupole (bunch length) oscillations are observed, again starting during acceleration after transition crossing and at the flat-top.

Acceleration

At the longitudinal emittance compatible for producing the nominal emittance $\varepsilon_1 = 0.35$ eVs (matched area definition, [8]) at extraction, the quadrupole oscillations are naturally well damped (Fig. 6, left). The mode spectrum shows only small amplitudes with minor impact on beam quality. This changes when increasing the longitudinal beam

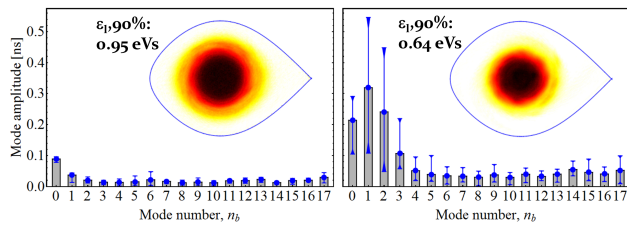


Figure 6: Mode spectrum of the quadrupole coupled-bunch instability after transition crossing for two different longitudinal emittances. The intensity per bunch at extraction is $N_b = 2.0 \cdot 10^{11}$ ppb.

density. The longitudinal emittance is reduced by about 50% by decreasing the controlled longitudinal blow-up (Fig. 6, right). The higher density appears to be above the threshold of the instability and the dominant amplitudes of the quadrupole coupled-bunch oscillations grow by almost an order of magnitude.

Flat-top

At the flat-top the dipole instabilities are again well controlled by the feedback system. It has no effect though on the quadrupole instabilities (Fig. 7) slowly developing during the time which is normally used for synchronisation and quadrupole splitting. Analysing the quadrupole oscillations at the end of the flat-top reveals the mode spectrum shown in Fig. 8. As for the dipole modes (Fig. 3) the mode numbers, $n_b = 4$ and 5 are strongest, indicating that dipole and quadrupole oscillations are excited by the same impedance source.

Measurements at the flat-top confirm that the feedback has no effect on quadrupole oscillations.

HIGHER HARMONIC RF SYSTEM

For the RF manipulations at the flat-top the PS is equipped with RF systems at 20 MHz, 40 MHz and 80 MHz. The 20 MHz system has been operated as a higher-harmonic RF system in the past [9], showing only a slight stability improvement when set in counter-phase with respect to the main RF system. Motivated by the experience with the double-harmonic RF configuration in the SPS [10] with a

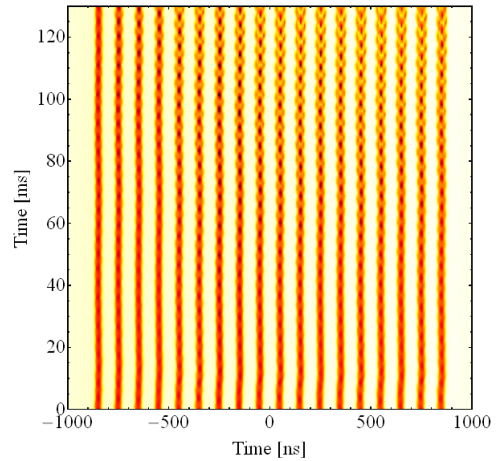


Figure 7: Mode spectrum of the quadrupole coupled-bunch instability at flat-top. The equivalent intensity per bunch at extraction is $N_b = 2.0 \cdot 10^{11}$ ppb.

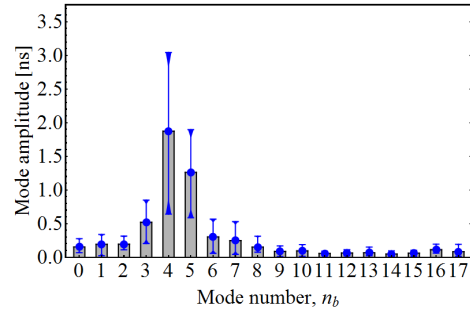


Figure 8: Mode spectrum of the quadrupole coupled-bunch oscillation at the flat-top (Fig. 7).

harmonic number ratio of four, recent studies concentrated on the 40 MHz RF system to increase the synchrotron frequency spread within the bunch.

At the flat-top the effect on stability of a double-harmonic RF system, 10 MHz and 40 MHz, adding some extra voltage at $h = 84$ in addition to the principal RF harmonic of $h = 21$ has been investigated. The higher-harmonic RF voltage has been applied in counter-phase (bunch lengthening mode) and in phase (bunch shortening mode).

Fig. 9 summarizes stabilisation due to the double-harmonic RF system. Applying the voltage at $h = 84$ in bunch lengthening mode has no measurable effect on the quadrupole coupled-bunch oscillations (Fig. 9, top) while switching only the phase of the 40 MHz to bunch shortening mode (Fig. 9, bottom) stabilizes the beam. Already 10% of the voltage of the main RF system is sufficient to significantly reduce the quadrupole instability.

The studies in 2017 with the double-harmonic RF system were focused on the mitigation of the quadrupole coupled-bunch oscillations in combination with the feedback suppressing the dipole modes. Preliminary tests in 2016 were nonetheless performed showing that also dipole instabilities are well damped by the double-harmonic RF system [11].

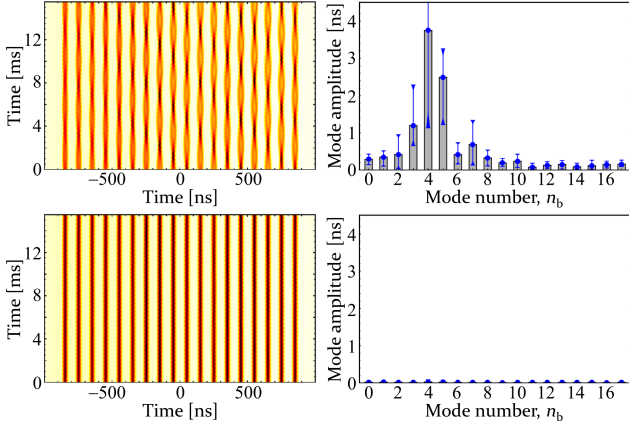


Figure 9: Quadrupole coupled-bunch oscillations in a double-harmonic RF system, 10 MHz and 40 MHz at a voltage ratio of about 10%, the lowest ratio tested. The relative phase of the 40 MHz RF voltage has been set to bunch lengthening (top) and bunch shortening (bottom) mode.

The synchrotron frequency spread within the bunch is significantly increased in the presence of the higher-harmonic RF system (Fig. 10). For a bunch with the nominal longitudi-

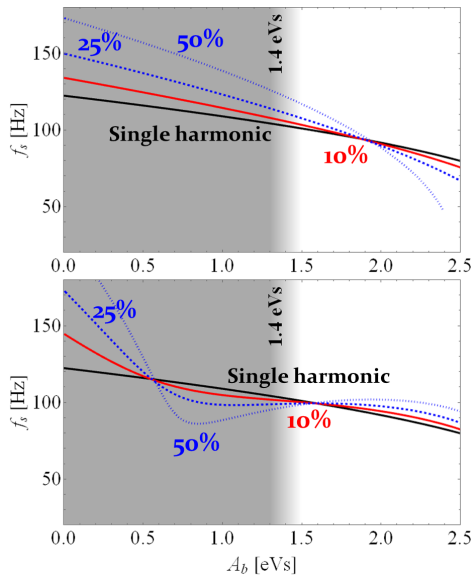


Figure 10: Synchrotron frequency distribution in the single harmonic RF system with an RF voltage of 20 kV at $h = 21$ (black) at the flat-top in the PS. In combination with voltage from a higher harmonic RF system at $h = 42$ (top) and $h = 84$ (bottom), the synchrotron frequency spread increases, depending on the voltage ratio [11].

dinal emittance of $\varepsilon_1 = 4 \cdot 0.35 \text{ eVs} = 1.4 \text{ eVs}$ a harmonic number ratio of four is most efficient to increase the synchrotron frequency spread within the bunch. Voltage ratios above 25% result in saddle points in the synchrotron frequency distribution detrimental for stability [10].

Although longitudinal stabilisation has been demonstrated, the existing 40 MHz RF cavities are optimized for

large RF voltage at fixed frequency. They can hence only be operated at or close to the flat-top and not during acceleration, when the quadrupole coupled-bunch oscillations occur first.

CONCLUSIONS

Longitudinal coupled-bunch instabilities with a reproducible mode spectrum are observed in the CERN PS. The mode pattern changes between acceleration and flat-top. The instabilities are most likely driven by the impedance of main cavities at 10 MHz. At the arrival on the flat-top the RF voltage is reduced and unused cavities are short-circuited by gap relays, hence changing their impedance and the resulting mode spectrum. With a wide-band coupled-bunch feedback in place, dipole oscillations are suppressed up to an intensity of $N_b = 2.0 \cdot 10^{11}$ ppb. Above this intensity dipole and quadrupole coupled-bunch instabilities occur. The feedback, designed to cover all possible dipole modes, has no effect on the quadrupole instabilities. As a complementary approach, an existing 40 MHz RF system has been operated as a higher-harmonic RF system for beam studies. It proved very efficient in damping the quadrupole coupled-bunch instability at the flat-top. Suppressing the instability during acceleration would require a dedicated RF system, capable of sweeping with the increasing revolution frequency. Such a system is now under study.

ACKNOWLEDGEMENTS

The authors would like to thank Matthias Haase and Mauro Paoluzzi for their support of the operation of the Finemet cavity. They are also grateful to Elena Shaposhnikova for having suggested to study longitudinal stability with a double-harmonic RF system at the flat-top.

REFERENCES

- [1] S. Persichelli *et al.*, “Impedance Studies for the PS Finemet® Loaded Longitudinal Damper”, IPAC14, Dresden, Germany, 2014, p. 1708.
- [2] L. Ventura *et al.*, “Excitation of Longitudinal Coupled-bunch Oscillations with the Wide-band Cavity in the CERN PS”, IPAC16, Busan, Korea, 2016, p. 1724.
- [3] R. Garoby *et al.*, “Demonstration of Triple Splitting in the CERN PS”, EPAC00, Vienna, Austria, 2000, p. 304.
- [4] H. Damerau *et al.*, “RF Manipulations for Higher Brightness LHC-type Beams”, IPAC13, Shanghai, China, 2013, p. 2600.
- [5] H. Damerau *et al.*, “Longitudinal Performance with High-density Beams for the LHC in the CERN PS”, HB2010, Mohrschach, Switzerland, 2010, p. 193.
- [6] F. Pedersen, F. Sacherer, “Theory and Performance of the Longitudinal Active Damping System for the CERN PS Booster”, PAC77, Chicago, Illinois, USA, 1977, p. 1396.
- [7] H. Damerau *et al.*, “Longitudinal Coupled-bunch Instabilities in the CERN PS”, PAC07, Albuquerque, New Mexico, USA, 2007, p. 4180.

- [8] J.-F. Comblin *et al.*, “A Pedestrian Guide to Online Phase Space Tomography in the CERN PS Complex”, PS/RF/Note 2001-010 Revised, CERN, Geneva, Switzerland, 2001.
- [9] C. M. Bhat *et al.*, “Stabilizing Effect of a Double-harmonic RF System in the CERN PS”, PAC09, Vancouver, British Columbia, Canada, 2009, p. 4670.
- [10] E. Shaposhnikova *et al.*, “Beam Transfer Functions and Beam Stabilisation in a Double Harmonic RF System”, PAC2005, Knoxville, Tennessee, USA, 2005, p. 2300.
- [11] H. Damerou, L. Ventura, “Longitudinal Coupled-Bunch Instability Studies in the PS”, Injector MD Days 2017, CERN, Geneva, Switzerland, 2017, p. 59.

FEEDBACK SYSTEMS FOR MULTIBUNCH BEAM DIAGNOSTICS AND INSTABILITIES SUPPRESSION*

Alessandro Drago,

Istituto Nazionale di Fisica Nucleare, Laboratori Nazionali di Frascati, Frascati, Italy

Abstract

Transverse instabilities in storage rings can limit both beam and single bunch currents. The vacuum chamber impedance can be a source of instabilities for stored beams of positive and negative charges. Furthermore, parasitic e-clouds can produce other undesirable effects to stored beams of positive charges. Transverse bunch-by-bunch feedback systems are implemented in storage rings as active devices for instability suppression and for state of art beam diagnostics.

In this paper the following topics are discussed: basics on bunch-by-bunch feedback for lepton storage rings; beam diagnostics by using feedback; a new feedback design proposed for the electron-positron Future Circular Collider (FCC-ee).

INTRODUCTION

Transverse instabilities in storage rings can limit both beam and single bunch currents.

The vacuum chamber impedance, by means of producing wake-fields at the bunch passage, can be a source of instabilities for positively and negatively charged stored beams. Moreover, also parasitic e- clouds in the vacuum chamber can give undesired or destructive effects for positively charged stored beams.

Transverse bunch-by-bunch feedback systems are implemented in storage rings as active devices for instability suppression and for state of art beam diagnostics.

A FEEDBACK SIMPLE MODEL

As beginning we propose a very simple model of the bunch motion that can be easily studied by writing a software simulator, and that could be interesting from an academic/educational point of view too. This model is fitting to be implemented by using the state-space formalism, for example.

Bunch-by-bunch feedback systems work in the time domain kicking each bunch of particles (considered as a charged rigid body).

Following this approach, the classic harmonic oscillator equation describing small oscillations can be used as a model. For the n-th bunch the formula will be:

$$\ddot{x}_n + 2d_r \dot{x}_n + \omega_v^2 x_n = c_f * (V_n^{fb} - V_n^{wf})$$

where

x_n = position displacement in the horizontal (or vertical) plane from the equilibrium orbit of n-th bunch;

d_r = natural damping rate;

ω_v = resonance angular frequency (betatron_fractional_tune * 2 * π * revolution_frequency);

c_f = conversion factor (note that c_f it is not a pure number);

V_n^{fb} = kick voltage applied by the feedback to the n-th bunch (correction signal computed for the n-th bunch);

V_n^{wf} = kick voltage produced by the wake-fields and applied to the n-th bunch (i.e. voltage produced by the vacuum chamber impedance).

It is interesting to note that by using this formula, the feedback correction kick (V_n^{fb}) behaves as the opposite of the term (V_n^{wf}) generated by the ring impedance.

This simple model can be used to evaluate the effect of the bunch-by-bunch feedback with different setups. In order to build a real time system, very fast analogue and digital electronics are necessary to implement a correction kick algorithm for each bunch [1,2,3]. Furthermore, by using a special technique tested in the longitudinal plane, it is possible to control the quadrupole (head-tail) motion by using the same feedback that implements a more complicated system setup [4]. The most common algorithm is based on a Finite Impulse Response (F.I.R.) filter computing for each bunch per turn an individual correction signal as in the following formula:

$$y_n = k * \sum_i c_i * x_{i,n}$$

where y_n is the correction value, k is the gain, c_i is the i-th filter coefficient and $x_{i,n}$ is the i-th acquired value of the n-th bunch.

It is important to note that some parts of the feedback system itself add impedance to the ring: the pick-up, often made by steel buttons, and the kickers, usually made by two copper striplines or, in the longitudinal case, by a cavity in aluminium or copper.

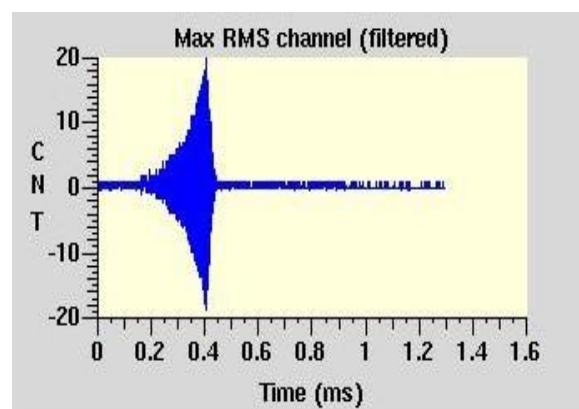


Figure 1: Horizontal oscillations of 500 mA e+ beam (feedback turned off for 0.4 ms). The vertical scale is in arbitrary counts (CNT).

BEAM DIAGNOSTICS BY USING FEEDBACK

To understand if the feedback performances are adequate, it is necessary to evaluate the fastest modal growth rate of the instabilities. The feedback itself can be used to make this measurement. In order to accomplish the goal, it is necessary to turn off the feedback for a short period of time or, in other words, to open the loop.

In Figure 1 the horizontal oscillation of the DAFNE positron beam with 500mA is shown. The signal shows the most oscillating bunch of the train. The feedback is turned off for 0.4 ms. The off period has to be carefully chosen based on the (foreseen or observed) growth rate of the instability. The instability growth is exponential.

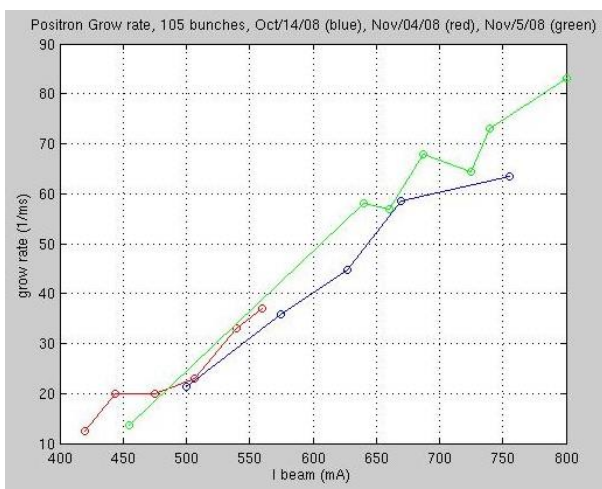


Figure 2: Growth rates (1/ms) of the fastest horizontal e+ mode vs. the beam current (mA)

In Figure 2 the e+ horizontal mode growth rates are reported for DAFNE. The measures are collected in 2008 by using the diagnostic capability of the feedback and recorded in three different days (indicated by three colours). Data are coherent versus beam current if the ring parameters do not change. From the theory [5,6] we expect a linear behaviour versus beam current. A precise error estimate is difficult to obtain because this kind of measurement is extrapolated after a long processing of the raw data and it strongly depends on the human operator skill. Nevertheless, the error seems reasonable because the linear behaviour appears evident. The horizontal growth rates are plotted versus DAFNE e+ beam current between 400 and 800 mA [7,8].

To mitigate instability caused by the presence of the e- clouds, twelve clearing electrodes have been installed in the positron ring in the year 2011. The distance of the electrodes from the beam axis is 8 mm in the four wigglers and 25 mm in the eight bending magnets. How can we evaluate the correct working of the clearing electrodes? A very good method (but not the only one) to evaluate their performance is by measuring the growth rates (by means of the feedback system) versus different voltages applied

to the electrodes at various beam currents [9,10], as shown in Figure 3. In this case the behaviour linearity is much less evident. This fact can be motivated by the observation that changing the electrode voltage has also the collateral effect to slightly influence the beam trajectory and optics, that are important ring parameters. After these measurements the voltage has been raised up to 500 V, changing in the meanwhile the polarity too, to find the best use of the electrodes.

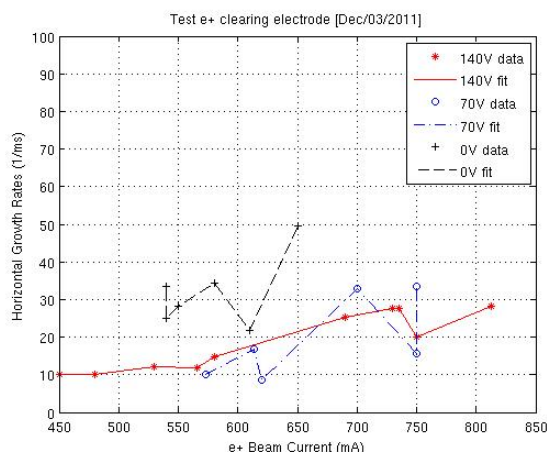


Figure 3: Growth rates (1/ms) of the fastest mode vs. the beam current (mA) with different voltages applied to the clearing electrodes

In addition, there are other beam diagnostic measures implemented at DAFNE by using the feedback systems that, as a matter of principle, could also be made by other tools. First of all, synchronous phase spread measurements along the bunch train have been taken by acquiring data from the front end phase shifter of the longitudinal feedback.

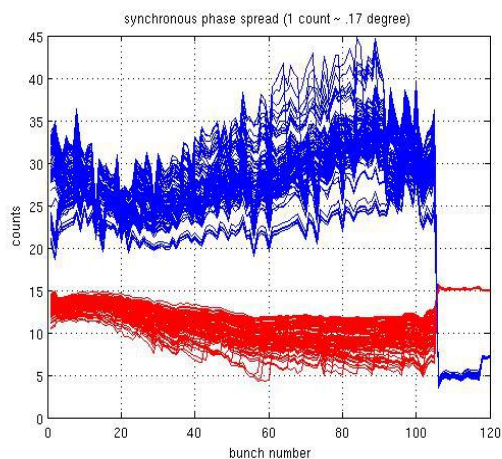


Figure 4: Synchronous phase spread (counts) versus the bunch number for electron (blue) and positron beam (red). Note that the signal acquisitions are plotted with infinite persistence on the display.

In Figure 4 the synchronous phase spread (in counts) is acquired versus bunch number with beam currents up to 1.4 A for the e-, and up to 1 A for the e+. One count corresponds to ~ 0.17 degree. The spread measured is 2.72 degrees for e- and 1.7 degrees for e+. See for example [11], a recent reference, for a comparison.

Moreover, by using feedback it is possible to get real time fractional tune measurements for the beam and also for each bunch separately. This method for tune measuring can be used when the other colliding beam (if any) does not produce tune shift or Landau damping [12-16].

After converting the beam motion recorded by the feedback in the frequency domain by an FFT routine, it is possible to get a rejection negative peak resultant by the feedback response at the frequency where the tune is located and where the S/N ratio is highest. If the feedback gain is large enough, the rejection negative peak will be evident [17]. This approach has been confirmed by frequent comparisons with the traditional measurement technique by using spectrum analyser and white noise excitation.

By following this approach, the bunch-by-bunch fractional tune diagnostics can be implemented without turning off the feedback and by using the transverse system to record long data streams for each bunch. As example for the e- beam with 1 A stored in 90 bunches, the betatron fractional tune spread is ~ 0.001 for both horizontal and vertical oscillations (close to the error threshold). On the contrary, for the e+ beam with 0.7 A stored in 90 bunches the betatron fractional tune spread is as follows:

- 0.008 (from .106 to .114), with clearing electrodes off;
- 0.004 (from .109 to .113), with clearing electrodes on.

For the positron the effect of the e-clouds is evident from the large tune spread, and hence, this is another technique to evaluate if the clearing electrodes are working well.

R&D FOR FCC-EE FEEDBACK

As an interesting R&D case, a new feedback design proposed for FCC-ee is presented in the following.

The bunch-by-bunch feedback systems for FCC-ee should be designed on the basis of the experience acquired working on the lepton circular colliders in the last two decades. Along the past years a common way to approach these systems has been carried on for PEP-II, KEKB, DAFNE, and, later, for SuperB and SuperKEKB. Feedback systems for circular light sources are only apparently very similar, nevertheless they have to cope with different performance requirements and beam currents.

Having in mind the approach developed for the previous lepton colliders, what is necessary to damp the beam oscillations in FCC-ee, is "simply" getting the position displacement (in the horizontal, vertical or longitudinal plane) for each bunch in every turn, and, after computing the correction signal, applying it to the selected bunch as soon as possible. The systems will be designed to work in the time domain without considering in detail the modes which are actually acting in the ring. Of course a

bunch-by-bunch feedback leads to a system design that is mainly digital. Considering the difference between transverse and longitudinal feedback systems, the digital processing unit (DPU) is identical while the analogue parts (front end and back end), the power amplifiers and the kickers are quite different. Another difference is the expected tune value that is usually much lower for the longitudinal plane as compared to the transverse ones.

Analysing the FCC-ee characteristics and taking into account the beam dynamics point of view, three possible cases can be considered as feedback design strategies [18,19,20]:

- a) slow or very slow instabilities (growth rates slower than 10 revolution turns)
- b) fast instabilities (growth rates up to 3 revolution turns)
- c) extremely fast instabilities (growth rates around 1-2 turns or even less).

These three approaches are based on the experience acquired with several lepton colliders showing that one feedback system cannot damp growth rates faster than 10 turns. As consequence different approaches must be studied to achieve more challenging goals.

Before discussing how to proceed to cope with the different cases, there are some preliminary requirements to consider. First of all, it is necessary a very good β function at the pick-up to have a decent signal-to-noise ratio before processing it. Also a good β at the kicker is required to have the best performance for the voltage applied to each bunch. Regarding the fractional tune value, it is important to note that if it is too small ($< .10$) the correction signal computing will become slower, because more acquisitions are necessary to fill the F.I.R. filter response, worsening the feedback damping time.

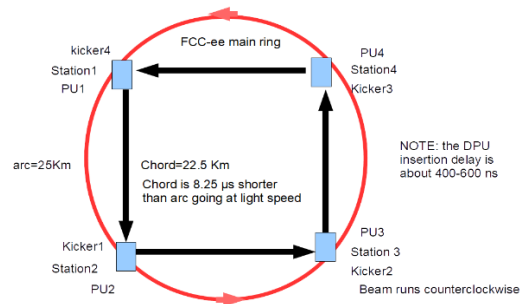


Figure 5: proposed feedback sketch for option c). Note that PU is for pick-up and DPU for digital processing unit

Let's now discuss the three cases described above, with the goal of maintain the standard mixed analogue and digital technologies developed for the feedback in the past. Only the a) case can be based on the usual well known approach, in which many parts are commercially available. Indeed, increasing the gain over a certain limit has only the effect to saturate the feedback. Moreover, the present feedback systems can process up to a few thousand

buckets. As a consequence, new and more powerful digital processing units (DPU) have to be built for the a) case as well to cope with a very high harmonic number (of the order of 100k). Another possible issue can arise due to the possible very low frequency of the modes that have to be damped. Indeed, the kickers and the power amplifiers feeding the correction signal must have the appropriate bandwidth. Moreover, even if power amplifiers are commercial devices, they have to be checked carefully to work in pulse mode at low frequencies, too. A similar feature is necessary for the kickers. As said above, this “usual” feedback design is foreseen to have a damping rate of 10 revolution turns, as the experience acquired in the past and present colliders has showed.

Analysing the b) case, that considers instability growth rates up to 3 revolution turns, a different and more powerful scheme has to be implemented. Indeed, only one feedback system does not guarantee to manage correctly enough power to damp the oscillations without system saturation. The experience made at DAFNE in 2007 by implementing two complete feedback systems in the same horizontal plane as described in [21], clearly highlights that the damping rate is mainly limited by the noise coming from the pick-up and not by the noise generated inside the feedback itself. A high beam current makes worse the signal-to-noise ratio leading to a feedback saturation. Moreover, saturation or excess of feedback gain can induce an enlargement of the bunch dimension. This effect is more dangerous in the vertical plane and it can also be amplified by the kick given by beam-beam collisions. Implementing four co-operative systems spaced by a distance of a quarter of the main ring can overcome the gain saturation limit with the benefit to achieve a feedback damping rate of the order of $10/4=2.5$ revolution turns.

Finally considering the c) case with instability growth rates of the order of 1-2 turns or even slightly less, a very different design scheme is necessary. Indeed, the solution found for the b) case is not sufficient. To achieve a faster damping rate, it is necessary to apply the correction signal earlier than in the previous scheme (able to kick only after one revolution period). Again, four systems are proposed but they are not enough. The way to implement a new faster design consists in putting the kicker with a distance of a quarter of the ring downstream the feedback pick-up. To be effective the correction signal has to arrive at the kicker before the bunch, in a sort of “*feeding forward*”. This is possible because the path along the chord (for the signal) is shorter than the path along the arc (for the beam), as shown in Figure 5. A signal transmission system with about the speed of light is of course necessary. The new hollow optical fibre technology [22] is a state-of-art for cabled transmission and it seems in this moment the best solution to the problem. Otherwise, a standard radiofrequency transmission system can be used. With this scheme the feedback damping rate should be pushed up to 0.625 revolution turns ($10/4=0.625$).

Note that in both the b) and c) cases the author has proposed *four* systems (and not *two, three, or five*, etc.) just

for practical reasons but, of course, a different number of systems can also be also evaluated.

In conclusion, instability growth rates of the order of one revolution turn require a very strong R&D program to implement the above proposed innovative feedback design. Less critical instability growth rates can be solved by a more moderate R&D program.

Now analysing the feedback systems from the ring impedance point of view, it is noteworthy to underline that the three feedback design options have different impacts. The first option requires just one cavity kicker for the longitudinal case and two stripline kickers for the transverse planes, whereas both the b) and c) options need four cavity kickers and eight stripline kickers thus increasing consequently the ring impedance. However, for each feedback (horizontal, vertical, longitudinal) system, the more suitable solution can be implemented by the design option that is best fitting to cope with the instability grow rate.

CONCLUSION

Transverse instabilities can limit both beam and single bunch currents. Source of instabilities are vacuum chamber impedance and (for positive charge stored beams) parasitic e- clouds. Bunch-by-bunch feedback systems are extremely useful tools for both beam diagnostics and instabilities suppression in storage rings. A simple feedback model is proposed for a software simulator based on state-space formalism.

Bunch-by-bunch feedback systems are implemented in storage rings as active devices for instability suppression and for state of art beam or bunch-by-bunch diagnostics.

For FCC-ee, the feedback systems should be based on the designs developed for other previous e+/e- colliders (PEP-II, KEK, DAFNE, SuperB, SuperKekB) able to achieve damping rates up to 10 revolution turns.

By implementing multiple co-operative feedback systems and maintaining the usual design scheme it will be possible to damp instability growth rate up to 3 revolution turns, if necessary.

Damping in about 1 revolution turn or slightly less will be possible only by changing the usual feedback strategy. An innovative bunch-by-bunch “*feeding forward*” system is proposed for this challenging goal.

ACKNOWLEDGEMENT

This work was supported in part by the European Commission under the HORIZON2020 Integrating Activity project ARIES, grant agreement 730871.

Furthermore, the author wishes to remember many researchers with which it has been a pleasure to collaborate. First of all John Fox for all the ideas developed during the last 3 decades together with his SLAC team: H.Hindi, S.Prabhakar, D.Teytelman, A.Young, J.Olsen, C.Rivetta, J.Cesaratto, T.Mastoridis, and many others.

Thanks also to LNF feedback and kicker team (too many to be reported...), as well as to the ALS 90's feedback

team (J.Byrd, W.Barry, J.Corlett, G.Lambertson,) and to the KEK feedback team led by M. Tobiyama.

REFERENCES

- [1] J.Fox, et al. "Observation, Control and Modal Analysis of Coupled-Bunch Longitudinal Instabilities", EPAC'96 Proceedings, 1996.
- [2] S.Prabhakar, "New Diagnostics and Cures for Coupled-Bunch Instabilities", Stanford Univ. PhD thesis, SLAC-R-554, August 2001.
- [3] D.Teytelman, "Architectures and Algorithms for Control and Diagnostics of Coupled-Bunch Instabilities in Circular Accelerators". Stanford Univ. PhD thesis, SLAC-R-633, June 2003.
- [4] A.Drago, et al. "Longitudinal Quadrupole Instability and Control in the Frascati DAFNE Electron ring", PRST-AB, 6, 052801-1-11, 2003.
- [5] J.L. Laclare, "Bunched Beam Coherent Instabilities". Cern Accelerator School 1985. CERN 87-03, 21 April 1987.
- [6] M. Zobov et al., "Collective Effects and Impedance Study for the DAFNE F-Factory". LNF-95/041 (P), 31/7/1995.
- [7] A.Drago, "Fast Horizontal e+ instability measurements in DAFNE", PAC'09, TH5RFP057. Vancouver, Canada, 2009.
- [8] A.Drago, C.Vaccarezza, M.Zobov: "Analysis of Mechanisms Driving the Horizontal Instability in the DAFNE Positron Ring", G-67, 25/5/2006.
- [9] A. Drago et al., "Mitigation and control of instabilities in DAFNE positron ring". Apr 2012. 3 pp. e-Print: arXiv:1204.5016 [physics.acc-ph]. Presented at 2012 Beam Instrumentation Workshop (BIW12), April 15-19, 2012, Newport News, USA. Task 2.4 meeting, CERN, 13/06/2012: http://emetral.web.cern.ch/emetral/Task2point4OfHLLHCWP2/3rdMeeting_05-09-12/TUPG001_talk_r1.pdf
- [10] D.Alesini, A.Drago, A.Gallo, S.Guiducci, C.Milardi, M.Zobov, LNF-INFN; S.De Santis, LBNL; T.Demma, LAL; P. Raimondi, ESRF, "Experimental Measurements of e-Cloud Mitigation using Clearing Electrodes in the DANE Collider", IPAC2012 Proceedings, 2012. <http://accelconf.web.cern.ch/AccelConf/IPAC2012/papers/tuobc03.pdf>
- [11] W.Cheng et al., "Precise Synchronous Phase Measurements". Proceedings of IPAC2017, MOPAB152, Copenhagen, Denmark, 2017.
- [12] M. Migliorati et al., "Landau Damping of Longitudinal Multi-Bunch Instabilities in DAΦNE", DAΦNE Technical Note G-21, 13 September 1993.
- [13] P. Raimondi and M. Zobov, "Tune Shift in Beam-Beam Collisions with a Crossing Angle", DAΦNE Technical Note G-58, 26 April 2003.
- [14] M. Zobov and D. Shatilov, "Synchrotron Tune Shift and Tune Spread Due to Beam-Beam Collisions with a Crossing Angle", DAΦNE Technical Note G-72, 04 March 2010.
- [15] A.Drago et al., "Synchrotron Oscillation Damping Due to Beam-Beam Collisions", THOBRA01, oral talk presented at the first IPAC, Kyoto, Japan, May, 23-28, 2010.
- [16] A.Drago, P. Raimondi, M. Zobov, (INFN/LNF), D.Shatilov, (BINP), "Synchrotron Oscillation Damping by Beam-Beam Collisions in DAFNE", PRST-AB, 14, 092803 (2011).
- [17] A. Drago, "Tune measurements", talk presented at "Beam Dynamics meets Diagnostics" Workshop, 4-6/11/2015, Florence, Italy. <https://indico.gsi.de/event/3509/session/3/contribution/12>
- [18] A.Drago, "Feedback Systems for FCC-ee". Oral presentation at FCC Week 2016, Rome, Italy.
- [19] A.Drago, "Feedback Systems for FCC-ee". Oral presentation at eeFACT2016, 58th ICFA Advanced Beam Dynamics Workshop on High Luminosity Circular e+e-Colliders, 24-27 October 2016. Daresbury (UK). Slides & proceedings: <https://eventbooking.stfc.ac.uk/uploads/eeFact/dragotut3ah9.pdf>. <http://accelconf.web.cern.ch/AccelConf/eeFact2016/> <https://doi.org/10.18429/JACoW-eeFACT2016-TUT3AH9>
- [20] A.Drago, "Fast Feedback System Design Update". Oral presentation at the FCC Week 2018, Amsterdam, the Netherlands, April 9-13, 2018. <https://indico.cern.ch/event/656491/contributions/2918510/attachments/1628585/2594686/FCC-week-2018-Drago.pdf>
- [21] A. Drago, "Fast feedbacks for diagnostics and mitigation of e-cloud instability". Oral presentation at the International Linear Collider Workshop 2008, LCWS08 & ILC08. University of Illinois, Chicago, November 16-20, 2008.
- [22] F.Poletti et al., "Toward high-capacity fibre-optic communications at the speed of light in vacuum", Nature Photonics 7, 279-284 (2013).

THE FUTURE OF THE E-P INSTABILITY IN THE SNS ACCUMULATOR RING *

N.J. Evans[†], M.A. Plum, Oak Ridge National Laboratory, Oak Ridge, TN, USA

Abstract

Concerns about the e-p instability drove many decisions during the design of the accumulator ring for Oak Ridge's Spallation Neutron Source. To date, these decisions seem justified since e-p activity has been observed at the mm scale as a broadband transverse excitation but it has not been a limiting factor (or even a contributor to normal losses) during operation up to the design power of 1.4 MW. (This motion is attributed to e-p based on the broad, evolving spectrum 80-100MHz, and a fast rise time on the order of 10's - 100's of turns when RF buncher voltage is significantly reduced [1, 2].) However, the proton power upgrade (PPU) [3] will increase beam energy from 1.0 GeV to 1.3 GeV to allow 2.0 MW operation on the first target station, and eventually the Second Target Station project (STS) [4] will require an increase in beam current in the ring of about 50% above current operation resulting in 2.8 MW beam. This paper explores the potential for e-p induced beam instability during PPU and STS operation, the predicted effectiveness of existing e-p mitigation measures in the SNS ring, and potential experiments to test these predictions within current operational limitations.

SNS UPGRADES AND THE E-P INSTABILITY

The threshold number of protons, N_p , for e-p instability in a bunched beam may be expressed [5] as:

$$N_p \geq \frac{\pi R}{2 r_e} \left(\frac{64 m_p}{9\pi^2 m_e} \gamma_p \beta_p \right)^2 \left(\frac{b(a+b)}{R^2} \right) Q_\beta^2 \times \left(\frac{(1-f_e)}{f_e} \right)^2 \left(\frac{\Delta Q_e}{Q_e} \right)^2 \left(\eta \frac{\Delta p}{p} \right)^2 F \quad (1)$$

with

$$\left(\eta \frac{\Delta p}{p} \right)^2 F = \frac{\eta e V B W f_0}{\pi \gamma_p \beta_p^2 m_p h} (1 - \cos(\pi B W f_0)) \quad (2)$$

in terms of the machine radius (R), the classical electron radius (r_e), the proton and electron mass (m_p, m_e), the proton's relativistic factors (γ_p, β_p), the horizontal and vertical

beam radii (a, b assumed equal for electrons and the protons), the betatron tune of the proton beam (Q_β), the neutralization factor (f_e), the transverse oscillation frequency, and frequency spread of the electrons (Q_{β_e} and ΔQ_e), the phase slip factor ($\eta = 1/\gamma_T^2 - 1/\gamma_p^2$) the relative momentum spread of the protons ($\Delta p/p$), buncher voltage (V), revolution frequency (f_0), RF harmonic number (h), filling factor (F), and fractional bunch width (BW). We assume RF bunching dominates to calculate $\Delta p/p$, and that $f_e, \Delta Q_e/Q_e$ are roughly constant, based on experience at Los Alamos Proton Storage Ring, a close analog to the SNS case.

For the PPU project the SNS accumulator ring will be operated at 1.3 GeV instead of the current design energy of 1.0 GeV. The only changes to the ring lattice will be the replacement of two of the injection chicane magnets. From the relation given in eq. 1 the threshold intensity (N_p) depends on energy only through γ_p, β_p, η , and f_0 and is proportional to the factor $\gamma_p \beta_p \eta$. Evaluating $N_p(1.0 \text{ GeV}) / N_p(1.3 \text{ GeV}) = 1.17$ i.e., the instability threshold is 17% higher at 1.0 GeV compared to 1.3 GeV. Interpreting these numbers in light of the equation given, the threshold decreases because the SNS ring is operated below transition, and as the beam energy increases the phase slip factor, and thus the frequency spread of betatron oscillation decreases faster than the beam stiffness increases.

This estimate of the relative change in instability threshold is very rough and does not include the effect of changing space charge effects which we have considered to be constant. The scaling given here will need to be verified with experimental measurements of the threshold intensity at various energies. The e-p instability threshold is notoriously difficult to predict. For instance, the development of instability is highly dependent on longitudinal profile [6].

ACTIVE SUPPRESSION OF THE E-P INSTABILITY

Up to 1.4 MW the e-p instability has not been an operational limitation, but the spectral signature of e-p activity is clearly visible in BPM data, accounting for roughly a 0.5 mm, localized displacement of the beam centroid. During operation this instability can be controlled with RF bunching cavities, but can be induced by lower buncher voltage, especially the bunch flattening 2^{nd} harmonic station [6]. Running in this configuration, a transverse instability with a spectrum that shifts upward, and increases in bandwidth as it grows, with a growth rate on the order of 10-100's of turns ($\tau_{rev} = 1 \mu s$) can be observed, characteristics consistent with the e-p instability [7, 8].

Many features designed to mitigate e-p instability (TiN vacuum vessel coating, large ring apertures (10 cm), ded-

* This manuscript has been authored by UT-Battelle, LLC under Contract No. DE-AC05-00OR22725 with the U.S. Department of Energy. The United States Government retains and the publisher, by accepting the article for publication, acknowledges that the United States Government retains a non-exclusive, paid-up, irrevocable, world-wide license to publish or reproduce the published form of this manuscript, or allow others to do so, for United States Government purposes. The Department of Energy will provide public access to these results of federally sponsored research in accordance with the DOE Public Access Plan (<http://energy.gov/downloads/doe-public-access-plan>).

[†] nhe@ornl.gov

icated collimation region) will provide no additional safeguard under different operating scenarios. Here we consider the future efficacy of existing, active suppression measures. We assume that SNS operates very near the e-p threshold when evaluating the potential efficacy of the following active measures to suppress e-p instability.

RF Bunching

Linac beam is accumulated in the ring over 1000 turns with an injected $\Delta p/p \approx 8 \times 10^{-3}$ and a width of about 70% of the circumference of the ring, into a stationary h=1 bucket with some 2nd harmonic before being extracted to the target with $\Delta p/p \approx 2 \times 10^{-2}$, currently two turns after the last injected linac pulse. The longitudinal mismatch causes the injected beam to tumble with a synchrotron period of 1000-2000 turns, depending on the voltage. As the early injected beam rotates, the bunch becomes highly peaked without the second harmonic (though the maximum extent of the bunch in phase is defined by the most recently injected bunch), this peaked beam can lead to the development of the e-cloud that leads to e-p instability [9].

It is well known, that increasing the buncher voltage, despite increasing the mismatch, creates a more stable beam, which has been attributed to the increased transverse tune spread that comes from increasing $\Delta p/p$ in a machine with non-zero chromaticity [10]. Additionally, a second harmonic can be used to flatten the longitudinal distribution with the primary purpose of modifying the development of the e-cloud that drives the e-p instability. This dependence on the longitudinal shape of the beam has been studied in simulation, and experiment [8, 11]. The effect of the buncher on the spectrum of broadband motion is shown in fig. 1.

The RF buncher design consists of 40 kV of h=1, and 20 kV of h=2 RF but each harmonic is currently run at 8 kV during production. We will attempt to make a very rough estimate of the increase in accumulated proton threshold before e-P still available with the existing RF system. Here we assume that it is necessary to maintain the 1:1 ratio of h=1 to h=2 voltage to achieve a similar current profile, that is for the second harmonic to counteract the bunch shortening induced by the bunch rotation from the first harmonic station. We can achieve up to a 150% increase in voltage, and thus threshold charge assuming the trend we currently observe continues. Even assuming SNS currently operates near the threshold value, this would provide sufficient damping to maintain stability with the estimated 17% decrease in threshold at 1.3 GeV even as charge is increased 50% to reach STS beam power. This estimate is made assuming that the relationship between increasing the RF amplitude and an increased e-p threshold holds, but this relationship may break down above some amplitude, a situation which will need to be considered in simulation, or through more experimental investigations.

Transverse Feedback

In case the RF bunching cavities should prove inadequate, SNS has a broadband transverse feedback system developed

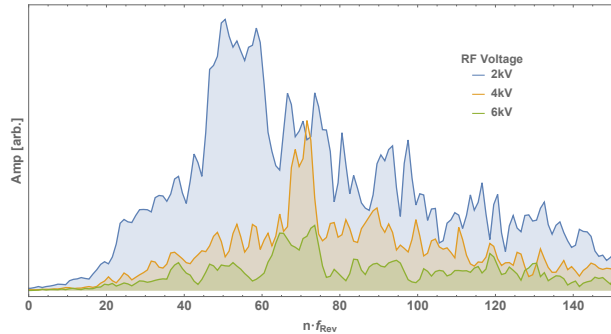


Figure 1: The spectral content of the lower sidebands at extraction for several values of the buncher voltage showing a reduction in oscillation power as the voltage is increased.

expressly to actively suppress e-p induced oscillation over the bandwidth observed in early experimental investigations and simulations. This system is documented extensively in [2]. Data showing the effect of the transverse feedback system on mm scale broadband oscillations we attribute to e-p interaction taken during operation at 1.2 MW are shown in fig. 2. The motion shown in fig. 2 causes no operational problems even without the damper, but can be enhanced by reducing the RF buncher voltage as demonstrated in fig. 1. Although the transverse feedback system is designed to suppress e-p, we hope we can avoid running with active feedback for two reasons: 1) predictions about the strength of the e-p oscillation, and the effectiveness of a feedback system for the type of broadband spectra associated with e-p are very difficult to make, and 2) the necessity of another active system for routine operation introduces a failure point that we hope to avoid, especially if the RF system, which is a part of routine operation in order to maintain the extraction gap, will suffice.

CONCLUSIONS

We estimate the PPU energy upgrade to the SNS accelerator complex will lower the e-p threshold in the ring by about 17%. This estimate makes several assumptions which may prove wrong: that the effect of space charge will be roughly the same as the energy is increased, and can be held constant for the planned increase in intensity; that the neutralization factor, and fractional tune spread of the electron cloud are roughly constant. We plan to carry out experiments to: test assumptions of e-p threshold scaling with energy, verify linear behavior of threshold with increased buncher voltage, and benchmark threshold intensity for current operation.

If these assumptions are at least approximately true, the existing margin in the RF bunching system should be sufficient to raise the estimated e-p threshold above the operating intensities for both PPU and STS. The damper system is available to provide additional suppression of e-p induced transverse motion if needed.

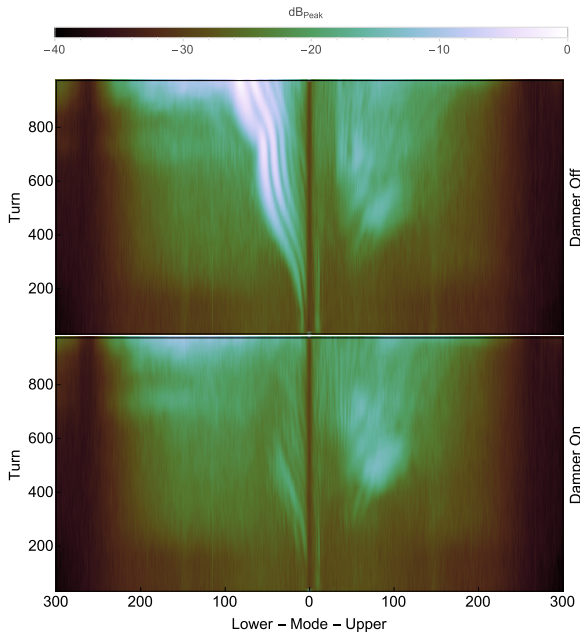


Figure 2: The spectral content of the upper and lower sidebands with the damper system on and off. With a revolution frequency of 1 MHz the excitation attributed to the e-p instability spans 40-100 MHz and is clearly suppressed by the damper system. Figure reproduced from [2].

REFERENCES

- [1] S. Cousineau et al. Instability Observations in the Spallation Neutron Source Accumulator Ring, HB2008, Nashville, Tn, 2008
- [2] N.J. Evans et al. Damping the e-p instability in the SNS accumulator ring, Nuclear Inst. and Methods in Physics Research, A, 885 (2018) 21-29
- [3] J. Galambos et al., Conceptual Design Report Proton Power Upgrade Project, ORNL/TM-2016/672, August 2017
- [4] J. Galambos, D. E. Anderson, D. Bechtol, et al., Technical Design Report, Second Target Station, ORNL/TM-2015/24, January 2015
- [5] R. Macek, Observations of the e-p Instability at PSR Electron Cloud Feedback Workshop, Bloomington, IN, March 15-18, 2004, <http://physics.indiana.edu/shylee/ap/mwacp/epfeedback.html>
- [6] Z. Liu et al., Effect of Bunch Shape on Electron-Proton Instability, Proceedings of IPAC2010, Kyoto, May 23-28, 2010, p. 2090
- [7] M. Blaskiewicz, Electron cloud instabilities in the Proton Storage Ring and Spallation Neutron Source, PRSTAB 6, 014203 (2003)
- [8] A. Shishlo et al., Self-Consistent Electron-Cloud Simulation for Long Proton Bunches, Particle Accelerator Conference, Knoxville, Tn 2005
- [9] V. Danilov, Z. Liu Studies of the Effect of 2nd Harmonic on the e-P instability and RF Control of Instabilities, HB2010 Morshach, Switzerland, 2010
- [10] R. Macek et al., Active damping of the e-p instability at the Los Alamos Proton Storage Ring, Journal of Applied Physics 102, 124904 (2007)
- [11] Z. Liu, Linear Optics Correction and Observation of Electron Proton Instability in the SNS Accumulator Ring (Ph.D. thesis), Indiana University, 2011

ELECTRON CLOUD EFFECTS

G. Iadarola* and G. Rumolo
CERN, Geneva, Switzerland

Abstract

Secondary electron emission in combination with the electromagnetic fields generated by a bunched beam can lead to the formation of electron clouds in the beam chambers of particle accelerators. The interaction of the circulating beam with the e-cloud can lead to transverse instabilities, beam losses, transverse emittance degradation. Moreover, the electrons impacting on the chamber's walls induce other unwanted effects like energy deposition (particularly critical for superconducting machines) and vacuum degradation. This contribution summarizes the mechanisms leading to the formation of the e-cloud, the effects that it can have on the performance of an accelerator, the methods employed to study the phenomenon and different techniques that have been developed to reduce or suppress its formation.

INTRODUCTION

Over the last five decades electron cloud effects have been observed in several circular accelerators operating with positively charged particles [1, 2]. A synthesis of the main observation in different machines is given Tab. 1.

The mechanism leading to the formation of an e-cloud in the beam chamber of a particle accelerator is illustrated schematically in Fig. 1 [3, 4]. "Primary" or "seed" electrons can be generated by a bunch passage due to the ionization of the residual gas or to photo-emission from the chamber's wall induced by the beam synchrotron radiation. These electrons can be accelerated by the electric field of the beam, typically to energies in the order of hundreds of electronvolts. When an electron with these energies impacts on the walls, secondary electron emission can occur and multiple low-energy electrons can be emitted. These "secondary electrons" have lower kinetic energy (~ 10 eV). In case they impact the wall, there is a high probability of them being absorbed without generating any further secondary. However, if the delay between subsequent bunches (bunch spacing) is sufficiently short, before impacting on the wall they can be accelerated by the following bunch passage, which strongly increases their probability of generating more secondaries. For a long bunch train, this can lead to an avalanche electron multiplication and to the formation of a dense e-cloud in the chamber (this regime is often called beam-induced "multipacting"). This mechanism makes the electron density larger for the bunches at the tail of bunch trains.

The e-cloud can induce unwanted effects on the circulating beam such as transverse instabilities, transverse emittance blow-up and particle losses. Other unwanted effects are vacuum degradation due to electron-stimulated desorption

and power deposition (heat loads) on the chamber's walls (particularly critical for superconducting devices) [5].

MAIN FACTORS INFLUENCING THE ELECTRON CLOUD FORMATION

Observing the sketch in Fig. 1, it is possible to identify different factors that influence the e-cloud buildup process.

A very important role is played by the beam chamber. Its geometry affects the electron acceleration and time-of-flight between impacts. It also defines the boundary conditions for the calculation of the electric field generated by the beam and by the electrons themselves. Moreover the chamber surface properties will define the amount of electrons generated by photoemission and, most importantly, the probability of secondary emission occurring when an electron impacts on the wall [6, 7].

The secondary emission process is described by the Secondary Electron Yield (SEY) function, which is defined as the ratio between the impinging electron current and the emitted electron current and depends strongly on the energy of the impinging electrons (the SEY is often indicated with the symbol " δ "). Typical SEY curves are shown in Fig. 2. A synthetic parameter which is often used to describe the surface is the maximum of the SEY curve (indicated as SEY_{\max} or δ_{\max}). The dependence of the SEY on the energy of the impacting electrons is typically non-monotonic. As a result, there will be a defined energy range, indicated in red in Fig. 2, for which $\delta(E) > 1$ and the surface globally behaves like an electron emitter. For the e-cloud buildup to occur it is necessary to have a significant fraction of the impacting electrons with energies within this range. The SEY is also dependent on the angle of incidence of the electrons and, in particular, it tends to be higher for grazing angles.

The SEY depends on the chemical properties of the surface and can be affected by different processes. In particular, for several materials, the SEY decreases when the surface is exposed to an electron flux [8]. For this reason the e-cloud is, to some extent, a "self-healing" mechanism in the sense that the surface can be conditioned by exposing it to the e-cloud itself (this effect is called "beam-induced scrubbing").

The beam configuration also plays a major role in the e-cloud buildup process. As observed before a key parameter is the bunch spacing, which determines the amount of electrons surviving between consecutive bunch passages. In particular, the bunch spacing strongly affects the "multipacting threshold", defined as the value of δ_{\max} above which the avalanche multiplication occurs. An example is shown in Fig. 3 for the case of a bending magnet of the Large Hadron Collider (LHC). In this case, with the 25 ns bunch spacing, multipacting occurs for δ_{\max} values larger than 1.4 while with the 50 ns bunch spacing the e-cloud buildup only takes

* Giovanni.Iadarola@cern.ch

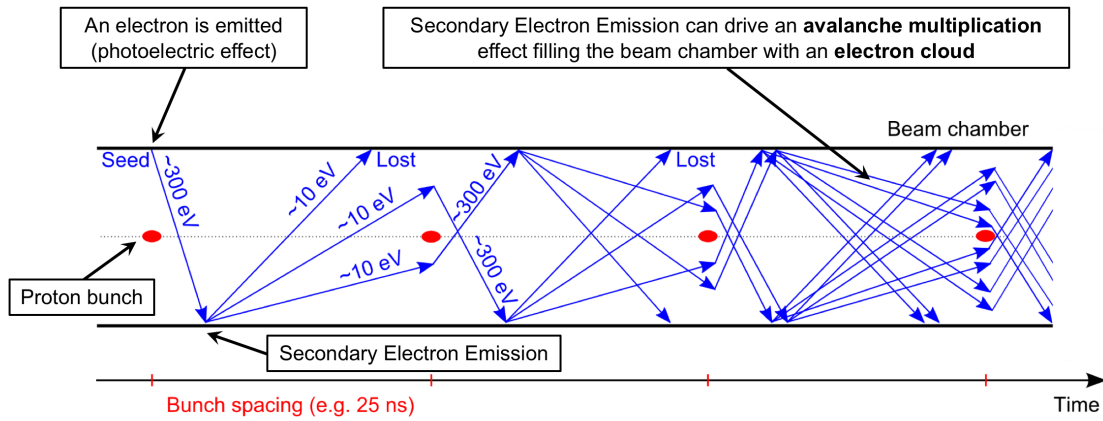


Figure 1: Schematic illustration of the e-cloud buildup process.

Year	Place	Observations
1965	Novosibirsk, Argonne ZGS, BNL AGS	Transverse instabilities.
1970s	CERN ISR, Bevatron	Transverse instabilities, vacuum degradation.
1988	Los Alamos PSR	Transverse instabilities.
1989	KEK PF	Multibunch instability for positron bunch trains
1999	CERN SPS and PS, KEKB and PEP-II	Pressure rise, transverse instabilities, effects on instrumentation, tune shifts along bunch train, emittance degradation.
2002	RHIC	Pressure rise, tune shift, transverse instabilities at transition.
2003-2009	Tevatron, SNS, DaΦne, ANKA, PETRA III, J-PARC main ring	Vacuum degradation, transverse instabilities, transverse blow-up, heat load on cryogenic devices.
2008-present	Cesr-TA	A program to study electron cloud issues is conducted.
2010-present	LHC	Vacuum degradation, transverse instabilities, beam degradation, heat loads in cryogenic devices.
2014	FERMILAB recycler	Transverse instabilities.
2016-present	SuperKEKB	Dynamic pressure rise, beam degradation.

Table 1: Summary of the main observations of e-cloud effects in particle accelerators (largely based on [1]).

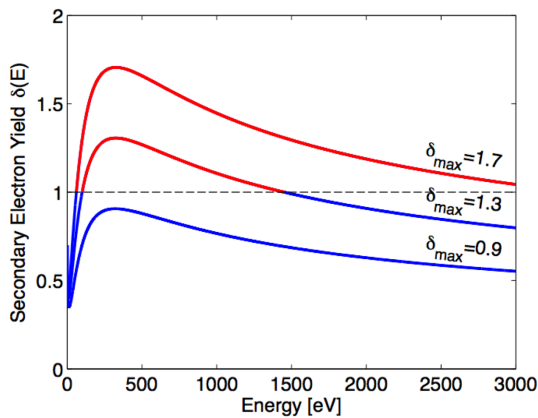


Figure 2: Examples of SEY curves for different values of the δ_{max} parameter.

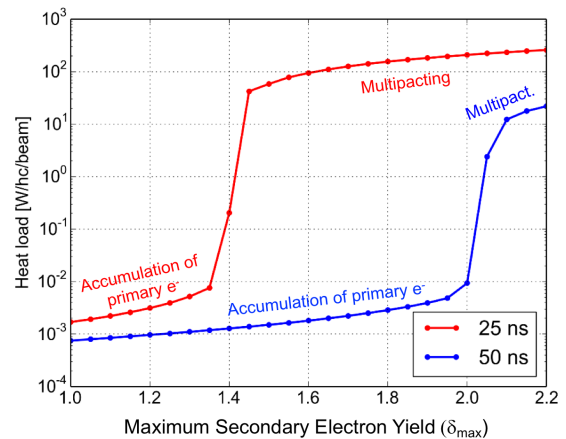


Figure 3: Heat load in the LHC bending magnet for 25 ns and 50 ns bunch spacing (PyECLLOUD simulations).

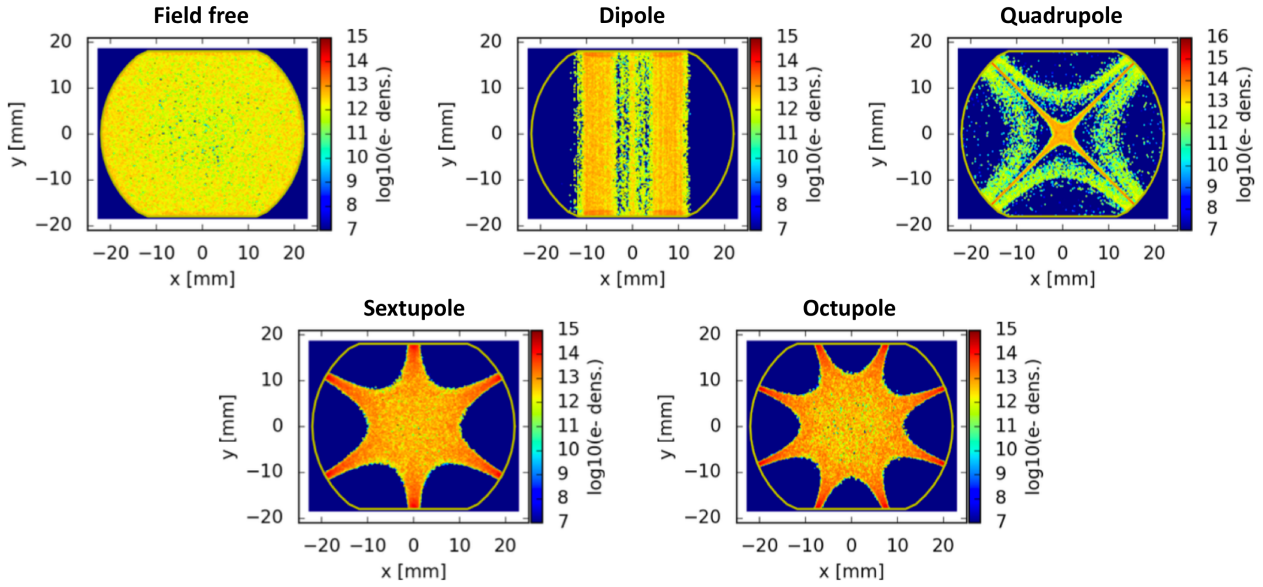


Figure 4: Electron distribution in LHC arc components with different magnetic field configurations (PyECLLOUD simulations).

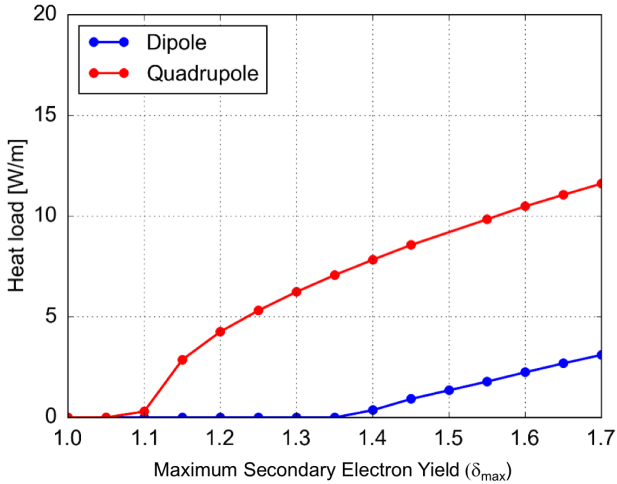


Figure 5: Heat loads generated by e-cloud the LHC dipole and quadrupole magnets (PyECLLOUD simulations for 25 ns bunch spacing).

place for $\delta_{max} > 2.0$. Other beam parameters such as bunch intensity and bunch length also influence the e-cloud dynamics, as they change the acceleration received by the electrons from the beam.

Due to the very low kinetic energy, the electron trajectories are strongly influenced by externally applied magnetic fields. For large enough magnetic fields, the electrons spin around the field lines. This effect, together with the shape of the SEY curve and the beam electric field, determines very characteristic patterns in the distribution of the electrons within the beam chamber as shown in Fig. 4.

In quadrupole magnets and higher order multipoles, due to the presence of magnetic field gradients, magnetic trapping

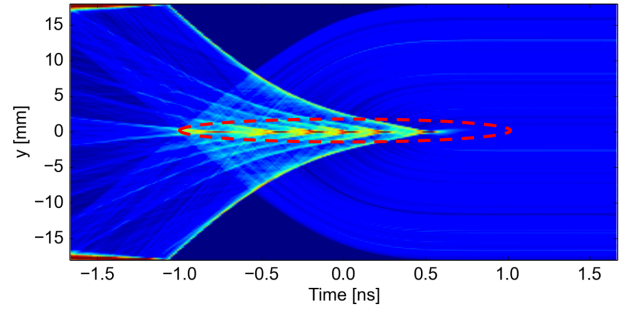


Figure 6: Electron cloud density evolution in the horizontal plane of a bending magnet during the passage of a bunch (PyECLLOUD simulation).

can occur [9]. Electrons can survive several bunch passages and accumulate energy from more than one bunch, reaching energies up to a few kiloelectronvolts. In the case of the LHC quadrupoles this results in heat loads that are much stronger compared to the dipole magnets, as shown in Fig. 5 [10].

EFFECT OF THE ELECTRON CLOUD ON THE BEAM DYNAMICS

When a bunch of positively charged particle travels in an e-cloud, electrons are attracted towards the bunch and “fly” through it, exerting significant electromagnetic forces on the beam particles. In particular, the electron density at the beam location increases during the bunch passage (“pinch” effect) as illustrated in Fig. 6. As a consequence of this dynamics, several effects on the circulating beam can be observed.

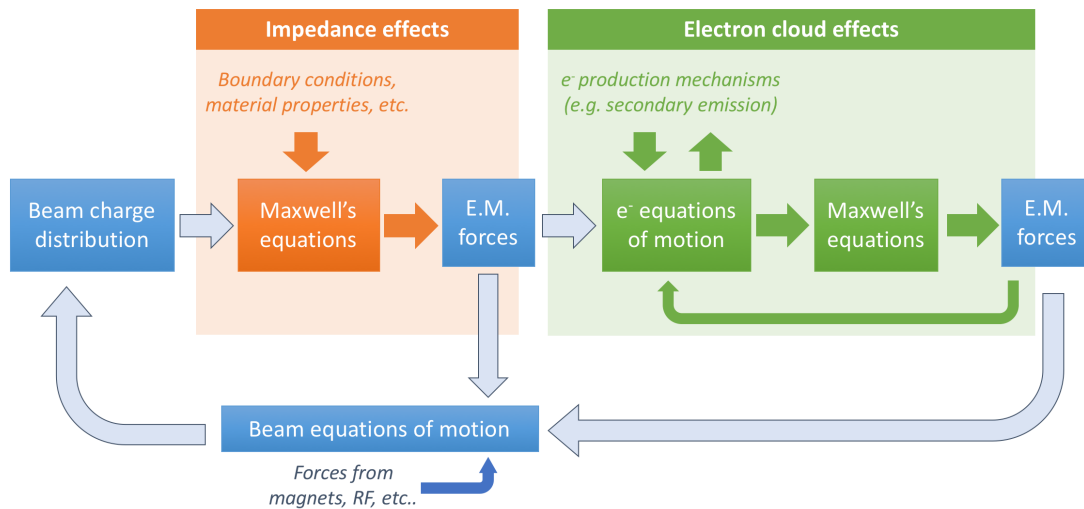


Figure 7: Block diagram illustrating the mechanism of beam instabilities driven by e-cloud.

Instabilities

The interaction of the beam with the e-cloud can generate transverse instabilities [11–13]. A block diagram of the coupled dynamics of the beam and the e-cloud is shown in Fig. 7. The orange box represents conventional impedance effects: the beam charge distribution generates electromagnetic fields in the beam chambers, which enter as a driving term in the beam equation of motion, causing modifications in the beam distribution. In this case the relation between the beam distribution and the resulting forces on the beam is linear and time-invariant. It can therefore be described by its pulse response (wakefield) and the effect on a generic distribution can be obtained using the linear superposition (convolution integral). In the presence of electrons in the chamber, the electromagnetic forces of the beam will also participate in the electrons' equation of motion and possibly drive the electron multipacting. The electron cloud in turn generates electromagnetic forces, which act back on the beam. The fast motion of the electrons, makes the response of the “e-cloud system” (green box in Fig. 7) neither linear nor time invariant. Therefore the wakefield formalism cannot be used for the description of these phenomena.

The interaction with the e-cloud introduces an additional closed loop in the diagram in Fig. 7, which can amplify the beam oscillations triggering a transverse instability. An e-cloud can drive both coupled-bunch and single-bunch instabilities.

Coupled-bunch instabilities driven by e-cloud have been observed in several machines (e.g. CERN PS and SPS, KEKB, FERMILAB Recycler). Bunches at the tail of the trains are the most affected as they encounter a larger electron density. These instabilities result from alterations of the e-cloud buildup due to transverse oscillations of the beam. They have been successfully modeled analytically using a simple cloud-bunch coupling relation [14, 15]. Typically these instabilities can be effectively controlled with conventional (bunch-by-bunch) transverse feedback systems.

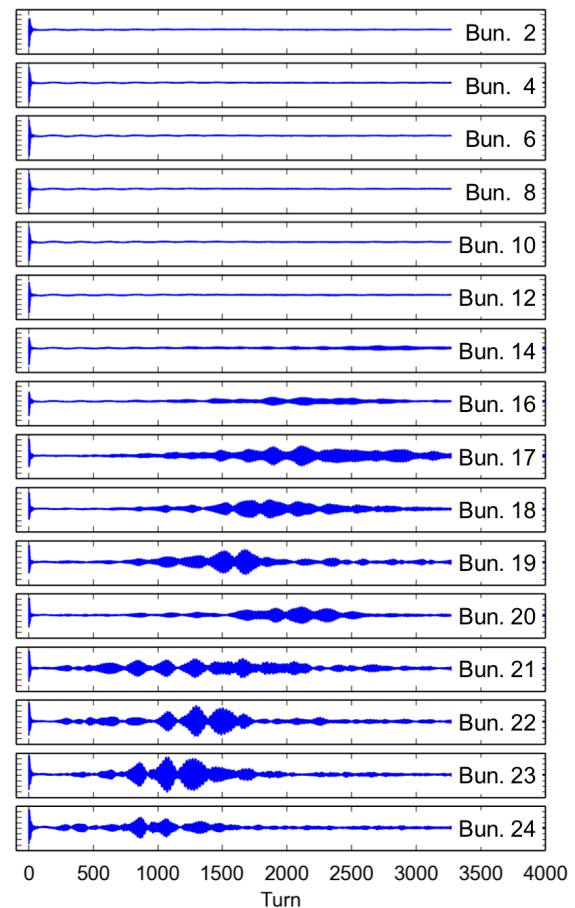


Figure 8: Position measurements for different bunches in a train right after its injection into the LHC. Transverse instabilities can be observed at the tail of the bunch train.

Single bunch instabilities are driven by the motion of the electrons during an individual bunch passage (electron pinch). Typically groups of bunches at the tail of the bunch trains are simultaneously affected but no correlation is ob-

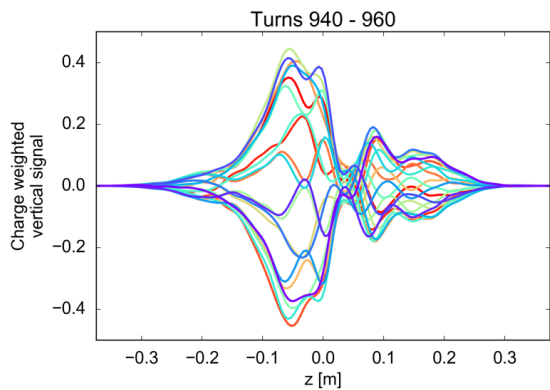


Figure 9: Slice-by-slice position centroid (charge weighted) along an LHC bunch undergoing an e-cloud instability. The different traces correspond to 20 consecutive turns (PyECLOUD-PyHEADTAIL simulation).

served in the centroid motion of the different bunches (an example is shown in Fig. 8). These instabilities can develop very rapidly (with rise-times in the order of $10^2 - 10^3$ turns) and result in beam losses and strong transverse emittance blow-up. As electrons move very fast during the bunch passage, single bunch instabilities driven by e-cloud are characterized by a fast intra-bunch motion, as shown in Fig. 9. For this reason, these instabilities cannot be damped effectively with conventional transverse feedback systems. However, they can be mitigated to some extent operating with large chromaticity and/or with strong amplitude detuning introduced by octupole magnets [16], often at expense of the achievable beam lifetime and emittance preservation. Efforts are ongoing for the development of high-bandwidth feedback systems capable of damping the observed intra-bunch motion [17].

Other effects on the beam

Even when electron densities are low enough not to trigger instabilities, the effect of the e-cloud is still visible on several beam properties.

The presence of the electrons introduces extra focusing forces which in most cases result in a positive shift of the coherent betatron tune, increasing along the bunch train (an example is shown in Fig. 10) [18].

When electrons are accelerated by a bunch passage, energy is transferred from the beam to the electron cloud. In a synchrotron, this results in a shift of the bunch stable phase with respect to the RF system [19]. Tune shift and stable phase measurements are often used as indirect e-cloud diagnostics.

The forces exerted by the e-cloud on the beam particles depend non-linearly on the particle's positions. This can excite resonant lines in the tune diagram and induce quite large tune spreads, especially in combination with octupoles and chromaticity settings that are required to protect the beam from e-cloud instabilities. This results in slow particle losses, emittance growth and bunch shortening (loss of par-

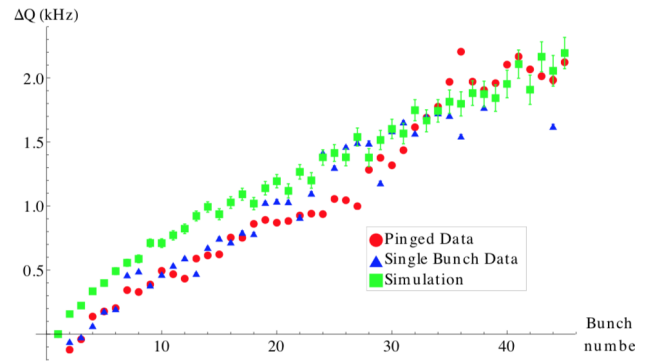


Figure 10: Simulated and measured tune shift for different bunches of a bunch train in the CESR-TA ring (from [18]).

ticles having large longitudinal amplitude). Figure 11 shows the tune footprint estimated for one of the last bunches of an LHC train at injection energy (450 GeV). The asymmetry of the footprint with respect to the unperturbed tune (black star) is introduced by the e-cloud. In order to avoid beam losses due to the interaction with the resonance $Q_v = .33$ it was necessary to change the machine tune settings as shown in Fig. 11 [20].

OTHER EFFECTS ON MACHINE PERFORMANCE

Together with the aforementioned unwanted effects on the beam, the e-cloud can pose other limitations to the operation of an accelerator.

Electrons impacting on the walls of the beam pipe can deposit a significant power on the chamber walls. Looking at the illustration in Fig. 1 one can see that only a small fraction of the energy of the impinging electrons is carried by the secondary electrons, while a much larger fraction is dissipated in the walls. This aspect is particularly critical for superconducting machines, where the cooling capacity on the beam chamber is very limited. In the LHC beam screens are installed, which are operated at temperatures higher than the superconducting coils, in order to ease the extraction of beam induced heat loads [21]. When operating with nominal bunch spacing (25 ns) e-clouds develop in the superconducting arc magnets generating heat loads that are much higher than observed with larger bunch spacings (a comparison between 25 ns and 50 ns is shown in Fig. 12) [22]. In order to operate reliably with the 25 ns bunch spacing a dedicated feed-forward control had to be developed in order to dynamically adapt the cryogenic regulations using the measured properties of the circulating beam, based on pre-computed e-cloud models [23].

The flux of electrons impinging on the walls also generates vacuum degradation due to electron-stimulated desorption [24]. This can pose different problems, for example increased background in collider experimental regions and

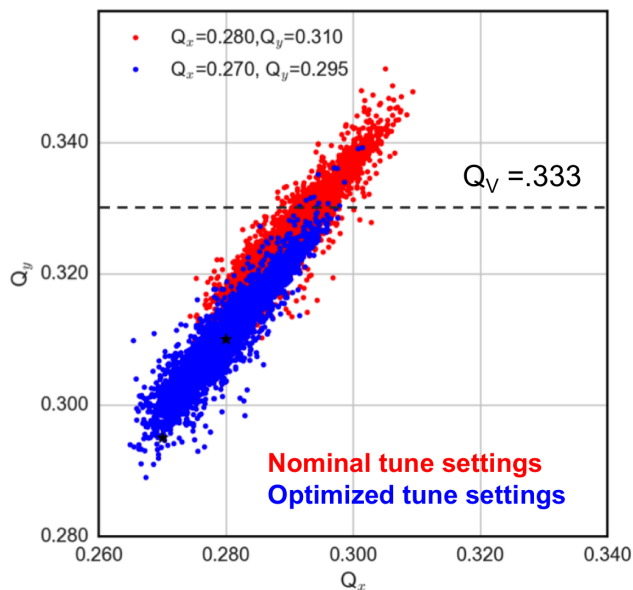


Figure 11: Tune footprints evaluated for a LHC bunch at injection including the effect of octupoles powered at 26 A, $Q'_{x,y}$ at 15 units, and EC in dipole and quadrupole magnets. The dashed line represents the third order resonance $Q_y = .33$. The black star represents the unperturbed tune for the optimized settings.

risk of breakdown in high voltage devices like kickers or electrostatic septa.

The presence of e-cloud can also induce malfunctions on beam diagnostic devices [25].

NUMERICAL MODELING

The understanding of e-cloud phenomena heavily relies on MacroParticle (MP) simulations. The full modeling of the coupled dynamics of the beam and the e-cloud is computationally very heavy, as it involves multiple space and time scales. In particular one needs to simulate the electron dynamics over the entire beam chamber ($\sim 1 - 10$ cm wide) while having enough spacial resolution within the beam transverse size ($\sim 0.1 - 1$ mm). Moreover, while the electron motion happens at the 1 ns time-scale, the effects on the beam stability are visible only when the action of the e-cloud is accumulated over many turns (the typical instability rise-times are in the range $\sim 1 - 10$ s).

Fully self-consistent simulations have been made only rarely and require considerable computing resources ($\sim 10^3$ CPUs) [26]. More often the problem is studied in two stages [27, 28]:

1. e-cloud “build-up simulations” employ Particle-In-Cell (PIC) methods to study exclusively the dynamics of the electrons and the multipacting process using an unperturbed beam distribution. Examples of buildup codes are CLOUDLAND, E-CLOUD and its evolution PyE-CLOUD, PEI, POSINST.

2. “Beam-dynamics simulations” study the interaction of the beam (typically a single bunch) with a given initial electron distribution obtained from a buildup simulation. Even with these simplifications, the more demanding cases (e.g. LHC at high energy) can be computationally very demanding, requiring advanced computational techniques (e.g. multi-grid Poisson solvers) and the usage of parallel computing resources. Examples of this kind of simulation codes are CMAD, HEAD-TAIL and its evolution PyE-CLOUD-PyHEADTAIL, PEHTS.

MITIGATION TECHNIQUES

Several techniques have been developed to mitigate the electron cloud formation, which can be grouped in two categories:

- Techniques relying on modifications of the surface behavior. The most widely used are:
 - Beam induced conditioning or “scrubbing” consists in operating the accelerator with beam configurations that enhance the e-cloud production. For several materials, the exposition of the surface to the electron flux decreases the SEY mitigating the e-cloud [29];
 - Morphological changes of the surface: the SEY can be reduced by increasing the surface roughness (using for example laser ablation), or introducing macroscopic grooves [30–32];
 - Coating of the surface with materials which have intrinsically low SEY (e.g. amorphous carbon, TiN, NEG) [33].
- Techniques acting on the electron dynamics. They aim in particular at decreasing the probability of electrons surviving between consecutive bunch passages:
 - Electric fields can be applied in the beam chambers using so called “clearing electrodes” to push secondary electrons back on the surface [34];
 - Weak longitudinal magnetic fields can be applied using solenoids or permanent magnets to bend the secondary electron trajectories back on the surface [35, 36].

These techniques are included in the designs for several ongoing and future projects like SuperKEKB, High Luminosity LHC and the design study for Future Circular Colliders (FCC).

ACKNOWLEDGMENTS

The authors would like to thank G. Arduini, P. Dijkstal, K. Li, L. Mether, E. Metral, A. Romano, G. Skripka for their important input to the present contribution.

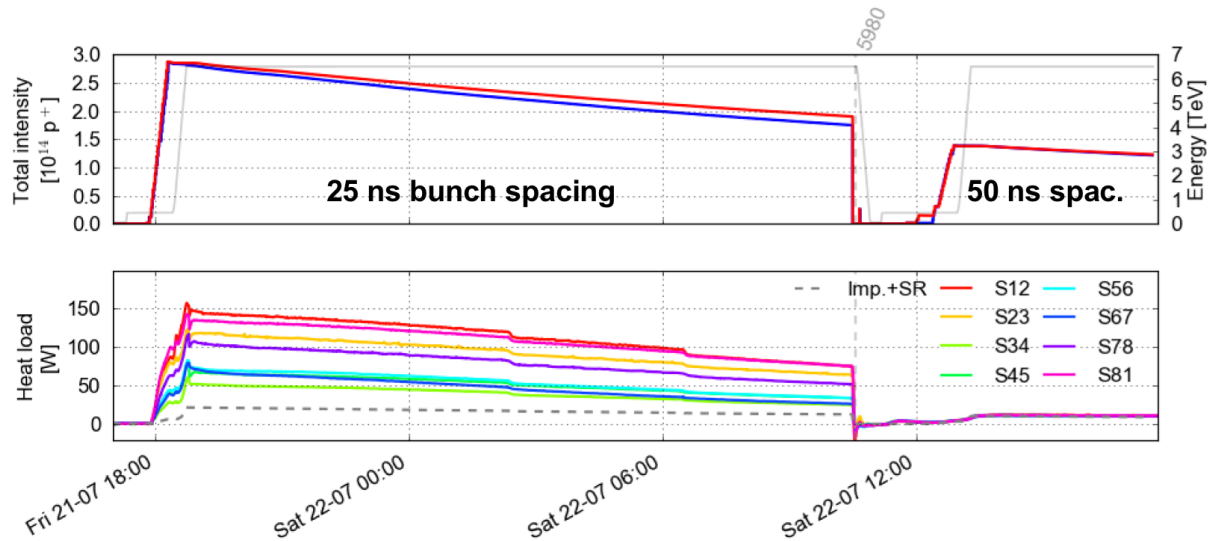


Figure 12: Average heat loads measured in the half-cells of the LHC arcs with two different bunch spacings [22].

REFERENCES

- [1] F. Zimmermann, “Electron-Cloud Effects in past and future machines - walk through 50 years of Electron-Cloud studies,” in *Proceedings, 5th Workshop on Electron-Cloud Effects (E-CLOUD’12): La Biodola, Isola d’Elba, Italy, June 5-9, 2012, 2013*.
- [2] R. Cimino and T. Demma, “Electron cloud in accelerators,” *International Journal of Modern Physics A*, vol. 29, no. 17, p. 1430023, 2014.
- [3] M. A. Furman, “Formation and dissipation of the electron cloud,” in *Proceedings of the 2003 Particle Accelerator Conference*, vol. 1, pp. 297–302 Vol.1, May 2003.
- [4] G. Iadarola, “Electron cloud studies for CERN particle accelerators and simulation code development.” CERN-THESIS-2014-047, 2014.
- [5] G. Rumolo, F. Ruggiero, and F. Zimmermann, “Simulation of the electron-cloud build up and its consequences on heat load, beam stability, and diagnostics,” *Physical Review Special Topics-Accelerators and Beams*, vol. 4, no. 1, p. 012801, 2001.
- [6] M. A. Furman and M. T. F. Pivi, “Probabilistic model for the simulation of secondary electron emission,” *Phys. Rev. ST Accel. Beams*, vol. 5, p. 124404, Dec 2002.
- [7] R. Cimino, I. R. Collins, M. A. Furman, M. Pivi, F. Ruggiero, G. Rumolo, and F. Zimmermann, “Can low-energy electrons affect high-energy physics accelerators?,” *Phys. Rev. Lett.*, vol. 93, p. 014801, Jun 2004.
- [8] F. Le Pimpec, R. E. Kirby, F. K. King, and M. Pivi, “Electron conditioning of technical aluminium surfaces: Effect on the secondary electron yield,” *Journal of Vacuum Science & Technology A*, vol. 23, no. 6, pp. 1610–1618, 2005.
- [9] M. G. Billing, J. Conway, E. E. Cowan, J. A. Crittenden, W. Hartung, J. Lanzoni, Y. Li, C. S. Shill, J. P. Sikora, and K. G. Sonnad, “Measurement of electron trapping in the cornell electron storage ring,” *Phys. Rev. ST Accel. Beams*, vol. 18, p. 041001, Apr 2015.
- [10] P. Dijkstal, G. Iadarola, L. Mether, and G. Rumolo, “Simulation studies on the electron cloud build-up in the elements of the LHC Arcs at 6.5 TeV,” *CERN-ACC-NOTE-2017-0057*, Oct 2017.
- [11] K. Ohmi and F. Zimmermann, “Head-tail instability caused by electron clouds in positron storage rings,” *Phys. Rev. Lett.*, vol. 85, pp. 3821–3824, Oct 2000.
- [12] G. Rumolo and F. Zimmermann, “Electron cloud simulations: beam instabilities and wakefields,” *Phys. Rev. ST Accel. Beams*, vol. 5, p. 121002, Dec 2002.
- [13] A. Romano, O. Boine-Frankenheim, X. Buffat, G. Iadarola, and G. Rumolo, “Electron cloud buildup driving spontaneous vertical instabilities of stored beams in the large hadron collider,” *Phys. Rev. Accel. Beams*, vol. 21, p. 061002, Jun 2018.
- [14] G. Arduini, T. Bohl, K. Cornelis, W. Höfle, E. Métral, and F. Zimmermann, “Beam observations with electron cloud in the CERN PS and SPS complex,” *CERN-2005-001*, 2005.
- [15] S. A. Antipov, P. Adamson, A. Burov, S. Nagaitsev, and M.-J. Yang, “Fast instability caused by electron cloud in combined function magnets,” *Phys. Rev. Accel. Beams*, vol. 20, p. 044401, Apr 2017.
- [16] K. S. B. Li and G. Rumolo, “Mitigation of Electron Cloud Instabilities in the LHC Using Sextupoles and Octupoles,” *Conf. Proc.*, vol. C1205201, pp. 3084–3086, 2012.
- [17] J. M. Cesaratto, J. D. Fox, C. H. Rivetta, D. Alesini, A. Drago, A. Gallo, F. Marcellini, M. Zobov, S. De Santis, Z. Paret, A. Ratti, H. Qian, H. Bartosik, W. Hofle, and C. Zannini, “SPS Wideband Transverse Feedback Kicker: Design Report,” *CERN-ACC-NOTE-2013-0047*, Dec 2013.
- [18] M. G. Billing, G. Dugan, M. J. Foster, D. L. Kreinick, R. E. Meller, M. A. Palmer, G. A. Ramirez, N. T. Rider, M. Rendina, K. Sonnad, J. P. Sikora, H. A. Williams, R. L. Holtzapple, J. Y. Chu, and J. W. Flannagan, “Status of electron cloud dynamics measurements at CESR/TA,” in *Proceedings, 2nd International Conference, IPAC 2011, San Sebastian, Spain, September 4-9, 2011*, p. MOPS084, 2011.

- [19] J. F. Esteban Müller, P. Baudrenghien, T. Mastoridis, E. Shaposhnikova, and D. Valuch, “High-accuracy diagnostic tool for electron cloud observation in the LHC based on synchronous phase measurements,” *Phys. Rev. ST Accel. Beams*, vol. 18, p. 112801, Nov 2015.
- [20] A. Romano, G. Iadarola, K. Li, and G. Rumolo, “Macroparticle Simulation Studies of the LHC Beam Dynamics in the Presence of Electron Cloud,” in *Proceedings, 8th International Conference, IPAC 2017, Copenhagen, Denmark, May 14-19, 2017*, p. TUPVA018, 2017.
- [21] E. Hatchadourian, P. Lebrun, and L. Taviani, “Supercritical Helium Cooling of the LHC Beam Screens,” *LHC-Project-Report-212*, p. 5 p, Jul 1998.
- [22] G. Iadarola, G. Rumolo, P. Dijkstal, and L. Mether, “Analysis of the beam induced heat loads on the LHC arc beam screens during Run 2,” *CERN-ACC-NOTE-2017-0066*, Dec 2017.
- [23] B. Bradu, A. Tovar González, E. Blanco Viñuela, P. Plutecki, E. Rogez, G. Iadarola, G. Ferlin, and B. Fernández Adiego, “Compensation of beam induced effects in LHC cryogenic systems,” in *Proc. of International Particle Accelerator Conference (IPAC’16), Busan, Korea, May 8-13, 2016*, 2016.
- [24] S. Y. Zhang, M. Bai, M. Blaskiewicz, P. Cameron, A. Drees, W. Fischer, D. Gassner, J. Gullotta, P. He, H. C. Hseuh, H. Huang, U. Iriso-Ariz, R. Lee, W. W. Mackay, B. Oerter, V. Ptitsyn, V. Ponnaiyan, T. Roser, T. Satogata, L. Smart, D. Trbojevic, and K. Zeno, “Rhic pressure rise and electron cloud,” in *Proceedings of the 2003 Particle Accelerator Conference*, vol. 1, pp. 54–56 Vol.1, May 2003.
- [25] W. Höfle, “Observations of the electron cloud effect on pick-up signals in the SPS,” *CERN-SL-2000-007-DI*, 2000.
- [26] M. A. Furman, J. L. Vay, and M. Venturini, “Direct Numerical Modeling of E-Cloud Driven Instability of Three Consecutive Batches in the CERN SPS,” *Conf. Proc.*, vol. C1205201, pp. 1125–1127, 2012.
- [27] E. Benedetto *et al.*, “Review and comparison of simulation codes modeling electron-cloud build up and instabilities,” in *9th European Particle Accelerator Conference (EPAC 2004) Lucerne, Switzerland, July 5-9, 2004*, 2004.
- [28] G. Iadarola, E. Belli, K. Li, L. Mether, A. Romano, and G. Rumolo, “Evolution of Python Tools for the Simulation of Electron Cloud Effects,” in *Proceedings, 8th International Particle Accelerator Conference (IPAC 2017): Copenhagen, Denmark, May 14-19, 2017*, p. THPAB043, 2017.
- [29] G. Iadarola, B. Bradu, P. Dijkstal, L. Mether, and G. Rumolo, “Impact and Mitigation of Electron Cloud Effects in the Operation of the Large Hadron Collider,” in *Proceedings, 8th International Particle Accelerator Conference (IPAC 2017): Copenhagen, Denmark, May 14-19, 2017*, p. TUPVA019, 2017.
- [30] G. Tang, A. C. Hourd, and A. Abdolvand, “Nanosecond pulsed laser blackening of copper,” *Applied Physics Letters*, vol. 101, no. 23, p. 231902, 2012.
- [31] R. Valizadeh, O. B. Malyshev, S. Wang, S. A. Zolotovskaya, W. Allan Gillespie, and A. Abdolvand, “Low secondary electron yield engineered surface for electron cloud mitigation,” *Applied Physics Letters*, vol. 105, no. 23, p. 231605, 2014.
- [32] R. Valizadeh, O. B. Malyshev, S. Wang, S. A. Zolotovskaya, A. W. Gillespie, and A. Abdolvand, “Low Secondary Electron Yield Engineered Surface for Electron Cloud Mitigation,” *Appl. Phys. Lett.*, vol. 105, p. 231605, 2014.
- [33] P. C. Pinto, S. Calatroni, H. Neupert, D. Letant-Delrieux, P. Edwards, P. Chiggiato, M. Taborelli, W. Vollenberg, C. Yin-Vallgren, J. Colaux, and S. Lucas, “Carbon coatings with low secondary electron yield,” *Vacuum*, vol. 98, pp. 29 – 36, 2013. 14th Joint Vacuum Conference/12th European Vacuum Conference/11th Annual Meeting of the Deutsche Vakuum Gesellschaft/ 19th Croatian-Slovenian Vacuum Meeting, 04-08 June 2012, Dubrovnik, Croatia.
- [34] Y. Suetsugu, H. Fukuma, L. Wang, M. Pivi, A. Morishige, Y. Suzuki, M. Tsukamoto, and M. Tsuchiya, “Demonstration of electron clearing effect by means of a clearing electrode in high-intensity positron ring,” *Nuclear Instruments and Methods in Physics Research Section A: Accelerators, Spectrometers, Detectors and Associated Equipment*, vol. 598, no. 2, pp. 372 – 378, 2009.
- [35] H. Fukuma, J. Flanagan, K. Hosoyama, T. Ieiri, T. Kawamoto, T. Kubo, M. Suetake, S. Uno, S. S. Win, and M. Yoshioka, “Status of solenoid system to suppress the electron cloud effects at the kekb,” *AIP Conference Proceedings*, vol. 642, no. 1, pp. 357–359, 2002.
- [36] Y. Suetsugu, K. Shibata, T. Ishibashi, K. Kanazawa, M. Shirai, S. Terui, and H. Hisamatsu, “First commissioning of the superkekb vacuum system,” *Phys. Rev. Accel. Beams*, vol. 19, p. 121001, Dec 2016.

STUDIES FOR THE SPS TRAVELLING WAVE CAVITIES UPGRADE

P. Kramer^{1*}, C. Vollinger, CERN, Geneva, Switzerland

¹also at Institute of High Frequency Technology (IHF), RWTH Aachen University, Germany

Abstract

The Super Proton Synchrotron (SPS) 200 MHz accelerating system poses an intensity limitation for the planned High Luminosity (HL)-LHC upgrade due to excessive beam loading as well as higher-order modes (HOMs) contributing to a longitudinal multi-bunch instability. The mitigation of these HOMs together with a shortening of the cavities is therefore an essential part of the LHC Injectors Upgrade (LIU) project. A brief introduction to the accelerating structure as well as its present and future cavity configurations is given. First conclusions are drawn from lab measurements performed on three spare cavity sections regarding tuning and beam impedances. The following studies on longitudinal impedance are targeted towards the shorter cavity configuration used in the future. The particular difficulties inherent to the HOM-damping of this configuration are identified and illustrated. Taking these findings into account, a first improved HOM-damping scheme with regard to the scheme in use today is developed.

INTRODUCTION

The accelerating system of the SPS in today's configuration cannot support beam intensities required for the planned High Luminosity (HL)-LHC upgrade [1, 2]. The limitation is twofold: Heavy beam loading at such high intensities limits the available accelerating voltage and higher-order modes (HOMs) drive the beam unstable, creating a longitudinal multi-bunch instability with a threshold of about 20% below the desired operational intensity of $2.4 \cdot 10^{11}$ p/b. A large share of this known instability is expected to be driven by HOMs of the multi-stem Travelling Wave Cavities (TWCs) around 630 MHz. Macro-particle simulations show that an additional damping of these HOMs by a factor of two to three is required with regard to the HOM-damping already in place today [1]. Within the framework of the LIU project, the TWCs therefore undergo thorough studies in both their present and future configurations, especially regarding their longitudinal impedance. Implementation of the solutions to both of the above mentioned problems has to start already in 2019. The goal of the performed studies is to develop a broad understanding of the accelerating system that was developed almost half a century ago and also to establish new, reliable HOM-damping schemes that can ensure a good cavity performance for the required beams in the HL-LHC era.

* patrick.kramer@cern.ch

GENERAL STUDIES ON THE SPS ACCELERATING SYSTEM

The periodic multi-stem drift-tube structure

A single cell of the periodic 200 MHz accelerating structure consisting of the outer envelope, drift tube, horizontal stems and pedestals was already introduced in [3] and is shown again in Fig. 1 for convenience. Basically, the lon-

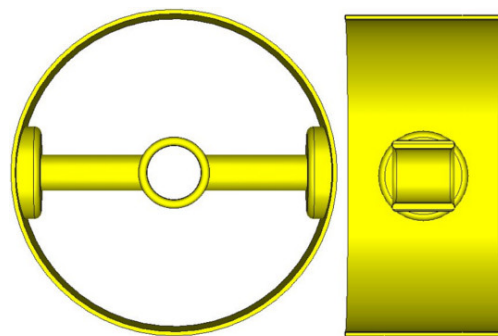


Figure 1: A single cell of the SPS 200 MHz accelerating structure (front and longitudinal-cut view).

gitudinal electric field necessary for particle acceleration builds up between the drift-tubes of two consecutive cells with $\lambda/2$ wavelength spacing. However, the stems also support unwanted longitudinal fields at the uneven harmonics of this fundamental mode which are possibly deteriorating to beam quality.

For practical handling reasons the structure is divided into sections with a length of 4.114 m each consisting of 11 single-cells (inner diameter of circular envelope is 0.75 m). One of three spare sections is shown in Fig. 2 together with an end-plate terminating the periodic structure while providing access for the symmetric fundamental power couplers (FPCs) to the left and right of the beam axis as well as ports used for HOM-damping. An additional access port for this purpose is available on top of each cell. /

With the FPCs being matched in the fundamental frequency range, the accelerating structure is essentially a stem and drift-tube loaded waveguide operated in travelling wave mode. Excess RF power not transferred to the beam is terminated in a load. However, as the cutoff frequencies of the first waveguide mode for the on-axis tube and the coaxial feeder lines to the FPCs are at 1.3 GHz and 0.74 GHz, respectively and as the FPCs act as near perfect reflectors for most frequencies outside the fundamental passband, the accelerating structure can be approximated as a standing wave cavity for large parts of the HOM spectrum. For convenience, the accelerating structure is in general called cavity in the fol-



Figure 2: Spare cavity section with access ports for FPCs and HOM-damping. A part of the measurement setup used for on-axis perturbation measurements is shown as well.

lowing, keeping in mind that it is operated in travelling wave mode in the fundamental passband (FPB).

Present and future cavity configurations

Today's cavity configuration with two 4- and two 5-section cavities is in use since 1980 [4]. Since the first installation of the accelerating system in 1976, three types of HOM-couplers were added to each cavity. A transverse coupler working at 460 MHz and a longitudinal one for 628 MHz were already installed within the first year of operation after the corresponding transverse and longitudinal beam instabilities had been observed [5–7]. A third type of HOM-coupler was installed a few years later for a transverse instability caused by a HOM at 938 MHz [8–10]. A part of the simulation model for the cavities of varying lengths is shown in Fig. 3, indicating also the placement of the three HOM-coupler types. The 460 MHz and 628 MHz couplers are placed in a regular pattern on each individual section and are also independent of the section count. In total four 460 MHz HOM-couplers per cavity are situated on the two end-plates. Today's longitudinal damping scheme with four regularly placed 628 MHz couplers per section is shown as well. The 938 MHz HOM-couplers are placed in an irregular pattern, but are installed in pairs as this reduces their influence on the FPB.

The present cavity configuration is not suited for future HL-LHC beam intensities due to excessive beam loading. The SPS power plants will therefore receive an upgrade and the two long 5-section cavities will be rearranged to four 3-section cavities by also making use of two spare sections [1, 2]. This reduces the total beam coupling impedance (including the impedance of the FPB), but also the beam loading per cavity, and therefore increases the available accelerating voltage for future beam intensities.

Cavity tuning

The relative frequency swing during acceleration in the SPS is small enough (0.44 % in the 70s, 0.065 % today), that a travelling wave structure can provide the required band-

width in its fundamental passband. For a standing wave cavity however, the frequency swing would require tuning and therefore an adjustable element in the tunnel. As such devices often come with reliability issues, this is one of the main advantages that led to the use of travelling wave structures in the SPS [7]. The accelerating structure was optimized for acceleration with $\pi/2$ -mode. As this mode features the largest spacing to adjacent modes, it has to the advantage that the FPCs can be designed fairly broadband so that other high impedance modes present in the FPB and excited by the beam are damped by the terminating loads. This is an important aspect that also has to be taken into account for the upcoming FPC upgrade. A redesign is necessary due to future increased power handling requirements as well as space restrictions in the long straight section housing the accelerating system [11].

Although the travelling structure does not have to be tuned during operation, it was necessary to conduct a one-time tuning per section before its first commissioning [7]. The tuning can thereby account for manufacturing tolerances and shifts the operating mode to the desired frequency that is common to all sections, putting the $\pi/2$ -mode in perfect synchronism with the beam at this particular frequency. Tuning is accomplished by adjusting the length of the stems resulting in the pedestals protruding more or less into the structure (see Fig. 1), which increases or lowers the individual cell frequencies respectively.

The tuning of the available three spare sections of which two will be needed for the upgrade was already briefly studied. Whilst spares 1 and 2 were in storage in a fully assembled state, the envelope of spare section 3 first had to be equipped with separately stored drift tube assemblies of different stem lengths. The resonant frequencies of the FPBs were then measured in standing wave mode without FPCs, see Fig. 4. Although all three spare sections were measured with very weak coupling of the measurement probes to the cavity modes, a slight variation was inevitable, being most likely the source of the observed difference in S-Parameter amplitude during the transmission measurements. These measurements show clearly that the resonances of spare 3 are detuned with respect to the two other spares. This detuning amounts to around 300 kHz at the center of the FPB. Further studies regarding the tuning of the $\pi/2$ travelling mode and the possible influences of HOM-couplers are planned once the spare sections are available for further measurements. The goal is to carry out a tuning of spare 3, such that it can be used as a working backup for the HL-LHC era.

Verification of simulation models

New HOM damping schemes for future operation of the accelerating structure shall at first instance be found by simulation. To obtain confidence in the simulation models, agreement between simulated and measured results is constantly studied. Classic resonant bead-pull perturbation measurements were carried out on all three spare sections with the goal to verify geometry factors over the whole frequency

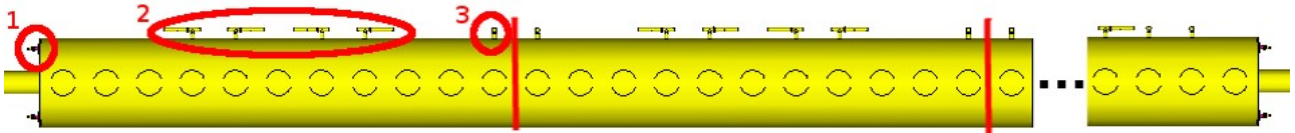


Figure 3: Clipped simulation model of a multi-section cavity showing the regular placement of 460 MHz (1) and 628 MHz (2) HOM-couplers as well as the irregular placement of 938 MHz couplers (3).

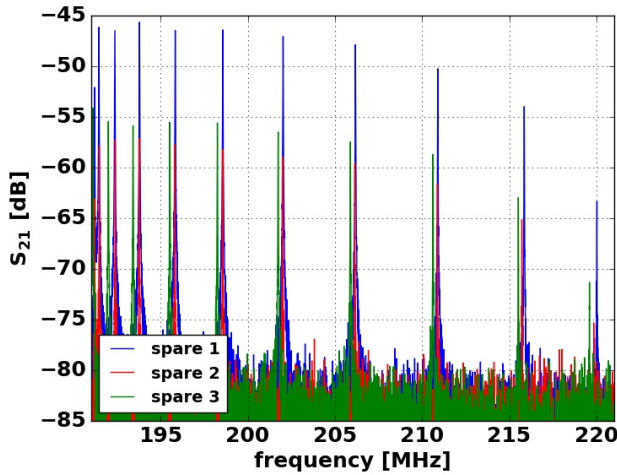


Figure 4: Comparison of the fundamental resonant frequencies in the three spare sections.

range of interest. The results and the comparison to simulation is shown in Fig. 5. Data points obtained by simulation seem to have the tendency to be below their measured counterparts. An obvious structural difference results from the use of a single stem length for all drift tube assemblies in simulation whereas in the actual sections the stem lengths vary on the order of several millimetres for tuning reasons. Slightly lower geometry factors can as well be observed for

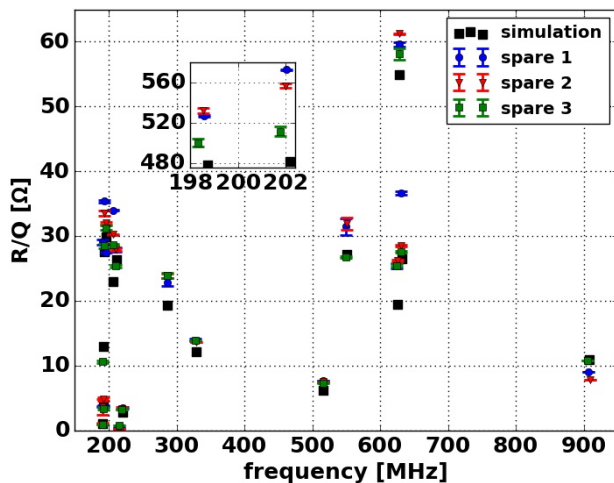


Figure 5: Comparison of simulated and measured standing mode geometry factors of single section cavities in the frequency ranges of interest.

the detuned spare section 3, which is especially visible in the FPB. Overall, the agreement between simulation and measurement as well as amongst the three spare sections is good. We verified our simulation models also by other means like S-Parameter measurements on the full scale SPS cavities and so far we were able to provide for all cases good predictions for what could be expected from measurements.

LONGITUDINAL IMPEDANCE OF FUTURE 3-SECTION CAVITIES WITH TODAY'S HOM-DAMPING SCHEME

As already mentioned previously, the multi-stem structure also generates strong on-axis electric fields at its third harmonic passband around 600 MHz. Fig. 5 shows that this passband also features high geometry factors. The longitudinal impedance of a 3-section cavity including today's FPCs obtained from wakefield simulation is shown in Fig. 6 on a logarithmic scale. The impedances around 630 MHz are not fully converged despite a simulated wake length of 3 km. Eigenmode simulation suggests a peak impedance of 5.2 MΩ at this frequency. The impedance of this standing wave HOM is several times higher than the impedance of the FPB as it is not damped by the FPCs. The FPB however is simulated in travelling wave mode. Fig. 6 also shows the performance of the present 630 MHz damping scheme if it were to be applied to the future 3-section cavities. Obviously, the existing 628 MHz-coupler introduces significant damping over a wide frequency range and heavily damps the modes

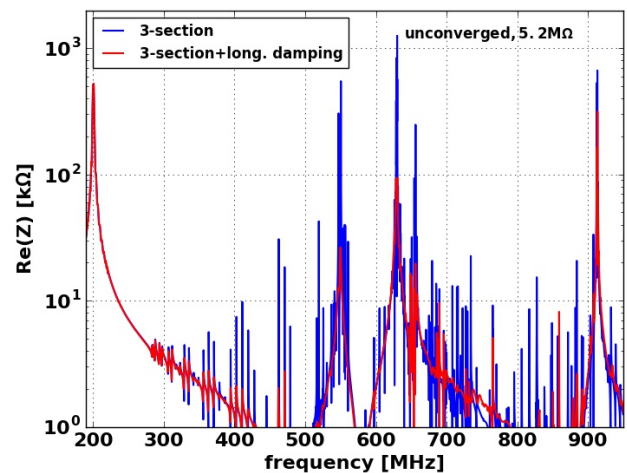


Figure 6: Longitudinal impedance of a 3-section cavity with and without the present longitudinal HOM-damping scheme.

around 630 MHz. This HOM-coupler basically consists of a notch filter for the FPB and a $50\ \Omega$ load for the HOMs. The good performance of the coupler has been confirmed by more detailed analyses and transmission measurements on full scale cavities installed in the SPS. More details of this coupler are shown in [3]. The addition of 12 couplers of the original damping scheme introduces merely a slight shift to higher frequencies on some modes of the FPB. Otherwise, the FPB is left untouched. Three impedance peaks can be distinguished in the potentially dangerous 630 MHz frequency range for this configuration. Particle simulations suggest no significant threat to beam stability for planned intensities due to the HOMs at 550 MHz and 914 MHz [12].

LONGITUDINAL HOM-DAMPING FOR FUTURE 3-SECTION CAVITIES

The longitudinal passbands around and above the third harmonic frequency of the periodic structure are shown in Fig. 7. These passbands were obtained from a single cell

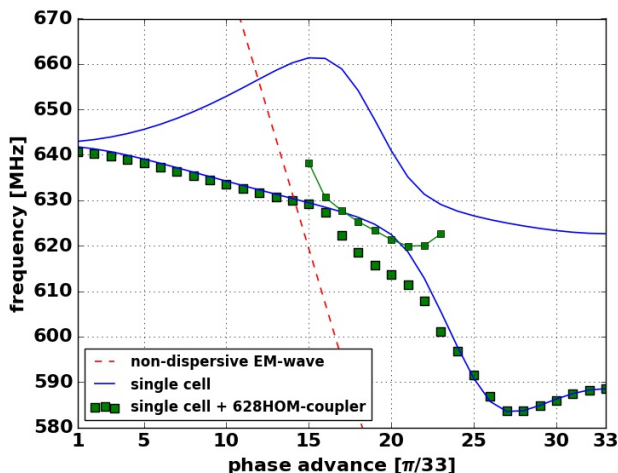


Figure 7: Dispersion diagram for the third harmonic and next higher longitudinal passbands for a single-cell (blue) and a single-cell with a 628 MHz HOM-coupler (green) simulation.

simulation with periodic boundaries on the two longitudinal boundary-planes of the model (see Fig. 1). A step in phase advance between these boundaries of integer multiples of $\pi/33$ was used to obtain the mode frequencies that exist in a 3-section cavity. The frequencies obtained from this infinite periodic set-up are in good agreement with the frequencies in a 33-cell cavity shorted by end-plates. The dashed line indicates that highest interaction between cavity and beam should be expected at 630 MHz. The passband around the third harmonic is also outlined in Fig. 7 for the case that a 628 MHz HOM-coupler is inserted at the top of the cell. Heavy perturbation can be observed in the frequency range with strong coupling of the HOM-coupler. The next higher passband is deformed by the presence of the HOM-coupler such that additional HOMs are created in this dangerous frequency range. The periodic simulation setup presumes that a

coupler is positioned in every cell. This will not necessarily be the case in a final damping scheme. It is nevertheless obvious that the HOM field configurations inside the cavity can get highly perturbed by the presence of this coupler. The HOM-coupler itself is therefore an essential part in the analysis of cavity impedance and possibly poses itself an obstacle to HOM-damping.

The performance of the present damping scheme with HOM-couplers placed on top of cells 4,5,7 and 8 on each section as shown in Fig. 3 was analysed on a 1-section cavity as an intermediate step. All modes of the 1-section cavity with an integer multiple of $\pi/11$ phase advance will also exist in multi-section cavities together with additional potentially hazardous modes. Nevertheless, as the mode with highest impedance is damped massively and as the HOM-coupler also acts on most other HOMs in the frequency range, it was sufficient for operations in the late 1970s to focus only on the damping of modes with a $\pi/11$ phase advance. For this purpose the damping scheme of a 1-section cavity could simply be copied to all other sections of the multi-section cavity to ensure sufficient HOM-damping. In addition, the technical means to investigate the impedance of long multi-section cavities with justifiable effort were most likely not available at that time. It can therefore also be concluded that the present 628 MHz HOM-coupler was solely developed on a 1-section cavity although the corresponding instability was observed during operation with 5-section cavities.

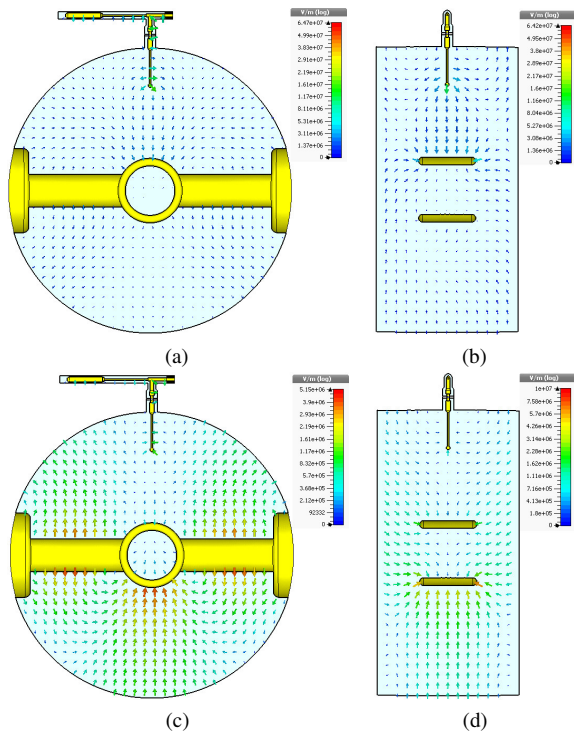
In a 1-section cavity, the most deteriorating mode with a shunt impedance of $1.8\ \text{M}\Omega$ is simulated at 629 MHz with a phase advance of $5\pi/11$ per cell. This mode receives huge damping by a factor of 80 when including the four HOM-couplers of the present damping scheme. Due to different stem lengths on the actual sections this mode is measured at a slightly lower frequency and therefore corresponds to the mode the 628 MHz-coupler was targeted to. Although also all other high impedance modes in the passband receive strong damping, nevertheless two modes with significant impedances remain at 623 MHz and 627 MHz.

It is investigated as a next step, if the HOM-damping scheme applied to a 3-section cavity is sufficient for planned future beam intensities. Particle simulations suggest that the beam coupling impedance of a 3-section cavity in the deteriorating frequency range from 620 MHz to 630 MHz ideally should not surpass $24\ \text{k}\Omega$ [12]. As roughly a dozen modes exist in this frequency range whose impedance spectra overlap, the impedance of each mode must be mitigated to values well below $24\ \text{k}\Omega$. The three modes with highest impedance in a 3-section cavity with today's damping scheme installed are shown in Tab. 1. Thereby, the mode with a phase advance of $15\pi/33$ was already mentioned above as it also exists in a 1-section configuration. Despite the damping by a factor of 80, its impedance is still too high for future beam intensities. The two other modes are special to the 3-section configuration. The mode with phase advance $14\pi/33$ is synchronous with the beam (cf. Fig. 7) resulting in its high geometry factor.

Table 1: Most deteriorating modes for a 3-section cavity with today's longitudinal damping scheme.

f [MHz]	Q	R/Q [Ω]	R [k Ω]	ϕ [rad]
627.7	5600	5.9	33.0	$17\pi/33$
629.2	445	92	40.9	$15\pi/33$
630.3	394	137	54.0	$14\pi/33$

The mode with $17\pi/33$ phase advance is peculiar as it features a significantly higher quality factor compared to the two other HOMs. This mode does not seem to undergo strong damping with the present HOM-damping scheme and considering again Fig. 7 it is determined to be merely created by the addition of the 628 MHz couplers. The electric field profiles of both $17\pi/33$ modes shown in Fig. 7 are presented in Fig. 8. Both modes seem to have approximately


 Figure 8: Field profiles of $17\pi/33$ modes with (a,b) damped mode at 622.2 MHz and (c,d) undamped mode at 627.7 MHz.

the same field profiles when mirrored at an imaginary horizontal axis centred on the stems. The mode with a frequency of 622.2 MHz has strong electric field in the upper half of the single-cell and is therefore well damped, whereas the undamped mode with the same phase advance has strong field in the lower half of the cavity. By adding HOM-couplers on-top of the cavity, the top/bottom symmetry is broken and the field profile of this mode is pushed into the lower part of the cavity. As a result, the mode receives less damping from the top ports. Due to this and due to the too low field strength in the upper cavity half, also other probe geometries for field pick-up were found to be insufficient. The situation

will even deteriorate if more couplers are added for further damping of the two low-Q modes. This is confirmed by additional HOM-couplers in cells marked by red bars in Fig. 9 in which the electric field of these modes is strong. In this configuration the impedance of the $17\pi/33$ mode is increased to 47 k Ω . Considering that only four longitudinal HOM-couplers were added and that in the current overall HOM-damping setup also transverse couplers are placed on top of the cavities (cf. Fig. 3), this is an enormous increase. In addition, the impedance of the two low-Q modes is still not sufficiently reduced.

One can now think of basically two strategies to achieve the required damping: First, avoiding the $17\pi/33$ mode impedance to become pronounced while still sufficiently damping the two other HOMs. And second, damping not only the low-Q, but also the $17\pi/33$ mode. It has to be considered, that due to the existing damping the quality factors are already quite low and that there are no access ports in the bottom of the cavity dedicated to HOM-damping. No further access ports can be drilled into the cavity sections. It is therefore obvious that increased HOM mitigation by a factor of three and more is a very challenging task - no matter the strategy chosen. The remainder of this contribution will investigate if sufficient damping can be achieved by only using the dedicated HOM-ports at the top of the cavity.

Essentially, one would think that less invasive, shorter pick-up probes are necessary to avoid the $17\pi/33$ mode impedance become pronounced. Indeed, simulations on an infinite periodic single-cell show that by reducing the probe length of the existing 628 MHz HOM-coupler the quality factor of the $17\pi/33$ mode is reduced. However, reduced damping of the $14\pi/33$ mode due to this measure is even more significant. A change in geometry factors in the same manner can also be observed. From this trade-off a probe configuration can be expected that levels the impedance of the $17\pi/33$ mode with at least one of the low-Q HOMs. One such configuration is shown in Fig. 9. Here, the probes of the HOM-couplers were shortened in the positions in which the field profile of the $17\pi/33$ mode is most susceptible to the perturbation of the 628 MHz HOM-couplers. Most HOM-couplers however have to remain untouched to ensure sufficient HOM-damping in general. The damping performance of this configuration is illustrated in Tab. 2 showing the characteristics of the three modes with highest impedance. The

Table 2: Most deteriorating modes for a 3-section cavity with HOM-damping scheme marked blue in Fig. 9.

f [MHz]	Q	R/Q [Ω]	R [k Ω]	ϕ [rad]
627.6	5172	5.8	30.0	$17\pi/33$
629.2	325	90	29.3	$15\pi/33$
630.2	244	125	30.5	$14\pi/33$

trade-off described above leads to a balancing of the HOM impedances around 30 k Ω . Although this is already a considerable improvement, the HOM impedance is still to high

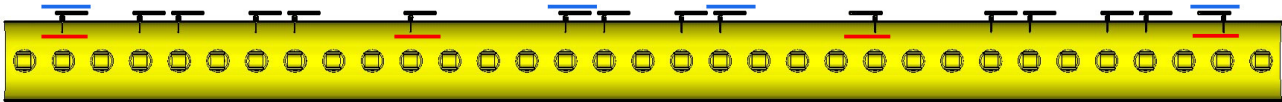


Figure 9: A first improved HOM-damping scheme for future 3-section cavities with added HOM-couplers marked by red and couplers with shorter probes by blue bars.

for HL-LHC beam intensities. All simulations in this contribution were conducted with CST Microwave Studio [13] and the essential results confirmed by ACE3P [14].

CONCLUSIONS AND OUTLOOK

As two additional sections will be required for the 200 MHz accelerating system, the three available spare sections were evaluated regarding tuning and beam coupling impedance. It was shown that one section is out of tune with respect to the others. The tuning mechanism as well as possible tuning procedures need to be studied in more detail. Proper tuning should lead to even better agreement in geometry factors amongst the spare sections. This contribution also showed that today's longitudinal HOM damping scheme applied to 3-section cavities is not sufficient for future HL-LHC beam intensities. The problems inherent to damping improvements were illustrated by simulation of a periodic single-cell approach incorporating the existing 628 MHz HOM-coupler. The effect that couplers installed at the top-ports can push electromagnetic fields in the lower cavity half was identified. This results in the creation of a high-Q mode in addition to the high-R/Q modes present in the 33-cell cavity geometry. It was demonstrated that sufficient damping of this high-Q mode from the access ports available at the top of the cavity can not be achieved. Satisfactory damping of the high-R/Q modes is challenging as well as their quality factors are already very low by employing today's damping scheme. Therefore, the following problem has been identified that needs to be overcome to achieve LIU goals: HOM-mitigation is required in the lower cavity half where access ports are scarce. Merely nine ports for vacuum pumping are available as well as one access on the two cavity end-plates each.

REFERENCES

- [1] E. Shaposhnikova et al. Removing Known SPS Intensity Limitations for High Luminosity LHC Goals. (CERN-ACC-2016-289):MOPOY058. 3 p, 2016.
- [2] E. Shaposhnikova, E. Ciapala, and E. Montesinos. Upgrade of the 200 MHz RF System in the CERN SPS. (CERN-ATS-2011-042), Aug 2011.
- [3] N. Nasresfahani, P. Kramer, and C. Vollinger. Equivalent Circuit Modelling of Travelling Wave Accelerating Structures and Its Applications. 2017.
- [4] T. Linnecar and E. Shaposhnikova. Resonant impedances in the SPS. Technical Report SL-Note-96-49-RF, CERN, Geneva, Aug 1996.
- [5] L. Evans and R. Lauckner. Suppression of 460 MHz transverse instability after transition. Technical Report CERN-SPS-COMMISSIONING-REPORT-71, CERN, Geneva, Aug 1977.
- [6] D. Boussard, T. Linnecar, and A. Millich. Damping of longitudinal instability at high energy. Technical Report CERN-SPS-COMMISSIONING-REPORT-20, CERN, Geneva, Aug 1976.
- [7] G. Dôme. The SPS acceleration system travelling wave drift-tube structure for the CERN SPS. (CERN-SPS-ARF-77-11):26 p, May 1977.
- [8] R. Lauckner and T. Linnecar. The transverse coupled bunch mode instability at 940 MHz in the SPS. Technical Report CERN-Improvement-Report-186, CERN, Geneva, Sep 1980.
- [9] R. Lauckner and T. Linnecar. Damping of the 938 MHz RF cavity resonance. Technical Report SPS-DI-MST-ME-83-16. SPS-ME-83-16-DI-MST. CERN-SPS-ME-83-16-DI-MST, CERN, Geneva, Nov 1983. DI-MST : Directorate, Machine Study Section.
- [10] F. Caspers and G. Dôme. The 938 MHz resonant damping loops for the 200 MHz SPS travelling wave cavities. Aug 2012.
- [11] E. Montesinos. private communication.
- [12] J. Repond. private communication.
- [13] CST AG. Darmstadt, Germany, <http://www.cst.com/>.
- [14] ACE3P. https://portal.slac.stanford.edu/sites/ard_public/acd/.

MODELING OF FAST BEAM-ION INSTABILITIES*

L. Mether[†], EPFL, Lausanne, Switzerland
 A. Oeftiger, G. Rumolo, CERN, Geneva, Switzerland

Abstract

Beam-induced ionisation of residual gas in the vacuum chamber generates ions, which in an electron machine can accumulate around a passing bunch train. If the density of trapped ions becomes sufficiently high, a fast beam-ion instability will be excited. The development of the instability can be prevented by keeping the pressure of the residual gas below a certain value. This contribution describes the modeling of fast beam-ion instabilities and presents simulation studies of ion trapping and the evolution of the instability in the FCC-ee. Threshold ion densities for exciting the instability are estimated in order to deduce acceptable vacuum pressures for operation.

INTRODUCTION

The presence of residual gas in the vacuum chamber of a particle beam leads to the formation of electrons and ions through beam-induced ionisation. In the case of an electron beam, the generated electrons will be repelled by the beam and move towards the chamber walls, whereas ions are accelerated towards the centre of the chamber by the attractive beam force. The ions may be trapped by subsequent bunches and oscillate around the bunch train centroid, or be over-focused and lost on the walls if the kick from the beam is sufficiently strong. If a significant ion density builds up along the bunch train, coherent motion of the beam ensues and a fast beam-ion instability develops [1].

Ion trapping depends on several machine and beam parameters, as well as on the composition of the residual gas. A trapping condition can be derived from the linear approximation of the Bassetti-Erskine formula [2] for the field of a Gaussian beam and the stability condition of a linear beam trajectory. Ions of mass number A are trapped if

$$A > A_{\text{tr},x,y} = \frac{Nr_p \Delta T_b c}{2\sigma_{x,y}(\sigma_x + \sigma_y)}, \quad (1)$$

where r_p is the classical proton radius and c is the speed of light. The trapping mass number $A_{\text{tr},i}$ depends on the bunch spacing ΔT_b , the bunch intensity N , and the transverse beam sizes σ_x and σ_y . For an ion to be trapped, its mass number must be larger than the trapping mass number of both transverse planes. For flat bunches, typical in electron machines, the beam field and the induced kick on the ions are stronger in the vertical plane. Hence the instability occurs in the vertical plane and the trapping mass number is determined by the vertical condition.

* Work supported by the Swiss State Secretariat for Education, Research and Innovation, SERI

[†] lotta.mether@cern.ch

If ions of mass number A are trapped along a train of bunches according to Eq. (1), the rise time of the induced instability for bunch number n_b can be written as

$$\tau_{x,y}^{i,2} \propto \frac{\gamma^2 A \omega_\beta}{n_b^4 N^3 P^2 T_b c} (\sigma_x + \sigma_y)^3 \sigma_{x,y}^3, \quad (2)$$

where ω_β is the betatron frequency. The instability develops faster for larger residual gas pressures P as well as for larger bunch numbers, i.e. the instability sets in at the tail of the bunch train. Furthermore, for a given pressure, the instability develops faster for smaller ion mass numbers, as long as the ions are trapped.

The results reviewed above are based on the linear approximation of the beam field, which underestimates ion trapping by overestimating the kick on ions outside of the core of the beam. With the full beam field, ions may be trapped and influence the beam even if their mass number is below the trapping mass number Eq. (1). In this contribution we present numerical simulations of the fast beam-ion instability in the electron ring of the FCC-ee, which is under design within the future circular collider project [3]. Ion trapping for mass numbers above and below the trapping mass is studied and the effect of the ions on the beam is compared in the two regimes. Viable partial pressures for common vacuum species are identified and mitigation strategies are discussed.

MACHINE PARAMETERS

The FCC-ee may be vulnerable to the fast beam-ion instability in particular at Z-pole operation due to the large number of bunches foreseen for operation in this mode. Selected design parameters at the time of this study are summarised in Table 1. The operational bunch spacing has not yet been fixed in the machine design. Here we use a bunch spacing ΔT_b of 2.5 ns which is the shortest considered spacing and hence the most critical for the fast beam-ion instability.

Table 1: FCC-ee parameters for Z production

Parameter	Symbol, Unit	Value
Energy	E [GeV]	45.6
Circumference	C [m]	97749.14
Bunch intensity	N	1.7×10^{11}
Geometric hor. emittance	ε_x [nm]	0.27
Geometric ver. emittance	ε_y [pm]	1.0
Bunch length	σ_z [mm]	3.5
Harmonic number	h_{RF}	130680
Number of bunches	[1/beam]	16640
Vertical damping time	τ_y^d [turns]	2533

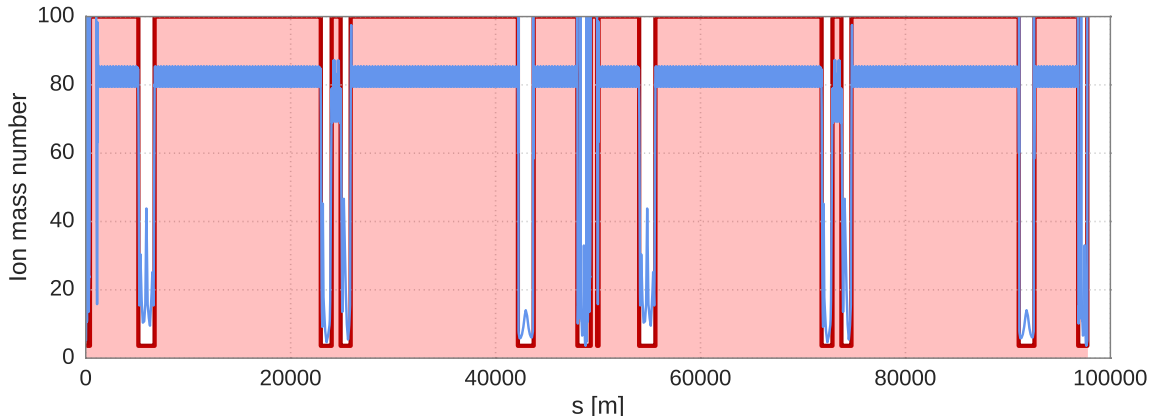


Figure 1: Trapping condition, Eq. 1, along the machine circumference. The trapping mass number for the real lattice is shown in blue and for the model of the straight sections in red.

For the study we consider the following residual gas species: H_2 , CO and CO_2 , with mass numbers and ionization cross-sections [4], σ , as indicated in Table 2. In order to study the trapping of different mass numbers and to determine individual partial pressure thresholds for the instability, each species is simulated independently.

Table 2: Residual gas species

Species	A	σ [MBarn]
H_2	2	0.5
CO	28	2.0
CO_2	44	2.0

SIMULATION MODEL

The simulations have been performed using the PyECLOUD and PyHEADTAIL macro-particle tracking tools [5, 6], with the following method based on the FASTION code [7, 8]. The machine lattice is divided into a number of segments, each of which is represented by an interaction point where the beam-ion interaction along the segment is modelled in 2D. Ions are generated bunch by bunch, and the beam-ion interaction is simulated separately for each bunch along the train.

The simulations are done in the strong-strong regime, where both the beam and the ion cloud are represented by sets of macro-particles. This allows us to model not only the bunch centroid motion, but also emittance growth and other multi-particle effects. The ion macro-particles are regenerated in every interaction point, whereas the beam macro-particles, defined by their phase space variables, are transported between the interaction points using the linear transverse transfer matrices. Synchrotron radiation damping has not been included in the simulation model, instead we compare the rise times found in the simulations to the vertical damping time of the machine (see Table 1).

Since the dynamics of the beam-ion interaction are highly sensitive to the transverse beam size, the ions are kicked

with different strengths in different locations of the machine, according to the optics functions. Ideally the number of segments and interaction points would be chosen such that the machine lattice is comprehensively sampled. For a machine of the size of the FCC, however, this is not viable within a reasonable computation time. Instead, we model the machine using a smooth approximation with identical lattice functions in all segments and determine the required number of segments based on a convergence scan.

Because the lattice functions vary widely between the arcs of the machine and the straight sections, the two cases are simulated independently. This approach allows us to determine in which parts of the machine the pressure limits are more stringent, as well as to compare the trapping of various ion species at two different beam sizes. The arcs, which cover 86.6% of the machine, are modelled with a smooth approximation over the entire circumference with equal distances and phase advances between segments. To model the 13.4% of straight sections, each individual straight section is divided into a number of equidistant interaction points, while the arcs simply transport the beam between straight sections. To account for the different phase advances covered by the various straight sections, the phase advance between segments varies for each straight section. In both cases the lattice functions are selected to give the lowest trapping mass number within the corresponding part of the machine. The linear trapping condition along the machine circumference is shown in Fig. 1 in blue. The red curve shows the trapping mass in the model of the straight sections. A study of the number of kicks and segments needed in the arcs shows good convergence as of around 500 kicks. In the straight sections the number is scaled with respect to the length to 80 kicks per turn.

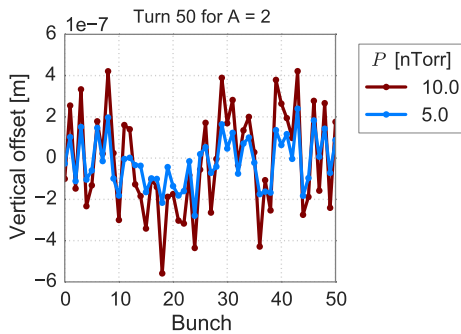
From Fig. 1 we can see that none of the ion species under study are trapped by the beam in the arcs of the machine, according to the trapping condition Eq. (1). In the straight sections, on the other hand, both CO and CO_2 are trapped according to Eq. (1), while H_2 remains below the trapping mass. As will be evident from the simulation results in the

following sections, some ions do in reality stay trapped along at least a part of the bunch train also in the arcs. However, they are less strongly trapped than in the straight sections, where the trapping mass number is significantly lower.

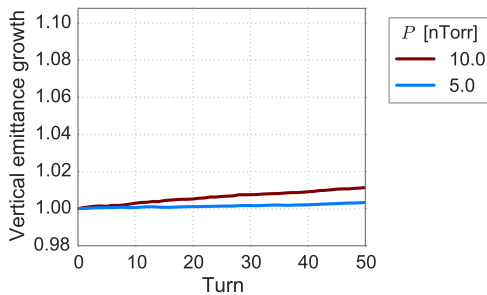
Due to the heavy computational burden of the simulations, only a limited number of bunches and turns can be simulated within a reasonable time. For the studies presented here, bunch trains of 50–200 bunches have been studied over 50 turns around the machine. Over this time, the expected vertical damping due to synchrotron radiation is 4%. The individual gas pressures have been scanned from the pTorr range to a few tens of nTorr.

H₂ TRAPPING AND BEAM STABILITY

Figure 2 shows the impact of hydrogen gas in the arcs on a train of 50 bunches over 50 turns. Even for two relatively high pressures only a very marginal effect on the bunch train can be seen. In particular, the rate of emittance growth shown in Fig. 2b is slower than the expected shrinkage due to synchrotron radiation damping. Hence we do not expect hydrogen to cause any problems in the arcs of the machine for partial pressures up to 10 nTorr. These results are consistent with the expectations from the trapping condition, Eq. (1), and indicate that H₂⁺ ions are not trapped in significant amounts along the bunch train.



(a) Vertical bunch centroid offsets after 50 turns.

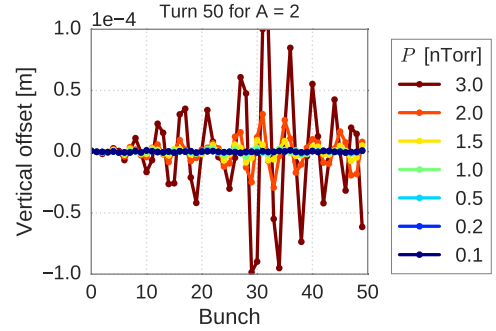


(b) Vertical emittance growth of most unstable bunch.

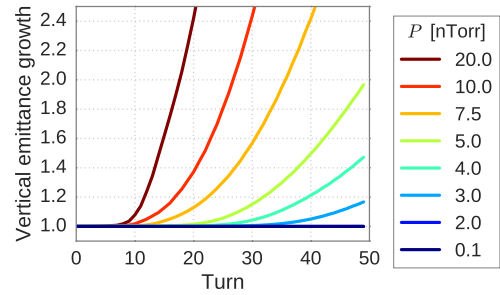
Figure 2: Bunch train evolution with selected pressures of H₂ ($A = 2$) gas in the arcs.

In contrast, in the straight sections, which have a much lower trapping mass number due to the higher beta functions, hydrogen ions do have a significant effect on the beam, although they are not trapped according to Eq. (1). The

effect of hydrogen gas in the straight sections on a train of 50 bunches over 50 turns is shown in Fig. 3. While the ions receive smaller kicks in the straight sections due to the weaker beam fields compared to the arcs, the consequently increased trapping allows for more ions to accumulate along the bunch train, with a noticeable effect on the beam. Within 50 turns, excitation of centroid motion sets in at a pressure of 0.5 nTorr, whereas significant emittance growth is observed from pressures of 3 nTorr.



(a) Vertical bunch centroid offsets after 50 turns.



(b) Vertical emittance growth of most unstable bunch.

Figure 3: Bunch train evolution with selected pressures of H₂ ($A = 2$) gas in the straight sections. Note that the two graphs display different pressures.

CO AND CO₂ TRAPPING AND BEAM STABILITY

Figures 4a and 4b show the vertical centroid displacements of a train of 50 bunches after 50 turns with respectively CO and CO₂ gas in the arcs. The factor of vertical emittance growth (excluding the effect of radiation damping) for the most unstable bunch along the train is shown in Fig 5. Although the mass numbers of both species are well below the trapping mass number for the arcs, they are significantly heavier than hydrogen and are clearly able to generate fast beam-ion instabilities in the arcs.

The lowest pressure leading to significant centroid displacement is 0.2 nTorr for CO and 0.05 nTorr for CO₂, whereas emittance growth occurs from 0.5 nTorr for CO and from 0.1 nTorr for CO₂. Indeed, we can observe that the effect on the beam is stronger for CO₂ than for CO. For any given pressure, the instability sets in after fewer turns and grows faster for CO₂ compared to CO. This behaviour is

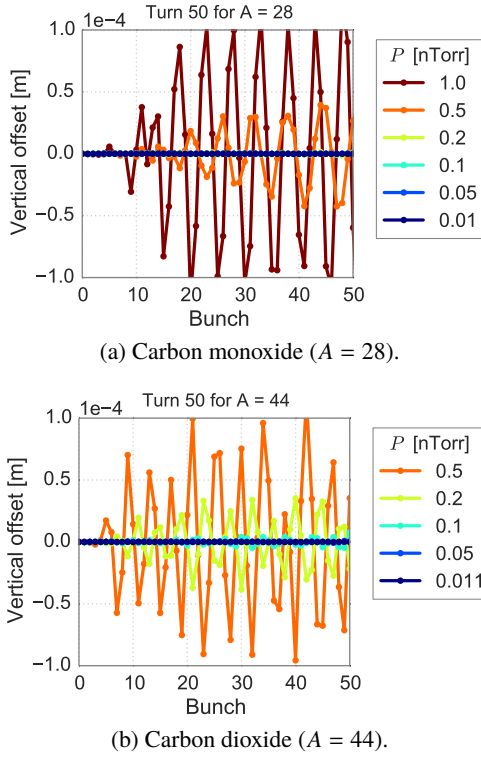


Figure 4: Vertical bunch centroid offsets after 50 turns with selected pressures of CO and CO₂ gas in the arcs.

contrary to what would be expected for strongly trapped ions, Eq. (2), where a faster developing instability is predicted for smaller mass numbers, and indicates qualitatively different instability dynamics when ions are not fully trapped.

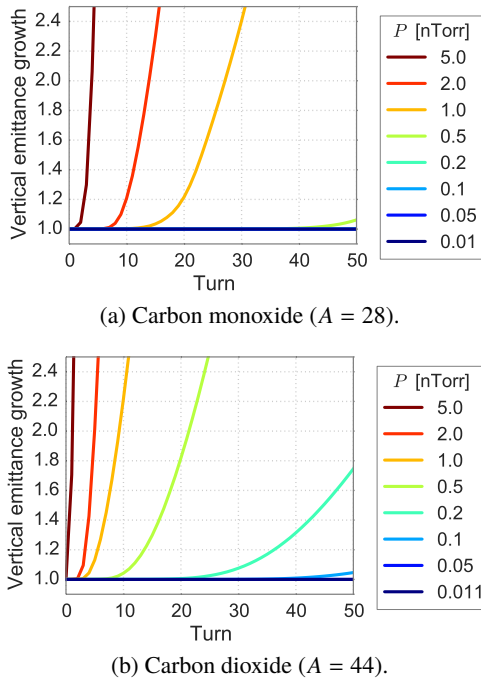


Figure 5: Vertical emittance growth of the most unstable bunch for CO and CO₂ gas in the arcs.

In the straight sections both species are expected to be trapped along the beam and give rise to fast beam-ion instabilities. This is confirmed by Fig 6, which displays the vertical centroid offsets across a bunch train after 50 turns with CO and CO₂ gas in the straight sections, respectively. The lowest pressure leading to significant centroid displacement is 10 pTorr for both species.

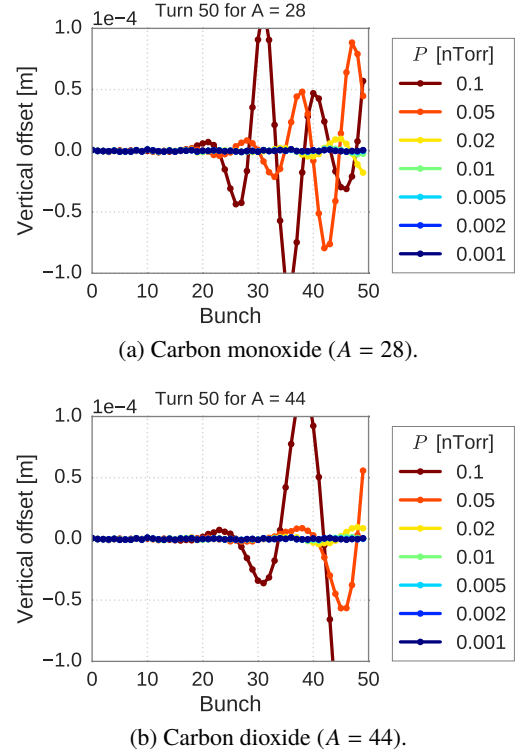


Figure 6: Vertical bunch centroid offsets after 50 turns with selected pressures of CO and CO₂ gas in the straight sections.

WEAK VERSUS STRONG TRAPPING

In the straight sections, the threshold pressures lie more than an order of magnitude below the values in the arcs, although they cover only 13.4% of the machine circumference, indicating a much stronger trapping of the ions in the straight sections. We can also observe a contrast in the dynamics of the instability between the arcs and the straight sections, as illustrated in Fig. 7. In the straight sections, the expected behaviour of a fast beam-ion instability due to ion trapping is observed: the instability first sets in at the tail of the bunch train, and after a given number of turns extends over an increasing part of the bunch train for increasing pressure, approaching the head of the train. This dynamical behaviour applies to both the vertical emittance (see Fig. 7b) and the centroid motion along the bunch train and is similar for both species.

In the arcs, on the other hand, as well as for hydrogen in the straight sections, an increase in emittance growth along the bunch train is observed only at the beginning of the train, with all trailing bunches experiencing a similar amount of

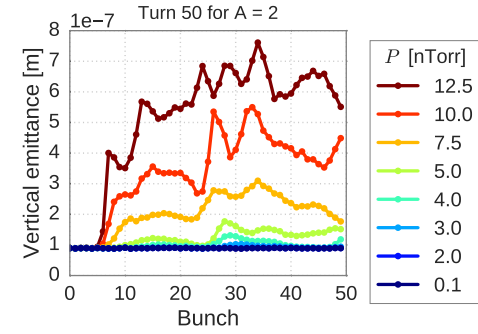
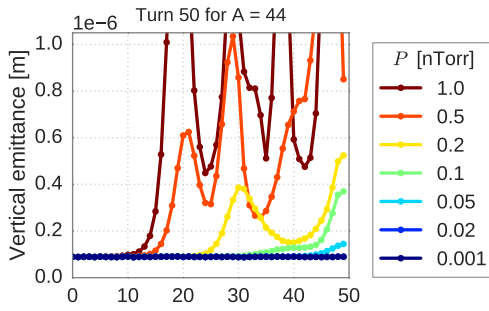

 (a) Hydrogen ($A = 2$).

 (b) Carbon dioxide ($A = 44$).

Figure 7: Vertical emittances of a bunch train after 50 turns with H_2 and CO_2 gas in the straight sections. Note that the two graphs display different pressures.

emittance growth (see Fig. 7a). This is illustrated also in Fig. 8, which shows the rise time of the instability (estimated from the emittance growth) for selected individual bunches along a train with CO and CO_2 gas, respectively. One can note that the rise time saturates after about 10-20 bunches and is essentially independent of the bunch number for most part of the train. This pattern is observed regardless of the residual gas pressure, the length of the bunch train, and the number of turns simulated — only the level of emittance growth that the train is saturated at varies depending on the pressure and the number of turns simulated. Also the envelope of the centroid motion along the bunch train exhibits a similar behaviour.

CONCLUSION

We can conclude that two different regimes for ion trapping have been observed with different consequences for beam stability, depending on the residual gas and beam parameters. When the trapping condition, Eq. (1), is satisfied, fast beam-ion instabilities with the behaviour expected from the linearised treatment occur. However, even when Eq. (1) is not fulfilled, ions can effectively be trapped and induce fast beam-ion instabilities. In our examples this occurs for H_2 in the straight sections and CO, and CO_2 in the arcs. In these cases the instability for a given ion mass and a given pressure is weaker than in the trapping regime, and also behaves qualitatively different. In particular, the evolution of the in-

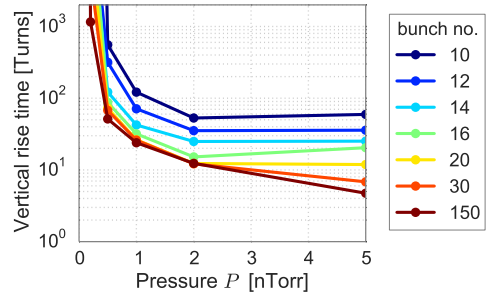
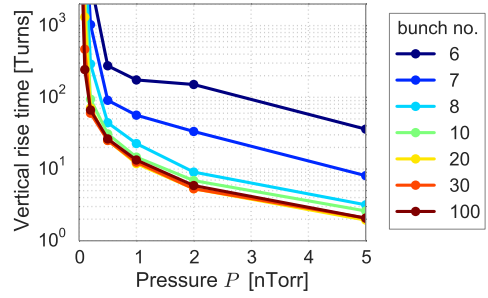

 (a) Carbon monoxide ($A = 28$).

 (b) Carbon dioxide ($A = 44$).

Figure 8: Vertical rise times for selected bunch numbers as a function of CO and CO_2 gas pressure in the arcs.

Table 3: Pressure thresholds for residual gas species

	H_2	CO	CO_2
Arc model	—	0.1 nTorr	0.02 nTorr
Straight sections	0.2 nTorr	5 pTorr	5 pTorr

stability doesn't seem to depend on the number of preceding bunches in a train, except for the first 10-20 bunches. This behaviour could possibly be explained by limited trapping of the ions, which consequently might oscillate around the train only for a certain number of bunch passages before being lost. In the future, it would be interesting to study in more detail the ion behaviour in this non-linear regime, e.g. the typical ion-beam interaction length and how it varies with the ion mass, as well as the frequencies involved in the instabilities, which are related to the non-linear ion oscillations.

The highest pressures found to be stable over 50 bunches and 50 turns for each considered species in the arcs and straight sections are summarised in Table 3. These values correspond to the allowed partial pressures for each species, with eventual constraints on the total pressure depending on the composition of the residual gas. In case the constraints presented here cannot be fulfilled by the vacuum system, there are several mitigation strategies that can be employed in order to relax them.

A standard mitigation strategy for the fast beam-ion instability is the inclusion of clearing gaps. However, the specific behaviour of the partly trapped species implies that, in those cases, mitigation can only be achieved by going to very short trains of around 10 bunches or less. In the straight sections,

on the other hand, additional clearing gaps are expected to increase the threshold pressure. For this approach to raise the threshold pressure with a certain factor, however, the train length would need to be reduced by the same factor, which means only a limited gain can be achieved in this way.

A more promising strategy would be to increase the bunch spacing. According to the trapping condition, Eq. (1), the minimum trapped mass number is directly proportional to the bunch spacing, indicating that increasing the spacing reduces the amount of ion trapping. Based on an additional simulation case, a bunch spacing of 7.5 ns raises the threshold pressure with at least a factor 20 compared to 2.5 ns for CO₂ gas in the arcs. A similar effect can be expected to occur also for CO in the arcs and H₂ in the straight sections. However, the effect may not be as strong for the heavier species in the straight sections, since the trapping condition there is significantly lower. In the straight section model, both CO and CO₂ would still be strongly trapped for a bunch spacing of 17.5 ns, whereas 19.6 ns is the theoretical maximum spacing for the design number of bunches. To accurately determine the pressure constraints for any given bunch spacing, further studies sampling in detail the lattice functions in the straight sections should be performed.

Finally, since the fast beam-ion instability is a coupled-bunch instability with no significant intra-bunch motion, a bunch-by-bunch feedback can typically efficiently suppress the instability, see e.g. [9]. Since the rise times of the instability for the lowest unstable pressures are relatively long, as seen in Figs. 3 and 5, a feedback system with a damping time of 10–100 turns should be able to increase the pressure threshold by more than a factor of 10. However, it is not clear that a feedback system would prevent the emittance growth associated with ion trapping.

ACKNOWLEDGEMENTS

The authors would like to thank R. Kersevan for helpful discussions.

REFERENCES

- [1] T. O. Raubenheimer and F. Zimmermann, “Fast beam-ion instability. I. Linear theory and simulations”, *Phys. Rev. E* 52, 5487–5498, 1995.
- [2] M. Bassetti and G. Erskine, “Closed expression for the electrical field of a two-dimensional gaussian charge”, Technical Report, CERN-ISR-TH/80-06, 1980.
- [3] F. Zimmermann *et al.*, “FCC-ee Overview”, proceedings of HF2014, Beijing, China, paper THP3H1, 2014.
- [4] A.G. Mathewson and S. Zhang, “Beam-Gas Ionisation Cross Sections at 7.0 TeV”, Technical Report, LHC-VAC/AGM, 1996.
- [5] G. Iadarola *et al.*, “Evolution of Python Tools for the Simulation of Electron Cloud Effects”, proceedings of IPAC’17, Copenhagen, Denmark, paper THPAB043, 2017.
- [6] K. Li *et al.*, “Code Development for Collective Effects”, proceedings of HB2016, Malmö, Sweden, paper WEAM3X01, 2016.
- [7] G. Rumolo and D. Schulte, “Fast ion instability in the CLIC transfer line and main linac”, proceedings of EPAC’08, Genoa, Italy, 655–657, 2008.
- [8] L. Mether, G. Iadarola and G. Rumolo, “Numerical Modeling of Fast Beam Ion Instabilities”, proceedings of HB2016, Malmö, Sweden, paper WEAM4X01, 2016.
- [9] A. Chatterjee *et al.*, “Fast ion instability at the Cornell Electron Storage Ring Test Accelerator”, *Phys. Rev. ST Accel. Beams* 18, 064402, 2015.

IMPEDANCE THEORY AND MODELING

E. Métral[†], Geneva, Switzerland

Abstract

The “impedance” limits the performance of all the particle accelerators where the beam intensity (or beam brightness) is pushed, leading to beam instabilities and subsequent increased beam size and beam losses, and/or excessive (beam-induced RF) heating, which can deform or melt components or generate beam dumps. Each equipment of each accelerator has an impedance, which needs to be characterised and optimised. This impedance is usually estimated through theoretical analyses and/or numerical simulations before being measured through bench and/or beam-based measurements. Combining the impedances of all the equipment, a reliable impedance model of a machine can be built, which is a necessary step to be able to understand better the machine performance limitations, reduce the impedance of the main contributors and study the interplay with other mechanisms such as optics non-linearities, transverse damper, noise, space charge, electron cloud, beam-beam (in a collider), etc.

INTRODUCTION

As the beam intensity increases, the beam can no longer be considered as a collection of non-interacting single particles: in addition to the “single-particle phenomena”, “collective effects” become significant [1-4]. At low intensity a beam of charged particles moves around an accelerator under the Lorentz force produced by the “external” electromagnetic fields (from the guiding and focusing magnets, RF cavities, etc.). However, the charged particles also interact with themselves (leading to space charge effects) and with their environment, inducing charges and currents in the surrounding structures, which create electromagnetic fields called wake fields. In the ultra-relativistic limit, causality dictates that there can be no electromagnetic field in front of the beam, which explains the term “wake”. It is often useful to examine the frequency content of the wake field (a time domain quantity) by performing a Fourier transformation on it. This leads to the concept of impedance (a frequency domain quantity), which is a complex function of frequency.

If the wall of the beam pipe is perfectly conducting and smooth, a ring of negative charges (for positive charges travelling inside) is formed on the walls of the beam pipe where the electric field ends, and these induced charges travel at the same pace with the particles, creating the so-called image (or induced) current. But, if the wall of the beam pipe is not perfectly conducting or contains discontinuities, the movement of the induced charges will be slowed down, thus leaving electromagnetic fields (which are proportional to the beam intensity) mainly behind.

An ICFA mini-workshop on “Electromagnetic Wake

Fields and Impedances in Particle Accelerators” was held in 2014 in Erice [5] to review the recent developments and main current challenges in this field. They concerned the computation, simulation and measurement of the (resistive) wall effect for cylindrical and non cylindrical structures, any number of layers, any frequency, any beam velocity and any material property (conductivity, permittivity and permeability); the electromagnetic characterization of materials; the effect of the finite length of a structure; the computation and simulation of geometrical impedances for any frequency; the computation and simulation (in time and frequency domains) of all the transverse impedances needed to correctly describe the beam dynamics (i.e. the usual driving or dipolar wake, the detuning or quadrupolar wake, the angular wake, the constant and nonlinear terms, etc.); the issue of the wake function needed (inverse Fourier transform of the impedance, response to a delta-function) vs. the wake potential obtained from electromagnetic codes (i.e. response to a usually Gaussian pulse); the simulation of all the complexity of equipment like kickers, collimators and diagnostics structures; etc.

This paper is structured as follows: the first section discusses some historical considerations, while the second one reviews some theoretical aspects. The third section analyses the numerical techniques and the fourth one the analytical computations. The fifth section examines in detail the particular and important case of the transverse (resistive) wall impedance in the presence of coatings (with a better or a worse conductor). Finally, the sixth section concludes this review.

HISTORICAL CONSIDERATIONS

The workshop discussed previously [5] was dedicated to A.M. Sessler, who passed away just before it on 17/04/2014 and who, together with V.G. Vaccaro, introduced the concept of impedance in particle accelerators.

The first mention of the impedance concept appeared on November 1966 in the CERN internal report “Longitudinal instability of a coasting beam above transition, due to the action of lumped discontinuities” by V.G. Vaccaro [6]. Then, a more general treatment of it appeared in February 1967 in the CERN yellow report “Longitudinal instabilities of azimuthally uniform beams in circular vacuum chambers of arbitrary electrical properties” by A.M. Sessler and V.G. Vaccaro [7]. The concept of wake field came two years later, in 1969, in the paper “The wake field of an oscillating particle in the presence of conducting plates with resistive terminations at both ends” by A.G. Ruggiero and V.G. Vaccaro [8]. This was the beginning of many studies, which took place over the last five decades, and today, impedances and wake fields continue to be an important field of activity,

[†] Elias.Metral@cern.ch

(these are the convolutions of the wake functions with the beam distribution; here it is just a point charge). The Fourier transform of the wake function is called the impedance. As the conductivity, permittivity and permeability of a material depend in general on frequency, it is usually better (or easier) to treat the problem in the frequency domain, i.e. compute the impedance instead of the wake function. It is also easier to treat the case $\beta \neq 1$. Then, an inverse Fourier transform is applied to obtain the wake function in the time domain. Two important properties of impedances can be derived. The first is a consequence of the fact that the wake function is real, which leads to

$$\begin{aligned} [Z_m''(\omega)]^* &= Z_m''(-\omega), \\ -[Z_m^\perp(\omega)]^* &= Z_m^\perp(-\omega), \end{aligned} \quad (6)$$

where $*$ stands for the complex conjugate and $\omega = 2\pi f$ is the angular frequency. The second is a consequence of Panofsky-Wenzel theorem (with the wave number $k = \omega/v$)

$$Z_m''(\omega) = k Z_m^\perp(\omega). \quad (7)$$

Another interesting property of the impedances is the directional symmetry (Lorentz reciprocity theorem): the same impedance is obtained from both sides if the entrance and exit are the same. In the case of a cavity, an equivalent RLC circuit can be used (with three parameters which are the shunt impedance R_{sh} , the inductance and the capacity). In a real cavity, these three parameters cannot be separated easily and some other related parameters are used, which can be measured directly such as the resonance frequency f_r , the quality factor Q (describing the width of the resonance) and the damping rate (of the wake). When the quality factor is low, the resonator impedance is called ‘‘broad-band’’, and this model (with $Q = 1$) was extensively used in the past in many analytical computations.

The situation is more involved in the case of non axisymmetric structures (due in particular to the presence of the quadrupolar wake field, see below) and for $\beta \neq 1$, as in this case some electromagnetic fields also appear in front of the source particle. In the case of axisymmetric structures, a current density with some azimuthal Fourier component creates electromagnetic fields with the same azimuthal Fourier component. In the case of non axisymmetric structures, a current density with some azimuthal Fourier component may create an electromagnetic field with various different azimuthal Fourier components. If the source particle (1) and test particle (2) have the same charge, and in the ultra-relativistic case, the transverse wake potentials can be written (taking into account only the linear terms with respect to the source and test particles and neglecting the coupling terms)

$$\begin{aligned} \int_0^L F_x ds &= -q^2 [x_1 W_x^{\text{driving}}(z) - x_2 W^{\text{detuning}}(z)], \\ \int_0^L F_y ds &= -q^2 [y_1 W_y^{\text{driving}}(z) + y_2 W^{\text{detuning}}(z)], \end{aligned} \quad (8)$$

where the driving term is used here instead of dipolar and detuning instead of quadrupolar (or incoherent) and where $x_{1,2}$ and $y_{1,2}$ are the horizontal and vertical coordinates of the source (1) and test (2) particles. In the frequency domain, Eq. (8) leads to the following generalized impedances

$$\begin{aligned} Z_x[\Omega] &= x_1 Z_x^{\text{driving}} - x_2 Z^{\text{detuning}}, \\ Z_y[\Omega] &= y_1 Z_y^{\text{driving}} + y_2 Z^{\text{detuning}}. \end{aligned} \quad (9)$$

Note that in the case $\beta \neq 1$, another quadrupolar term is also found. From Eqs. (8) and (9), the procedure to simulate or measure the driving and detuning contributions can be deduced. In the time domain, using some time-domain electromagnetic codes like for instance CST Particle Studio, the driving and detuning contributions can be disentangled. A first simulation with $x_2 = 0$ gives the driving part while a second one with $x_1 = 0$ provides the detuning part. It should be noted that if the simulation is done with $x_2 = x_1$, only the sum of the driving and detuning parts is obtained. The situation is more involved in the frequency domain, which is used for instance for impedance measurements on a bench. Two measurement techniques can be used to disentangle the transverse driving and detuning impedances, which are both important for the beam dynamics (this can also be simulated with codes like Ansoft-HFSS). The first uses two wires excited in opposite phase (to simulate a dipole), which yields the transverse driving impedance only. The second consists in measuring the longitudinal impedance, as a function of frequency, for different transverse offsets using a single displaced wire. The sum of the transverse driving and detuning impedances is then deduced applying the Panofsky-Wenzel theorem in the case of top/bottom and left/right symmetry. Subtracting finally the transverse driving impedance from the sum of the transverse driving and detuning impedances obtained from the one-wire measurement yields the detuning impedance only. If there is no top/bottom or left/right symmetry the situation is more involved and requires more measurements.

Finally, all the transverse impedances (dipolar or driving and quadrupolar or detuning) should be weighted by the betatron function at the location of the impedances, as this is what matters for the transverse beam dynamics.

NUMERICAL TECHNIQUES

Analytical computations are possible only if the structures are fairly simple. In practice this is often not the case and one has to rely on numerical techniques. First numerical wake field computations were performed in time domain by V. Balakin et al. in 1978 [9] and T. Weiland in 1980 [10]. As for highly relativistic bunches, due to causality, wake fields can catch up with trailing

particles only after traveling the catch-up distance (see before), this motivated to compute wakes in linacs by using a mesh that moves together with the bunch: the moving mesh technique was introduced by K. Bane and T. Weiland in 1983 [11].

Nowadays many methods are available for beam coupling impedance simulations [3]:

- Time Domain (TD) method,
- Frequency Domain (FD) method,
 - Eigenmode methods,
 - Methods based on beam excitation in FD,

and the main ElectroMagnetic (EM) codes currently used are

- ABCI,
- Ansys HFSS,
- CST Studio (MAFIA),
- GdfidL,
- ECHO2D,
- ACE3P,
- Etc.

In TD, Finite Differences Time Domain (FDTD) and Finite Integration Technique (FIT) with leapfrog algorithm for the time stepping are used. More specialized techniques are the Boundary Element Method (TD-BEM), the Finite Volume method (FVTD), the Discontinuous Galerkin Finite Element Method (DG-FEM) or Implicit methods. The bunch length and the wake length are the two important parameters for TD impedance computations and the criterion for the time step is also referred to as the Courant-Friedrichs-Lewy (CFL) criterion. The TD simulations are suitable at medium and high frequencies, and particularly in perfectly conducting structures.

In FD, Eigenmode methods are used when high quality factor structures are under investigation and high accuracy is required.

The methods based on beam excitation in FD are well suited at low frequencies, where the CFL criterion poses a strong requirement on the time step. Due to the uncertainty principle, lower frequencies require computing longer wakes. As the time step is fixed by structure properties via the CFL criterion, this leads to the necessity to compute many time steps. The FD methods prevail for low frequency, low velocity of the beam and dispersively lossy materials.

The particularly difficult components to simulate are those, which combine elements of geometric wake fields and resistive elements (like tapered collimators or dielectric structures), the surface roughness and small random pumping slots (such as e.g. in Fig. 3).

Finally, the EM properties of some materials (vs. frequency) are not well known and should be measured with precision before performing simulations to allow for reliable results.

ANALYTICAL COMPUTATIONS

Analytical computations are usually used to compute the (resistive) wall impedance of multi-layered vacuum chambers, beam screens and collimators over

a huge frequency range, as they are usually much faster and precise than simulation codes, which are facing several issues depending on the frequency range (number of mesh cells, etc.). Three formalisms are usually adopted:

- Transmission-line,
- Field matching,
- Mode matching.

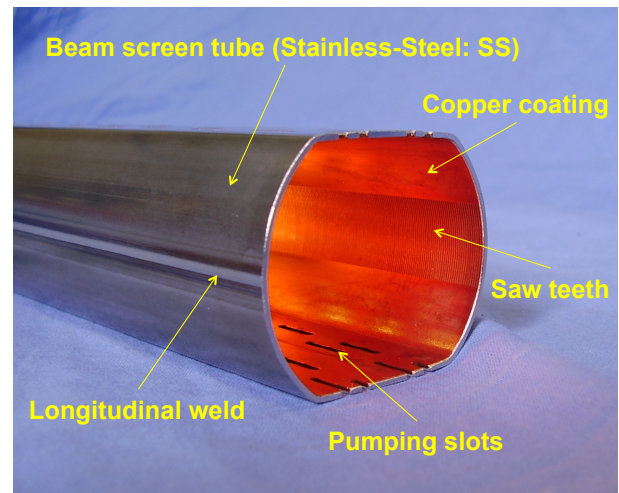


Figure 3: Sketch of the LHC beam screen.

For a cylindrical beam pipe or two parallel plates, with any number of layers, any beam velocity and any electric conductivity, permeability and permittivity, the IW2D code was derived using field matching [12], which is valid when the length of the structure is (much) larger than the beam pipe radius (or half gap in the case of two parallel plates) [3].

In the LHC, the wall impedance of the numerous collimators (see Fig. 4) represents a significant fraction of the total machine impedance. The important parameters are the beam pipe radius (or half gap in the case of two parallel plates), the thickness of the different layers and the skin depth, which is plotted vs. frequency in Fig. 5 for three different materials. Assuming for simplicity first the case of a (round) LHC collimator, the transverse wall impedance is represented in Fig. 6, exhibiting three regimes of frequencies:

- Low-frequency or “inductive bypass” regime,
- Intermediate-frequency or “classical thick-wall” regime,
- High-frequency regime.

Before discussing in detail the first two regimes, which are of interest for the LHC, let’s have a closer look at the third (high-frequency) regime, which is zoomed in Fig. 7. A resonance is clearly revealed (the formula giving the resonance frequency is shown in Fig. 7, where Z_0 is the free-space impedance, σ_{DC} is the DC conductivity and τ is the relaxation time.), whose physical interpretation was provided by K. Bane [13]. The beam/wall interaction can be thought of occurring in two parts: first the beam loses

energy to the high frequency resonator and then, on a longer scale, this energy is absorbed by the walls.

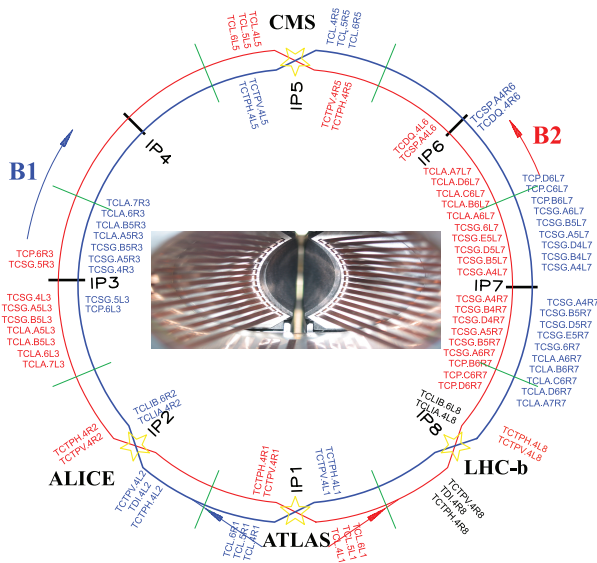


Figure 4: The numerous collimators of the LHC, whose distance to the beam is of few mm. Courtesy of S. Redaelli.

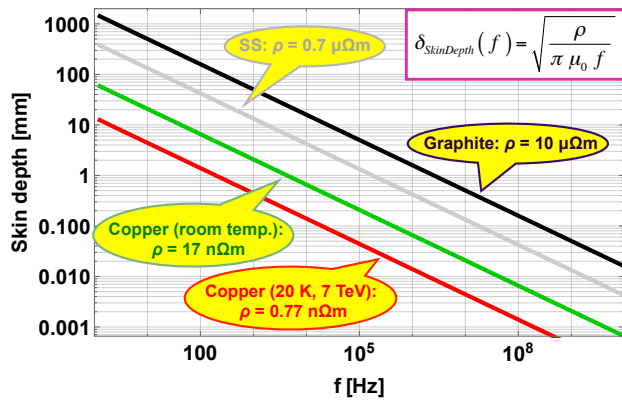


Figure 5: Skin depth versus frequency for different resistivities: stainless steel, graphite and copper (at room and cryogenic temperatures).

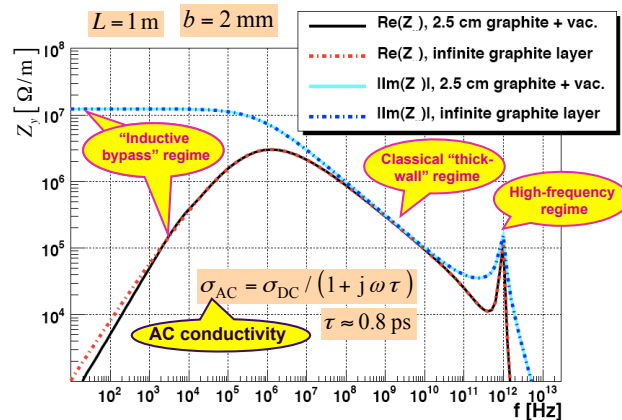


Figure 6: Transverse wall impedance for the case of a (round) LHC collimator.

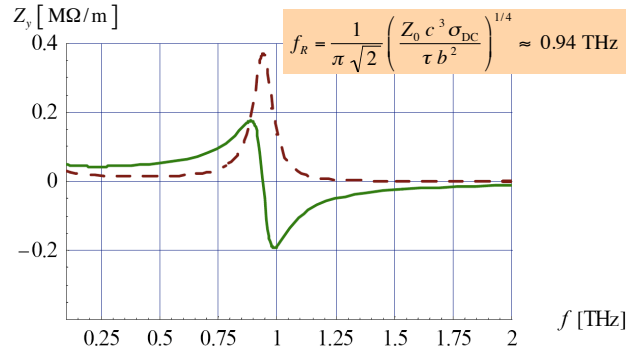


Figure 7: Zoom of the third (high-frequency) regime of Fig. 6: real (in brown) and imaginary (in green) parts of the transverse impedance.

In the case of resistive elliptical beam pipes, Yokoya form factors [14] for the dipolar and quadrupolar impedances are usually used (see Fig. 8): these form factors are numbers to be multiplied to the results obtained with the circular geometry (with the height of the elliptical beam pipe h equal to the radius b of the circular beam pipe). However, it should be reminded that several assumptions were made as concerns both the frequency and the material. Generalised form factors have been deduced from IW2D for two parallel plates compared to the circular case and two examples are shown in Fig. 9 [15].

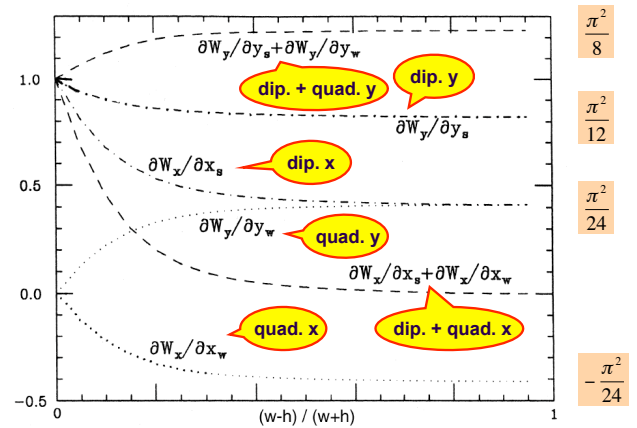


Figure 8: Yokoya form factors for dipolar and quadrupolar impedances in resistive elliptical pipes (compared to the circular case) [14]. The height of the elliptical beam pipe is h and the width is w (the case where $w = h$ corresponds to the circular case).

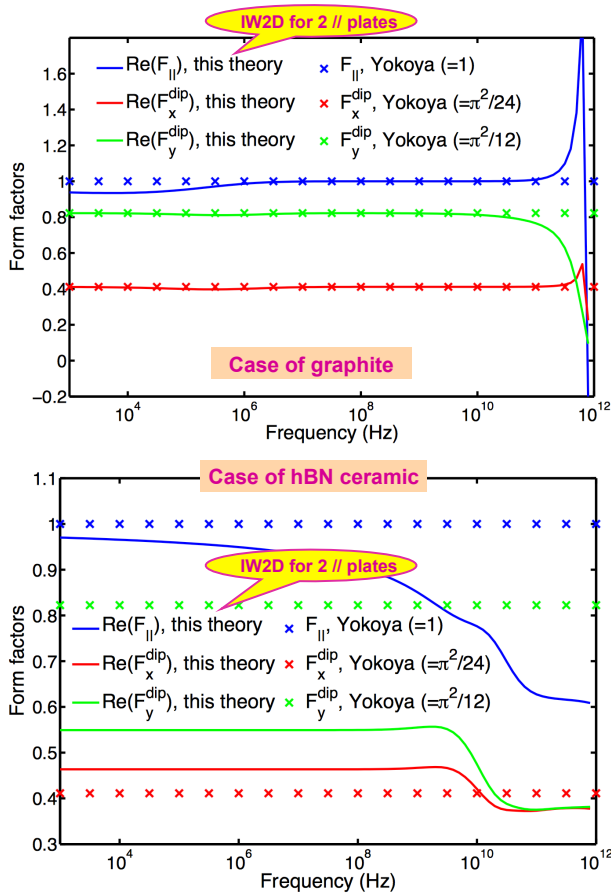


Figure 9: Generalised form factors (compared to the circular case) from the IW2D code (mentioned as “this theory”) for the case of graphite (upper) and hBN ceramic (lower) [15].

TRANSVERSE WALL IMPEDANCE AND COATINGS

Assuming a round beam pipe with a length of 1 m with only one layer going to infinity, the first two frequency regimes are depicted in Fig. 10 for two different beam pipe radii and conductivities.

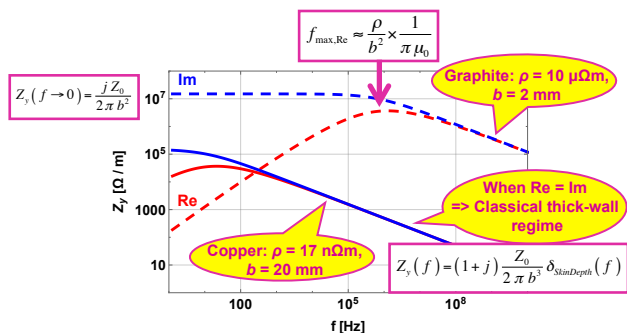


Figure 10: Transverse wall impedance assuming a round beam pipe with a length of 1 m and only one layer going to infinity.

The effect of a copper coating inside a round beam pipe with a length of 1 m, one layer of stainless steel going to infinity and a radius of 20 mm, is represented in Fig. 11 [16,17]. It is shown that the imaginary part of the impedance is always reduced while a too high thickness of the coating can considerably increase the real part of the impedance at low frequencies (as the better conductor keeps the induced current closer to the beam).

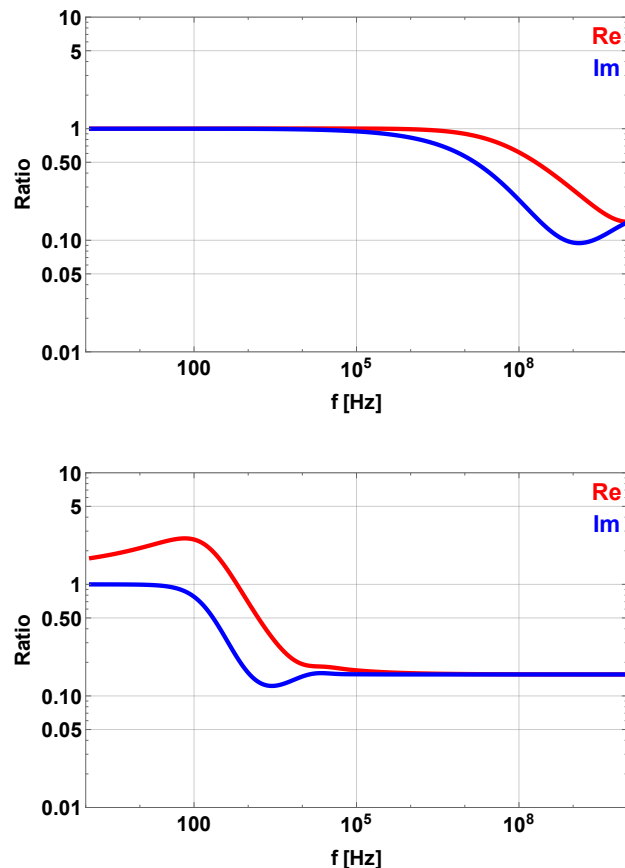


Figure 11: Effect of a copper coating (at room temperature) inside a round beam pipe with a length of 1 m, one layer of stainless steel going to infinity and a radius of 20 mm. Ratio of the impedance (real and imaginary parts) with the coating of thickness (from top to bottom) 1 μm and 1000 μm to the impedance without the coating.

The effect of a copper coating inside a round beam pipe with a length of 1 m, one layer of graphite going to infinity and a radius of 2 mm, is represented in Fig. 12 [16,17]. As before (but with an effect, which is amplified), it is shown that the imaginary part of the impedance is always reduced while a too high thickness of the coating can considerably increase the real part of the impedance at low frequencies (as the better conductor keeps the induced current closer to the beam).

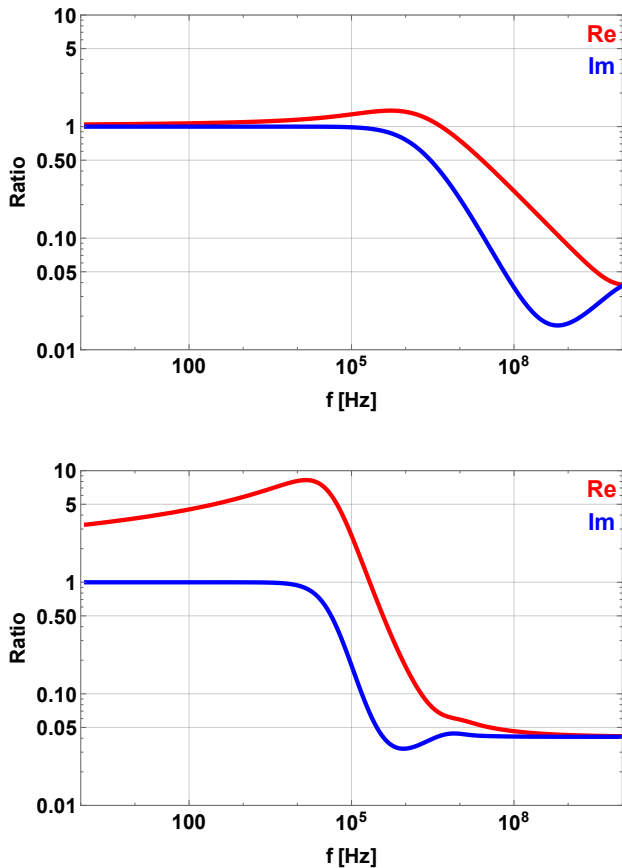


Figure 12: Effect of a copper coating (at room temperature) inside a round beam pipe with a length of 1 m, one layer of graphite going to infinity and a radius of 2 mm. Ratio of the impedance (real and imaginary parts) with the coating of thickness (from top to bottom) 1 μm and 50 μm to the impedance without the coating.

The effect of a graphite coating (e.g. as could be used to reduce the secondary emission yield and relevant electron cloud effects) inside a round beam pipe with a length of 1 m, one layer of copper (at room temperature) going to infinity and a radius of 20 mm, is represented in Fig. 13 [16,17]. In this case, it is shown that if the coating thickness is sufficiently small, the real part of the impedance does not change but only the imaginary part increases at high frequency. For larger coating thicknesses, even the real part of the impedance will be significantly higher for high frequencies, which could have detrimental effects for beam stability.

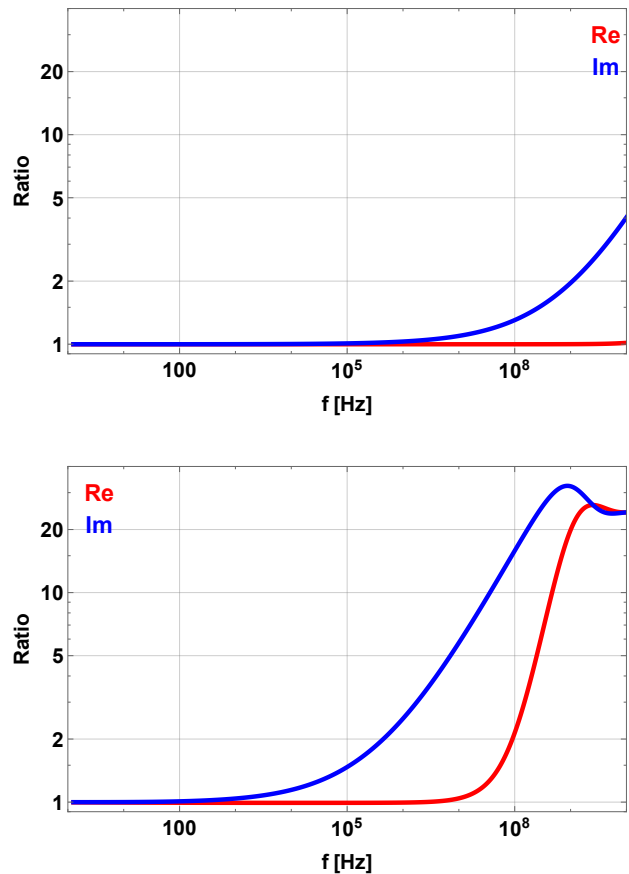


Figure 13: Effect of a graphite coating inside a round beam pipe with a length of 1 m, one layer of copper (at room temperature) going to infinity and a radius of 20 mm. Ratio of the impedance (real and imaginary parts) with the coating of thickness (from top to bottom) 1 μm and 50 μm to the impedance without the coating.

CONCLUSION

The first mention of the impedance concept appeared on November 1966 in the CERN internal report “Longitudinal instability of a coasting beam above transition, due to the action of lumped discontinuities” by V.G. Vaccaro [6]. This was the beginning of many studies, which took place over the last five decades, and today, impedances and wake fields continue to be an important field of activity, as concerns theory, simulation, bench and beam-based measurements. Furthermore, several extensions of the impedance concept appeared over the years for space charge, electron cloud and CSR (Coherent Synchrotron Radiation).

Even if the impedance is fifty-one years old, most of the particle accelerators do not have a sufficiently precise impedance model and there are still challenges for the future, such as e.g. with the new surface treatments, which need to be implemented to fight against electron cloud.

REFERENCES

- [1] A.W. Chao, *Physics of Collective Beam Instabilities in High Energy Accelerators*, New York: Wiley, 371 p, 1993. [Online]. Available: <http://books.google.fr/books?id=MjRoQgAACAAJ>.
- [2] K.Y. Ng, *Physics of Intensity Dependent Beam Instabilities*, World Scientific, 776 p, 2006.
- [3] E. Métral et al., Beam instabilities in hadron synchrotrons, *IEEE Transactions on Nuclear Science*, Vol. 63, No. 2, 50 p, April 2016.
- [4] E. Métral (issue editor) and Y.H. Chin (editor in chief), *ICFA Beam Dynamics Newsletter No. 69*, Theme: collective effects in particle accelerators, 310 p, December 2016.
- [5] E. Métral and V.G. Vaccaro (chairmen), *ICFA mini-workshop on "Electromagnetic Wake Fields and Impedances in Particle Accelerators"*, Erice (Italy), 24-28/04/2014 (<https://indico.cern.ch/event/287930/>).
- [6] V.G. Vaccaro, Longitudinal instability of a coasting beam above transition, due to the action of lumped discontinuities, CERN internal report, ISR-RF/66-35, November 18, 1966.
- [7] A.M. Sessler and V.G. Vaccaro, Longitudinal instabilities of azimuthally uniform beams in circular vacuum chambers with walls of arbitrary electrical properties, CERN 67-2, February 6, 1967.
- [8] A.G. Ruggiero and V.G. Vaccaro, The wake field of an oscillating particle in the presence of conducting plates with resistive terminations at both ends, *LNF - 69/80*, December 23, 1969.
- [9] V. Balakin et al., Beam dynamics of a colliding linear electron-positron beam (VLEPP), *Tech. Rep. SLAC Trans 188*, 1978.
- [10] T. Weiland, Transient electromagnetic fields excited by bunches of charged particles in cavities of arbitrary shape," CERN ISR-TH/80-24, *Tech. Rep.*, 1980.
- [11] K.L.F. Bane and T. Weiland, Wake force computation in the time domain for long structures, *SLAC-PUB-3173*, *Tech. Rep.*, 1983.
- [12] N. Mounet, The LHC transverse coupled-bunch instability, Ph.D. dissertation, EPFL, 2012, thesis No. 5305.
- [13] K.L.F. Bane, The short range resistive wall wake-fields, *SLAC/AP-87*, June 1991 (AP).
- [14] K. Yokoya, Resistive wall impedance of beam pipes of general cross section, *Part. Accel.*, vol. 41, 3-4, p. 221, 1993.
- [15] N. Mounet and E. Métral, Generalized form factors for the beam coupling impedances in a flat chamber, *Proceedings of IPAC'10, Kyoto, Japan*.
- [16] E. Métral, Transverse resistive-wall impedance from very low to very high frequencies, *CERN-AB-2005-084*, August 2005.
- [17] E. Métral, Impact of impedance effects on beam chamber specifications, "Beam Dynamics meets Vacuum, Collimation and Surfaces" workshop, Karlsruhe, Germany, 08-10/03/2017 (<https://indico.gsi.de/event/5393/>).

VLASOV SOLVERS AND MACROPARTICLE SIMULATIONS

N. Mounet*, CERN, Geneva, Switzerland

Abstract

We review here two essential methods to evaluate growth rates of transverse coherent instabilities arising from beam-coupling impedance in a synchrotron, namely Vlasov equation solvers and tracking simulation of macroparticles. We will discuss the basics of the two methods, reviewing in particular the theoretical grounding of Vlasov solvers – giving all the necessary formulas in the case of the DELPHI solver. We will then assess the advantages and limitations of the two methods, by showing a number of practical applications, both in hadrons machines such as the CERN LHC and SPS, and in lepton synchrotrons such as LEP. In particular, we will show how the Vlasov solver DELPHI can help understanding the relative lack of success in trying to stabilize the transverse mode coupling instability using a reactive or resistive transverse feedback in LEP.

INTRODUCTION

Beam instabilities due to self-interaction fields in synchrotrons have been a matter of concern since the early days and the pioneer works of Laslett et al [1] and of Vaccaro and Sessler [2], the latter introducing the concept of beam-coupling impedance. Such instabilities can be critical in limiting the machine performance, in particular in the transverse plane. One can mention for instance the Large Electron Positron collider (LEP) transverse mode coupling instability (TMCI) that was limiting the single-bunch current to less than 1 mA [3–7], or more recently the transverse instabilities observed in the Large Hadron Collider (LHC) during run I and II at top energy, which led to the use of very high current in the octupolar magnets (close to the maximum available) to provide enough Landau damping [8, 9].

A number of methods can be used to assess beam stability in a synchrotron and the efficiency of mitigation techniques to overcome instabilities, such as a transverse feedback system, or Landau damping from optics non-linearities. Historically, one of the first attempts to understand theoretically coherent beam instabilities was done thanks to Vlasov formalism [10], e.g. in the work of Sacherer [11]. This approach considers the phase space as a continuous medium and finds the modes that can develop upon the action of impedance, resorting to perturbation theory to solve the equation.

Another approach is to use tracking simulations in which the beam is rather looked as a collection of macroparticles which are tracked down the full ring, in an attempt to be as realistic as possible. In that case, the goal is to observe directly the time evolution of the beam transverse motion.

These two methods are currently widely used and will be the focus of these proceedings. Among the other ap-

proaches that exist, one can mention the circulant matrix model (CMM) [12–15], which discretizes the longitudinal phase space in fractions of hollow rings, building a one-turn map for each part of the distribution defined. Instability modes can be found from the diagonalization of the one-turn matrix. Also, it is worth mentioning that Vlasov equation is sometimes solved in time domain rather than in mode domain; for instance Ref. [16] does so using Lie algebraic techniques and exponential operators.

In these proceedings we will first describe the theory underlying Vlasov solvers operating in mode domain. Then the approach adopted in macroparticles tracking codes will be explained, before showing some limitations and assets of each method with the help of practical examples in the CERN LEP, LHC and SPS (Super Proton Synchrotron). Our concluding remarks will follow.

Note that in all the following we use SI units and the $e^{j\omega t}$ convention for the Fourier transform, i.e. unstable modes exhibit a tune shift with a negative imaginary part.

VLASOV SOLVERS: THEORY

Since as early as 1972, several (semi-)analytical Vlasov solvers for the transverse plane have been theorized and/or implemented. As a non-exhaustive list one can mention (in chronological order): Sacherer integral equation [11] and Sacherer analytical formulas giving complex tunes shifts [17, 18], Besnier formalism with orthogonal polynomials [19, 20], Laclare eigenvalue formalism [21], the code MOSES (MMode-coupling Single bunch instability in an Electron Storage ring) [22, 23], Chao's general formulation [24], Scott Berg's theory [25], Karliner and Popov's theory for impedance-driven instabilities with a feedback system [26], the nested head-tail Vlasov solver (NHTVS) [27], the semi-analytical code DELPHI (for Discrete Expansion over Laguerre Polynomials and Head-tail modes to compute Instabilities) [28] and the code GALACTIC (for GARNIER-LACLARE Coherent Transverse Instabilities Code) [29].

All these approaches have a common theoretical grounding, based on Vlasov equation [10] and the perturbation theory used to solve it in mode domain. We will provide here an outline of the formalism, following closely the approach of Chao [24, chap. 6], and adding a few recent developments to include a bunch-by-bunch transverse feedback damper, as in Refs. [26–29].

Vlasov equation expresses the conservation of the local phase space density over time for a collection of collisionless particles (hence excluding any effect from intra-beam scattering) under the influence of external electromagnetic forces. This includes the self-interaction field from the beam-coupling impedance because it can be seen as a collective field from the ensemble of particles. The forces have to be non-dissipative, which excludes from the following treat-

* nicolas.mounet@cern.ch

ment the effect of synchrotron radiation. Note that damping and diffusion from synchrotron radiation can be introduced using the Fokker-Planck equation [30] – see e.g. Ref. [31] for an example of Vlasov-Fokker-Planck solver in the context of storage rings and light sources.

Vlasov equation, written for the general phase space distribution density ψ , reads

$$\frac{d\psi}{dt} = 0. \quad (1)$$

Choosing the independent variable to be the longitudinal position along the accelerator orbit, $s = vt$ with v the beam longitudinal velocity and t the time, and focusing our study on the y transverse plane, we can write the single particle unperturbed 4D Hamiltonian as

$$H_0 = \frac{Q_y}{R} J_y - \frac{1}{2\eta} \left(\frac{\omega_s}{v} \right)^2 z^2 - \frac{\eta}{2} \delta^2, \quad (2)$$

with $Q_y = Q_{y0} + Q'_y \delta$ the vertical tune which includes here both the unperturbed tune Q_{y0} and the chromaticity Q'_y , R the machine physical radius, $\eta = \alpha_p - \frac{1}{\gamma^2}$ the slippage factor (α_p being the momentum compaction factor), ω_s the synchrotron angular frequency, ($z, \delta = \frac{dp}{p}$) the longitudinal phase space coordinates inside the beam, and (J_y, θ_y) the action-angle variables defined from the (y, p_y) vertical coordinate and momentum as

$$J_y = \frac{1}{2} \left(\frac{Q_{y0}}{R} y^2 + \frac{R}{Q_{y0}} p_y^2 \right), \quad (3)$$

$$y = \sqrt{2J_y \frac{R}{Q_{y0}}} \cos \theta_y, \quad p_y = \sqrt{2J_y \frac{Q_{y0}}{R}} \sin \theta_y. \quad (4)$$

Lattice non-linearities in the transverse plane are neglected at this stage (but we will see later how to include them back to treat Landau damping) and the linear coupling between the x and y planes is assumed to be zero. We consider now the effect of a transverse dipolar impedance and a transverse feedback, both in the y coordinate, hence excluding other kinds of collective effects such as direct space charge, beam-beam effects, or electron cloud. The impedance and feedback are assumed to be lumped in a single point of the circular synchrotron; this simplification can be made, provided: 1/ the instabilities are much slower than a single turn around the machine, and 2/ the impedances are weighted appropriately by the β functions ratio between their actual location and the location where the lumped impedance is applied (see e.g. Refs [32, 33]). To include the effect of both impedance and damper, we add to the unperturbed Hamiltonian a perturbation of the form

$$\Delta H = -\frac{y}{E} F_y(z, s), \quad (5)$$

where E is the total energy of a particle, and $F_y(z, s)$ the vertical force due to the impedance and/or damper, felt by a particle at a longitudinal position z inside the beam. As in Ref. [24, chap. 6], for convenience we will use the polar

coordinates (r, ϕ) in the longitudinal plane, such that z and δ can be expressed as

$$z = r \cos \phi, \quad \frac{\eta v}{\omega_s} \delta = r \sin \phi. \quad (6)$$

Neglecting the impact of chromaticity and of F_y on the longitudinal invariant¹, the unperturbed stationary distribution can be written [24, chap. 6]

$$\psi_0(y, p_y, z, \delta) = f_0(J_y) g_0(r), \quad (7)$$

with f_0 and g_0 two distribution functions. To find eigenmodes arising from the beam-coupling impedance we use perturbation theory and add to ψ_0 a perturbation of the general form [24, chap. 6]

$$\begin{aligned} \Delta \psi(s, y, p_y, z, \delta) &= e^{j\Omega s/v} f_1(J_y, \theta_y) \cdot g_1(r, \phi) \\ &= e^{j\Omega s/v} \sum_{k=-\infty}^{+\infty} f_1^k(J_y) e^{jk\theta_y} \\ &\quad \cdot e^{-\frac{jQ'_y z}{\eta R}} \sum_{l=-\infty}^{+\infty} R_l(r) e^{-jl\phi}, \end{aligned} \quad (8)$$

with $\Omega = \omega_0 Q_c$ the angular frequency of the eigenmode looked for ($\omega_0 = 2\pi f_0 = v/R$ being the angular revolution frequency and Q_c the complex tune shift of the mode), and where we have expanded both f_1 and g_1 as Fourier series. Writing Vlasov equation for the total perturbed distribution $\psi_0 + \Delta \psi$ and using the full Hamiltonian $H_0 + \Delta H$ to get the derivatives vs. s of J_y, θ_y, z and δ , one can show that all $f_1^k(J_y)$ must be zero except $f_1^{\pm 1}(J_y)$, and that $f_1^1(J_y)$ is negligible provided Q_c is close to Q_{y0} (which is a very robust assumption). Defining $f(J_y) \equiv f^{-1}(J_y)$ and $\omega_s = \omega_0 Q_s$ we get

$$\begin{aligned} \sum_{l=-\infty}^{+\infty} R_l(r) \left[\frac{f(J_y)(Q_c - Q_{y0} - lQ_s)}{f'_0(J_y) \sqrt{\frac{2J_y R}{Q_{y0}}}} \right] e^{-jl\phi} = \\ \frac{R e^{-j\frac{Q_c s}{R}}}{2E} F_y(z, s) e^{\frac{jQ'_y z}{\eta R}}, \end{aligned} \quad (9)$$

which means that the term between square brackets is constant, and

$$f(J_y) = D f'_0(J_y) \sqrt{\frac{2J_y R}{Q_{y0}}}, \quad (10)$$

with D proportional to the dipolar moment of the beam. The remaining unknowns are the radial functions $R_l(r)$.

After expressing the force $F_y(z, s)$ from the combined effect of the dipolar impedance $Z_y(\omega)$ and of the transverse bunch-by-bunch damper of damping time n_d turns (which can be seen as a purely imaginary wake function of constant

¹ This makes the system slightly non Hamiltonian in principle, but the corresponding terms can be neglected when the system remains far from synchro-betatron resonances, and as long as the transverse beam size remains small [24, chap. 6].

amplitude, i.e. a delta function in frequency domain), in terms of the $R_l(r)$, and plugging the resulting expression into Vlasov equation, one can get the following extension of Sacherer integral equation [11]:

$$\begin{aligned}
 (\Omega - Q_{y0}\omega_0 - l\omega_s)R_l(\tau) = & -\kappa g_0(\tau) \sum_{l'=-\infty}^{+\infty} j^{l'-l} \\
 & \cdot \int_0^{+\infty} \tau' R_{l'}(\tau') \left[\mu J_l(-\omega_\xi \tau) J_{l'}(-\omega_\xi \tau') d\tau' \right. \\
 & \left. + \sum_{p=-\infty}^{+\infty} Z_y(\omega_p) J_l((\omega_\xi - \omega_p)\tau) J_{l'}((\omega_\xi - \omega_p)\tau') \right], \quad (11)
 \end{aligned}$$

with J_l the Bessel functions and²

$$\begin{aligned}
 \omega_\xi &= \frac{Q'_y \omega_0}{\eta}, & \omega_p &= (n + pM + [Q_{y0}])\omega_0, \\
 \kappa &= -j \frac{N f_0 e^2 M}{2\gamma m_0 c Q_{y0}}, & \tau &= \frac{r}{v}, & -\kappa\mu &= j \frac{\omega_0}{n_d}, \quad (12)
 \end{aligned}$$

where N is the number of particles per bunch, γ the relativistic mass factor, m_0 the particles mass, e the elementary charge, $[Q_{y0}]$ the fractional part of the tune, M the number of bunches and n the coupled-bunch mode number (between 0 and $M - 1$).

In most of the aforementioned codes and theories, Sacherer integral equation ultimately translates into an eigenvalue problem by either

- expanding the radial functions $R_l(\tau)$ over a complete basis set (typically orthogonal polynomials such as Laguerre polynomials as e.g. in the codes MOSES [22, 23], DELPHI [28] and the approach of Karliner and Popov [26], or Jacobi polynomials in Besnier's method [20]),
- considering a specific, easy to solve, longitudinal distribution, e.g. the airbag distribution (this case can be solved almost fully analytically [24, chap. 6]), or a superposition of such airbag distributions [27],
- solving the equation in frequency domain, i.e. by considering as the unknown the amplitude of the spectrum at ω_p of the signal observed at a pickup:

$$\sigma_l(p) \propto \int_0^{+\infty} J_l((\omega_p - \omega_\xi)\tau) R_l(\tau) \tau d\tau, \quad (13)$$

as done in Laclare's formalism [21] and in GALACTIC [29].

² The normalization of the damper gain is set in such a way that when $Z_y = 0$ and $Q'_y = 0$, one should get a purely imaginary frequency shift equal to $j \frac{f_0}{n_d}$ (corresponding to a damping time of n_d turns). Under these assumptions the right hand side of Eq. (11) is non zero only for $l = 0$, and only the term $l' = 0$ remains in the sum. Multiplying Eq. (11) by τ , integrating from 0 to $+\infty$, and knowing that $\int_0^{+\infty} d\tau \tau g_0(\tau) = \frac{1}{2\pi}$, one then gets the normalization equality $-\kappa\mu = j \frac{\omega_0}{n_d}$.

In any case one ends up with an eigenvalue problem of the general form

$$(\Omega - Q_{y0}\omega_0)\alpha_{ln} = \sum_{l'=-\infty}^{+\infty} \sum_{n'=0}^{+\infty} \alpha_{l'n'} (\delta_{ll'} \delta_{nn'} l\omega_s + M_{ln,l'n'}), \quad (14)$$

where the α_{ln} coefficients represent the eigenmode looked for, δ_{lk} is the Kronecker delta, and $M_{ln,l'n'}$ is an infinite matrix extending over respectively radial and azimuthal mode numbers l and n . The eigenvalues provide the coherent mode frequency shifts, among which the most unstable ones can be easily spotted by looking at their imaginary part. To solve the problem numerically, the matrix has to be truncated, and the convergence of the truncation has in principle to be checked. In the Appendix we describe how the final eigenvalue problem is obtained and solved in the case of the DELPHI code.

Note that the problem can be simplified even further by considering only a single azimuthal mode at a time, as in e.g. the low-intensity version of Laclare's approach.

Each of the methods described above has its assets and drawbacks: the approaches using an expansion over orthogonal polynomials are very general as they can be used with any impedance and any longitudinal distribution, but they end-up with matrix coefficients involving a weighted sum of impedance terms taken at an infinite number of betatron sidebands, the calculation of which might be computationally intensive; the airbag methods are very efficient but assume a certain shape for the longitudinal distribution; and Laclare's approach gives rise to easy-to-compute matrix elements, but these explore only a finite frequency domain, such that a smooth impedance might require a very large matrix size to get reliable results.

Note that in the widely used Sacherer's approach [17], the problem is simplified even further by assuming *a priori* a given functional form for the radial functions $R_l(\tau)$ (or equivalently, of the spectrum amplitude $\sigma_l(p)$) and computing the right hand side of Eq. (11) to get the complex frequency shifts.

Finally, Landau damping from amplitude detuning due to lattice non-linearities, can be introduced in several ways:

- using the stability diagram theory: first the coherent frequency shifts are obtained by solving the eigenvalue problem (14) without considering any tunespread; then the stability is checked *a posteriori* by comparing the complex frequency shifts obtained to the stability region calculated using dispersion integrals of the unperturbed transverse distribution [1, 18, 34–37],
- including the tunespread in Vlasov equation from the beginning when computing the coherent modes, as done in e.g. Refs. [28, 38]. Rather than an eigenvalue problem of the form (14), one then has to solve a more general, non-linear equation to get the complex coherent

ent tuneshift $Q_c = \frac{\Omega}{\omega_0}$:

$$\det \left(\left[\delta_{ll'} \delta_{nn'} \frac{\omega_0}{I_l(Q_c)} \right] + [M_{ln, l'n'}] \right) = 0, \quad (15)$$

with the dispersion integrals $I_l(Q_c)$ given by (considering here the octupoles as the only source of detuning)

$$I_l(Q_c) = \iint_0^{+\infty} \frac{\frac{\partial f_0(J_x, J_y)}{\partial J_y} J_y dJ_x dJ_y}{Q_c - Q_{y0} - a_{yy} J_y - a_{yx} J_x - l Q_s}, \quad (16)$$

where a_{yy} and a_{yx} are the detuning coefficients from the octupoles, and where for clarity we have reintroduced the dependency on the horizontal action J_x of the transverse unperturbed distribution f_0 .

THE MACROPARTICLE TRACKING APPROACH

One of the most reliable ways to assess beam stability in a machine is to run time domain macroparticles tracking simulations. A number of codes are able to deal with impedance effects, among which one can mention HEADTAIL [39–41] and PyHEADTAIL [42, 43] (with the inclusion of electron-cloud effects), ORBIT [44] and PyORBIT [45] (where the direct space-charge forces are also included), MTRISM [46] (for coupled-bunch instabilities), MUSIC [47] (with an optimized algorithm for wake functions given by a sum of resonators), BEAMBEAM3D [14, 48] and COMBI [14, 49] (with the inclusion of beam-beam effects), SBTRACK and MBTRACK [50–53] (for storage rings and light sources).

In e.g. the HEADTAIL and PyHEADTAIL codes, the bunches are sliced longitudinally; slices contain a number of macroparticles, each representing a fraction of the bunch charge – typically there are much less macroparticles than actual particles in the bunch, but enough to get a good representation of the phase space. Each individual macroparticle i is tracked through the ring which is subdivided into one or several sections, and essentially goes through two steps per section: 1) wake fields kicks are applied, and 2) its transverse phase space coordinates are linearly transported to the next section. In addition, once per turn the synchrotron motion is applied to the longitudinal coordinates.

The kicks due to impedance $\Delta x'_i$, $\Delta y'_i$ and $\Delta \delta_i$ are computed straightforwardly using the time domain counterparts of the impedances, namely the longitudinal, horizontal and vertical wake functions $W_{||}$, W_x and W_y respectively:

$$\begin{aligned} \Delta x'_i &= C \sum_{z_S > z_{S_i}} n_S W_x(z_{S_i} - z_S, x_S, y_S, x_{S_i}, y_{S_i}), \\ \Delta y'_i &= C \sum_{z_S > z_{S_i}} n_S W_y(z_{S_i} - z_S, x_S, y_S, x_{S_i}, y_{S_i}), \\ \Delta \delta_i &= -C \sum_{z_S \geq z_{S_i}} n_S W_{||}(z_{S_i} - z_S), \end{aligned} \quad (17)$$

where $C = \frac{e^2}{E_0 \beta^2 \gamma}$, $\beta = \sqrt{1 - \gamma^{-2}}$, E_0 is the rest mass of the elementary particles (protons, electrons or ions) and e the

elementary charge. S_i is the slice containing the macroparticle i , and n_S , x_S , y_S , z_S are resp. the number of particles, transverse positions and longitudinal position, of each slice S (z decreases when going toward the tail of the bunches)³. The slices S are used here only for the computation of the convolution of the wake functions with the bunch profile, and the slicing has to be fine enough for the features of the wake functions to be taken into account appropriately, as well as to allow the proper modes to develop. Tunespread (and therefore Landau damping) from external non-linearities is taken into account in a straightforward manner, by simply computing the transport properties of each macroparticle as a function of its phase space coordinates – this works equally well in the transverse and longitudinal planes. Wake functions can include several terms, e.g. W_x is in general given by

$$\begin{aligned} W_x(z, x_S, y_S, x_{S_i}, y_{S_i}) &= W_x^{dip}(z) x_S + W_{xy}^{dip}(z) y_S \\ &+ W_x^{quad}(z) x_{S_i} + W_{xy}^{quad}(z) y_{S_i}, \end{aligned} \quad (18)$$

where *dip* stands for “dipolar” and *quad* for “quadrupolar” (coupled terms – i.e. wakes in the x direction but proportional to the y position and vice versa – being also taken into account). Depending how far the code goes in the wake sums, multiturn effects are included.

Most of the codes mentioned above rely on a similar slicing to compute the effect of impedance, at the notable exceptions of ORBIT [44] and MUSIC [47] which have implemented optimized ways to take into account specific impedances such as those given by a superposition of resonators.

We should finally stress that the usefulness of most codes depend on the availability of post-processing tools able to make their outputs human-readable and/or comparable to real machine data. Examples of applications where such post-processing tools are used, can be found in the references quoted above.

PRACTICAL EXAMPLES AND COMPARISON BETWEEN THE TWO APPROACHES

Vlasov solvers and macroparticle simulations, when applied on the same situation and when both are well converged, give the same result, as they are just two different ways to solve the same problem. One striking example is the benchmark obtained between the MOSES Vlasov solver and HEADTAIL in Ref. [54], which is reproduced in Fig. 1. In this plot the coherent motion simulated with HEADTAIL was post-processed with SUSSIX [55] and displayed using white dots, whose size and brightness are both non-linear functions of their spectral amplitude (large bright dots have a higher amplitude than small dark dots).

³ In the above expressions the sums run over all slices and bunches before the slice of the macroparticle considered, which is correct only for $\beta = 1$. Actually, in PyHEADTAIL the implementation is more general and for low energy machines the “wake in front” can be included as well.

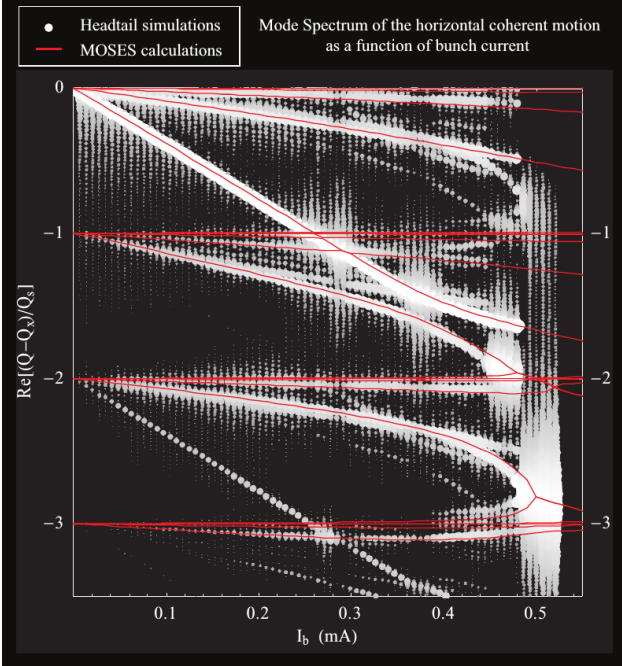


Figure 1: Comparison between HEADTAIL (white dots) and MOSES (red lines) mode spectra, as a function of bunch intensity, in the case of the SPS at injection energy ($p = 26 \text{ GeV}/c$), with a broadband resonator impedance of $10 \text{ M}\Omega/\text{m}$ (cutoff frequency 1 GHz , quality factor $Q = 1$), zero chromaticity, $Q_s = 3.24 \cdot 10^{-3}$, $Q_x = 26.185$, r.m.s. bunch length $\sigma_z = 21 \text{ cm}$ and r.m.s. momentum spread $\sigma_\delta = 9.3 \cdot 10^{-4}$. Courtesy B. Salvant [54].

Macroparticle simulations, nevertheless, can assess stability in complex, realistic situations, typically out of reach to a Vlasov solver, for instance: localized impedance sources (going beyond the lumped impedance approximation), any kind of feedback damper, synchrotron radiation damping, and even the combination of impedance with other collective effects such as space-charge, electron cloud, or beam-beam. As an example we show in Fig. 2, extracted from Ref. [14], the growth rate of a strong mode arising from the coupling between impedance and beam-beam effects, as a function of chromaticity, damper gain and with either long-range separation (10σ , where σ is the RMS transverse beam size) or head-on collisions. This illustrates the potential of the macroparticle tracking approach: in this case it is able to evaluate the combined effect of impedance, damper, chromaticity, and beam-beam interactions in the strong-strong regime, which all together involves such mechanisms as high order headtail instabilities, mode coupling, non-linearities and Landau damping.

This kind of “brute force” simulation approach is very useful and can provide both a complete vision of the problem studied and accurate answers – if the impedance model is precise enough. Yet, if many sophisticated machine and beam features can be included almost at will in such tools, one obvious drawback is that they can be very computationally intensive, limiting their usability, for instance, in cases

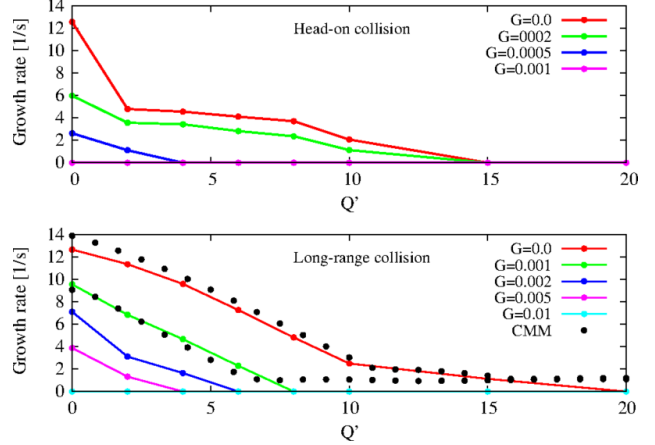


Figure 2: Instability growth rate as function of damper gain $1/n_d$ (with n_d defined in Eq. (12)) and chromaticity for long-range (bottom) and head-on (top) single-bunch collision in the LHC, obtained with the BEAMBEAM3D code [48], in a situation where the beam-beam tune shift is adjusted to be at the location of a mode coupling instability between coherent beam-beam dipole modes and high order headtail modes. The black dots are from calculations using the circulant matrix model (CMM) [13, 15]. Courtesy S. White *et al* [14].

where the combined effect of coupled-bunch and intra bunch motion has to be evaluated, for slow instabilities, or for those requiring a large latency time to develop. Also, the interpretation of simulation results can be tricky when it comes to understand the mechanism underlying the instabilities observed.

More fundamentally, as a time domain tool such simulations are essentially unable to predict what happens after an infinite time, hence a difficulty when it comes to state that a given configuration is stable. To illustrate this point, we show in Fig. 3 the result of HEADTAIL simulations for a single bunch in the LHC, with various octupole currents. While the effect of Landau damping is clearly observed with increasing non-linearities, the stability threshold is uneasy to determine: for instance, with 130A the beam seems more unstable than with 120A, and it remains unclear if the beam is really stable even at 150A or is going to become unstable if we simulate more turns. Conversely, had we stopped the simulation of the 110A case at 10^5 turns we would have probably concluded that the beam is stable, while it is not if we go further in the simulation.

On the other hand, slow instabilities are usually not a problem for Vlasov solvers, because they operate in “mode domain” such that any unstable mode, being slow or fast, will be spotted. They are also typically much less computationally intensive than macroparticle simulations, at least when they are based on (semi-)analytical formulas. This comes at the price of having a range of applicability less broad than macroparticle tracking. Moreover, any additional ingredient to be put in such a solver typically requires pages of analytical derivations; for example adding the Q'' term in the theory presented in the first section (and doing so

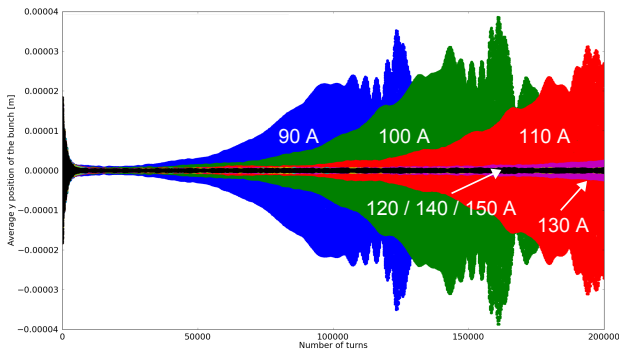


Figure 3: Vertical centroid motion vs. number of turns from HEADTAIL simulations, for a single bunch in the LHC at 4TeV/c, $Q'_y=6$, with respectively 2.5eV.s and 2mm.mrad of longitudinal and normalized vertical emittances, $N = 1.7 \cdot 10^{11}$ protons, and various octupole currents. Both the amplitude detuning and the second order chromaticity Q'' due to the octupoles are included in the simulations. We use the LHC impedance model from Ref. [56].

without the stability diagram approximation), is much more difficult than adding the corresponding term in the detuning of a macroparticle tracked in HEADTAIL.

Still, the mode approach sometimes helps to get a better understanding of instabilities, so can complement advantageously and ease the interpretation of more realistic simulations. Moreover, the rapidity of the computations in conjunction with the fact that the matrix diagonalized can be re-used for different intensities or damper gain (see Eqs. (14) and (21)) gives the ability to perform large parameter scans, and therefore to get a better global view of the stability of a given machine. To illustrate this point, we re-investigate here the case of LEP transverse mode-coupling instability (TMCI) and try to explain the relative lack of success in the various attempts to stabilize it with a transverse bunch-by-bunch feedback [7]. Over the years of operation of LEP, at least two kinds of damper were tested: a reactive feedback, to prevent the azimuthal mode 0 to shift down and couple with the azimuthal mode -1 [12, 57, 58], and a resistive feedback, which was tried at LEP but never used in operation, and thought to be a good option by Karliner-Popov [26] five years after the LEP closure. It is also worth mentioning that there was in general a good agreement between measurements of the TMCI threshold (just below 1 mA) and the LEP impedance model [7].

To try to explain these observations, we show in Figs. 4 and 5 two-dimensional plots where the color represents the LEP transverse instability threshold⁴, obtained using the DELPHI Vlasov solver, as a function of the chromaticity and feedback gain, for respectively a resistive and a reactive feedback. It appears clearly that the resistive feedback does

⁴ Strictly speaking, the instability threshold here represents the TMCI threshold only at zero chromaticity; when the chromaticity deviates from zero, headtail instabilities may occur before the TMCI threshold is reached.

not improve the instability threshold, and the reactive one can improve it only marginally (at high feedback gain). This is in qualitative agreement with the observations in LEP.

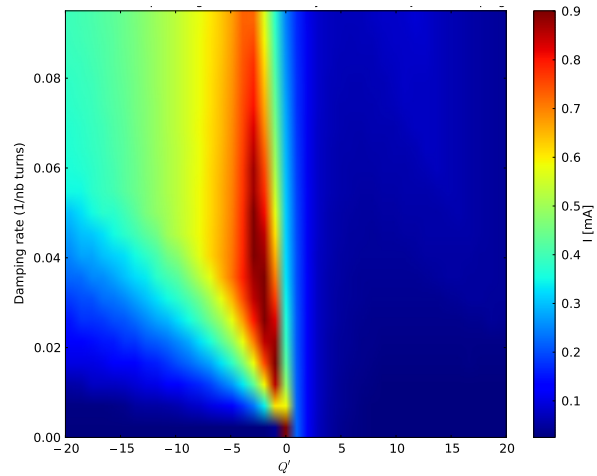


Figure 4: Transverse instability threshold (color) vs. chromaticity and damper gain of a transverse resistive feedback, from DELPHI, in LEP at 22 GeV, r.m.s. bunch length 1.3 cm, circumference 26.659 km, $Q_x = 76.194$, $Q_s = 0.108$ and $\alpha_p = 1.855 \cdot 10^{-4}$. The impedance model contains two broad-band resonators for the RF cavities and the bellows, of shunt impedances resp. 1.1 and 0.23 M Ω /m, cutoff frequencies resp. 2 and 12 GHz, and quality factors $Q = 1$. The instability threshold is defined as the intensity at which the growth rate exceeds the synchrotron damping rate.

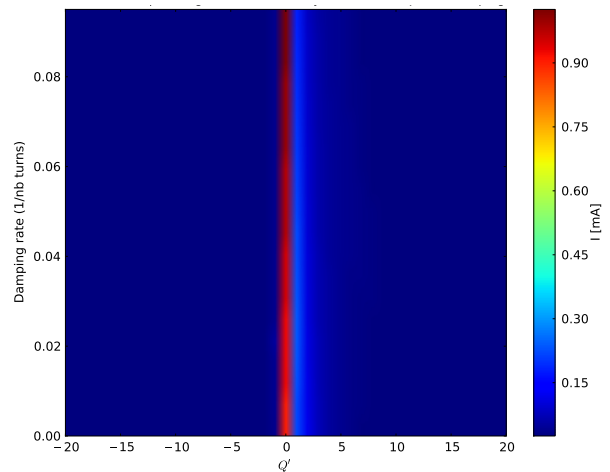


Figure 5: Transverse instability threshold (color) in LEP vs. chromaticity and damper gain of a transverse reactive feedback, from DELPHI. Parameters are the same as in Fig. 4.

CONCLUSION

In these proceedings we outlined the theoretical basis and assumptions behind typical Vlasov solvers, giving an

extended version of Sacherer integral equation in the case when a bunch-by-bunch damper is present. The general structure of the final eigenvalue problem was shown and the various strategies to solve it summarized. Explicit details and formulas were given in the case of the DELPHI code.

We also described the practical approach adopted in many macroparticle codes to simulate the effect of impedances. Comparing the two approaches through a few specific examples, we showed that Vlasov solvers and macroparticle simulations are two equivalent ways to predict coherent instabilities; they give essentially the same results when they can be applied to the same situation. On the other hand they differ a lot in their range of applicability, flexibility and speed.

While macroparticle simulation codes are simple in essence, so easily extensible, Vlasov solvers typically require complete re-derivations of complex analytical formulas when any ingredient has to be added. Macroparticle simulations can deal with very complex beam and machine configurations, and hence can be very computationally intensive, when Vlasov solvers are typically much faster, at the expense of having to be used in simplified and idealized situations. Still, macroparticle simulations are fundamentally unable to guess what happens after an infinite time, while Vlasov solvers, on the contrary, can spot even very slow growing modes.

The power of Vlasov solvers relies in the fact they can be used to make broad parameter scans; in that respect we used DELPHI to shed some light on the relative lack of efficiency of the feedback system to damp the TMCI in LEP, by showing the stability situation over a full range of chromaticities and damper gains.

ACKNOWLEDGMENT

The author warmly thanks Nicolo Biancacci, Xavier Bufat, Alexey Burov, Kevin Li, Elias Métral, Adrian Oeftiger, Giovanni Rumolo and Simon White for numerous useful discussions on the subject.

APPENDIX

Resolution of Sacherer Integral Equation in the DELPHI Code

In the codes DELPHI [28], MOSES [22] and in Karliner and Popov's approach [26], one expands the radial functions R_l over the (generalized) Laguerre polynomials $L_n^l(x) \equiv \frac{e^x x^{-l}}{n!} \frac{d^n}{dx^n} (e^{-x} x^{n+l})$ to solve Sacherer integral equation (11):

$$R_l(\tau) = \left(\frac{\tau}{\tau_b}\right)^{|l|} e^{-a\tau^2} \sum_{n=0}^{+\infty} c_l^n L_n^{|l|}(a\tau^2), \quad (19)$$

where τ_b is the total bunch length in seconds, a an arbitrary (fixed) parameter and c_l^n the coefficients of the expansion.

The unperturbed longitudinal distribution is also expanded over Laguerre polynomials

$$g_0(\tau) = e^{-a\tau^2} \sum_{k=0}^{n_0} g^k L_k^0(a\tau^2), \quad (20)$$

with g^k the expansion coefficients. Note that the first coefficient is fully defined by the normalization condition $\int_0^{+\infty} d\tau \tau g_0(\tau) = \frac{1}{2\pi}$, giving $g^0 = \frac{a}{\pi}$. The expansion (20) is performed initially and is truncated in order to get an accurate enough description of $g_0(\tau)$ - it is even exact and contains only one term in the case of a Gaussian distribution. On the other hand, truncation of the expansion of R_l in Eq. (19) sets the number of radial modes considered, and its accuracy has to be checked "on the fly" while the algorithm looks from eigenvalues. Using these decompositions, Sacherer integral equation (11) can be cast into an eigenvalue problem of the form (14) with

$$\begin{aligned} \mathcal{M}_{ln,l'n'} &= \frac{-j^{l'-l} n! k \tau_b^{|l|-|l'|}}{2^{|l|} (n+|l|)!} \left[\mu G_{ln}(-\omega_\xi, a) I_{l'n'}(-\omega_\xi, a) \right. \\ &+ \left. \sum_{p=-\infty}^{+\infty} Z_y(\omega_p) G_{ln}(\omega_p - \omega_\xi) I_{l'n'}(\omega_p - \omega_\xi, a) \right], \quad (21) \end{aligned}$$

using the two following integrals [59]

$$\begin{aligned} G_{ln}(\omega, a) &= (2a)^{|l|+1} \int_0^{+\infty} \tau^{1+|l|} L_n^{|l|}(a\tau^2) g_0(\tau) J_l(\omega\tau) d\tau \\ &= (\omega \cdot \text{sign}(l))^{|l|} e^{-\frac{\omega^2}{4a}} \\ &\cdot \sum_{k=0}^{n_0} g^k (-1)^{n+k} L_n^{k-n} \left(\frac{\omega^2}{4a}\right) L_k^{n+|l|-k} \left(\frac{\omega^2}{4a}\right), \quad (22) \end{aligned}$$

and

$$\begin{aligned} I_{ln}(\omega, a) &= \int_0^{+\infty} \tau^{1+|l|} L_n^{|l|}(a\tau^2) e^{-a\tau^2} J_l(\omega\tau) d\tau \\ &= \frac{\text{sign}(l)^{|l|}}{2a^{|l|+n+1} n!} \left(\frac{\omega}{2}\right)^{2n+|l|} e^{-\frac{\omega^2}{4a}}. \quad (23) \end{aligned}$$

In all the above, a is a fixed parameter on which one can play to optimize the algorithm, depending on the longitudinal distribution. For instance, for Gaussian longitudinal distributions we set it to $a = \frac{8}{\tau_b^2}$.

Convergence with matrix size is checked automatically by a loop which iterates the three following steps:

1. fix a number of azimuthal and radial modes, in order to truncate the matrix \mathcal{M} to a finite size,
2. compute all the elements of the matrix,
3. compute its eigenvalues. If the most unstable eigenvalue(s) (i.e. those with the highest growth rate) are converged (i.e. close enough to the values obtained in the previous iteration), the algorithm stops, otherwise we go back to the first step, increasing the number of radial and azimuthal modes.

The code DELPHI can be downloaded from Ref. [60].

REFERENCES

- [1] L. J. Laslett, V. K. Neil, and A. M. Sessler, “Transverse resistive instabilities of intense coasting beams in particle accelerators,” *Rev. Sci. Instrum.*, vol. 36, pp. 436–448, 1965.
- [2] A. M. Sessler and V. G. Vaccaro, *Longitudinal instabilities of azimuthally uniform beams in circular vacuum chambers with walls of arbitrary electrical properties*, CERN ISR-RF/67-2, 1967.
- [3] D. Brandt, K. Hübner, and S. Myers, *On LEP performance limits in 1999 and 2000*, CERN/SL/98-005, 1998.
- [4] D. Brandt and S. Myers, *LEP performance limits re-visited*, CERN/SL/98-074 DI, 1998.
- [5] D. Brandt, H. Burkhardt, M. Lamont, S. Myers, and J. Wenninger, “Accelerator physics at LEP,” *Rep. Prog. Phys.*, vol. 63, no. 6, pp. 939–1000, 2000.
- [6] D. Brandt *et al.*, “Measurements of impedance distributions and instability thresholds in LEP,” in *Proceedings of PAC’95, Dallas, Texas, USA*, 1995, pp. 570–572.
- [7] J. M. Jowett, *Beam dynamics at LEP*, CERN/SL/98-029 (AP), 1998.
- [8] E. Métral *et al.*, *Summary of the 2-day internal review of LHC performance limitations (linked to transverse collective effects) during run I (CERN, 25-26/09/2013)*, CERN-ACC-NOTE-2014-0006, 2014.
- [9] E. Métral *et al.*, *Summary of the half-day internal review of lhc performance limitations (linked to transverse collective effects) during run II (CERN, 29/11/2016)*, CERN-ACC-NOTE-2017-0005, 2017.
- [10] A. A. Vlasov, “On the kinetic theory of an assembly of particles with collective interaction,” *Russ. Phys. J.*, vol. 9, pp. 25–40, 1945.
- [11] F. J. Sacherer, *Methods for computing bunched-beam instabilities*, CERN/SI-BR/72-5, 1972.
- [12] V. V. Danilov and E. A. Perevedentsev, *Feedback system for elimination of the transverse mode coupling instability*, CERN/SL/93-38, 1993.
- [13] ———, “Feedback system for elimination of the transverse mode coupling instability,” *Nucl. Instr. Meth. in Phys. Res. A*, vol. 391, 1997.
- [14] S. White, X. Buffat, N. Mounet, and T. Pieloni, “Transverse mode coupling instability of colliding beams,” *Phys. Rev. ST Accel. Beams*, vol. 17, no. 041002, 2014.
- [15] X. Buffat, “Transverse beams stability studies at the Large Hadron Collider,” PhD thesis 6321, EPFL, 2015.
- [16] G. Dattoli, M. Migliorati, and A. Schiavi, “Study of coherent synchrotron radiation effects by means of a new simulation code based on the non-linear extension of the operator splitting method,” *Nucl. Instr. Meth. in Phys. Res. A*, vol. 574, pp. 244–250, 2007.
- [17] F. J. Sacherer, “Transverse bunched beam instabilities - theory,” in *9th International Conference on High Energy Accelerators, Stanford, California, USA*, 1974, pp. 347–351.
- [18] B. Zotter and F. J. Sacherer, “Transverse instabilities of relativistic particle beams in accelerators and storage rings,” in *1st International School of Particle Accelerators “Ettore Majorana”*, M. H. Blewett, Ed., CERN, Nov. 1976, pp. 175–218.
- [19] G. Besnier, “Stabilité des oscillations longitudinales d’un faisceau groupé se propageant dans une chambre à vide d’impédance réactive,” *Nucl. Instr. Meth.*, vol. 164, pp. 235–245, 1979.
- [20] G. Besnier, D. Brandt, and B. Zotter, *The transverse mode coupling instability in a large storage ring*, CERN LEP-TH/84-11, LHC Note 17, 1985.
- [21] J. L. Laclare, “Bunched beam coherent instabilities,” in *CAS - CERN Accelerator School : Accelerator Physics, Oxford, UK, 16 - 27 Sep 1985*, S. Turner, Ed., CERN, 1987, pp. 264–326.
- [22] Y.-H. Chin, *Transverse mode coupling instabilities in the SPS*, CERN/SPS/85-2, 1985.
- [23] ———, *User’s guide for new MOSES version 2.0*, CERN/LEP-TH/88-05, 1988.
- [24] A. W. Chao, *Physics of Collective Beams Instabilities in High Energy Accelerators*. John Wiley and Sons, 1993.
- [25] J. Scott Berg, “Coherent modes for multiple non-rigid bunches in a storage ring,” PhD thesis SLAC-R-478, Stanford Univ., 1996.
- [26] M. Karliner and K. Popov, “Theory of a feedback to cure transverse mode coupling instability,” *Nucl. Instr. Meth. in Phys. Res. A*, vol. 537, pp. 481–500, 2005.
- [27] A. V. Burov, “Nested head-tail Vlasov solver,” *Phys. Rev. ST Accel. Beams*, vol. 17, no. 021007, 2014.
- [28] N. Mounet, *DELPHI: An analytic Vlasov solver for impedance-driven modes*, CERN-ACC-SLIDES-2014-0066, 2014.
- [29] E. Métral, D. Amorim, S. Antipov, N. Biancacci, X. Buffat, and K. Li, “Destabilising effect of the LHC transverse damper,” in *Proceedings of IPAC’18, Vancouver, Canada*, 2018, pp. 3076–3079.
- [30] S. Chandrasekhar, “Stochastic problems in physics and astronomy,” *Rev. Mod. Phys.*, vol. 15, pp. 1–89, 1943.
- [31] R. L. Warnock, “Study of bunch instabilities by the nonlinear Vlasov–Fokker–Planck equation,” *Nucl. Instr. Meth. in Phys. Res. A*, vol. 561, pp. 186–194, 2006.
- [32] Y.-H. Chin, *Coherent synchro-betatron resonances driven by localized wake fields*, CERN/SPS/85-33, 1985.
- [33] P. B. Wilson and L. Rivkin, *Threshold current for the transverse instability in PEP*, SLAC, PEP-NOTE-374, 1982.
- [34] K. Hübner, A. G. Ruggiero, and V. G. Vaccaro, *Stability of the coherent transverse motion of a coasting beam for realistic distribution functions and any given coupling with its environment*, CERN ISR-TH-RF/69-33, 1969.
- [35] K. Hübner and V. G. Vaccaro, *Dispersion relations and stability of coasting particle beams*, CERN ISR-TH/70-44, 1970.
- [36] J. Scott Berg and F. Ruggiero, *Landau damping with two-dimensional betatron tune spread*, CERN SL-AP-96-71, 1996.
- [37] E. Métral and A. Verdier, *Stability diagram for landau damping with a beam collimated at an arbitrary number of sigmas*, CERN-AB-2004-019-ABP, 2004.
- [38] Y.-H. Chin, *Hamiltonian formulation for transverse bunched beam instabilities in the presence of betatron tunespread*, CERN/SPS/85-09, 1985.
- [39] G. Rumolo and F. Zimmermann, “Electron cloud simulations: Beam instabilities and wakefields,” *Phys. Rev. ST Accel. Beams*, vol. 5, no. 121002, 2002.
- [40] G. Rumolo and E. Métral, “Simulations of single bunch collective effects using HEADTAIL,” in *Proceedings of ICAP’06, Chamonix, France*, 2006, pp. 59–64.
- [41] N. Mounet, E. Métral, and G. Rumolo, “Simulation of multi-bunch instabilities with the HEADTAIL code,” in *Proceedings of ICAP’12, Rostock-Warnemünde, Germany*, 2012, pp. 262–266.

- [42] K. S. B. Li *et al.*, “Code development for collective effects,” in *Proceedings of ICFA Advanced Beam Dynamics Workshop on High-Intensity and High-Brightness Hadron Beams (HB’16)*, Malmö, Sweden, 2016, pp. 362–367.
- [43] E. Métral *et al.*, “Beam instabilities in hadron synchrotrons,” *IEEE Transactions on Nuclear Science*, vol. 63, no. 2, pp. 1001–1050, 2016.
- [44] A. Shishlo *et al.*, “The ORBIT simulation code: Benchmarking and applications,” in *Proceedings of ICAP’06*, Chamonix, France, 2006.
- [45] A. Shishlo, S. Cousineau, J. Holmes, and T. Gorlov, “The particle accelerator simulation code PyORBIT,” *Procedia Computer Science*, vol. 51, pp. 1272–1281, 2015, International Conference On Computational Science, ICCS 2015.
- [46] A. Koschik, “Simulation of transverse multi-bunch instabilities of proton beams in LHC,” PhD thesis, Tech. Univ. Graz, 2004.
- [47] M. Migliorati and L. Palumbo, “Multibunch and multiparticle simulation code with an alternative approach to wakefield effects,” *Phys. Rev. ST Accel. Beams*, vol. 18, p. 031 001, 3 2015.
- [48] J. Qiang, M. A. Furman, R. D. Ryne, W. Fischer, and K. Ohmi, “Recent advances of strong–strong beam–beam simulation,” *Nucl. Instr. Meth. in Phys. Res. A*, vol. 558, pp. 351–355, 2006.
- [49] T. Pieloni, “A study of beam-beam effects in hadron colliders with a large number of bunches,” PhD thesis 4211, EPFL, 2008.
- [50] R. Nagaoka, “Instability studies using evaluated wake fields and comparison with observations at SOLEIL,” in *Proceedings of EPAC’06*, Edinburgh, Scotland, 2006, pp. 2847–2849.
- [51] R. Nagaoka *et al.*, “Beam instability observations and analysis at SOLEIL,” in *Proceedings of PAC’07*, Albuquerque, New Mexico, USA, 2007, pp. 2019–2021.
- [52] R. Nagaoka, R. Bartolini, and J. Rowland, “Studies of collective effects in SOLEIL and Diamond using the multiparticle tracking codes sbrack and mbtrack,” in *Proceedings of PAC’09*, Vancouver, BC, Canada, 2009, pp. 4637–4639.
- [53] T. F. Günzel, U. Iriso, F. Perez, E. Koukovini-Platia, and G. Rumolo, “Analysis of single bunch measurements at the ALBA storage ring,” in *Proceedings of IPAC’14*, Dresden, Germany, 2014, pp. 1686–1688.
- [54] B. Salvant, “Impedance model of the CERN SPS and aspects of LHC single-bunch stability,” PhD thesis 4585, 2010.
- [55] R. Bartolini and F. Schmidt, *Sussix: A computer code for frequency analysis of non-linear betatron motion*, CERN-SL-Note-98-017, 1998.
- [56] N. Mounet, “The LHC transverse coupled-bunch instability,” PhD thesis 5305, EPFL, 2012.
- [57] R. Ruth, *Reactive feedback in the two particle model*, CERN-LEP-TH-83-22.
- [58] G. Sabbi, *Simulation of coupled-oscillator feedback*, CERN-SL-96-002-AP, 1996.
- [59] A. Erdélyi, W. Magnus, F. Oberhettinger, and F. G. Tricomi, *Tables of Integral Transforms*. McGraw-Hill, 1954, vol. 2.
- [60] N. Mounet, D. Amorim, and N. Biancacci, <https://github.com/amorimd/CloneDELPHI>, DELPHI repository, 2018.

A RECTANGULAR WAVEGUIDE WITH DIELECTRIC COATINGS AS A DEDICATED WAKEFIELD DECHIRPER AT ELBE*

F. Reimann[†], U. van Rienen, University of Rostock, Rostock, Germany
 P. Michel, U. Lehnert¹, Helmholtz-Zentrum Dresden-Rossendorf, Dresden, Germany

Abstract

Based on the Rayleigh-Ritz method and an eigenmode expansion of the wake function, we devised a semi-analytical description of the wakefield inside a dielectrically lined rectangular waveguide. We implemented this method and employed it to determine the geometrical parameters of a dedicated dechirper for the use at the light source ELBE in Dresden-Rossendorf. In 2016, a construction team at ELBE built a dielectrically lined rectangular waveguide with the given geometry. Subsequently, we carried out experiments with this prototype at ELBE. In this contribution, we present the model structure and compare the results obtained semi-analytically with experimental data.

INTRODUCTION

At ELBE, the linear accelerator facility of the Helmholtz-Zentrum Dresden-Rossendorf (HZDR), in particular, planned laser-plasma experiments and combined ELBE-laser experiments (e.g. on Thomson scattering) make an optimal compression of both the beam's length and energy width necessary. Relating to the typical bunch compression procedure using magnetic chicanes a general conflict exists, as this scheme basically sacrifices a narrow energy spread for small bunch lengths. The energy width is even significantly increased as the induced chirp 'survives' the chicane.

Previous to considering dechirpers for the task of reducing the final energy spread of the particle bunch, the above-mentioned issue was often solved by running the electron beam off-crest in an additional radio-frequency module driven at a higher harmonic of the accelerating mode. Yet, this method is inefficient concerning the ratio between its cost and the improvements to the beam quality as it is expensive both financially and spatially, and requires additional maintenance efforts.

A different concept that fulfils the purpose of reducing the energy spread of a particle beam is the so-called 'dechirper'. In this comparatively simple waveguide structure a wakefield is generated through either dielectric coatings or periodic corrugations in its walls.

Figure 1 serves to illustrate the general principle of the dechirper: before entering the dechirper, the head of the bunch has a lower energy than the tail, which constitutes the initial chirp. This bunch now passes through a dechirper structure and generates a wake potential, c.f. [1]. Along the uniform bunch profile the wake potential is nearly linear and corresponds to an energy loss. Depending on the position of

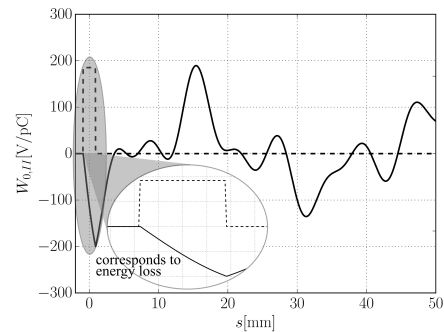


Figure 1: The longitudinal wake potential $W_{0,||}$ of an arbitrary uniform bunch generated in a rectangular dechirper. The zoomed-in part of the wake potential along the bunch shape (dashed line) corresponds to an energy loss.

the particle in the bunch, this energy loss differs. Particles in the tail of the bunch generally experience a larger energy loss. Overall, this energy modulation counteracts the original chirp of the bunch and reduces the energy spread.

The corrugated form of a cylindrical dechirper was proposed by Bane et al. as a dechirper for the NGLS at SLAC in [2]. In 2014, a scientific cooperation with a second group from Berkeley and the PAL in Korea, was able to implement a rectangular waveguide with corrugated walls as a dechirper at the PAL-FEL, [3].

Also in the year 2012, Antipov et al. suggested the use of a dielectrically coated rectangular waveguide as a silencer for the FACET (c.f. [4]) and reported on first successes of a cylindrical, dielectrically lined dechirper structure at the ATF at BNL, [5]. In [7] and [8], the same authors report on tests with an alumina-coated rectangular waveguide at ATF and show first experimental results for the tuning of the gap width of the dechirper and the resulting adjustment of the final wakefields determining the dechirp.

Despite these first experiments mentioned above, wakefield dechirping still remains a new field of study.

In cooperation with the HZDR, we started studies on both, the analytic properties of the dielectrically lined rectangular dechirper and its applicability for the specific situation at the ELBE accelerator facility, in 2013 (c.f. [9] and [10]). Subject of the research presented in this work is the dechirper prototype that the ELBE team constructed in 2016 which has subsequently been used in measurement experiments.

THE DECHIRPER PROTOTYPE USED AT ELBE

The general geometry of a rectangular waveguide with dielectric coatings can be seen in Fig. 2. The outer waveguide

* This work was partly supported by the German Federal Ministry for Research and Education under the contract number 05K13HR1.

[†] franziska.reimann@uni-rostock.de

is made of a highly conductive metal, in case of the ELBE dechirper aluminium. The dielectric plates are mounted to the top and bottom of the waveguide. Mechanical drives allow for a manipulation of the gap width between these two dielectrics.

The dechirper, which has a length of $L = 80$ cm, is inserted into the beam line within a cylindrical vacuum chamber. This chamber has a diameter of 10 cm, which limits the width of the dechirper and the maximum achievable gap width. A width of $a = 5$ cm has been chosen. The vacuum chamber also holds mechanical drives that allow for a tuning of the distance between the two dielectric plates even after the dechirper has been taken into operation. These drives also make it possible to close the dechirper entirely and bring the closed dechirper towards one side of the vacuum chamber. This removes it from the beam path far enough for it to have a negligible effect on the dechirper, and thus makes it possible for the dechirper to remain inside the beam line of ELBE even if no experiments with it are being performed. To simplify the geometry and the construction process, the terminating walls in x -direction have been left out in the prototype. The necessary electric termination in this transversal direction is instead provided by the walls of the vacuum chamber. Parameter studies have been performed to ensure that this deviation from the used model has no significant influence on the experimental results. These showed that the wakefield is not influenced by the width of the dechirper once a certain threshold is passed.

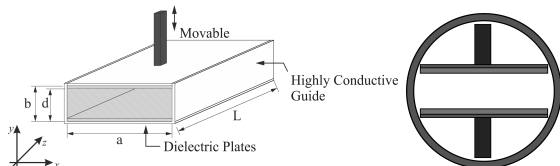


Figure 2: Left: Schematic depiction of the general model of a rectangular dechirper (with a length L , a width a and a total height of b) with dielectric coating (thickness $b - d$). Right: Schematic profile of the dechirper prototype inside the vacuum chamber.

Under these conditions and taking the mechanical drives into consideration, the maximum achievable gap width at ELBE was limited to 35 mm.

The coating material needs to be suited for the use in ultra-high vacuum. Especially glass-ceramics were considered in the design process due to their low propensity to outgas. In the end, MACOR was chosen for the dielectric coating. Its dielectric constant is $\epsilon_r = 6$ for the used sample, which is comparable to the permittivity of diamond, which has previously been proposed in [4].

The samples of MACOR used for the dechirper prototype at ELBE have a thickness of $b - d = 3$ mm (where b denotes the total height of the dechirper and d the position of the upper dielectric). The choice of this parameter has been subjected to manufacturing limitations. Parameter studies have been performed that indicate that thicker layers, as

used in this particular dechirper, are more favourable for the chosen dielectric.

The expected short-range wake potentials in this dechirper (gap width 12 mm) for different shapes of the electron pulse can be seen in Fig. 3. These theoretical benchmarks have been computed with our code *WIZARD*, which calculates the wake function inside the dielectrically lined rectangular dechirper semi-analytically. *WIZARD* is based on the fact that the eigenmodes of the here observed dechirper type can be analytically described, and computed semi-analytically. The wake function is then expanded into a series of these eigenmodes, which has the advantage that it delivers an analytical expression for the wake function. A detailed description of the algorithm behind *WIZARD* can be found in [6].

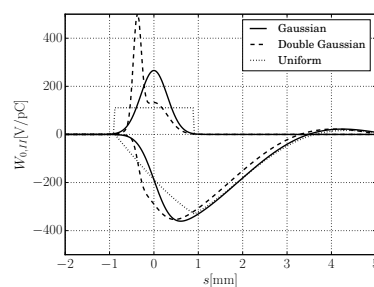


Figure 3: Wake potentials of different bunch shapes (solid line: Gaussian, dashed line: double Gaussian, dotted: uniform) of the same length derived from a convolution with the wake function of the model structure. The maximum amplitudes of the wake potentials over the length of the bunches are very similar for the different distributions, since these are dependent on the overlap of the wake function and the shape functions of the bunches, which have to be normed to the same area. The slopes of the wake potentials radically differ since they depend on the shape of the pulse.

Another aspect that should be mentioned is that at the maximum achievable gap width of 35 mm there will still be a wakefield generated inside the dechirper. Yet, its effect may be assumed to be very small and will thus be neglected. The state of the maximally opened dechirper will be regarded as the state of a ‘turned off’ dechirper, as a complete removal of the dechirper from the beamline as described above would require additional adjustments of the beam.

EXEMPLARY PHASE SPACE COMPUTATIONS

In this section, we present exemplary phase space computations that illustrate the dechirper effect on different bunch shapes. For this, the programme *WIZARD* has been utilised to calculate the wake function of an exemplary dechirper for different gap widths.

The energy shift introduced by the dechirper is proportional to the wake potential and the proportionality factor is the total charge of the pulse. This means that the form of the energy shift results directly from the particle distribution (c.f. Fig. 3) and, by implication, has nothing to do with the initial

energy distribution of the particle bunch, and neither with the total energy of the pulse. This means for the following phase space studies, the energy distribution of the particle beam can be chosen arbitrarily.

For the phase space of the test bunch in our studies, 1000 particles were created and randomly assigned a position according to the particle distributions introduced in the previous sections, and an energy according to a fixed energy distribution. This distribution has been chosen such that the effect of the dechirper is most easily visible for a total charge of

$$q_p = 100 \text{ pC},$$

which is the maximum achievable bunch charge of the ELBE thermionic gun that has been available for the experiments. More specifically, a Gaussian with a standard deviation of

$$\sigma_E = 1.6\bar{6} \text{ keV},$$

and a mean of

$$\mu_E = 5 \text{ keV},$$

has been chosen. This Gaussian was then imprinted with an energy chirp. This chirp has been introduced as a uniform increase in energy starting from $E_{low} = 100 \text{ keV}$, at the head of the bunch and ending at $E_{high} = 220 \text{ keV}$, at the tail of the bunch. The total energy width of the beam is thus 120 keV. The resulting position-dependent energy variation was then added to the original energy distribution and stored for all particles of the beam.

The initial phase space created in this way is then modulated using the wake potentials of different bunch shapes. Here, a single Gaussian profile (referred to as bunch 1 from now on), a double Gaussian (bunch 2) and a uniform particle distribution (bunch 3) of the same total lengths were used. The discretely computed wake potentials are interpolated using a one-dimensional, linear interpolation. This energy change is then added to the initial energy of the particle. This procedure is additionally performed for several gap widths to show the different behaviours of the dechirper in these cases. The gap widths 6 mm, 12 mm and 35 mm have been chosen as examples. The resulting phase spaces for the initial particle distribution and the dechirped beam are shown in the following figures.

Figure 4 shows the dechirping effect of the structure on the model Gaussian with the given energy distribution. The energy modulation is stronger with increasing gap width. The non-linear behaviour of this effect with respect to the gap width is also clearly visible. For a gap width of 35 mm, the effect of the dechirper on the phase space of the particle bunch is nearly negligible; just a slight modulation of the energy in the range of a few keV can be seen. This modulation is, as could be expected from Fig. 3, stronger at the tail than at the head of the bunch. A reduction of the gap width to 12 mm increases the effect of the dechirper. The curvature of the wake potential, also depicted in Fig. 3, is clearly imprinted on the formerly linear energy chirp. In the central region of the bunch between -0.5 mm and 0.5 mm , the

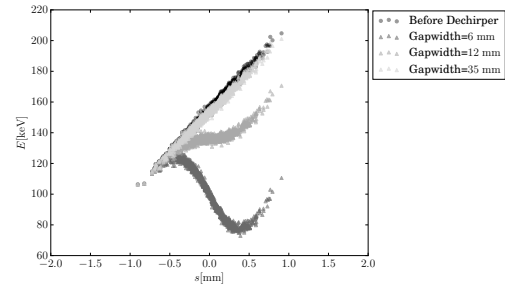


Figure 4: Phase space of bunch 1 before and after the model dechirper with varying gap widths. The overall energy reduction caused by the dechirper is, as intended, stronger on the tail of the bunch than on its head. The curvature of the wake potential shown in Fig. 3 is clearly visible in the curved, wave-like behaviour of the phase space after dechirping. Increasing the gap width from 6 mm to 12 mm significantly reduces the effect of the dechirper, increasing it further to 35 mm nearly completely negates it.

nearly uniform slope of the wake potential of the Gaussian pulse nearly compensates for the initial chirp, leading to a minimal energy width of $\approx 20 \text{ keV}$ in this region. This does not, however, include the head and tail of the bunch, which due to the curvature of the Gaussian pulse, increase the total energy width to $\approx 80 \text{ keV}$ for the total pulse. Decreasing the gap width even further to 6 mm again significantly increases the effect of the dechirper, so much in fact that it overcompensates the initial chirp and leads to a new chirp in the opposite direction, where the tail of the bunch has a lower energy than the head. This new phase space has now an energy width of $\approx -60 \text{ keV}$. This shows again the significant influence of the gap widths on the overall effect of the dechirper and the power of the tuning: within a range of just 3 cm of gap width, the initial energy chirp of the bunch can be either nearly left uninfluenced up to already significantly overcompensated by the dechirper.

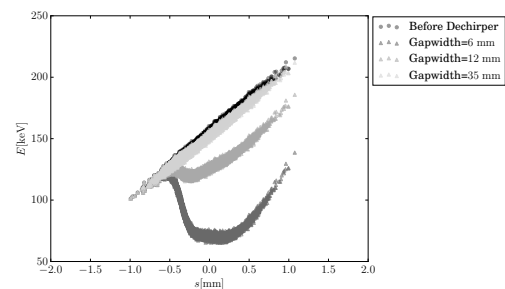


Figure 5: Phase space of bunch 2 before and after the model dechirper with varying gap widths. The curvature of the wake potential is visible in the behaviour of the phase space after dechirping, leading to a valley-like region in the centre of the dechirped phase space. An increase in the gap width again significantly reduces the effect of the dechirper.

Figure 5 shows a similar study conducted for the double Gaussian particle distribution. The effect of the dechirper

with varying gap widths is again clearly visible, from a nearly negligible effect at 35 mm to a very strong overcompensation of the initial chirp at 6 mm gap width. The behaviour of the wake potentials is again imprinted on the phase space after the dechirper. In the case of the 6 mm gap width it leads to a valley of nearly constant energy after the dechirper in the region between about -0.3 mm to 0.3 mm, which coincides with the second of the two Gaussians and subsequently the flatter part of the slope of the wake potential. Like for the single Gaussian, though, at the head and tail of the bunch, the energy width of the dechirped phase space increases to ≈ -50 keV. And even if the mentioned valley does have a very low local energy width, the global mean energy width was nevertheless reduced to just ≈ 60 keV.

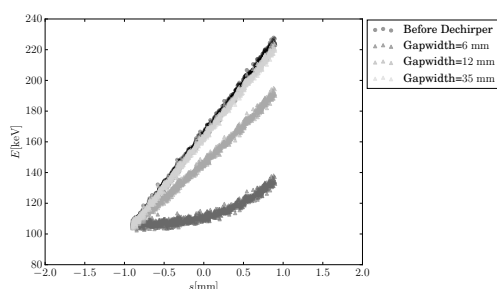


Figure 6: Phase space of bunch 3 before and after the model dechirper with different gap widths. Despite the uniform particle bunch, the dechirped phase space for the lowest gap width clearly shows a curvature.

Figure 6 shows the effect of the dechirper with varying gap widths on a uniform particle bunch. Again, the influence of the gap is easily visible. Due to the uniform pulse and its wake potential displayed in Fig. 3, the dechirped pulses show the least curvature compared to the other pulse forms. For the two larger gap widths, nearly no curvature is discernible, though for a gap of 6 mm width, it is clearly visible. This curvature results from the non-linearity of the wake function and has nothing to do with the shape of the pulse itself. What does influence this curvature, and thus the wake potential, is the length of the pulse compared to the length of the first flank of the wake function. For this pulse, the length of the pulse coincides with nearly the total length of the first flank of the wake function, and thus, all non-linearities in that region will influence the wake potential.

EXPERIMENTAL SET-UP

The measured quantity in the experiments conducted at ELBE was the particle energy spectrum of the beam. The dechirper effect, as shown in the previous sections, basically amounts to an overall energy loss and a narrowing of the energy width of the beam. In the energy spectrum, this would correspond to

1. a decrease of the average energy, and
2. a decrease of the standard deviation of the beam energy.

Depending on the gap width of the dechirper and the bunch charge of the particle beam, these changes will be more or less pronounced.

In the experiments, the studied bunches were generated by a thermionic particle gun. The maximum achievable pulse charge was limited to ≈ 100 pC. With previous parameter studies in mind, this corresponds to an energy loss of ≈ -40 keV that the particles of the bunch can maximally experience for an average gap width. This is very small compared to the usual chirp of the ELBE beam during normal operation, which is in the range of several MeV.

The small effect of the prototype compared to the usual chirp at ELBE poses an experimental challenge: the variations in the dechirp created by adjusting the gap width are insignificant compared to the initial chirp. To compensate for this, both the chicane and the second module were deactivated, so that a particle bunch without an initial chirp was used during the experiments. This has the advantage that the effect of the dechirper could be measured directly, and not in correlation with the initial chirp of the beam.

On the other hand, this also changes the objective of the experiments. The action of the dechirper on the particle beam can generally be understood as a summation of the phase space profile and the dechirp. This means that while the energy width of the initially chirped beam is compensated by the dechirp, the initially unchirped beam is imprinted with the profile of the dechirp. The general energy loss of the particles is not affected by whether or not the beam is initially chirped, so that a general decrease in the average energy of the spectrum of the particle bunch can still be expected. However, instead of narrowing the energy width of the spectrum, the dechirper will imprint the beam with its own phase space profile, and thus *widen* the spectrum. Therefore, the *standard deviation of the beam will increase*. This is technically the inverse effect of what the dechirper ideally should accomplish, but it can serve as a proof of principle.

Another limitation resulting from the circumstances at ELBE is that next to the energy spectrum, neither the longitudinal phase space, nor the particle distribution of the bunch, nor the bunch length could be measured directly. Both, the bunch length and also an approximated particle distribution, are reconstructed from measured data using phase-space tomography methods.

EXPERIMENTAL RESULTS

The energy spectra of the used particle bunch have been measured for different gap widths using an energy spectrometer behind the dechirper. From the spectra, the average energy and the standard deviation were calculated. The results for the maximum gap width of 35 mm were taken as a reference. The total bunch charge amounted to 60 pC for this particular bunch.

For the reconstruction of the phase space of the bunch used in the semi-analytical predictions of the results, a double Gaussian bunch profile was employed as it fits the re-

constructed phase spaces best and can be described analytically. The length of the particle bunch has been extracted from phase space tomography, and is assumed to be 3.6 mm throughout this section.

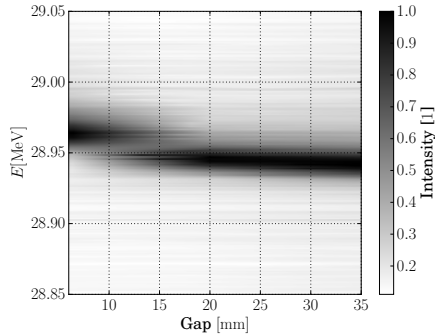


Figure 7: Normed total intensities of the energy spectra recorded for the measured bunch plotted over the gap width of the dechirper. The gap width has been increased in increments of 1 mm between 6 mm and 25 mm, and in increments of 5 mm until the dechirper’s maximum gap width of 35 mm was reached. The data has been interpolated for the gap widths that have not been measured. The white gap occurring between 10 and 15 mm gap width is due to there being two energy peaks.

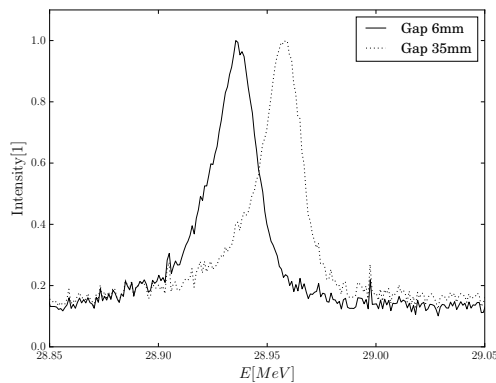


Figure 8: Normed intensities of the energy spectra, shown for the lowest and largest measured gap width from Fig. 7.

The shift of the high intensity peak at ≈ 28.95 keV towards lower energies in Fig. 7 and Fig. 8 clearly shows the energy reduction induced by the dechirper if the gap width is decreased. An increase in the width of the spectrum is not easily visible. In Fig. 9, the progression of the average energies and the standard deviations of the energy spectra of the chosen bunch are shown, measured for different gap widths and compared to data computed with *WizaRD*. Both quantities are referenced against the open dechirper, i.e. the dechirper with a gap widths of 35 mm in the figure. The semi-analytically predicted shift in the average energies for lower gap width is in the same order of magnitude, but lower than the experimentally observed shift. The

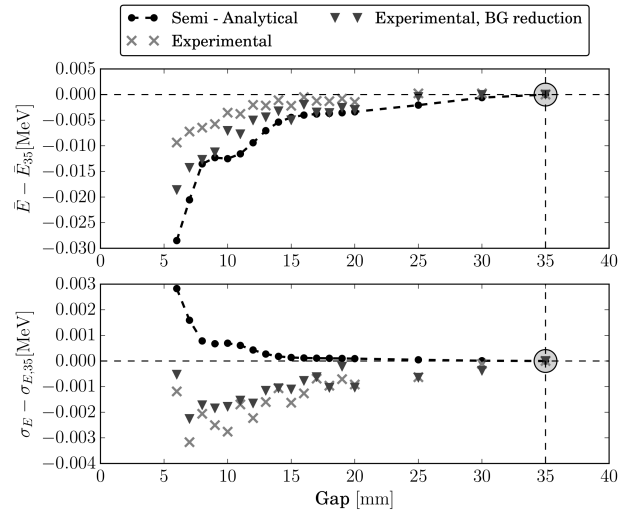


Figure 9: Progression of the average energies and the standard deviations of the energy spectra of the measured bunch for different gap widths of the dechirper. Both quantities are given in comparison to the case of the dechirper at 35 mm (marked in the figure). The figure shows the raw experimental data, the experimental data after a reduction of the background by a quadratic polynomial and the semi-analytical predictions carried out for the extracted bunch length assuming a double Gaussian bunch shape (dashed line).

discrepancy between both curves is highest for gap widths lower than 10 mm. When the background of the spectra is fitted with a quadratic polynomial (using an in-built Python function based on the non-linear least squares fitting technique) and subtracted, the accordance of the experimental and semi-analytical results can be increased. As an example, the discrepancy between the semi-analytical prediction and the experimental values is ≈ 20 keV for a gap width of 6 mm. Introducing the background reduction decreases this discrepancy to ≈ 10 keV.

For the standard deviations, the experimental results do not match the semi-analytical predictions. Both the raw data and the data after the background reduction suggest a minimal decrease of the standard deviation of the spectrum when decreasing the gap width. The semi-analytically calculated results, however, suggest an increase of the width of the spectrum for decreasing gap widths, which would be in better accordance with the generally expected (inverse) effect of the dechirper. However, both shifts are only in the range of a few keV and thus, as expected, very minimal.

SUMMARY

In this contribution, we have introduced the dechirper structure designed for ELBE. We have shown the energy modulating effect of the dechirper by using the semi-analytical programme code *WizaRD* to simulate the interaction between the employed particle beam and the generated wake potential for different pulse shapes. To complement these simulations, experiments with the prototype have been

performed at ELBE. These have shown the inverse dechirper effect on a beam without an initial energy spread in form of a decrease in the average energy of the bunch, which matches the semi-analytical predictions well. The predicted increase in the standard deviation of the energy spectrum of the particle beam could not be observed in the experimental series presented here and needs to be investigated further. This serves as a proof of principle of the dechirper's capability to influence the longitudinal phase space of the beam. In the future, we plan to expand on these studies and compare the prototype to other types of dechirpers in further experiments.

REFERENCES

- [1] F. Reimann and U. van Rienen, *Wakefields – An Overview*, CERN Yellow Report, in print.
- [2] K. Bane, *Corrugated Pipe as a Beam Dechirper*, SLAC-PUB-14925, (2012).
- [3] P. Emma et al., *Experimental Demonstration of Energy-Chirp Control in Relativistic Electron Bunches Using a Corrugated Pipe*, Phys. Rev. Lett., 112, 3, (2014), p. 034801.
- [4] S. Antipov, *Passive Momentum Spread Compensation by a “Wakefield Silencer”*, Proceedings of the Internat. Part. Accel. Conf. 2012, New Orleans, USA, (2012).
- [5] S. Antipov et al., *Experimental Observation of Energy Modulation in Electron Beams Passing through Terahertz Dielectric Wakefield Structures*, Phys. Rev. Lett., 108, 14, (2012), pp. 144801–144805.
- [6] F. Reimann et al., *Rayleigh–Ritz based expansion method for wakefields in dielectrically lined rectangular waveguides*, Journal of Comp. Phys., 372, (2018), pp. 299 - 315.
- [7] S. Antipov et al., *A tunable energy chirp correction*, Proceedings of the Part. Accel. Conf. 2013, Pasadena, USA, (2013), pp. 279–281.
- [8] S. Antipov et al., *Experimental Demonstration of Energy-Chirp Compensation by a Tunable Dielectric-Based Structure*, Phys. Rev. Lett., 112, 11, (2014), pp. 114801–114805.
- [9] F. Reimann et al., *Wakefield-Based Dechirper Structures for ELBE*, Proceedings of the Internat. Part. Accel. Conf. 2014, Dresden, Germany, (2014).
- [10] F. Reimann et al., *A dielectrically lined rectangular waveguide as a wakefield dechirper for ELBE*, 2015 Intl. Conf. on Electromagnetics in Advanced Applications, Torino, Italy, (2015).

EFFECT OF HOM FREQUENCY SHIFT ON BUNCH TRAIN STABILITY

J. Repond*¹, E. Shaposhnikova, CERN, Geneva, Switzerland

¹also at École polytechnique fédérale de Lausanne, Lausanne, Switzerland

Abstract

Future operation of the Large Hadron Collider (LHC) at CERN foresees an increase of the nominal luminosity by a factor of ten. The High-Luminosity LHC (HL-LHC) project necessitates good quality beam with increased intensity delivered by the injector chain. An important quality of the beam is its stability. In the LHC injector, the Super Proton Synchrotron (SPS), the longitudinal Coupled-Bunch Instability (CBI) during the acceleration ramp is a limiting factor in the production of high intensity beams. The main source of CBI is the 630 MHz Higher-Order Mode (HOM) in the 200 MHz travelling wave RF cavities. This HOM is already heavily damped by a series of longitudinal RF couplers. To achieve greater levels of damping, additional methods are under investigation using electromagnetic simulations. It has been shown in particle simulations that shifting the resonant frequency of the HOM can significantly improve the beam stability by up to 50%. The dependence of the instability threshold with the resonant frequency of the 630 MHz HOM is studied for an SPS bunch train of 72 bunches. The results of the macro-particle simulations are substantiated with an analytical model.

INTRODUCTION

Two independent travelling wave RF systems operate in the SPS for the production of the LHC proton beams. The acceleration system at 200 MHz [1] is supported by a second RF system at 800 MHz, operating as a Landau system in bunch-shortening mode [2]. Moreover, for nominal LHC intensity, the bunch emittance is blown-up in a controlled way during acceleration to ensure beam stability. However, this will not be sufficient to guarantee the stability of the HL-LHC beam. The acceleration system must therefore undergo significant upgrades. The available power per cavity will be raised and the number of cavities increased [3]. The new cavities are shorter than the existing ones to minimise power requirements and impedance. The updated acceleration system consists of two four-section and four three-section travelling wave RF systems [4]. Each section is made of eleven cells where RF probes and RF couplers are installed. Due to beam-loading in the cavities, a maximum voltage of 10 MV is only achievable at flat top (450 GeV) for an intensity of 2.4×10^{11} particles per bunch (ppb). In addition, a redesign of the low-level control of the 200 MHz RF system reduces further the beam-loading. Feedback and feedforward systems are part of the 200 MHz low-level RF and are expected to reduce the impedance seen by the beam up to a factor of 26 dB in the accelerating band after upgrade.

In the cavities an HOM in the 630 MHz passband is critical for beam stability. The mode is already heavily damped by a series of RF couplers and further damping is difficult to achieve without modifying the layout of the cavity. The natural spread of the HOM from cavity to cavity has been measured to be around 100 kHz [5]. The total shunt impedance seen by the beam is not sufficiently reduced by this spread and detuning the mode differently for each cavity, mechanically or by using new RF couplers, has been proposed as a solution for improved stability. Particle simulations show that a frequency spread of the HOM from cavity to cavity by a few MHz could already significantly improve the situation. Moreover, a full detuning of the mode by 10 MHz gives a major increase up to 50% of the intensity threshold. However, the mode in the 630 MHz passband appears to be rigid. Most of the stored energy is in the cavity volume [6] and the frequency cannot be shifted by 10 MHz with RF couplers. To understand the possible gain of a smaller shift, the mechanism behind the improvement of beam stability is studied in what follows.

The total HOM of the four three-section cavities and two four-section cavities without further damping can be modelled by a resonator with a shunt impedance $R_{sh} = 570$ k Ω and a quality factor $Q = 200$, with impedance

$$Z(f) = \frac{R_{sh}}{1 + iQ\left(\frac{f}{f_r} - \frac{f_r}{f}\right)} \quad (1)$$

and

$$W(\tau) = \begin{cases} \alpha R_{sh} & \text{if } \tau = 0, \\ 2\alpha R_{sh} e^{-\alpha\tau} \left(\cos(\bar{\omega}\tau) - \frac{\alpha}{\bar{\omega}} \sin(\bar{\omega}\tau) \right) & \text{if } \tau > 0, \end{cases} \quad (2)$$

is the Green's function of the electromagnetic field of the resonator with parameters

$$\alpha = \frac{\pi f_r}{Q} \quad \text{and} \quad \bar{\omega} = 2\pi f_r \sqrt{1 - \frac{1}{4Q^2}}. \quad (3)$$

$W(\tau)$ is also called the wake function and its Fourier transform is the impedance. The e-folding time of the wake function generated by the HOM is

$$\frac{1}{\alpha} = \frac{Q}{\pi f_r} \approx 100 \text{ ns}. \quad (4)$$

In the LHC beam, bunches are separated by 25 ns, therefore, several bunches are coupled through their wakefield which leads to possible CBI depending on beam intensity.

FREQUENCY DEPENDENCE OF INSTABILITY THRESHOLD

The CBI threshold is the lowest at SPS flat top. This statement is supported by measurements and analytical esti-

* joel.repond@cern.ch

mations [7]. Simulations and analysis below are then made at an energy of 450 GeV. The full SPS impedance model is used [8], containing various resonating elements, broad- and narrow-band, between 50 MHz and 4 GHz. The major contributors to the impedance model are the 200 MHz TW cavities. Both the accelerating band and HOMs bands contribute significantly. The fundamental passband is reduced by the feedback system. Two other significant contributions to the longitudinal impedance arise from the kicker magnets, with broad-band impedance, and the vacuum flanges acting mainly at high frequency (>1 GHz). Many smaller contributions are taken into account, from beam instrumentation devices to the resistive wall impedance. The impedance of these devices has been simulated and/or measured over many years. The complexity of the model makes analytical estimations difficult and particle tracking codes like BLoND [9], developed in the RF group at CERN, is used to study the impact on beam stability of the different components of the longitudinal SPS impedance model. The intensity threshold is determined performing scans of both intensity and longitudinal bunch emittance. Particle positions in phase space are tracked during a 2 seconds cycle assuming 10 MV at 200 MHz and 1 MV at 800 MHz for each intensity. The bunch distributions are generated in agreement with beam measurements in the SPS. Bunch profiles are computed by projection of the bunch phase space on the time axis and the quadrupole oscillations are extracted. The maximum amplitude of the bunch length oscillations (normalised by the average) is used to separate stable beam from the unstable one. The 630 MHz HOM excites dipole and quadrupole modes at the SPS flat top and both appear in simulation. Usually, bunch length oscillations are used as a criteria to define the stability threshold in simulations of bunch trains with the full impedance model.

Figure 1 shows the stability threshold for five different values of the HOM resonant frequency between 620 MHz and 640 MHz. In operation a spread in bunch length of $\pm 8\%$ is measured from bunch-to-bunch along the batch [10] which enforces some necessary margins on the intensity threshold. From simulations with the original HOM at 630 MHz it is observed that beam stability cannot be ensured at HL-LHC intensity. The stability threshold goes up if the HOM is damped by a factor of three keeping R_{sh}/Q constant. For an intensity lower than HL-LHC intensity, the upgraded RF power will allow to increase the voltage above 10 MV. The damping of the HOM by a factor of three is almost sufficient to guarantee beam stability. However, since the damping is difficult to achieve, other solutions were investigated. Shifting the original 630 MHz frequency by a few MHz improves stability as well. The HOM currently sits in an asymmetric region of reduced beam stability. A frequency shift in the positive direction increases stability further than a shift in the negative direction. For a resonant frequency of 640 MHz, simulations show a remarkable improvement of the stability threshold. This frequency corresponds to one of the beam spectrum lines related to bunch spacing (40 MHz). It is well known for a ring filled with equally spaced bunches

that a narrow-band impedance with a frequency sitting exactly on a beam spectral line cannot drive instability [11] but the overlap of the beam spectrum and the impedance increases power loss and heating. However, the 630 MHz HOM, already heavily damped to $Q = 200$, is not particularly narrow-band and a train of 72 bunches occupies only height percent of the machine. The first and last bunch of the beam are not coupled and beam spectrum lines are broader than in the full ring case. Nevertheless, simulations exhibit a similar improvement of the stability threshold. Contrary to the ideal case of a full ring the stability must be studied by solving the equations of motion bunch after bunch [12]. Due to the complexity of the machine impedance we choose to isolate the impedance of the 630 MHz and to simplify the equations by considering a single 200 MHz RF system. However, simulations in single and double RF systems give comparable results.

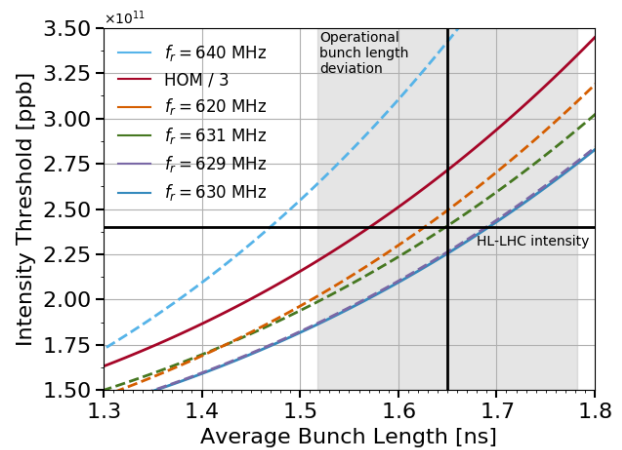


Figure 1: Stability threshold for 72 bunches at SPS flat top in a double RF system with 10 MV for the 200 MHz RF system and 1 MV for 800 MHz RF system in bunch-shortening mode. The full SPS impedance model is used and the resonant frequency of the HOM in the 630 MHz passband is shifted by different values. The horizontal line indicates the HL-LHC beam intensity and the vertical one the nominal bunch length. This bunch length has a spread in operation of $\pm 8\%$, indicated by the shaded area.

STABILITY OF TRAINS WITH POINT-LIKE BUNCHES

A point-like bunch model is already able to explain certain observations made in simulation for the LHC beam with a realistic bunch distribution. In such a model each one of the M bunches is represented by a single rigid particle carrying the total bunch intensity. The bunch i oscillates around its synchronous phase ϕ_i with a relative position in time $\tau_i = \frac{\phi_i}{\omega_{rf}}$ where ω_{rf} is the angular frequency of the RF system (Fig. 2). Initially centred in the RF bucket, bunches are separated by a distance τ_{bb} . The equations of motion are derived for small amplitude synchrotron oscillations without

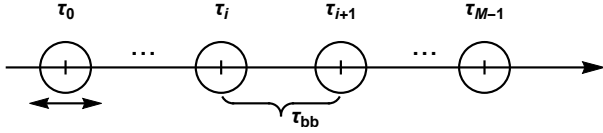


Figure 2: Point-like bunch model. Each bunch is represented by one rigid particle carrying the total bunch intensity. All bunches initially centred in the RF bucket are separated by a distance τ_{bb} and their position relative to the bucket centre are described by τ_i .

acceleration. This approximation is valid at the SPS flat top for a nominal bunch length of 1.65 ns. The behaviour of the bunch i is dictated by the equation

$$\ddot{\tau}_i + \omega_{s0}^2 \tau_i = \frac{\eta q}{\beta_s^2 E_s T_0} V_{ind}(\tau_i), \quad (5)$$

where V_{ind} is the voltage induced by the particles circulating ahead in the machine, T_0 the revolution period, q the charge of the bunch i , η the slip factor defined by $\delta T/T_0 = -\eta \delta p/p_s$ with δp the deviation from the synchronous momentum p_s , E_s the synchronous energy and $\beta_s c$ the velocity of the synchronous particle with c the speed of light. The SPS optics used in simulation (Q20) gives a slip factor $\eta \approx -3.1 \times 10^{-3}$. The synchrotron frequency $f_{s0} = \omega_{s0}/2\pi$ is defined by

$$\frac{\omega_{s0}^2}{\omega_0^2} = \frac{h V_{rf} \eta \cos \phi_s}{2\pi \beta_s^2 E_s}, \quad (6)$$

where V_{rf} is the amplitude of the RF voltage, h the harmonic number defined by $\omega_{rf} = h\omega_0$ and ϕ_s the phase of the synchronous particle with respect to the RF. For a longitudinal line density $\lambda(\tau)$, the general expression of the induced voltage is

$$V_{ind}(\tau) = -q N_b \int_{-\infty}^{\infty} \lambda(\tau') W(\tau - \tau') d\tau', \quad (7)$$

where N_b is the number of charges in the bunch. For point-like bunches the line density takes only discrete values. The wake function is expanded to linear order for small amplitude synchrotron oscillations. The zero order term can be discarded and only the first order term contributes to the dynamics. The equation of motion of the i^{th} bunch considering the interactions with all preceding neighbours is

$$\ddot{\tau}_i + \omega_{s0}^2 \tau_i = \kappa \sum_{k=0}^{i-1} W'[(i-k)\tau_{bb}](\tau_i - \tau_k), \quad (8)$$

with $\tau_{bb} = 25$ ns for an LHC beam and $\kappa = \frac{\eta q^2 N_b}{\beta_s^2 E_s T_0}$. For a resonator with $Q \gg 1$,

$$\frac{W'_{/l}(\tau)}{2\alpha^2 R_{sh}} = -e^{-\alpha\tau} \sqrt{4 + \left(\frac{\bar{\omega}}{\alpha} - \frac{\alpha}{\bar{\omega}}\right)^2} \sin(\bar{\omega}\tau + 1/Q). \quad (9)$$

The induced voltage cancels perfectly every τ_{bb} if the resonant frequency is

$$f_r = \frac{k - \frac{1}{\pi Q}}{\tau_{bb} \sqrt{4 - 1/Q^2}}. \quad (10)$$

In the SPS case with the 630 MHz HOM, this corresponds to frequencies $f_r \approx k \times 20$ MHz for $k = 1, 2, 3, \dots$ and therefore, if the resonant frequency of the mode is a multiple of 20 MHz, the growth rate of the instability is null. For a realistic bunch distribution, the bunch centre sees an induced voltage close to zero. This explains the improvement of the beam stability with realistic bunch trains for resonant frequencies of 620 MHz and 640 MHz. From Eq. (8), the growth time of the instability can be computed for the bunch i taking into account all preceding bunches,

$$\frac{1}{\mathfrak{I}(\omega)} = \left[\mathfrak{I} \left(\omega_{s0}^2 - \kappa \sum_{k=0}^{i-1} W'[(i-k)\tau_{bb}] \right)^{\frac{1}{2}} \right]^{-1}. \quad (11)$$

The expression (11) can be computed numerically for an intensity above threshold considering different number of bunches coupled, see Fig. 3. For the nearest neighbour inter-

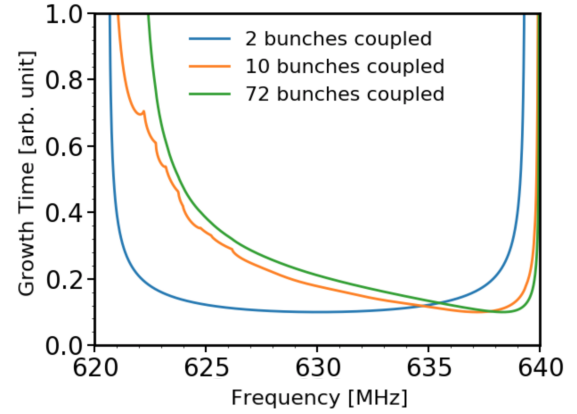


Figure 3: Instability growth time for a train of point-like bunches. An intensity above threshold is used and the sum in (11) is truncated for different lengths of interaction between bunches.

action the growth time appears to be symmetric between the two 20 MHz lines. An asymmetry appears when the number of bunches coupled increases. After adding more than 10 bunches the growth time does not change significantly. This result is reasonable since the wake function decreases by a factor 2.7 over four bunches. However, compared to the realistic bunch case, it suggests that a frequency shift in the positive direction degrades beam stability. This analytical estimation is confirmed by simulations of 72 point-like bunches (Fig. 4).

STABILITY OF REAL BUNCH TRAIN

With a realistic bunch distribution the induced voltage of each bunch is created over a finite length, which introduces a phase shift in the voltage overlap seen by the trailing bunches. The analytical bunch model can be extended by considering the induced voltage of a bunch with line density $\lambda(\tau)$ acting

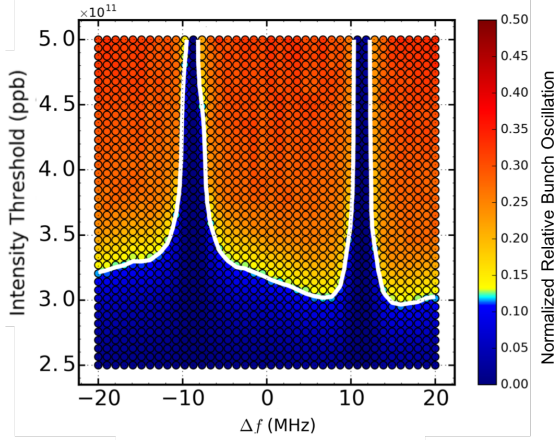


Figure 4: Intensity threshold simulated for 72 point-like bunches with 630 MHz HOM impedance only in a single 200 MHz RF system with a voltage of 10 MV. The resonant frequency is shifted from 630 MHz to 630 ± 20 MHz. Colours represent the maximum amplitude of the bunch position oscillations, normalised by the average one.

on the point-like bunches,

$$V_{ind}(\tau_{bb} + \Delta\tau) = -qN_b \int_{-\infty}^{+\infty} \lambda(\tau') W'(\tau_{bb} - \tau') d\tau' \Delta\tau. \quad (12)$$

In this case the instability growth time for the bunch i becomes

$$\frac{1}{\mathfrak{I}(\omega)} = \left[\Im \sqrt{\omega_{s0}^2 - \kappa \sum_{k=0}^{i-1} \int \lambda(\tau') W'[(i-k)\tau_{bb} - \tau'] d\tau'} \right]^{-1} \quad (13)$$

Assuming a Gaussian bunch with a bunch length of 1.65 ns, the expression (13) can be calculated numerically for an intensity above threshold, see Fig. 5. The picture is similar

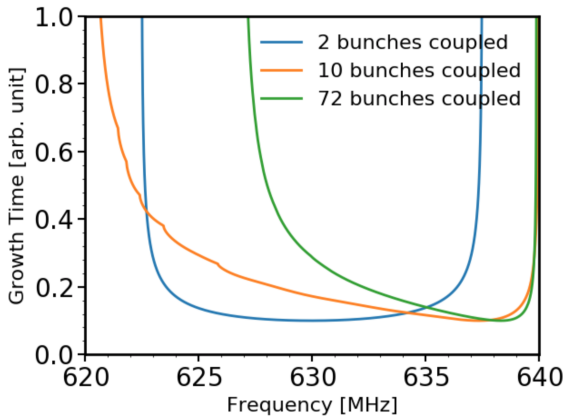


Figure 5: Instability growth time for a train of point-like bunches and an induced voltage generated by a Gaussian bunch of length 1.65 ns. An intensity above threshold is used and the sum in (13) is truncated for different lengths of interaction between bunches.

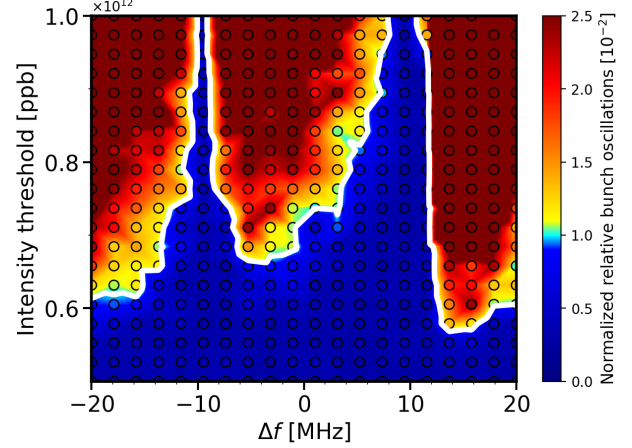


Figure 6: Intensity threshold simulated for 72 realistic bunches of length 1.65 ns with 630 MHz HOM impedance only. A single RF system at 200 MHz with a voltage of 10 MV is used. The resonant frequency is shifted from 630 MHz to 630 ± 20 MHz. Colours represent the maximum amplitude of the dipole oscillations of the last bunch in the train normalised by the average.

to the simpler point-like bunch model. The asymmetry between odd and even 20 MHz lines is comparable, indicating that synchrotron intra-bunch motion plays a significant role in determining stability threshold for a bunch train. Indeed, simulations at flat top with realistic bunches of 1.65 ns and the HOM impedance only (Fig. 6), exhibit the same asymmetry as the realistic SPS simulations (Fig. 1). The Figure 6 shows the threshold for the dipole oscillations but similar picture is obtained for the threshold of quadrupole oscillations. The stability improvement is the largest for resonant frequencies at 620 MHz and 640 MHz. At odd multiples of 20 MHz the symmetry is similar to the point-like bunch model but at even values the stability is reversed. These simulations indicate that the 630 MHz HOM is the main contributor to the instability and the interplay with other impedance sources does not necessarily has to be taken into account.

It should be noticed that even if a solution is found to modify the frequency of the HOM, in reality the possibilities of shifting the resonant frequency are limited. A frequency shift in the 640 MHz direction is beneficial for beam stability as long as the HOM damper can handle the increased heat-load. On the other side, the region of increased stability toward the 620 MHz notch is very narrow (Fig. 6) and a sufficient frequency shift cannot be achieved by means of RF couplers [6]. Note that, if the bunch spacing is increased to 50 ns—solution considered if the LHC suffers e-cloud effects—the 630 MHz band becomes a region of higher stability.

CONCLUSION

After upgrading the SPS, the effect of the 630 MHz HOM on beam stability must be reduced to enable the bunch in-

tensity required by the HL-LHC project. Further damping of the HOM through the use of RF couplers is difficult, but substantial improvement can be obtained by shifting its resonant frequency. The simulations indicate that the increase of intensity threshold, observed for a train of 72 bunches, is principally due to the change in HOM frequency. Similarly to the case of a ring filled with equally spaced bunches, if the resonant frequency overlaps a beam spectrum line or sits exactly between them, the bunches experience zero growth rate of instability. A shift of the mode frequency in the positive direction, toward the spectrum line at 640 MHz, is favourable for beam stability but increases the heat-load. On the contrary, a shift in the negative direction would have no detrimental effect on the heating but, it is observed, that the frequency band where the stability is improved is very narrow around 620 MHz. Since most of the mode energy is stored in the cavity volume, a sufficient detuning cannot be achieved by means of RF couplers. This mitigation scheme is therefore jeopardised and the efforts focus now on an improved damping scheme with an optimal positioning of new HOM couplers.

The point-like bunch model is able to account for the large gain in stability observed at resonant frequencies of 620 MHz and 640 MHz for bunch trains but has difficulties to reproduce some of the finer details observed with real bunches. Nevertheless, for odd values of 20 MHz harmonics, the threshold is similar to the point-like bunch model.

ACKNOWLEDGEMENTS

We would like to thank R. Calaga and N. N. Esfahani for fruitful proposals; T. Argyropoulos, K. Iliakis, A. Lasheen, J. E. Müller, D. Quartullo and H. Timko for their contributions to the BLonD code; A. Farricker, T. Kaltenbacher, P. Kramer, B. Salvant, J. Varela and C. Vollinger for the development of the SPS impedance model; S. Albright, J. Mitchell and A. Farricker for their help with the proofreading.

REFERENCES

- [1] G. Dôme, “Travelling Wave Drift-Tube Structure for the CERN SPS”, in *Proc. Proton Linear Accelerator Conference 1976*, Chalk River, Ontario, Canada, 1976.
- [2] T. Bohl, T. Linnecar, E. Shaposhnikova and J. Tuckmantel, “Study of different operating modes of the 4th RF harmonic Landau damping system in the CERN SPS”, in *Proc. EPAC’98*, Stockholm, Sweden, June 1998, Vol. 1-3, p. 978–980.
- [3] H. Damerou, et al., “LHC Injectors Upgrade, Technical Design Report”, CERN-ACC-2014-0337, CERN, Switzerland, December 2014.
- [4] E. Shaposhnikova, E. Ciapala, E. Montesinos, “Upgrade of the 200 MHz RF system in the CERN SPS”, in *Proc. IPAC’11*, San Sebastian, Spain, September 2011, paper MOPC058, pp. 214–216.
- [5] P. Kramer, C. Vollinger, “Studies for the SPS travelling wave cavities upgrade”, in *Proc. ICFA Mini-Workshop Workshop “Impedances and Beam Instabilities in Particle Accelerators”*, Benevento, Italy, September 2017, this proceeding.
- [6] N. N. Esfahani, P. Kramer and C. Vollinger, “Equivalent circuit modelling of travelling wave accelerating structures and its applications”, in *Proc. 47th EuMC*, Nuremberg, Germany, 2017, pp. 572–575.
- [7] E. Shaposhnikova, “Longitudinal stability of the LHC beam in the SPS”, CERN-SL-Note-2001-031, CERN, Switzerland, August 2001, pp. 12.
- [8] J. Varela et al., “An Extended SPS Longitudinal Impedance Model”, in *Proc. IPAC’15*, Richmond, Virginia, USA, 2015, paper MOPJE035, pp. 360–362.
- [9] H. Timko et al., “Benchmarking the Beam Longitudinal Dynamics Code BLonD”, in *Proc. IPAC’16*, Busean, Korea, May 2016, paper WEPOY045, pp. 3094–3097.
- [10] E. Shaposhnikova et al., “Removing Known SPS Intensity Limitations for High Luminosity LHC Goals”, in *Proc. IPAC’16*, Busean, Korea, May 2016, paper MOPOY058, pp. 989–991.
- [11] J. L. Laclare, “Bunched beam coherent instabilities”, in *Proc. CAS’85*, Oxford, UK, September 1985, pp. 264–326, (CERN-1987-003-V-1).
- [12] H. G. Hereward, “Limitations on Beam Quality and Intensity”, in *Proc. HEACC’71*, CERN, Geneva, Switzerland, September 1971, vol. C710920, p. 548.
- [13] K. Y. Ng, “Physics of intensity dependent beam instabilities”, Hackensack, USA, World Scientific (2006) 776 p.
- [14] A. W. Chao, “Physics of collective beam instabilities in high-energy accelerators”, New York, USA, Wiley (1993) 371 p.

IMPEDANCE AND INSTABILITIES IN HADRON MACHINES

B. Salvant, CERN, Geneva, Switzerland

Abstract

Coherent beam instabilities related to impedance effects represent one of the main limitations to increasing beam intensity in circular accelerators.

This contribution was presented at the ICFA mini-workshop on impedance and beam instabilities in particle accelerators on 18-22 September 2017 in Benevento, and aimed at providing a brief overview of the situation in circular hadron machines at the moment of the workshop.

INTRODUCTION

In his report on the CERN Intersecting Storage Rings (ISR), B. Zotter (1932-2015) highlighted that “already during the earliest ISR development runs it was found that part of the beam was lost suddenly when a certain current level was reached during stacking. This phenomenon repeated itself again and again at the same level, and was called ‘brickwall’ in the first moment of despair” [1]. As in this case, the performance reach of several machines has been limited by such collective phenomena, either in the longitudinal or transverse plane(s), and mitigations had to be found.

The case of lepton machines is dealt with in a contribution at the same workshop [2] and this contribution focuses on the specific case of hadron machines. The theory of instabilities and in particular impedance related instabilities was developed and summarised in great detail for instance in Ref. [3-9], and this contribution will start with listing the specificities of hadron machines, before attempting to give an overview of the instabilities experienced by hadron machines. The focus will be put on the main instability issues at the moment of the workshop (Rutherford Appleton Laboratory ISIS, GSI SIS18 and CERN LHC as CERN PS and SPS are covered in other contributions at this workshop [10-13]).

This contribution does not cover linear accelerators, since the beam break-up instability in proton and ion Linacs is generally above the space charge limit and can be efficiently mitigated by adding betatron frequency spread between the head and the tail of the bunch with a Radio Frequency Quadrupole (RFQ) or an adequate choice of bunch phase with respect to the RF (BNS damping) [14].

SPECIFICITIES OF HADRON MACHINES

Hadrons are made of protons and neutrons, whose rest mass is 1836 times that of the electron. It therefore requires much more force to accelerate and bend hadrons than electrons. As a consequence, the potential relativistic factor γ reach is much lower for hadrons for similar machine size. At lower γ synchrotron radiation plays a smaller role (both quantum excitation and damping),

which means that hadron machines would typically operate with larger beam emittance and bunch length with similar focusing forces. This is even worse for heavy ions, for which the accelerating and guiding forces scale with the ratio of the atomic charge Z to the atomic number A , which is always lower than unity due to the presence of neutrons. For collective effects the forces scale with Z^2/A .

Another consequence of the larger hadron mass is the much larger beam power for the same relativistic factor, and the impact of beam losses can be much more dramatic. This may lead hadron machines to require a collimation system to localize losses, and these collimators can represent a large contribution to the machine impedance (due to the current technology that requires having robust material with low atomic number close to the beam). The lower relativistic factor also means that space charge should have a stronger impact.

For stability purposes, operating with larger emittance means more tune spread available for Landau damping, stronger impact of octupoles on damping instabilities and that collimators and apertures should remain far from the beam, which reduces impedance.

Historically, the synchrotron tune – a critical parameter for stability – was typically much larger for lepton machines (of the order of 10^{-1}) than for hadron machines (of the order of 10^{-3}) [15]. Nevertheless, the synchrotron tunes of ESRF, SOLEIL, CERN SPS and LHC are for instance within the same order of magnitude (2 to $5 \cdot 10^{-3}$).

The longer bunch length requires less bandwidth for feedback systems to be effective on intra-bunch motion. In addition, the frequency spectrum excited by the beam does not reach very high frequencies, which are difficult to reach with simulations and measurements. The excited beam spectrum is typically lower than the beam pipe cut-off frequency in hadron machines, which is very good news for performing 3D numerical impedance simulations, but also means that resonant modes do not propagate in the beam pipe and remain trapped in the device: this is bad news for the device itself as it could be damaged, but good news for the neighbouring accelerator components.

It has to be noted that the energy reach of energy frontier hadron machines like LHC is now such that hadrons are also experiencing significant synchrotron radiation effects, and the transverse emittance (not normalized) is now in the same ballpark as light sources.

Most hadron machines operate in the strong space charge regime, with the notable exception of LHC, even though the impact of space charge at injection is still expected to be significant [16].

Finally, the vast majority of hadron synchrotrons use positively charged ions, and electron cloud phenomena should be accounted for.

OVERVIEW OF CIRCULAR HADRON MACHINES

Circular hadron machines have been located mainly in 8 countries (see Fig. 1):

- Canada (TRIUMF)
- France (CERN and GANIL)
- Germany (DESY, GSI and Julich)
- Japan (JPARC)
- Russia (IHEP)
- Switzerland (CERN and PSI)
- UK (RAL)
- USA (BNL, Fermilab, LANL and ORNL)

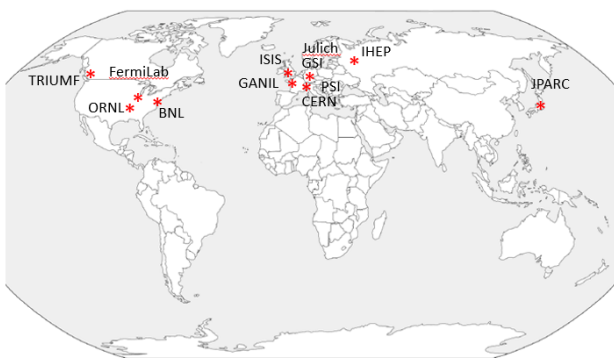


Figure 1: Location of circular hadron machines.

Instabilities were observed in most of the currently running machines (see Tab. 1). Looking at the “instabilities” column of this table, one can observe that instability issues are currently concentrated in RAL ISIS, GSI SIS 18, as well as CERN PS, SPS and LHC.

Table 1: status of instabilities in circular hadron machines. As shown in the legend below the table, a white box means that there is no observation of instability; a green box means that instabilities are observed and mitigated; an orange box means that instabilities are observed and are a worry for performance reach; and finally a red box means that instabilities currently limit performance. FB refers to presence of “feedback”, while “HH” to the presence of “higher order harmonic cavity”, and “chroma” to the use of chromaticity to help damping the relevant instabilities.

Laboratory	Machine	instabilities	longitudinal	transverse	electron cloud	TMCI	microwave	loss of Landau damping	vacuum instability	unexplained heating
BNL	AGS			FB						
	RHIC		HH					damped by 21st order cavity		
CERN	ELENA									
	AD									
	LEIR			FB						
	PSB			FB						
	PS		FB	FB						
	SPS		HH	FB						
	LHC		no HH	FB				?		
Fermilab	Booster		FB	FB						
	MI			FB						
	recycler			FB						
GANIL										
GSI	ESR									
	SIS18			no FB						
IHEP	U-70			FB						
JPARC	RCS			chroma						
	MIR			FB						
Julich	COSY			FB+chroma	cooler					
LANL	PSR			FB					heating the ferrite!	
ORNL	SNS			FB						
PSI	HIPAC									
RAL	ISIS			no FB						
TRIUMF	MC									

	no observations
	observation and mitigation
	worry
	limits performance

With the “longitudinal” column, one can see that machines use a feedback system or a higher order harmonic cavity as active damping methods. In the “transverse” column, one can notice that almost all machines have implemented an active damping for the transverse plane, and that SIS-18 and ISIS have transverse instability issues because a feedback system was not installed. Colleagues present at the workshop from RAL and GSI confirmed that a feedback system is planned to be installed.

The “electron cloud” column of Tab. 1 shows that electron cloud instabilities is an issue mainly in LHC for the injection of certain beams (e.g. the doublet beam used for beam scrubbing).

The following columns of the table (“TMCI” (Transverse Mode Coupling Instability), “microwave” instability, “loss of Landau damping” instability, “vacuum instability”) show if such instabilities were observed and are considered as threats to the machine performance. TMCI and microwave instabilities are observed in very few machines, while loss of Landau damping instability in longitudinal and/or transverse plane is observed in almost all machines, in particular when the feedback is switched off. Vacuum instability is only observed in SIS18, while the recent transverse instabilities in LHC were still not fully understood at the moment of the workshop.

Finally heating issues are concentrated in SPS and LHC.

The impact of the parameters planned for the major upgrades foreseen for the hadron machines modifies Tab. 1 into Tab. 2.

Table 2: status of instabilities for parameters planned for major upgrades of circular hadron machines. Same legend as Tab. 1.

Laboratory	Machine	instabilities	longitudinal	transverse	ecLOUD	TMCI	microwave	loss of Landau damping	vacuum instability	unexplained	heating
BNL	AGS			FB							
	RHIC	HH						damped by 21st order cavity			
CERN	ELENA										
	AD										
	LIU-LEIR			FB							
	LIU-PSB			FB							
	LIU-PS	FB		FB				CBI			
	LIU-SPS	HH		FB							
	HL-LHC	no HH		FB				?			
Fermilab	Booster	FB		FB							
	MI			FB							
	recycler			FB							
GANIL											
GSI	ESR										
	SIS18			no FB							
IHEP	U-70			FB							
JPARC	RCS			chroma							
	MR			FB							
Juelich	COSY			FB+chroma cooler							
LANL	PSR			FB				heating the ferrite!			
ORNL	SNS			FB							
PSI	HIP4										
RAL	ISIS			no FB							
TRIUMF	MC										

The push of performance required by the upgrades means that instabilities become more critical. This is clearly the case for the High Luminosity LHC (HL-LHC) and LHC Injectors Upgrade projects at CERN as well as in GSI and SNS.

For these upgrades, the requested increase in performance leads to reduce beam coupling impedance and/or damping mechanisms (higher harmonic cavities, feedback systems, improvement of optics to gain margin with respect to instability thresholds by reducing betatron tune shifts [10] or increasing betatron tune spread).

In this context, it is important to note that hadron circular machines require a significant investment and most were built a long time ago and upgraded. In fact, as Sophie Marceau [17], impedance theory was very young at the time of designing many of these machines, and impedance reduction was not an integral part of the design, as it is nowadays for instance for GSI SIS-100, JPARC rings, CERN LHC and HL-LHC. Many accelerator elements from the 1970s to 1990s are still present and a replacing all of them with impedance-optimized components would be very costly. A significant effort to patch these existing machines is therefore underway in view of heavy upgrades (see for instance [18]).

FOCUS ON TWO CURRENT INSTABILITY ISSUES

Headtail instabilities

Transverse Headtail instabilities were observed in both GSI SIS-18 and RAL ISIS, both from single bunch loss of

Landau damping (see Fig. 2) [19, 20]. These instabilities could be issues for the foreseen upgrades, but common damping techniques have not yet been installed and exploited (in particular feedback systems for both machines and even chromaticity control for ISIS since sextupoles had been removed to free space). Both labs therefore plan to install transverse feedback, as well as octupoles in SIS18 and in SIS100.

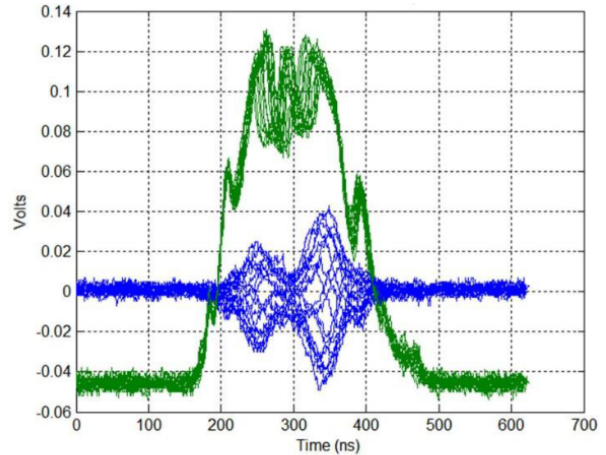


Figure 2: Sum (green) and delta (blue) vertical Beam Position Monitor (BPM) signals over several turns around 1 ms through the ISIS acceleration cycle. Courtesy Williamson et al [19]. A Headtail instability with 1 node is visible on the delta signal.

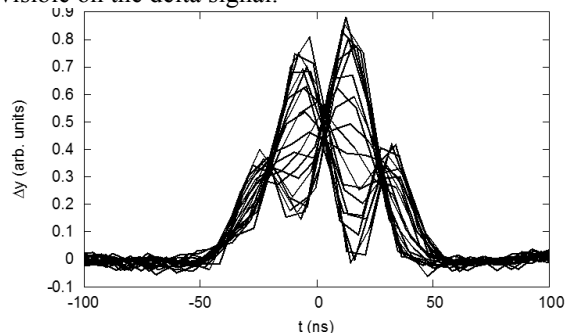


Figure 3: superimposed delta vertical BPM signals over several turns in SIS-18. Courtesy V. Kornilov [20]. A Headtail instability with 3 nodes is visible on the delta signal.

LHC: a testbed for beam instabilities

Since 2010, there has been many different types of beam instabilities observed in LHC (see Tab. 3). The evolution of beam parameters since 2010 (in particular of the bunch intensity, bunch spacing, number of bunches and beta function at the colliding points) as well as the mitigations put in place to avoid these instabilities and the improvement of diagnostics that allow catching more instabilities explain the staged occurrence of these instabilities.

Table 3: list of instabilities observed in LHC with their year of occurrence, plane, rise time and criticality for operation.

Instability type	Year observed	Longitudinal	Transverse	Rise time (for transverse instabilities)	Critical?
Single bunch loss of Landau damping instabilities	Since 2010	X			Not for LHC, but limits bunch length for HL-LHC
Longitudinal oscillations of colliding pairs	2016	X			No
Transverse loss of Landau damping	Since 2010 in various forms		X	1 to 10 s	Yes, requires high chromaticity, high octupole current, low linear coupling and large damper gain
Mode coupling instability with colliding beams	2012		X	~ 1 s	No
Electron cloud instabilities	Since 2011		X	~ 1 s	Yes for certain special beams
“16L2” instabilities	Since 2017		X	~ 0.1 s	Yes

Transverse Loss of Landau damping instabilities have been a concern since 2012, and have required increasing chromaticity, octupoles current, damper gain and damper bandwidth. A major breakthrough came in 2016 when linear coupling was identified as a critical machine parameter to keep under control along the LHC cycle to avoid Headtail instabilities [21] (see an example of such a Headtail instability in Fig. 4).

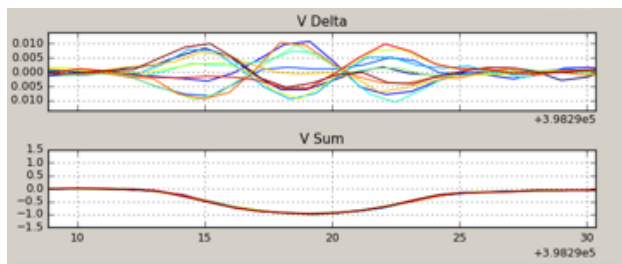


Figure 4: superimposed delta signals (top) and sum signals (bottom) from a vertical BPM (arbitrary units). Courtesy T. Levens. A Headtail instability with 2 nodes is visible on the delta signal.

The latter “16L2” instability has significantly affected the 2017 LHC run and is described in detail in [22]. It is believed that an accidental air inlet into the LHC beam vacuum with beam screen at 20 K has caused condensation and solidification of a significant amount of gas on the beam screen surface in and around the beam plug-in-

module [23]. The interaction of the LHC proton beam with flakes of these frozen gases is believed to lead to the following sequence of events [24, 25]:

- (1) Desorption of frozen nitrogen/oxygen flakes could be stimulated by electron multipacting.
- (2) The proton beam interacts with the flakes, generating a loss spike.
- (3) The flake undergoes phase transition to a gas and is ionized, generating a plasma of high density of electrons and ions in the beam path, both generating a very fast instability affecting mainly the tail of the LHC bunches (see Fig. 5).

Such fast instabilities were not observed before in LHC, and the complicated mechanism requires simulating the proton beam in presence of both electrons and ions.

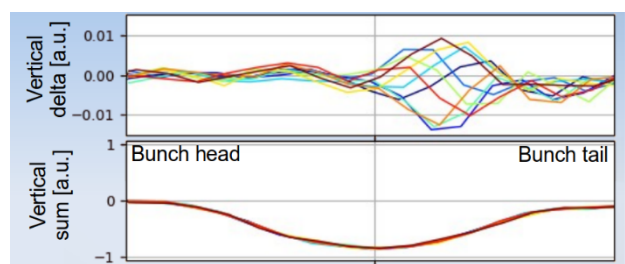


Figure 5: superimposed delta signals (top) and sum signals (bottom) from a vertical BPM (arbitrary units). Courtesy T. Levens and N. Biancacci. An instability with travelling wave pattern is visible on the delta signal and affects only the tail of the bunch.

LESSONS LEARNT FOR FUTURE HADRON MACHINES AND UPGRADES

Avoiding transverse feedback is not an option for high intensity operation and a combination with wideband feedback, octupoles, electron lens and/or RFQ should be investigated.

Proper control of chromaticity, amplitude detuning and linear coupling is crucial.

Electron-cloud suppression is critical and technical solutions include surface treatments that can have an impact on impedance contributions and therefore beam stability.

Impedance now drives major aspects of machine design, when we run at the limit of stability: beam screen aperture for the CERN FCC-hh project (Future Circular hadron Collider), collimator materials and gaps for HL-LHC, anti-electron cloud coatings, kicker shielding, below and pumping port shielding.

Finally, the experience of CERN PS, SPS and LHC shows that safe operation requires significant margins (e.g. factor of 2 for LHC) from predicted instability thresholds.

ACKNOWLEDGMENTS

This contribution owes all to the help and information provided by colleagues from the BE-ABP/HSC and BE-RF/BR sections as well as from the various labs present at the Benevento workshop.

REFERENCES

- [1] B. Zotter, "The transverse resistive wall instability in the ISR", CERN internal note, cern-isr-th-72-36, 18/09/1972 <http://cds.cern.ch/record/1255383/>
- [2] M. Migliorati, "Impedance and instabilities in lepton colliders", these proceedings.
- [3] A. W. Chao, "Physics of Collective Beams Instabilities in High Energy Accelerators", Wiley, 1993.
- [4] K.Y. Ng. "Physics of Intensity Dependent Beam Instabilities", World Scientific, 2006.
- [5] E. Métral, "Overview of Single-Beam Coherent Instabilities in Circular Accelerators", proceedings of the CARE workshop (2005).
- [6] J. L. Laclare, "Introduction to coherent instabilities : Coasting beam case", CAS course (1985)
- [7] J. L. Laclare, "Bunched beam coherent instabilities", CAS course (1985).
- [8] E. Métral and G. Rumolo, USPAS Course on Collective Effects, US Particle Accelerator School, June 2009. <http://uspas.fnal.gov/materials/09UNM/CollectiveEffects.html>
- [9] A. Sessler and V. Vaccaro, "Longitudinal instabilities of azimuthally uniform beams in circular vacuum chambers with walls of arbitrary electrical properties", CERN ISR Report 67-2 (1967).
- [10] H. Bartosik, these proceedings.
- [11] H. Damerau, these proceedings.
- [12] A. Lasheen, these proceedings
- [13] P. Kramer, these proceedings
- [14] S.Y. Lee, "Introduction to Linear Accelerators", in Accelerator Physics (P570) Lecture Notes, Indiana University, http://physics.indiana.edu/~shylee/p570/iu12/P570_04blina.c.pdf
- [15] S.Y. Lee, "Synchrotron tune", in Accelerator Physics (P570) Lecture Notes, Indiana University, http://physics.indiana.edu/~shylee/p570/iu12/P570_03.pdf
- [16] A. Oeftiger, these proceedings.
- [17] V. Vaccaro, these proceedings.
- [18] C. Vollinger, these proceedings.
- [19] V. Kornilov, private communication.
- [20] R.E. Williamson et al, "Simulations of the Head-tail Instability on the ISIS Synchrotron", Proceedings of HB2014, East-Lansing, MI, USA.
- [21] L. Carver, E. Métral et al, "Destabilising Effect of Linear Coupling in the LHC", proceedings of IPAC'2017, Copenhagen, Denmark.
- [22] B. Salvant *et al.*, "Experimental Characterisation of a Fast Instability Linked to Losses in the 16L2 Cryogenic Half-Cell in the CERN LHC", presented at IPAC'18, Vancouver, Canada.
- [23] J.M. Jimenez et al, "Observations, Analysis and Mitigation of Recurrent LHC Beam Dumps Caused by Fast Losses in Arc Half-Cell 16L2", presented at IPAC'18, Vancouver, Canada.
- [24] L. Grob and R. Schmidt, "Brainstorming on the 16L2 events", LHC Beam Operation Committee 82, 25.07.2017.
- [25] L. Mether, "16L2: Operation, observations and physics aspects", Proceedings of the LHC operation workshop 2017, Evian, 13/12/2017.

BEAM TRANSFER FUNCTION MEASUREMENTS AND TRANSVERSE STABILITY IN PRESENCE OF BEAM-BEAM*

C. Tambasco[†] J. Barranco, T. Pieloni, L. Rivkin, EPFL, Lausanne,
X. Buffat, E. Métral, CERN, Switzerland

Abstract

Instability thresholds are explored at the Large Hadron Collider (LHC) by means of the computation of the Landau Stability Diagram (SD). In the presence of diffusive mechanisms, caused by resonance excitations or noise, the SD can be reduced due to the modification of the particle distribution inside the beam. This effect can lead to a possible lack of Landau damping of the coherent modes previously damped by lying within the unperturbed SD area. The limitations derived from coherent instabilities in the LHC are crucial in view of future projects that aim to increase the performance of the LHC such as the High-Luminosity upgrade (HL-LHC) or Future Circular Collider (FCC). Simulation tools for the computation of the SD have been extended in order to take into account the incoherent effects from long particle tracking through the detailed model of the accelerator machine. The model includes among others beam-beam interactions and octupoles and the interplay between both is addressed. Finally the simulation results are compared to the Beam Transfer Function (BTF) measurements in the LHC.

INTRODUCTION

The beam coupling impedance drives the so-called head-tail instabilities [1] that are characterized by different modes of oscillations. Each mode is defined by a complex tune shift. The imaginary part is related with the rise time of the coherent instability and the real part with the coherent real tune shift. Coherent beam instabilities can be mitigated by chromaticity, transverse feedback and/or Landau damping. As long as the modes can be treated independently, the Landau damping is quantified by the dispersion integral for a given detuning $\omega_{x,y}(J_x, J_y)$ and particle distribution $\psi(J_x, J_y)$ as a function of the transverse actions J_x and J_y in each plane [2, 3]:

$$SD^{-1} = \frac{-1}{\Delta Q_{x,y}} = \int_0^\infty \int_0^\infty \frac{J_{x,y}}{\Omega - \omega_{x,y}(J_x, J_y)} \frac{d\psi}{dJ_{x,y}} dJ_x dJ_y, \quad (1)$$

where $\Delta Q_{x,y}$ are the complex tune shifts at the stability limit for each frequency Ω . The term $\omega_{x,y}(J_x, J_y)$ is the amplitude detuning (tune spread) generated by any non-linearities, including the beam-beam (BB) interaction during collisions. The dispersion integral is the inverse of the SD that defines the stability limit in the complex plane of the coherent tune

shifts. In order to be stabilized, the coherent impedance modes must lie inside the SD. In the LHC, the tune spread is mainly generated by the so-called Landau octupoles [3] and beam-beam interactions (long range and head-on) [4, 5] when in collision.

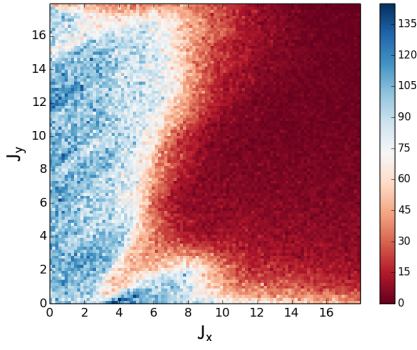
In case of diffusive mechanisms and/or reduced dynamic aperture with particle losses or redistributions, the shape of the SD may be modified by the particle distribution changes. Hence it is important to characterize the impact of the particle distribution on Landau damping that may differ from the one evaluated for a Gaussian particle distribution. Models have been extended to include the particle distribution changes during long term tracking by using the SixTrack code [6], in the presence of a realistic lattice configuration and excited resonances. The detuning with amplitude $\omega_{x,y}(J_x, J_y)$ in Eq. (1) is given by the tracking module of MAD-X [7, 8] for different machine configurations and optics. In 2015 a Beam Transfer Function (BTF) system was installed in the LHC in order to measure the Landau damping of the proton beams. The BTF is proportional to the dispersion integral (Eq. (1)) and it is sensitive to particle distribution changes. It is a direct measurement of the SD [9]. The impact of incoherent effects on the SDs are presented together with BTF measurements for various machine configurations and beam-beam interactions.

IMPACT OF INCOHERENT EFFECTS ON STABILITY DIAGRAMS

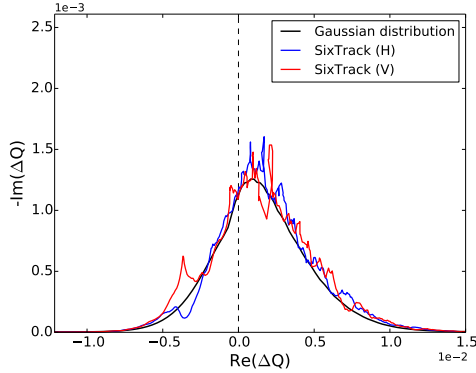
The term $d\psi/dJ_{x,y}$ in Eq. (1) is related to the particle distribution changes and may cause modifications of Landau damping w.r.t. the Gaussian distribution case. In order to take into account these effects, the models have been extended to compute the dispersion integral including the tracked particle distribution under the effects of a real lattice configuration by using the SixTrack code. At the first turn, a uniform distribution is generated, usually 10^6 particles, and tracked for 10^6 turns. The initial distribution is uniform between 0 to 6σ (in units of the rms beam size) in both planes, corresponding to 0-18 $J_{x,y}$ in terms of the (normalized) action variables. Before performing the integration, the re-distribution of the tracked particle distribution is weighted with a bi-dimensional exponential function. In the presence of strong machine non-linearities, particles may be subject to diffusion mechanisms due to excited resonances. SixTrack simulations have been performed for different octupole currents at the LHC injection energy (450 GeV) at collision tunes ($Q_x \sim 64.31$, $Q_y \sim 59.32$) for the normalized transverse beam emittance of $\epsilon = 2.0 \mu\text{m}$ in both planes. Figure 1 shows the tracked particle distribution for an octupole cur-

* Work supported by the Swiss State Secretary for Education, Research and Innovation SERI

[†] claudia.tambasco@cern.ch



(a) Tracked distribution with an octupole current of 35 A.



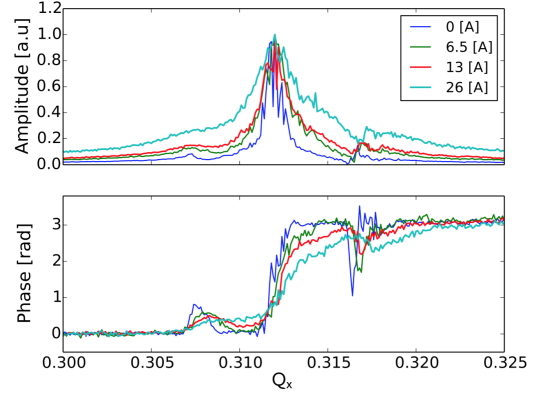
(b) Computed SD with an octupole current of 35 A.

Figure 1: Particle distribution from SixTrack tracking (a) at injection energy for the octupole current of 35 A and corresponding SDs (b). The color bar in the distribution plot represents the number of particles per bin.

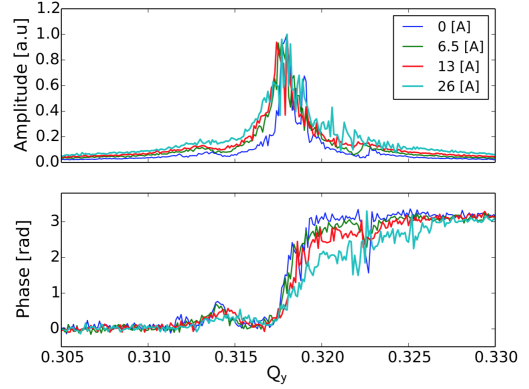
rent $I_{oct} = 35$ A (Fig. 1a) together with the corresponding SD (Fig. 1b). The solid black line is the computed SD for the Gaussian distribution case. The blue and the red lines represent the computed SD from tracked particle distribution, in the horizontal and the vertical plane, respectively. The SD increases as a function of the octupole current due to the larger tune spread in the beams. No important effects are visible for low octupole strength, while particle distribution changes are observed for an octupole current of 35 A (Fig. 1a) due to the excited resonances. In this case, a cut in the horizontal SD is visible on the side of the negative coherent tune shifts (the blue line in Fig. 1b).

BEAM TRANSFER FUNCTION MEASUREMENTS IN THE LHC

The installation of the BTF system in the LHC was justified by the frequent coherent instabilities observed at flat top energy in the LHC despite the fact that predictions indicate sufficient Landau damping of the coherent impedance modes [5, 10, 11]. From dedicated measurements, the observed instabilities seemed to be caused by the loss of transverse Landau damping. Therefore, the transverse BTF system was installed in the LHC in 2015 in collaboration with



(a) Horizontal plane.



(b) Vertical plane.

Figure 2: BTF measurements acquired for Beam 1 as a function of the octupole current.

the Beam Instrumentation team. During a BTF acquisition the chosen beam is safely excited, i. e. without causing losses or emittance blow up, at different betatron frequencies for a given number of turns. If the system is calibrated, the BTF gives a direct measurements of the SD, however, this is not the case for the LHC. Hence, in order to reconstruct the SD from BTF measurements, a fitting function is used [12]. The fitting function is parameterized as follows (assuming a reference case with linear detuning from the octupole magnets):

$$\begin{cases} \varphi(Q_{meas}) = \varphi [p_0 + p_1 \cdot (Q_{model} - Q_0)] \\ A(Q_{meas}) = p_2/p_1 \cdot A_{model}(Q_{model}). \end{cases} \quad (2)$$

The parameter p_0 gives the tune shifts w.r.t. the frequencies of the analytical detuning ($Q_{model} - Q_0$) with Q_0 the model bare tune. The parameter p_1 gives the measured tune spread w.r.t. the expected one. The tune spread factor is evaluated from the measured phase and it does not depend on the calibration factor. The model is the dispersion integral computed by using the PySSD code [4] that includes the tune spread evaluated from the tracking module of MAD-X. The factor p_2 gives the missing calibration factor of the amplitude response w.r.t. the reference case (A_{model}).

Measurements with single beam

Scans in octupole current have been performed at injection energy with collisions tunes ($Q_x \sim 64.31$, $Q_y \sim 59.32$).

A linear increase of the detuning with amplitude is expected as a function of the octupole current. The BTFs were acquired on the single bunch of Beam 1 in both planes for a current of 0 A, 6.5 A, 13 A and 26 A. The BTFs are shown in Fig. 2. By increasing the octupole strength, the phase slope decreases while the amplitude width increases. For the largest octupole strength (26 A) the larger tune spread is observed in the horizontal plane (Fig. 2a) w.r.t. the vertical plane (Fig. 2b). This was not expected since the detuning with amplitude due to the octupole magnets is symmetric in the two planes as shown in Fig. 3 for the current of 26 A. Figure 4 shows the measured tune spread factor as a function of the octupole current. The tune spread factor is obtained by applying the fitting function (Eq. (2)) w.r.t. the analytical case for the octupole current of 6.5 A. The horizontal plane is represented by the blue line while the vertical plane by the green line. The black line represents the expectations. A larger tune spread is measured in both planes w.r.t. expectations due to machine non-linearities at injection energy, consistently with optics measurements in 2015. The red shadow takes into account an error of $\pm 20\%$ for each case. As expected, the tune spread linearly increases as a function of the octupole current. In the vertical plane the linear behavior deviates for currents above 13 A, with a consequent reduction of the tune spread w.r.t. the horizontal plane. Particle losses were observed in the vertical plane related with the octupole current changes, as shown in Fig. 5, where Beam 1 losses are plotted at the primary collimators as a function of the octupole current (the dashed red line). In the presence of the transverse linear coupling, asymmetries in the tune spread are expected [13]. During the measurements the linear coupling was not corrected. The tune distribution in the presence of the linear coupling obtained by SixTrack tracking is shown in Fig. 6 where a cut in the vertical distribution is visible. The particle losses in the vertical plane due to a reduction of the dynamic aperture could explain the asymmetric behavior in the measured tune spread. The dynamic aperture of $\approx 3.5 \sigma$ was expected for a current of

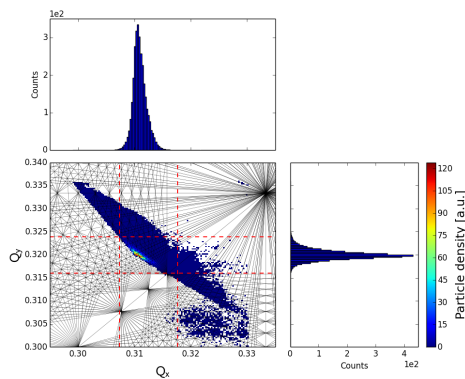


Figure 3: Two dimensional detuning up to 6σ particles obtained by SixTrack simulations for an octupole current of 26 A. The dashed red lines represent 3σ amplitude particles.

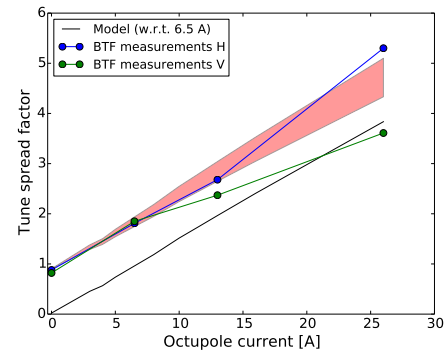


Figure 4: Measured tune spread factor in the horizontal plane (the blue line) and in the vertical plane (the green line) as a function of the octupole current. The black line represents the expectation. The red shadow takes into account an error of $\pm 20\%$ for each case.

26 A. In the presence of excited resonances and/or particle losses, increasing the tune spread inside the beams is not beneficial for Landau damping as demonstrated for the first time by BTF measurements in the LHC.

Measurements with beam-beam interactions

In order to measure the beam-beam long range contribution to Landau damping a crossing angle scan was performed at the end of the betatron squeeze. By reducing the crossing angle the separation of the beam-beam long range encounters reduces and their effects become stronger.

Measurements were acquired for positive octupole polarity, for which the tune spread from the long range beam-beam interactions adds up to the one given by the octupole magnets. Figure 7 shows the measured tune spread factor p_1 (Eq. (2)) as a function of the separation at the long range encounters w.r.t. the reference case of the nominal crossing angle ($370 \mu\text{rad}$). The black line represents expectations, and the blue line represents the measurements in the horizontal plane while the red line represents the measurements

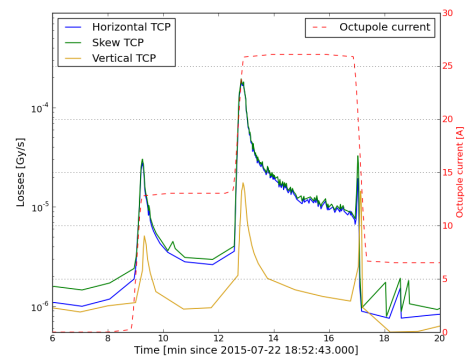


Figure 5: BLM losses at the primary collimators (vertical losses) as a function of the octupole current (the dashed red line).

in the vertical plane. An unexpected behavior was found w.r.t. models: a larger tune spread was measured in the horizontal plane while a smaller one in the vertical plane except for the last measurement at 9σ separation for which a strong dependency on the working point was observed. The red star represents the measured tune spread in the vertical plane with a reduced tune of $\Delta Q_y = -0.001$. In this condition, BTF measurements show an important reduction of the tune spread as visible in Fig. 8. The blue line is the vertical BTF amplitude response at the beginning of the tune scan, the green line corresponds to the tune reduction of $\Delta Q_y = -0.001$ and the red line corresponds to the tune increase of $\Delta Q_y = +0.001$ to the recovered initial tune. In this last case, the BTF response is fully recovered, showing that it is a reproducible effect. The tune spread reduction was not expected from the models unless the transverse linear coupling is introduced in the simulations. In the presence of linear coupling, an overall reduction is expected in both planes but with a more significant reduction in the vertical plane, for which particles towards the diagonal are lost,

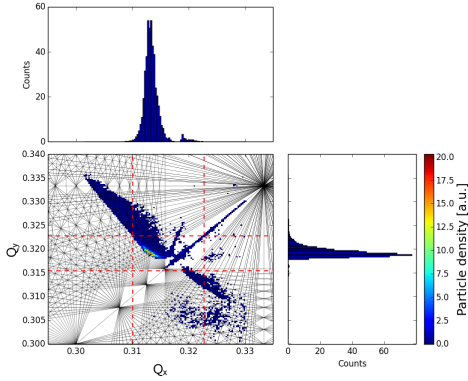


Figure 6: Two dimensional detuning up to 6σ particles obtained by SixTrack simulations for the octupole current of 26 A and in the presence of the linear coupling. The dashed red lines represent 3σ amplitude particles.

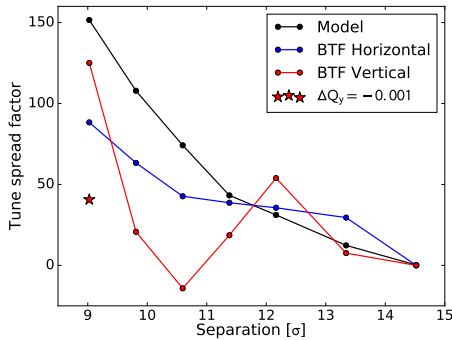


Figure 7: Measured tune spread factor as a function of the long range encounter separation at the IPs in units of the rms beam size. Measurements were acquired at the end of the betatron squeeze.

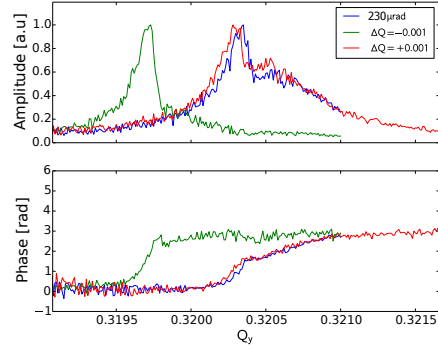
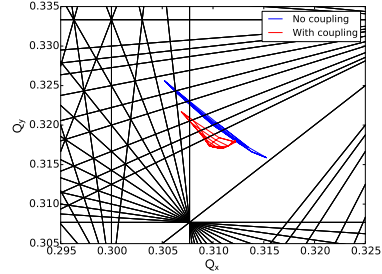
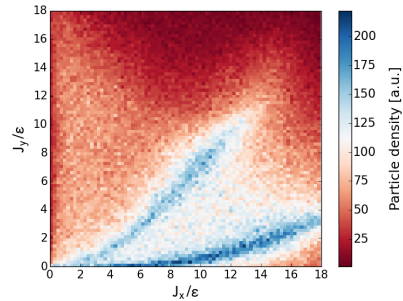


Figure 8: Vertical BTF response during the tune scan in the vertical plane. The blue line is the measured response at the beginning of the scan, the green line corresponds to the tune reduction of -0.001 and the red line are the measurements with the recovered initial tune value.



(a) Tune diagram up to 6σ particles.



(b) Tracked particle distribution.

Figure 9: Two dimensional tune diagram (a) in the presence of the transverse linear coupling (2012 configuration) and corresponding tracked particle distribution (b). The color bar in the distribution plot represents the number of particles per bin.

with a consequent cut in the tune footprint. An example of this effect is shown in Fig. 9 where the tune footprints (Fig. 9a) have been evaluated for the 2012 LHC configuration. During the 2012 run several coherent instabilities were observed at the end of the betatron squeeze. The long range beam-beam contribution was important due to the high beam intensity ($N_b = 1.6 \times 10^{11}$ p/bunch). The case without linear coupling corresponds to the blue color while the case with linear coupling corresponds to the red color. For this last case, as during BTF measurements, a negative

tune shift was also applied ($\Delta Q_y = -0.003$). The corresponding particle distribution obtained by SixTrack tracking is shown in Fig. 9b. The important deformation due to the linear coupling is visible in the tune footprint in red with a consequent reduction of the SD in the vertical plane as shown in Fig. 10 (the green line) where impedance modes are now at the edge of the stability. In the horizontal plane the increase of the SD is due to the clustering of the particle in the same direction that increases the contribution of the derivative $d\psi/dJ_{x,y}$ in the dispersion integral.

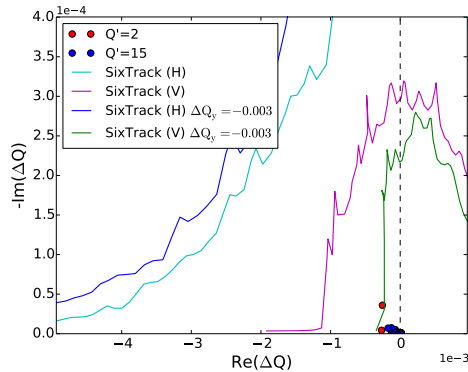


Figure 10: Stability diagrams at end of the betatron squeeze (2012 configuration) for positive octupole polarity and transverse linear coupling. The light blue line and the pink line represent the SD in the horizontal and vertical plane respectively with nominal tunes. The blue line and the green line represent the stability diagram in the horizontal and vertical plane, respectively, for a reduced tune in the vertical plane ($Q_y = 0.317$). The impedance coherent modes are included for a chromaticity of 2 units (red dots) and 10 units (blue dots).

CONCLUSION

The coherent stability not only depends on the tune spread in a beam but also on the particle distribution, as shown in Fig. 1 where the SD is deformed due to the particle distribution modification for a high octupole current of 35 A at injection energy (with collisions tunes). Beam Transfer Function measurements were acquired for different octupole strengths at injection energy. The results of these measurements showed the well reproducible tune spread in the horizontal plane and a much reduced tune spread in the vertical plane due to particle losses, as observed for the octupole currents above 13 A. The losses were due to the presence of the transverse linear coupling, that causes particle redistributions and reduces the dynamic aperture, expected to be less than 3.5σ . For the first time it was demonstrated by BTF measurements in the LHC, that a larger tune spread is not beneficial for Landau damping if diffusive mechanisms and/or particle distribution changes are present due to

a small dynamic aperture (less than 3.5σ). Measurements acquired at the end of the betatron squeeze for different crossing angles showed the unexpected asymmetric behavior in terms of tune spread and tune shifts between the horizontal and vertical plane. This can be reproduced by including the transverse linear coupling in the models that induces particle losses and redistributions. In this case, both the tune footprint and the stability diagram are modified. The sharp cut is visible in SD in the vertical plane (Fig. 10) due to the deformed tune footprint in the same direction (the red color in Fig. 9) while in the horizontal plane the clustering of the particle in this direction contributes increasing the SD due to the increase of the derivative $d\psi/dJ_{x,y}$ in the dispersion integral (Eq. (1)).

REFERENCES

- [1] G. Rumolo, Beam Instabilities, CAS - CERN Accelerator School: Advanced Accelerator Physics Course, Trondheim, Norway, 18 - 29 Aug 2013, pp.199-219 (CERN-2014-009)
- [2] J. Berg, F. Ruggero, "Landau Damping with two-dimensional betatron tune spread", CERN, Geneva, Switzerland, CERN-SL-96-071-AP, Dec. 1996.
- [3] J. Gareyte *et al.*, "Landau Damping, Dynamic Aperture and Octupoles in LHC", CERN, Geneva, Switzerland, LHC Project Report 91, Apr. 1997.
- [4] X. Buffat *et al.*, "Stability Diagrams of colliding beams", Phys. Rev. ST Accel. Beams 17 111002, 2014.
- [5] X. Buffat, Transverse beams stability studies at the Large Hadron collider, École Polytechnique Fédérale de Lausanne, CERN-THESIS-2014-246, September 2014
- [6] SixTrack, <http://sixtrack.web.cern.ch/SixTrack/>.
- [7] MAD-X, <http://mad.web.cern.ch/mad/>.
- [8] W. Herr, "Particle Tracking with MAD-X including LHC beam-beam interactions", CERN, Geneva, Switzerland, LHC Project Note 344.
- [9] J. Borer *et al.*, "Information from beam response to longitudinal and transverse excitation", IEEE Transactions of Nuclear Science, vol. NS-26 (3), June 1979.
- [10] T. Pieloni *et al.*, "Two beam effects", Proceedings of the 2014 Evian Workshop on LHC Beam Operation, CERN-ACC-2014-0319
- [11] N. Mounet *et al.*, "Impedance and instabilities", Proceedings of the 2014 Evian Workshop on LHC Beam Operation, CERN-ACC-2014-0319
- [12] C. Tambasco, Beam Transfer Function measurements and transverse beam stability studies for the Large Hadron Collider and its High Luminosity upgrad, École Polytechnique Fédérale de Lausanne, EPFL-THESIS-7867, August 2017
- [13] L.R. Carver *et al.*, "Destabilising effect of linear coupling in the LHC", THPAB040, Proceedings of IPAC 2017, Copenhagen, Denmark, 2017.

DESIGN OF LOW-IMPEDANCE DEVICES: THE NEW PROTON SYNCHROTRON BOOSTER ABSORBER SCRAPER (PSBAS)*

L. Teofili^{†,1,2}, I. Lamas, T. L. Rijoff, CERN, Geneva, Switzerland

M. Migliorati², University of Rome La Sapienza, Rome, Italy

¹ also at University of Rome La Sapienza, Rome, Italy; ² also at INFN, Rome, Italy

Abstract

At CERN the HL-LHC (High Luminosity Large Hadron Collider) and the LIU (LHC Injection Upgrade) projects call for an increase in beam parameters such as energy, intensity and brightness. To achieve this goal the whole accelerator complex will be upgraded. Systems, equipment and devices need to be redesigned and rebuilt accounting for the demanding new beam features. In this framework device impedance is a key parameter. It is essential to evaluate and to minimize the impedance of the component during its early design phase. This avoids beam instabilities and minimizes beam losses and induced heating. In this paper we outline general guidelines for a low-impedance design and we show how to implement them in a real case, taking as example the design of the new Proton Synchrotron Booster Absorber Scrapper (PSBAS). This is a key component aimed to remove the beam halo at the beginning of the LHC accelerator chain.

INTRODUCTION

During the coming years the CERN accelerator complex will be upgraded to improve its performance. An increase of the beam energy, intensity and brightness is foreseen in the framework of the projects LIU (LHC Injection Upgrade) [1] and HL-LHC (High Luminosity Large Hadron Collider) [2]. A large number of systems, equipment and devices will be redesigned taking into account the challenging new situation. Particularly, the raised intensity of the HL-LHC beams may lead to beam instabilities and high RF-heating. Thus, extra attention need to be given to electromagnetic and thermo-mechanical interactions between the beam and its surroundings. In this context, the electromagnetic beam-device coupling index, the device impedance, is becoming an increasingly important parameter. Its evaluation and minimization is essential during the device design phase to avoid beam instabilities and reduce beam losses and induced heating.

Geometrical features that lead to high impedance are well known by the impedance working community along with the way to cure them [3], [4]. However, little has been written on how to implement such curing methods on the design of real components. Such a task is far from being trivial since real components have to fulfill also other requirements as easy manufacturing and integration or size and cost constraints.

Thus, in the first part of this paper, we review the main geometric high impedance features most commonly encountered in device designs and the way to cure them. Subse-

quently, taking as an example the design of the new Proton Synchrotron Booster Absorber Scrapper (PSBAS), a key component aimed to remove the beam halo at the beginning of the LHC accelerator chain, we show how to apply these curing methods to realize the low impedance design of a real device.

METHODOLOGY

For the current investigation a careful analysis of the designs of various mechanical devices under development at CERN was carried out. It focused on the components directly exposed to the beam which are to be installed inside the synchrotrons, Proton Synchrotron Booster (PSB), Proton Synchrotron (PS), and Super Proton Synchrotron (SPS), or in the collider (LHC). For them impedance play a key role. Some of these devices, in their preliminary design, exhibited common geometric high-impedance features, well documented in literature [3], [4]. This could have potentially led to harmful consequences for the beam and for the device-itself. The high impedance geometric configurations were deeply investigated through numerical simulations with the aim of eliminating them or reducing their effects with simple and cost-effective modifications to the device design. They were considered individually and modelled in the CAD (computer aided design) tool of a Finite Integration Technique (FIT) software. Their basic geometrical quantity were considered as parameters in order to characterize the effects of their variation. In this work only the longitudinal impedance is discussed since, usually, solving it reduces also the transverse impedance. A careful analysis of the transverse impedance is left to future studies. The software used for simulations was CST Particle Studio[®] [5]; its time domain solver, Wakefield [6], is a well known and tested tool at CERN for device impedance computation [7], [8]. The knowledge acquired during these analysis was subsequently applied to enhance the impedance performances of the device with high impedance.

RESULTS: GENERAL GUIDELINES AND THE PSBAS CASE

In this section, initially, we present the three most common geometric high-impedance features found in most preliminary device designs. Their effects are analyzed and a possible simple and cost-effective design modification to eliminate them, or at least to reduce their detrimental impact, is proposed. Subsequently, as an example of real application of these curing modifications the design evolution of the PSBAS is presented.

* Work supported by LHC Injection Upgrade (LIU) project

[†] lorenzo.teofili@uniroma.it

Abrupt Changes of Section in Components

Abrupt changes of section were often recurring in the preliminary design of the analyzed devices. However, they should be avoided because they generate electromagnetic trapped modes (HOM) visible as well defined peaks in the impedance curve, (refer to Fig. 2).

In order to investigate abrupt changes of section effects, the geometry shown in Fig. 1 was simulated. The radius of the small pipe was considered fixed ($r_a = 5$ mm) while the radius of the larger pipe, r_b was parametrized. Compared to the case $r_a = r_b$, i.e. no section changes, for $r_b > r_a$ an increase in the impedance can be observed. In the case $r_b = 10$ mm no trapped modes are visible at the investigated frequencies, i.e. no peaks are present in Fig. 2. However, the same Fig. 2 shows that for $r_b \geq 35$ mm trapped modes start to appear, although the beneficial effects of the taper results in lower impedance peak values. This can be clearly seen comparing the results of the abrupt section change geometry (Fig. 2) with the ones of the tapered configuration (Fig. 4). Further, considering the r_b value which leads to the worst case scenario (i.e. the highest r_b considered) we investigated the effects of variation in the taper length. The result is shown with a dashed line in Fig. 4, revealing the beneficial effects of a longer taper which further decrease the peak impedance of the modes.

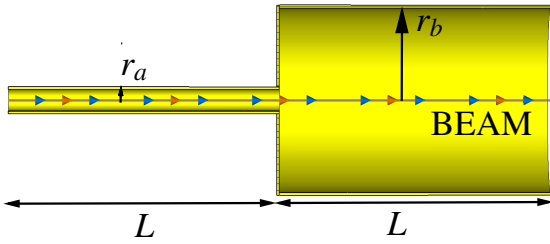


Figure 1: Abrupt section change geometry model: $r_a = 5$ mm, $L = 100$ mm, $r_b =$ parametrized.

An easy solution to the problem is tapering. To investigate its effects, the geometry of Fig. 1 was modified, adding a conical connection of length L_t between the two pipes as illustrated in Fig. 3. The radius of the small pipe, the length of the pipes and the length of the conical taper were considered

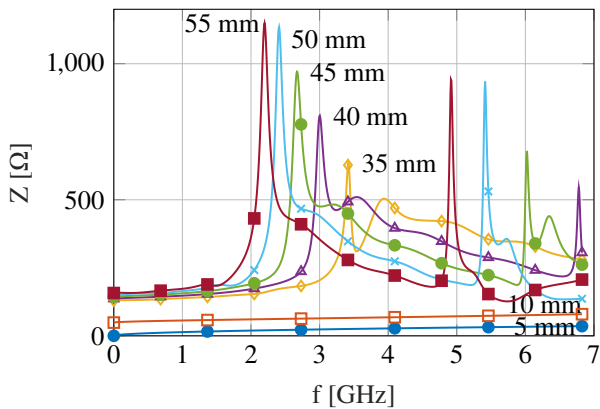


Figure 2: Abrupt section change configuration. Longitudinal impedance modulus computed for different values of r_b .

fixed ($r_a = 5$ mm, $L = 100$ mm, $L_t = 50$ mm) while the radius of the larger pipe, r_b was parametrized. The results of the simulations are reported in Fig. 4. In the case $r_b > r_a$ there is an impedance increase in comparison to the case $r_a = r_b$, i.e. no section changes. The non tapered configuration has the same qualitative behaviour. For $r_b = 10$ mm no trapped modes are visible at the investigated frequencies, in this case virtually no differences can be found between tapered and not tapered configurations. As for the configuration without taper (Fig. 2) for $r_b \geq 35$ mm trapped modes start to appear, although the beneficial effects of the taper results in lower impedance peak values. This can be clearly seen comparing the results of the abrupt section change geometry (Fig. 2) with the ones of the tapered configuration (Fig. 4). Further, considering the r_b value which leads to the worst case scenario (i.e. the highest r_b considered) we investigated the effects of variation in the taper length. The result is shown with a dashed line in Fig. 4, revealing the beneficial effects of a longer taper which further decrease the peak impedance of the modes.

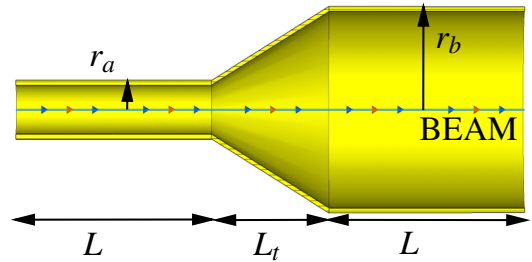


Figure 3: Tapered section change geometry model: $r_a = 5$ mm, $L = 100$ mm, $L_t = 50$ mm, $r_b =$ parametrized.

Gaps

Gaps and absence of electrical connections among components were another, quite common, high impedance feature found in the preliminary designs analyzed. Gaps should be avoided because they create capacitive effects leading to

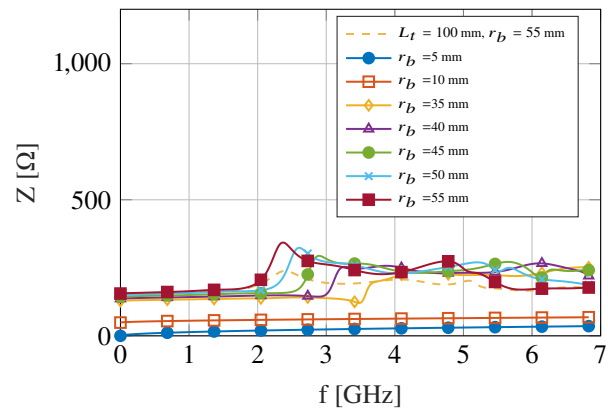


Figure 4: Tapered section change configuration. Longitudinal impedance modulus for different values of r_b .

high impedance values at low frequencies, which are very dangerous for RF heating [9]. In order to study their effects the geometry shown in Fig. 5 was simulated. The length and the radius of the pipes were considered fixed ($r = 5$ mm and $L = 100$ mm) while the gap between the pipes, g , was parametrized.

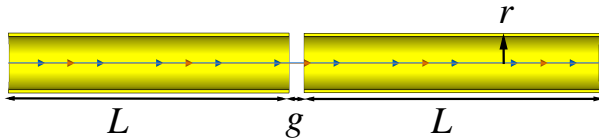


Figure 5: Open gap model geometry: $r = 5$ mm, $L = 100$ mm, $g =$ parametrized.

Impedance simulation results are reported in Fig. 6 for different values of g . The capacitive effects of the gap results in high impedance at very low frequencies. The impedance peaks values increase with the distance between the pipes. This is consistent with the results obtained in [4]. Other peaks at higher frequency can be seen from Fig. 6. According to [4], they map trapped modes in the gap.

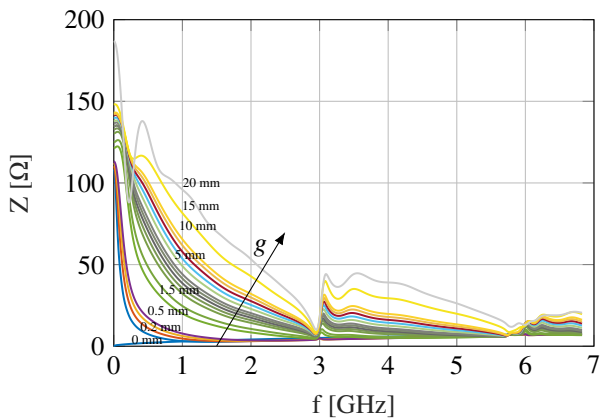


Figure 6: Open gap model geometry, longitudinal impedance modulus computed for different values of g .

The easy solution to the detrimental effects of a gap is the gap elimination by connections. Figure 7 shows the same geometrical layout of Fig. 5 with the addition of two symmetrical electrical connections between the two pipes. For simulations the length and the radius of the pipes were considered fixed ($r = 5$ mm and $L = 100$ mm) while the gap between the pipe, g , was parametrized. The obtained results, reported in Fig. 8, demonstrate the effectiveness of applying connections. Comparing the impedance of the open gap geometry, Fig. 6, with the impedance of the same geometry with connections, Fig. 8, one notices that impedance at very low frequencies is drastically reduced for all gap sizes when connections are added. However, in the connected geometry a new trapped mode is present, around 2 GHz. It was not found in the open gap configuration. No shown results demonstrate that it strongly depends on the contacts

shape and on the number of connection points. This resonant mode can be shifted to higher frequencies simply adding more connections. Impedance behaviour for frequencies higher than 3 GHz seems not to be affected by the connection. Comparing the results shown in Fig. 6 and Fig. 8 a similar trend can be observed in this range.

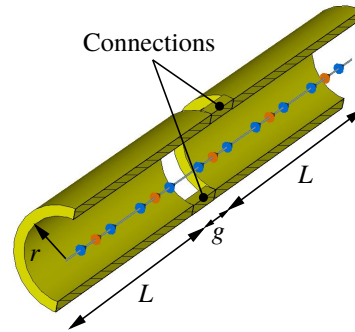


Figure 7: Gap with connections model geometry: $r = 5$ mm, $L = 100$ mm, $g =$ parametrized.

Parasitic Cavities

The last high impedance feature noticed during the design analysis was the presence of parasitic cavities. Every empty volume that is directly seen by the beam potentially behaves like a parasitic cavity, i.e. it extract energy from the beam in order to excite its resonant modes. This leads to really high peaks in the impedance curve of the device and it is very dangerous due to long range instability effects [10]. It is well recognized in literature that in the case of a cavity a key role is played by the wall material, particularly the electrical conductivity σ strongly influences the peak impedance of the mode. The cavity geometry shown in Fig. 9 was simulated considering different wall materials.

The impedance modulus of the mode that resonates at the lowest frequency is reported in Fig. 10, where only a small range of frequencies around the mode has been considered.

The most common way to solve this problem is the use of RF-shieldings. RF-shielding is a metal screen that blocks

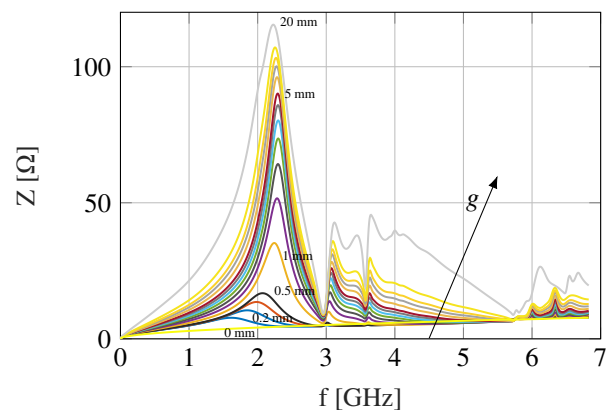


Figure 8: Gap with connection model geometry. Longitudinal impedance modulus for different values of g .

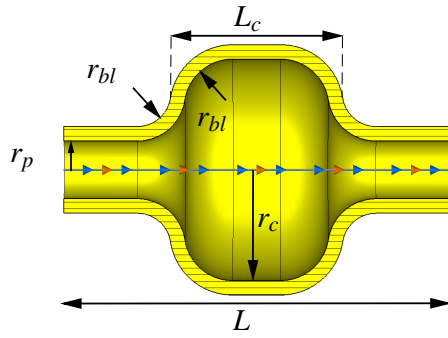


Figure 9: Unshielded cavity geometry: $r_p = 60$ mm, $L = 800$ mm, $r_{bl} = 100$ mm, $L_c = 300$ mm, $r_c = 230$ mm.

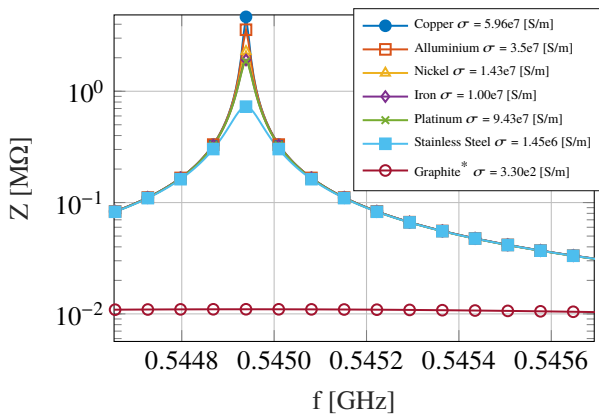


Figure 10: Unshielded cavity geometry. Longitudinal impedance computed for different values of the material electrical conductivity σ . Logarithmic scale.

electromagnetic interactions between the beam and the empty volume. The RF-shielding can have different shapes in order to better fit the geometry they have to shield. An example of shielding is proposed in Fig. 11, where the geometry of the previous parasitic cavity (refer to Fig. 9) has been modified adding ten metallic tubes on a circle connecting the inner pipe with the outer one.

The results of the electromagnetic simulations on the shielded cavity geometry (Fig. 12) show a striking impedance reduction of about 6 orders of magnitude if com-

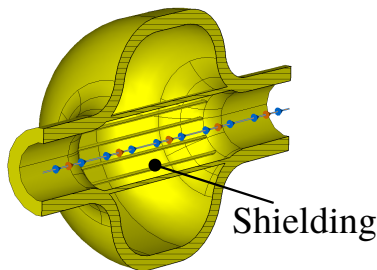


Figure 11: Shielded cavity geometry model.

pared with the results of the no-shielded configuration in Fig. 12 due to the fact that the resonant mode has disappeared.

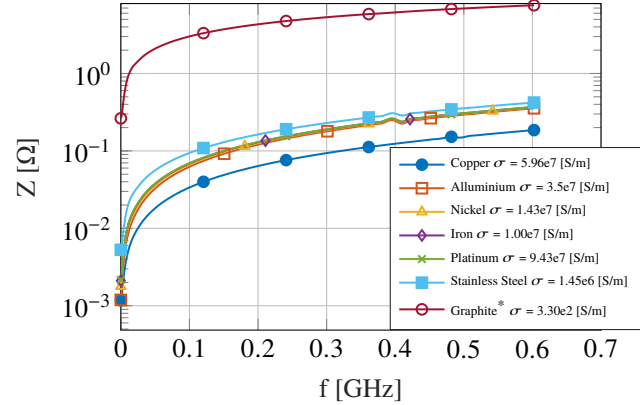


Figure 12: Shielded cavity geometry. Longitudinal impedance modulus computed for different values of the material electrical conductivity σ . Logarithmic scale.

The PSBAS case

As discussed previously, the outlined general guidelines need to be used in order to improve impedance performances in poor devices. In the following, as an example of their application, we summarize the evolution of the PSBAS design from the preliminary high impedance design to the final low impedance one.

The PSB scraper (refer to Fig. 13) is a device to be installed in the PSB at CERN. Its purpose is to clean the beam halo, at the very early stage of acceleration, absorbing it in two graphite blocks. Due to particular application needs, two working configurations were required: movable mask in and movable mask out, Fig. 13b. This led to the design of a movable central part.

The electromagnetic properties of the equipment were assessed through simulations with CST Particle Studio[®]. According to the simulation results, we iterated on the mechanical design applying the previously outlined low impedance design guidelines in order to obtain the final low impedance design. The high impedance characteristics of the PSBAS preliminary design are shown in Fig. 13c on the CST simulated model. In the preliminary PSBAS design, shown in Fig. 13a and 13b, impedance mitigation measurements were already taken: the replacement vacuum chamber was acting as a shielding against the vacuum tank, a potential parasitic cavity, preventing it from resonating. However, they were not sufficient and the impedance behaviour of the device was unacceptable. To allow an easy motion of the movable graphite mask, the latter was not electrically connected to the rest of the device along the beam path direction. Thus, gaps were presents in this design, leading to the generation of high order modes, trapped there. Moreover, such a design presents an unshielded empty volume around the fixed graphite mask. The discussed features generated trapped modes at frequencies lower than 0.4 GHz. The latter is considered as the acceptable lower limits for HOMs in the PSB machine [11].

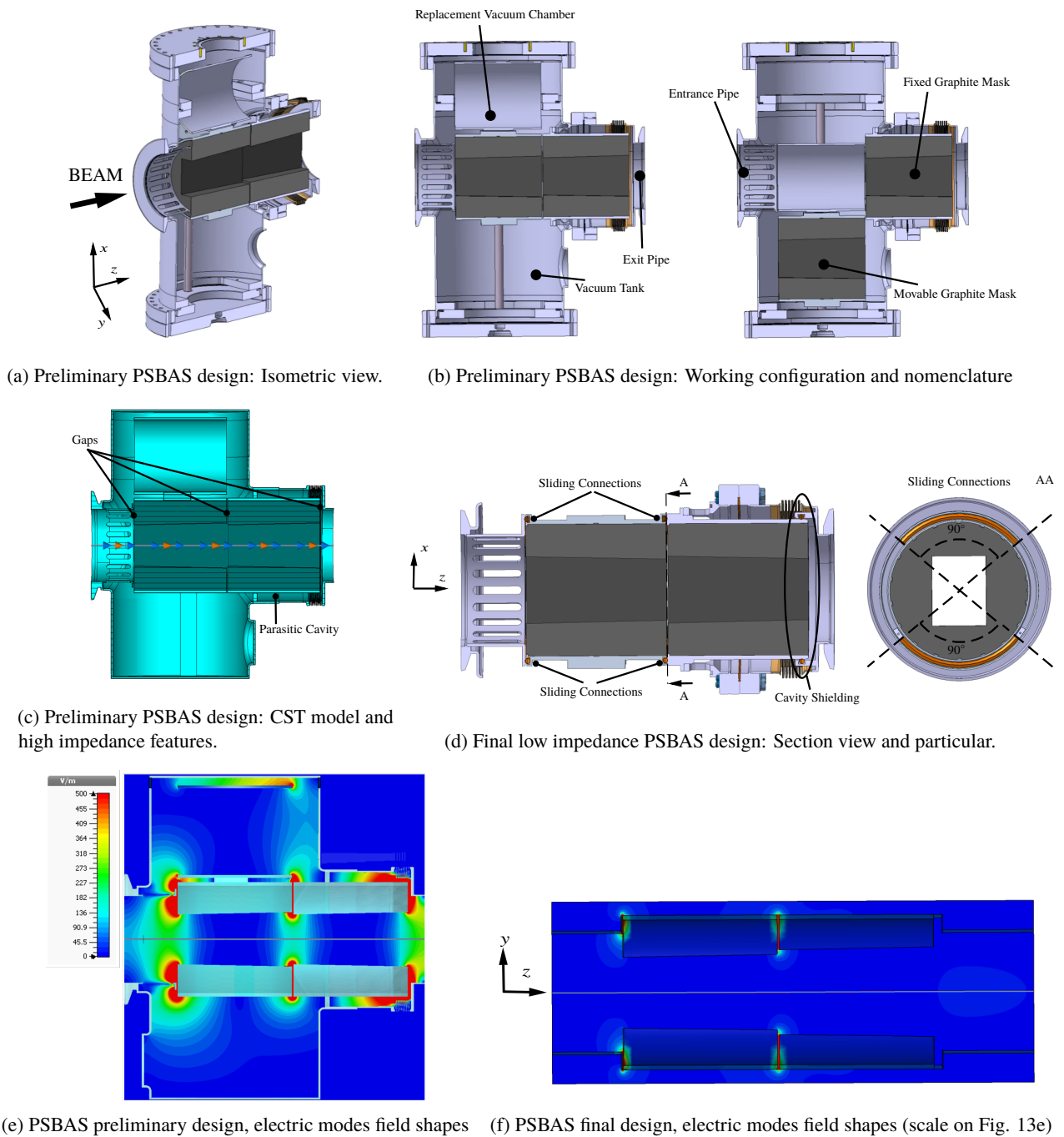


Figure 13: Different Geometries of the PSBAS: preliminary and final low impedance design

Therefore, the preliminary PSBAS design, with an HOM at 1.8 GHz, was not impedance compliant. The results of the electromagnetic simulations, electric modes field shapes and device impedance, are shown in Fig. 13e and 14.

The preliminary design was subsequently modified as shown in Fig. 13d:

- Electric sliding connections between movable and fixed parts were added to eliminate the gap effects.
- The parasitic cavity was shielded by a geometrical modification.

This led to an impedance compliant design, eliminating the modes at low frequencies and decreasing the impedance of the device of three orders of magnitude if compared with the previous performances. The results of the electromagnetic simulations, field shapes of the electric modes and device impedance, are shown in Fig. 13f and 14. Please note that in both the final and preliminary PSBAS design there are abrupt changes of section between the graphite masks and the pipes. No attenuation method was applied to reduce their effects because, due to operational and space

constraints, it was impossible to add taper. However, the contribution of the section changes is negligible.

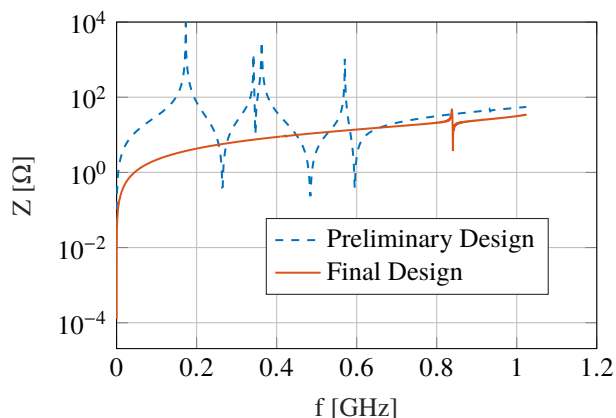


Figure 14: PSBAS final vs PSBAS preliminary design, Longitudinal Impedance Modulus. Logarithmic scale.

CONCLUSION

Prior work has documented the importance of reducing the impedance of accelerator devices and so of the whole machine [3], [8]. However, the majority of the previous studies focus on the impedance induced effects on the beam dynamics. They show geometric configurations that lead to a high impedance device and suggest cure methods, however, most of the time these approaches remain unapplied in a real case, thus ignoring limitations such as device component motion, space constraints, costs etc. In this paper, we reviewed the most common high impedance geometric features usually present in a preliminary device design and simple and cost-effective way of modifying geometries to obtain low impedance designs. Subsequently, we showed how to apply these methods to improve the impedance performance of a real, complex, device, the Proton Synchrotron Booster Absorber Scraper. We obtained a striking impedance reduction between the preliminary and the final design of almost three orders of magnitude with small increase in cost and complexity of the device itself. Therefore, this study indicates that, considering since the beginning not only mechanical and operational requirements, but also impedance requirements, it is possible to produce low impedance - cost effective components without affecting their main functionalities. This is a key approach for the conception of components for the LIU project and will be even more important for future hadron accelerators which are likely to have even higher intensity and lower emittance beams.

REFERENCES

- [1] J. Coupard *et al.*, “LHC Injectors Upgrade Projects at CERN”, in *Proc. 7th Int. Particle Accelerator Conf. (IPAC’16)*, Busan, Korea, May 2016, paper MOPOY059, pp. 992–995.
- [2] G. Apollinari, A. Bejar, O. Bruning, M. Lamont, L. Rossi, “High-Luminosity Large Hadron Collider (HL-LHC) : Preliminary Design Report”, CERN, Geneva, Switzerland, Rep. CERN-2015-005, Dec. 2015.
- [3] L. Palumbo, V. G. Vaccaro, “Wake Fields and Impedance”, in *Proc. CERN Accelerator School (CAS)*, Eger, Hungary, 1995, paper LNF-94/041 (P), pp. 331–390.
- [4] Y. Shobuda, Y. H. Chin and K. Takata, “Coupling impedances of a gap in vacuum chamber”, *Phys. Rev. ST Accel. Beams*, vol. 10, no. 4, p. 044403, Apr. 2007.
- [5] CST Studio Suite, <https://www.cst.com/products/csts2>
- [6] CST Studio Suite: Eigenmode Solver, <https://www.cst.com/products/cstmws/solvers/eigenmodesolver>
- [7] C. Zannini, “Electromagnetic Simulation of CERN accelerator Components and Experimental Applications”, Ph.D. thesis, Phys. Dept., Ecole Polytechnique, Lausanne, Switzerland, 2010.
- [8] B. Salvant, “Impedance model of the CERN SPS and aspects of LHC single-bunch stability”, Ph.D. thesis, Phys. Dept., Ecole Polytechnique, Lausanne, Switzerland, 2013.
- [9] M. Furman, H. Lee and B. Zotter, “Energy loss of bunched beams in RF cavities”, Lawrence Berkeley Laboratory, Berkeley, California, Rep. SSC-086, 1986.
- [10] K. Ng, *Physics of intensity dependent beam instabilities*: World Scientific, 2006.
- [11] Updated status of the PSB impedance model, https://indico.cern.ch/event/319950/contributions/740766/\attachments/616601/848489/PSB_impedance_model_update.pdf

THE BIRTH AND CHILDHOOD OF A COUPLE OF TWIN BROTHERS

V. G. Vaccaro, INFN Sezione di Napoli, Naples, Italy

Abstract

The context in which the concepts of Coupling Impedance and Universal Stability Charts were born is described in this paper. The conclusion is that the simultaneous appearance of these two concepts was unavoidable.

INTRODUCTION

At beginning of 40's, the interest around proton accelerators seemed to quickly wear out: they were no longer able to respond to the demand of increasing energy and intensity for new investigations on particle physics.

Providentially important breakthrough innovations were accomplished in accelerator science, which produced leaps forward in the performances of particle accelerators.

The first breakthrough: the Phase Stability

Based on the principles stated by Vladimir Veksler and Edwin McMillan a proton synchrotron was built at Brookhaven National Laboratory, named Cosmotron. Its construction started in 1948 and it reached its full energy in 1953. It was the first particle accelerator to break into the GeV wall, accelerating protons up to 3.3 GeV. Since Brookhaven's Cosmotron went into operation in the early 1950's, scientists quickly realised that achieving even higher energies was going to be difficult. Calculations showed that, using existing technology, building a proton accelerator 10 times more powerful than the 3.3 GeV Cosmotron would require 100 times as much steel.

The second Breakthrough: the Alternating Gradient

While the cosmotron shape was strictly toroidal and the magnetic field task was to guide and to focus the beam at the same time, a second breakthrough was performed: the strong focusing. Its principle, independently discovered by Nicholas Christofilos (1949) and Ernest Courant (1952), allowed the complete separation of the accelerator into the guiding magnets and focusing magnets, shaping the path into a round-cornered polygon and drastically reducing the transverse dimensions of the beam.

Without strong focusing, a machine as powerful as the Alternating Gradient Synchrotron (AGS) would have needed apertures (the gaps between the magnet poles) between 0.5 m and 1.5 m instead of apertures of less than 0.1 m. The construction of AGS was accomplished and shortly after the one of PS.

Looking Far

Even before the successful achievements of PS and AGS, the scientific community was aware that another step forward was needed. Indeed, the impact of particles against fixed targets is very inefficient from the point of view of the energy actually available: for new experiments, much more efficient could be the head on collisions between counter-rotating high-energy particles.

With increasing energy, the energy available in the Inertial Frame (IF) with fixed targets is incomparably smaller than in the head-on collision (HC). If we want the same energy in IF using fixed targets, one should build gigantic accelerators. In the fixed target case (FT), according to relativistic dynamics, an HC-equivalent beam should have the following energy.

$$E_{FT} = 2\gamma E_{HC}$$

The challenge was to produce intense and high-collimated beams and make them collide.

Two Forerunners: Wideroe and Touschek

Bruno Touschek was born in Vienna where he attended school. Because of racial reasons, he was not allowed to finish high school. However, he tried to continue his studies in a precarious way. After Anschluss (1938), he moved to Hamburg, where nobody knew of his origins. There he met Rolf Wideroe, with whom he started cooperating in building a betatron and discussing on Wideroe's visionary thoughts. Wideroe is variously credited with the invention the betatron, the linac, the synchrotron and storage rings for colliding beams, and, certainly, he built the first pair of linac drift tube for accelerators (Sessler and Wilson). Among others, Wideroe exposed his ideas about colliding beams. In the meanwhile, Touschek was discovered and arrested by the Gestapo in 1945. Wideroe was visiting him in prison, bringing cigarettes, food and, during these meetings, they continued to talk about the betatron and accelerators in general. Incidentally, in that context Touschek conceived the idea of radiation damping for electrons. When the Allied army reached Hamburg, Wideroe, suspected of collaboration, was arrested. The situation was reversed: Touschek started to pay visit to Wideroe. Sometime after, he was found not guilty and released. After war, Touschek roamed around Europe. Finally, in 1952 he decided to stay in Rome permanently, receiving the position of researcher at the National laboratories of the Istituto Nazionale di Fisica Nucleare in Frascati, near Rome.

THE COLLIDER AGE

Collider Contest: Frascati vs Princeton

The idea to build colliders attracted many accelerator scientists. A contest between Princeton and Frascati Laboratories started: both labs were developing collider programs. Princeton chose an eight-shaped structure: two circular rings in which electrons were circulating with the same orientation, meeting in one collision point. Frascati team, which took the field later, was even more audacious: they used a single ring with "counter-rotating" beams of electrons and positrons.

The enterprise began on March 7, 1960, when Bruno Touschek held a seminar at Frascati Laboratories. He was proposing to build an electron-positron storage ring. On March 14, a preliminary study demonstrated the feasibility of the proposal. The storage ring was named ADA (Anello Di Accumulazione = Storage Ring). Touschek pointed out the extreme scientific interest of high-energy collisions between particles and antiparticles, and the simplicity of realization of such an accelerator. The machine was conceived as a feasibility experiment to provide a sound basis for the realization of electron-positron colliders of larger centre of mass energy and luminosity. The total cost of the project (converted to the present purchasing power) was around 800.000 €.

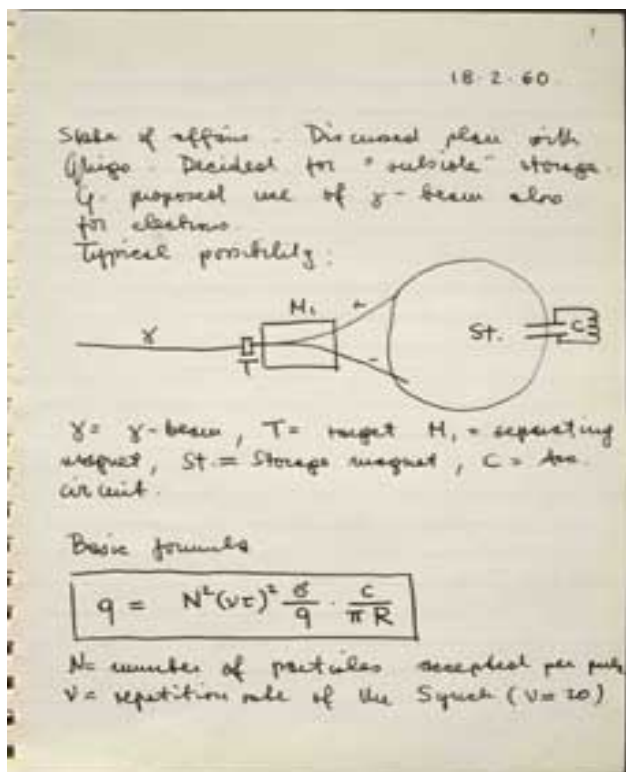


Figure 1: Sketch from Touschek notebook of e^-e^+ collider

ADA was brought to operation in February 1961. A first stored beam of few electrons was obtained at the end

of May 1961, using the Frascati Electron Synchrotron as an injector. On March 14, a preliminary study demonstrated the feasibility of the proposal. ADA then moved to LAL-Orsay, Paris, with a more powerful injector. Here, on February 1964 the first electron-positron collisions were detected. The success was encouraging for boost for the ISR (Intersecting Storage Ring at CERN) designers.



Figure 2: ADA collider at INFN Laboratori Nazionali di Frascati.

Clouds are appearing

The vast impact of ADA Collider opened a new chapter of accelerator physics: it was the first particle-antiparticle collider and the first electron-positron storage ring. In addition to this grand accomplishment, the machine was also able to prove the idea that one could accelerate and make beams of particles and antiparticles collide in the same machine.

Many laboratories started programs to accelerate and store particles in order to prove the feasibility of intense beams. The most important one was the Intersecting Storage Ring at CERN. Surprisingly enough, a longitudinal instability below transition energy was discovered in 1963 in the MURA 40 MeV electron accelerator. At the same time the observation of vertical instabilities took place in the MURA 50 MeV [1]. At that time, it was a common place that above transition energy, a beam could be unstable: since it was postulated that the prevalent electromagnetic (EM) interaction with the vacuum pipe was capacitive, as we would define it nowadays with the

present lexicon. Furthermore, it was not known that there could exist some stabilizing mechanism.

The Analysis of Instabilities. A Step Forward.

An interpretation of the phenomenon was given by two companion papers [2,3] appeared in 1965 on the Review of Scientific Instruments, one concerning longitudinal coherent instability and the second one transverse coherent instability.

The novelty was the use of Vlasov equation where it is assumed that the beam particles have an energy distribution function. The problem is solved by means of perturbative techniques that lead to a dispersion relation. The role of Landau damping of the instability coming from the energy spread was emphasized. The pipe is supposed circular, smooth, and lossy and with circular or rectangular cross section. In both papers it examined the case of absence of frequency spread and it was found that the rise-time depends on the conductivity of the pipe. However, allowing for a finite spread, the stability criteria obtained from the dispersion relation do not involve the pipe losses. It is worth of note that the stability criteria were derived assuming Gaussian or Lorentzian distribution functions. The stream of research born in 1965 and still lasting gave and gives results that have fundamental importance for particle accelerator.

An Intermezzo for Pedestrians

The phenomenon of beam instabilities in circular accelerator can be understood resorting to pictorial representation of Fig. 3. This follows the explanation that I gave to myself when I first tackled the beam instability problem.

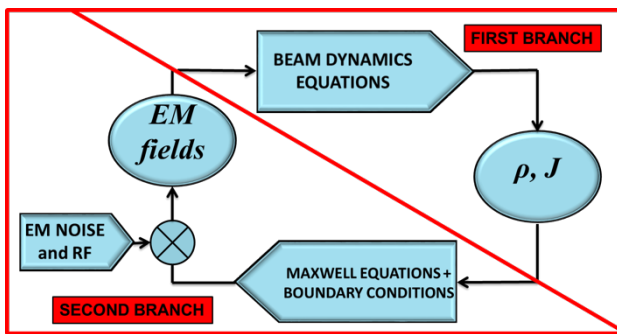


Figure 3: Block diagram of the coupling between EM equations and dynamics equation.

Like many modulational instabilities, the present one is triggered by the electric field noise. Let us take a frequency component $\Delta E_N(\omega) = \Delta E_N \exp(j\omega t)$. This component will act as the initial input of the beam dynamics equation. The field noise $\Delta E_N(\omega)$ acting on the charged particles introduces a small modulation on the beam cur-

rent having the same frequency as the noise; at the same time, the interaction of the perturbed current with the surrounding medium produces an additional electric field. This process is continuous, but one may represent it step-wise, turn-by-turn. Let us introduce integrated values over one turn

$$\Delta V_N(\omega) = \langle 2\pi R \Delta E_N(\omega) \rangle$$

defined as input voltage. One may define the transfer function (input-output) $Y_D(\omega)$ in the frequency domain for the beam dynamics branch; this quantity relates the perturbed current to the voltage $\Delta V_N(\omega)$. Therefore, the perturbed current in the beam will be represented as:

$$\Delta I_1(\omega) = Y_D(\omega) \Delta V_N(\omega)$$

Then, the perturbed current, acting as input to Maxwell's equations (namely interacting with the surrounding medium via electromagnetic fields), will produce after one turn a perturbed electric field $\Delta E_1(\omega)$. Similarly, by taking $\Delta V_1(\omega) = \langle 2\pi R \Delta E_1(\omega) \rangle$, one may define $Z_{EM}(\omega)$ for the electromagnetic branch

$$\Delta V_1(\omega) = Z_{EM}(\omega) \Delta I_1(\omega)$$

Allowing for the second turn, the **total** perturbed current will be the sum of the new one and the perturbed previous current. The latter is affected by a factor $\alpha(\omega)$, in modulus smaller than one, which takes into account its damping over one turn:

$$\begin{aligned} \Delta I_2(\omega) &= \alpha(\omega) \Delta I_1(\omega) + Y_D(\omega) Z_{EM}(\omega) \Delta I_1(\omega) \\ &= \{ \alpha(\omega) + Y_D(\omega) Z_{EM}(\omega) \} \Delta I_1(\omega) \end{aligned}$$

The quantity α comes from a realistic picture of the phenomenon. In general, the particles exhibit a spread in their velocities. Therefore, any unevenness in the beam tends to dissolve over time.

After n turns:

$$\Delta I_n(\omega) = \{ \alpha(\omega) + Y_D(\omega) Z_{EM}(\omega) \}^n \Delta I_1(\omega) \quad (1)$$

It is apparent that the perturbed current has only two possibilities: it may diverge (instability) or converge (stability) to zero. It will certainly diverge if there is no damping ($\alpha = 1$). In all the other cases, the beam is conditionally stable. We may infer some general features of the phenomenon:

- The perturbed current is proportional not only to the perturbing field but also to the unperturbed current, namely $Y_D(\omega) \propto I_0$.
- The perturbed current is inversely proportional to the relativistic mass of the charged particle, namely $Y_D(\omega) \propto 1/\gamma m_0$.

The above analysis is only qualitative since it cannot predict under what conditions the beam will be stable or not. However, it indicates that the coupling between the EM beam interaction with the surrounding medium and the beam dynamics must be formulated in a self-consistent way.

As a conclusion, the problem will lead to two concepts: Coupling Impedance and Stability Diagrams.

An Impedance is in the Air. The First Twin is brought to Light

When I was hired by CERN on June 1966, I joined the RF group of the Intersecting Storage Ring (ISR) Department. ISR was under construction and was destined to be the world's first hadron collider. It ran from 1971 to 1984, with a maximum centre of mass energy of 62 GeV. At that time at CERN, there was big concern about stability of the beams because of large number and various kind of lumped equipment (300 pairs of clearing electrodes, pickups, cavities etc.), which could be "seen" by the beam. Unfortunately, the stability criteria did not apply to the situation of ISR. I was committed to work on this problem. The task was to introduce in the dispersion relation the contribution of a lumped element, e.g. cavity of impedance Z_c (eventually clearing electrodes, too)

$$I_i = \text{const} \langle 2\pi R E_\theta \rangle \int \frac{d\psi_0(W)}{dW} \frac{dW}{[\omega - n\omega_0(W)]} \quad (2)$$

where I_i is the incipient perturbed current in the beam, ω the frequency of the instability, ω_0 is the revolution frequency, $\psi_0(W)$ is the energy dispersion function.

The procedure is described in Ref. [4]. The impressed voltage at the cavity gaps V_i is calculated assuming that the image current that loads the cavity is equal to the perturbed beam current I_i . The field distribution in the accelerator is expanded in travelling waves inside the pipe. Then, only the n-th harmonic is retained which is riding with the perturbation. Therefore, the mean integral in the above equation may be written as

$$\langle 2\pi R E_\theta \rangle = -Z_c I_i \quad (3)$$

The concept of coupling impedance was later extended to a pipe with uniform properties. Of course, the above procedure consisted in a brute force approach. Its validity is restricted to wavelengths much larger than the cavity gap and of the pipe radius; however, this limitation does not affect the principle. It only needed a self-consistent formulation of the EM problem for the lower branch of Fig. 3. Fifty years have passed since. In the meantime, exact approaches were performed resorting to

numerical codes or to analytical-numerical techniques such as the mode matching.

Few months after my arrival, Andy Sessler (2012 Fermi award), on leave of absence from LBL, joined the ISR-RF group. At that time CERN was a crossroads of the most prominent accelerator scientists. I was lucky enough to meet Ernest Courant (1986 Fermi award), Claudio Pellegrini (2014 Fermi award), with whom I was co-author of a paper on wake fields, Fernando Amman (director of Laboratori di Frascati and ADA project), John Lawson, AN Skrinsky (Director of Institute of Nuclear Physics of Novosibirsk), who were all paying visits at CERN for discussions on ISR design. I was committed to Sessler and I showed him the manuscript of my results. He reviewed it, making corrections, suggesting integrations and then he stated that the report had to appear with my name only. However, the paper was issued in closed distribution restricted to AR and ISR Scientific Staff.

REFERENCES

- 1) V.K. Neil and A.M. Sessler
Longitudinal Resistive Instabilities of Intense Coasting Beams in Particle Accelerator
Rev. Sci. Instr. 36, 429 (1965)
 - 1) A.M. Sessler and V.G. Vaccaro
Longitudinal Instabilities of Azimuthally Uniform Beams in Circular Vacuum Chambers of Arbitrary Electrical Properties (in preparation).
- Distribution: (closed) AR and ISR Scientific Staff.

Figure 4: Last page of Ref. [4].

At the same time, he proposed a general treatment of impedance of arbitrary electrical properties [5]. However, none of us gave importance to this concept. We rather underlined that the concept of coupling impedance is a handy concept. This is very well illustrated by Sessler in one of his papers [6]: "It was emphasized — and, it was the main point of [5] -- that Z described the impedance of the wall elements and as, thus, amenable to computation--or measurement--by means of all the standard techniques employed in electrical engineering. —OMISSIS— This engineering technique was applied to a number of problems--such as helical conducting walls [7] and allowed complicated structures to be readily analysed. For example, the impedances presented in Section 1.5 of this paper may be employed to study the azimuthal stability of beams interacting with various elements such as pickup electrodes." Probably this feature was one of the factors that determined the success of the beam coupling impedance concept.

The Second Twin. The Universal Stability Charts

The introduction of the beam coupling impedance concept is tightly linked to the analysis of the dispersion relation. The first step was done: a simplification in the analysis of complicated structures (transfer function of the lower branch in Fig. 3). The second step was devoted to make an analogous simplification in manipulating the transfer function of the upper branch and is already indicated in the same paper of the first step in Ref. [4]. The success of the first one influenced the advancement of the second one. Except special cases, Eq. 2 cannot be solved analytically; namely, given the impedance, the distribution function, the harmonic number n and the function $\omega_0(W)$ it is not in general possible to find analytically for any distribution function the frequency ω of the instability, if any.

It is worth of note that in Eq. 18 in Ref. [4] (see Fig. 5) it is apparent the drift toward a new formulation but the drift is not yet accomplished. There is a reactive impedance (X/n) of the lumped element, but it is not so for the space charge; the impedance is expressed in cgs [cm/sec]; there is the classical proton radius: all aspects that nowadays are superseded. Furthermore, the stability inequality comes from the solution of the dispersion relation with a Lorentzian distribution function. As shown in Fig. 7, for a Lorentzian distribution function, this is possible and a parabola delimits the stability region.

$$\frac{X}{n} \leq \frac{1}{f} \left\{ -\frac{\gamma^{-2}}{R} \left[1 + 2 \ln \frac{b}{a} \right] + \frac{1}{r_p} \frac{\pi}{2N} \left[\gamma^{-2} - \gamma^{-2} \right] \gamma \beta^2 \left(\frac{\Delta p}{p} \right)^2 \right\}$$

where r_p is the proton classical radius and f the circulation frequency of the particles.

Figure 5: Eq. (18) in Ref. [4].

I felt that such a large stability region could be unphysical. An indicator of this issue is the divergence of its second order momentum. Therefore, I was intrigued on what could happen with a truncated cosine distribution. The solution of the dispersion relation was facilitated because I had to perform the integration on the imaginary axis. I had tackled the problem of the normalization of the spread in order to make a reasonable confrontation with the Lorentzian distribution.

the inequality (18) becomes, if $v \ll U$

$$\frac{X}{n} \leq \left\{ \frac{C_f}{r_p} - \frac{\pi}{2N} \left[\gamma^{-2} - \gamma^{-2} \right] \gamma \beta^2 \left(\frac{\Delta p}{p} \right)^2 - \frac{\gamma^{-2}}{R} \left[1 + 2 \ln \frac{b}{a} \right] \right\} \frac{1}{f}$$

where C_f has the value

$$C_f = \frac{4}{\pi} S_i \left[\frac{\pi}{2} \right] \approx 0.29$$

Figure 6: Eq. (19) in Ref. [4]

The results are reported in Fig. 8. The absence of long tails and the finiteness of the second order momentum drastically reduce the stability margin. I asked Sessler what he thought of this finding. He said: "Go on!".

Later on, the complete stability was calculated and I remarked that it was including a finite region of the impedance plane. One may notice that the formula of Fig. 6 is written with the classical radius r_p and that the impedance is still measured in cgs system dimensions. Nowadays, accelerator scientists would be horrified!

As a conclusion, I would like to stress that the two brothers are real twins. Maybe the second one had a slower growth. They are actually Siamese twins, because the existence of one is the reason of existence of the other.

I did not continue my studies because there was no interest on the subject. Afterwards, I knew that my contract would not be renewed. Therefore, I felt free to work on the subject that was sleeping since many months. A collaboration with Alessandro Ruggiero was set up, which tackled the problem by another point of view: find the coupling impedance for a given value of the complex frequency ω , assuming a linear dependence of ω_0 on W . The results are represented in Fig. 7 where the curves at constant rise-time, i.e. with a constant frequency shift, are drawn. The procedure was repeated for various distribution functions [2]. Therefore, we had to perform analytically the integral assigning the same distribution used in Ref. [8] and some others, that could seem reasonable:

$$Z(\omega) = - \frac{1}{const \int \frac{d\psi_0}{dW} \frac{dW}{[\omega - n\omega_0(W)]}}$$

This is just a conformal mapping of the complex variable ω into the complex variable Z . The interest is to explore the region where the imaginary part of ω is negative, namely where the oscillation is exponentially increasing. A particular interest was devoted to the mapping of the lines where the frequency is real with a vanishing imaginary part, namely

$$\omega = \omega_r + j_0$$

This procedure gave quite surprising results:

- The mapping of the lower, half plane covers almost entirely the Z plane.
- The mapping of the upper half plane covers the same region Z plane.
- There is a "neutral region" which is covered by none of the two mappings and is defined as the stable region
- The stable region is finite if the tails of the distribution function have a finite area.
- The stable region of a mono-energetic distribution (infinitesimal tails) is the positive imaginary axis.

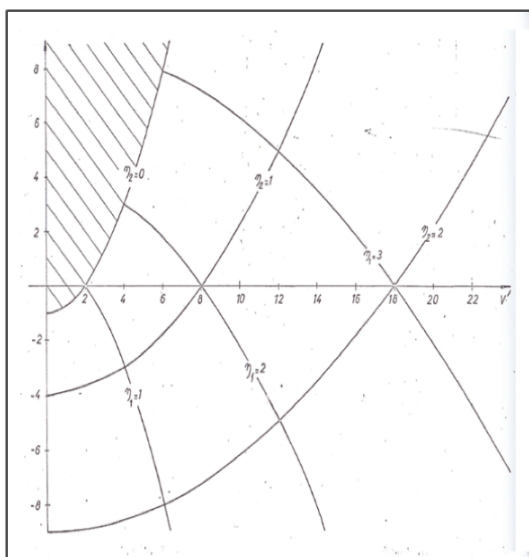


Figure 7: Longitudinal stability chart for Lorentzian distribution function with curves at constant rise-time and frequency shift

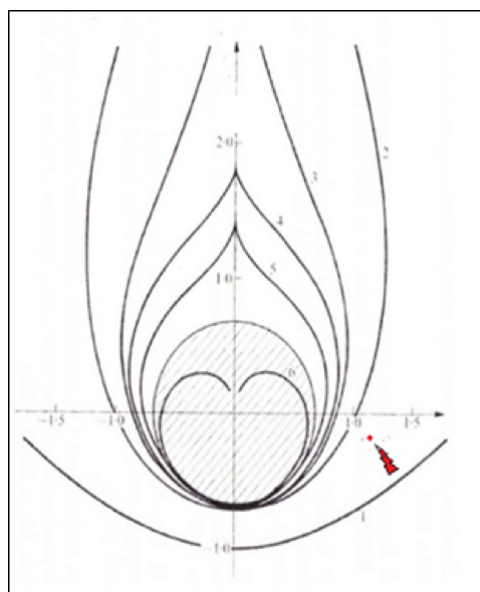


Figure 8: Stability boundaries for various distributions functions

Fig. 7 reports the result of the mapping for a Lorentzian distribution function, the same one adopted in Ref [2,3]. The impedance is normalized in such a way to get a universal stability diagram. The dashed domain is the stability region, the contour of which is a parabola. It is apparent that the stable domain is infinite. The coupling Impedance of smooth pipe has small real part due to the pipe resistivity and a large positive imaginary (normalized) part, from the diagram of Fig. 2 one could infer that the beam should be stable, that was the same conclusion

inferred by the authors. Other distribution functions were taken. The results are reported in Fig. 8 where the stability boundaries are drawn:

- 1- Lorentzian
- 2- Gaussian
- 3- 4th order Parabola. $\psi = (1 + x^2)^4$
- 4- 3rd order Parabola. $\psi = (1 + x^2)^3$
- 5- 2nd order Parabola. $\psi = (1 + x^2)^2$
- 6- Truncated cosine region.

According to the available data, the working point of MURA accelerator is very close to the imaginary axis and has a very large imaginary component. This is represented in red in Fig. 8. This means that, the detected instability is compatible the results obtained from the Vlasov equation, provided that one takes a realistic distribution function. That was an excellent result confirming that correctness of the Vlasov equation approach.

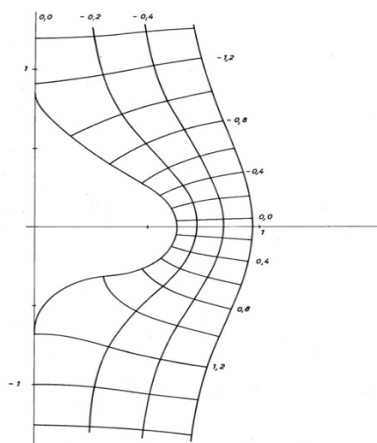


Figure 9: Transverse stability chart with curves at constant rise-time and frequency shift.

Then, when the picture of the longitudinal instability phenomenon was clear, the problem of transverse instability was tackled. The successful aftermaths stimulated the extension of the research on transverse instabilities. An example is reported in Fig. 9, in this case it is taken into account not only the frequency spread but also the distribution functions of the betatron amplitude oscillation.

This year the Coupling impedance and universal stability charts turn fifty-two, but they do not show it.

REFERENCES

- [1] C.P. Curtis et al., Proc. of the International Conference on High Energy Accelerators (Atomizdat, Moscow, 19639)
- [2] V.K. Neil and A.M. Sessler, Rev. Sci. Instr. 36,429 (1964)
- [3] L.J. Laslett, V.K. Neil, and A.M.Sessler, Rev. Sci. Instr. 36,436 (1964)

THE BIRTH AND CHILDHOOD OF A COUPLE OF TWIN BROTHERS

- [4] V.G. Vaccaro, Longitudinal Stability of an Intense Coasting Beam in a Circular Accelerator CERN, ISR-RF/66-35, 1966
- [5] A.M. Sessler, V. G. Vaccaro, Longitudinal Instabilities of Azimuthally Uniform Beams in Circular Vacuum Chambers with Walls of Arbitrary Electrical Properties. CERN-Report ISR-RF 67-2 (1967)
- [6] A.M. Sessler, Beam-Surrounding Interaction and the Stability of Relativistic Particle Beam, PAC1971-1039
- [7] A.M. Sessler Passive Compensation of Longitudinal Space Charge Effects in Circular Accelerators: the Helical Insert. CERN-Report ISR-RF 68-1 (1968)
- [8] A.G. Ruggiero, V. G. Vaccaro, Solution of the Dispersion Relation for Longitudinal Stability of an Intense Coasting Beam in a Circular Accelerator. CERN-Report ISR-TH 68-33 (1968).

NEEDS AND SOLUTIONS FOR MACHINE IMPEDANCE REDUCTION

C. Vollinger*, A. Farricker, T. Kaltenbacher, P. Kramer, B. Popovic
CERN, Geneva, Switzerland

Abstract

Particle beams with highest possible beam intensities are requested nowadays, hence in modern circular accelerators, the consideration of beam coupling impedance issues is of increasing relevance. Classical sources of beam coupling impedance are RF-systems, injection and extraction kickers, but also beam diagnostic elements such as wire scanners where the object itself forms an undesired cavity, and beam pipe transitions, namely tapers or steps. Optimally, for any machine, impedance mitigation shall take place already during the design phase. However, for older existing machines, often considerable hardware changes would be required to obtain a significant impedance reduction. In these cases, the required geometry changes for reducing beam coupling impedance are costly to be carried out, hence retro-fitted solutions such as impedance shields or damping mechanisms are required.

For both approaches, different impedance mitigation strategies are available and their selection also depends on the needs, i.e., the type of problem that is arising. Single bunch instabilities, for example, require an optimization of the object geometry with the goal to reduce R/Q, whereas multi bunch instabilities or heating will ask for different measures. In this presentation, we will explain about typical sources of beam coupling impedances and how they could be circumvented. Possibilities to reduce beam coupling impedance in existing machine elements are included and applied solutions, such as impedance shields or HOM dampers will be presented as well.

INTRODUCTION

The desired operational beam intensity at flat top for the CERN Super Proton Synchrotron (SPS) as injector for high luminosity LHC (HL-LHC) runs is 2.4×10^{11} ppb for a bunch length $\tau = 1.65$ ns and 25 ns spacing [1]. These intensities can be reached only if the interaction of the particle beams with the surrounding structure is known, at least approximately, i.e., a good description of machine elements is required. Known impedance sources are distinguished between machine elements with potentially large individual contribution as, e.g. accelerating cavities and kickers, and other components of which the individual contribution is considered to be small, but which exist in large quantities, such as vacuum valves, beam pipe flanges, vacuum pumping ports, etc. We describe all contributions with a resonator model of a resonant frequency f_{res} , quality factor Q , and a resonant bandwidth Δf , where $Q = \frac{f_{\text{res}}}{\Delta f}$. Considering the type of instability that is triggered by a certain impedance contribution, we can distinguish between **nar-**

rowband impedances for which $\Delta f \ll \frac{1}{\tau}$ and **broadband impedances** for which $\Delta f \gg \frac{1}{\tau}$. If we accept a certain randomness in this division by ignoring the additional dependence on bunch spacing, this allows to categorise our mitigation methods. This way, narrow-band impedances mainly cause coupled bunch instabilities since the resulting wakefield of these resonances remains sufficiently long to affect many bunches. Narrow-band impedances can be reduced by methods that can be denoted as de-Qing, i.e. damping of undesired resonant modes by usually passive means as the introduction of HOM-couplers, or resonance-broadening methods, such as the insertion of absorber ferrites which create losses at a certain frequency. Contrary to this, broadband beam impedances lead only to single bunch instabilities for which usually not the quality factor, but the geometry factor R/Q has to be reduced by changing the overall geometry. This can be obtained either by selecting a suitable geometry for the machine element or by introducing a shield within an existing structure. The usual approach is to calculate the contribution of individual components separately, and once an individual contribution is known, optimisation of this machine element starts. It is, however, well known that this approach is insufficient if the individual elements are coupled to each other. In the following, we will give examples of geometries that appear to be simple, but are electromagnetically complex, as well as how oversimplifications of geometries can give misleading results. Finally, an example is given how in addition to the improvement of individual impedance contributions also the rearrangement of consecutive machine elements can lead to a considerable impedance gain.

MITIGATION ON INDIVIDUAL MACHINE ELEMENTS

Although electron cloud related impedances should not be forgotten since they have been observed in virtually all high energy machines and are typically mitigated by surface treatments as coating or other measures, we will not consider this topic here. Equally, the introduction of absorber ferrites or other lossy material usually comes with the risk of creating a heat-transfer issue if used in vacuum. We will not show such examples here either. Instead, we concentrate on **geometrical changes** since we consider those as the first choice in impedance mitigation, and demonstrate beam impedance mitigation by worked examples taken from the SPS, the last leg in the injector chain for the Large Hadron Collider (LHC). Geometrical changes are usually implemented such that the build-up of resonances is suppressed from the very start, e.g. by reducing the volume of the outer vessel of a machine element to avoid that low frequency resonances build up. In many cases, e.g. for heating issues, it is equally sufficient to

* Christine.Vollinger@cern.ch

shift a critical mode to higher frequencies, hence out of the contributing beam spectrum, e.g. by inserting impedance shields or shorting elements such as bridges, RF-contacts or the like. In addition, HOM-couplers are routinely used to take out resonances in a structure that cannot be avoided from the machine element's geometry, and a detailed worked example is shown in this proceedings in the studies for the 200 MHz travelling wave cavities for the SPS [9]. Finally, as was mentioned already before, using examples also taken from the SPS, we will demonstrate how the re-working of existing machine sections by sorting its individual elements can lead to a considerable reduction of the overall contribution to beam impedance.

Vacuum Pipe Flanges of SPS (Example 1)

The vacuum flanges (VF) in the SPS can be divided in two groups classified by their interconnecting beam pipes [2]. Impedance-wise, the most concerning are circular VF-connections with a bellow attached and connected to flat beam pipe types since those are shaping an unintended pill-box-type cavity with corrugated walls. At the time, the round flanges were chosen, for example, to allow the connection of a rectangular beam-pipe of inner width $w=156$ mm (as is used in the bending magnets MBA-type of the SPS) with a beam-pipe of a quadrupole magnet with the same inner width, but with an elliptical contour. A number of shielding designs can be found for these VFs, all developed with the goal to provide a smooth transition for the different beam pipe shapes. Most of these designs feature RF-contacts, RF-bridges, or both elements, to provide electrical contact between the different parts as well as to the outer VF body, this way, suppressing resonances. These RF-fingers can be completely fixed on both ends, fixed-touching or spring-driven [2] [3], however, their performance depends on a flawless installation that guarantees that the RF-fingers are well-connected. Different from these designs, we were looking for the development of an impedance shield for these VF interconnections that can provide electrical continuity with a maximum mechanical robustness to longitudinal and lateral movements. This type of shield was originally suggested by Ogiwara [4] who also tested different materials as well as different braid-woven patterns for shields [5].

Fig. 1 shows the illustrations of a cut-through of an unshielded VF with bellows (a), and the same vacuum flange with a braided shield fixed on support plates (b). The stainless steel braided shield is highlighted in red. The vacuum flange shield designs have to be compatible with variations in the alignment of the two connecting vacuum chambers, i.e., have to comply to misalignments in the longitudinal as well as in the transverse planes. Fig. 2 visualises how the stainless steel braid (shown in red) can provide smooth continuity by connecting the different beam pipe contours; cut-through (a) and view from the outside (b) with fixed RF-fingers of the support-plate highlighted in yellow. In the case shown, a change of vacuum pipe contour from elliptical QF-type (left side) to rectangular MBA-type (right side) is required. The installation of the stainless steel braid effectively

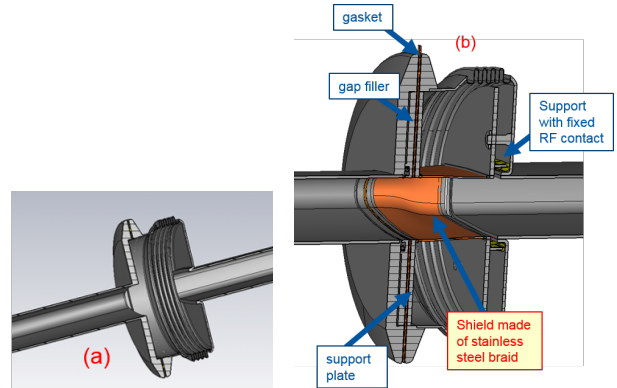


Figure 1: Illustrations of a cut-through of unshielded vacuum flange (VF) with 4-convolution bellows attached (left), and the VF equipped with a braided shield for impedance reduction (right).

suppresses the contribution of the bellows to beam coupling impedance. More details on the braided shield study can be found in a detailed publication [6]. The simulated longitudinal impedance of the SPS vacuum flanges with/without the braided shields is shown in Fig. 3. A comparison of the traces shows that most resonances are effectively suppressed by the shield installation (compare red trace (unshielded VF) to the black trace (with braided shield)). An exception is the resonance at about 1.4 GHz, on which a reduction of impedance contribution and a slight shift of the resonance frequency can be observed. This remaining resonance is building up in the gasket area of the shielded vacuum flanges, where a very flat circular unintended cavity of 2 mm height remains due to the gasket thickness. Consequently, this resonance can be suppressed by closing the gasket gap, e.g. through insertion of a modified gasket shape which will then lead to the blue trace (see [6] for details). Beam dynamics

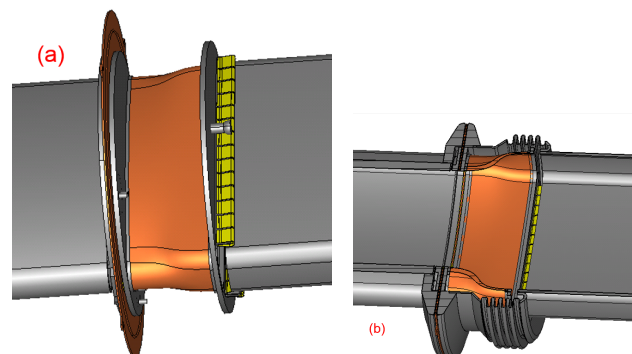


Figure 2: Illustrations of braided shield continuity between different beam-pipe shapes (a), and a cut-through view of braided shield for impedance reduction with fixed RF-contacts (b).

simulations [8] give a clear indication about the need of shielding the VFs and reduce the current contribution to the longitudinal beam impedance. The effect of shielded VFs, however, is visible in simulations for intensity threshold only if other measures are applied in addition. Most important in this respect are the HOMs resulting from the 200 MHz TWC,

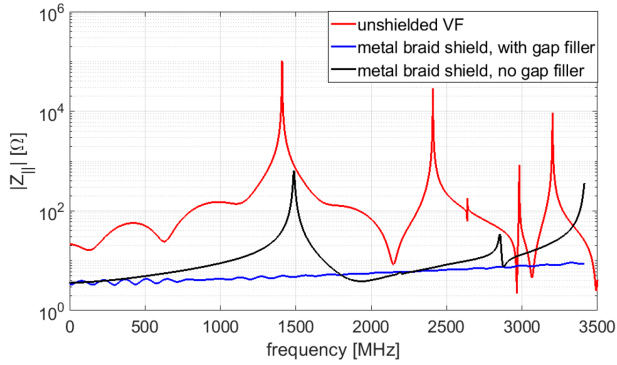


Figure 3: Comparison of simulation results for the longitudinal impedance contribution of one SPS vacuum flange connecting an MBA beam-pipe to a QF beam-pipe. Red: unshielded VF, black: VF equipped with braided shield, blue: VF equipped with braided shield and modified gasket (gasket gap filled). The closing of the flat unintended cavity at the gasket location suppresses the remaining resonance at about 1.5 GHz.

where currently a HOM-reduction factor of 2 to 3 is targeted and appears reachable [9]. Note that these simulations [7] were performed for the situation with 72 bunches in the SPS after an RF-upgrade on the 200 MHz TWC to reach a total accelerating voltage of 10 MV. As can be seen in Fig. 4, for a HOM-reduction in the 200 MHz cavity of a factor of three, an additional 10 % can be gained by shielding the VFs.

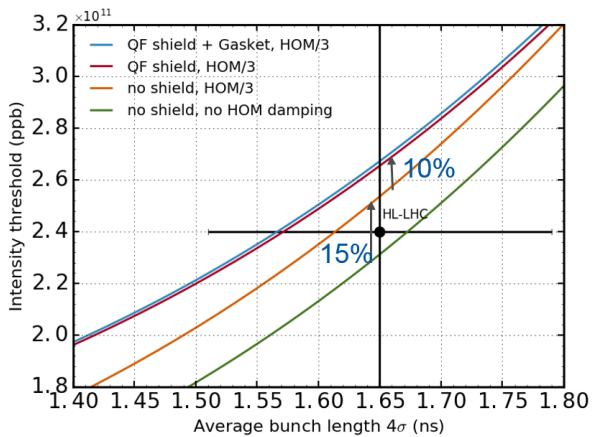


Figure 4: Simulation results for intensity threshold on the SPS 450 GeV/c flat top with 72 bunches spaced by 25 ns for an RF-voltage of 10 MV at 200 MHz and 1 MV at 800 MHz. The simulation compares the situation of shielded and unshielded vacuum flanges connecting an MBA-type beam-pipe to an elliptical QF-type beam pipe. Courtesy of J. Repond [8].

UHV Gate Valve of PS (Example 2)

In the framework of the development of an impedance model for the CERN Proton Synchrotron (PS), priority was given to the modeling of machine elements of which the

contribution to the overall beam impedance is known to be significant as, e.g. the accelerating cavities, and the kickers. However, smaller passive machine parts like the ultra-high vacuum (UHV) gate valves or beam pipe bellows equally have to be modelled as these are expected to contribute due to the large number of elements installed in the PS. For the PS UHV gate valves, a simplified impedance model existed for the calculation of transverse impedance. This model mainly represented the integrated dimensions of the structure since due to proprietary rights of the manufacturer, no geometrical model exists of this structure. We have therefore taken assumptions on the mechanical part inside the outer body of the gate valve. It could be shown from simulations, that leaving out these parts will result in an entirely different impedance contribution, i.e. to a misleading interpretation of the longitudinal impedance. Fig. 5 shows the previous impedance model (a), and the modified geometry (b) including the mechanical part.

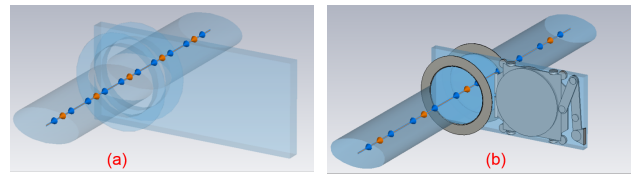


Figure 5: PS UHV geometrical gate valve models. Simplified geometry (a), and improved model including the inner parts that represent the valve mechanism (b).

Due to lack of geometry knowledge, the simulation model of the PS UHV valves had to be benchmarked by means of EM-measurements to ensure that the assumed geometry correctly represents its main features with respect to beam impedance. For this purpose, we connected RF-pipes on both sides of the valve such that EM-measurements with a vector network analyser could be carried out by inserting capacitively coupling coaxial RF-probes. It should be noted that a direct connection of measurement probes to the valve is not possible as this would have a strong effect on the resonances since in the main body of the valve, coupling could not be sufficiently reduced. The RF-probes are inserted on-axis into the connected beam pipes to detect resonances from transmission measurements. In all cases, it has been assured that only a weak coupling of the probe to the valve's resonance of less than approx. 100 mdB took place in order to avoid a falsification of the measurement trace.

Fig. 6 shows the comparison of simulated transmission measurements obtained from the model in CST [10] (dashed lines) and the measured traces for the three most significant resonances at approx. $f_{res} = 1207$ MHz, 1346 MHz, and 1504 MHz that could be excited with the centered probe positions. Eigenvalues have been calculated with the beam pipes terminated by short planes to allow additional cross-checks of the resonance frequencies.

As can be seen from the comparison of the traces, the measured resonances of TE_{111} (at 1.207 GHz) and TE_{116} (at 1.346 GHz) could be precisely reproduced from the sim-

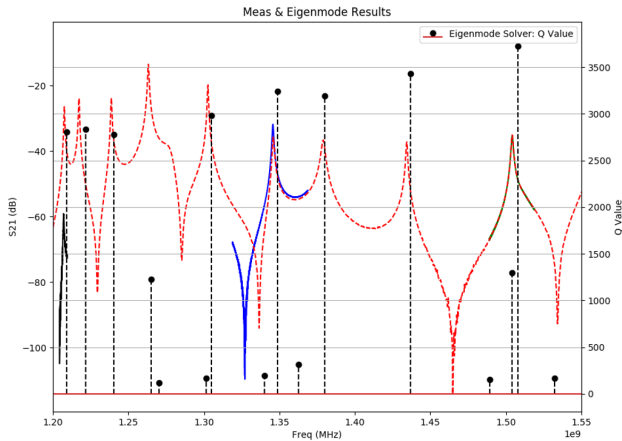


Figure 6: PS UHV gate valve: Comparison between simulations (both Eigenmode and transmission solver results) and measurements taken with a VNA using coaxial RF-probes.

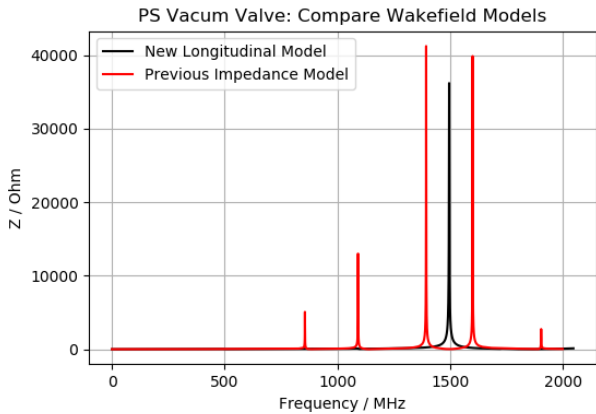


Figure 7: Simulated longitudinal beam impedances as obtained from an oversimplified valve geometry, and a more precisely modeled valve containing the inner mechanism.

ulated transmission, as well as the resonance frequency of TM_{010} (at 1.504 GHz). Note that the TM_{010} is at a higher frequency than the two TE-modes resulting from the change of the resonator geometry by adding the beam pipes. It should also be mentioned that the selected measurement set-up restricts the positioning of the measurement probes onto the beam axis. Consequently, due to the resulting field configuration, only a limited number of the modes that are truly resonating in the valve can be excited. The good reproduction of the three peaks, however, give sufficient confidence in the correct reproduction of the valve's geometry for impedance calculation. Fig. 7 shows the calculated longitudinal impedance obtained from the earlier simplified geometry (shown in Fig. 5 (a)) compared to the improved longitudinal model (Fig. 5 (b)) from which a longitudinal beam impedance contribution of about 36 k Ω could be attributed to one valve. In total, there are 10 valves of this type used in the PS.

Kicker Magnet (KFA45) of PS (Example 3)

The fast kickers of the PS like the so-called KFA45, consist of a variable number of magnet modules contained in one common vacuum tank. Each of these magnet modules is geometrically built of intersecting parts of alternating aluminum plates and ferrite sections that are supported within an aluminum framework. These ferrites must be modeled accurately, since they behave as attenuators at lower frequencies, whereas at higher frequencies, they become transparent.

A multitude of modes are supported by the ferrites and the spacing between the plates. Additionally, due to the close proximity of these sections heavy coupling between the modes in the modules takes place. Further modes are observed within the vacuum tank itself; these are supported by the framework of the modules and the plate-ferrite sections.

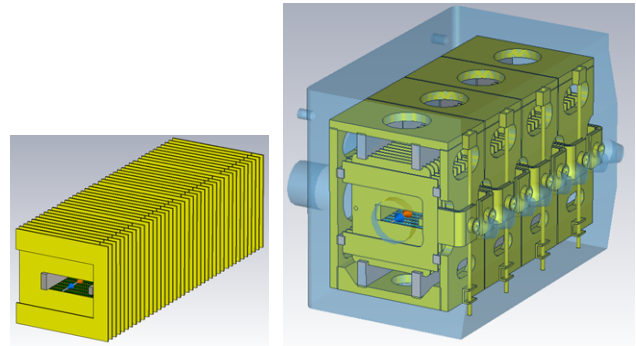


Figure 8: Models of the geometry of the fast kickers, simplified model (left) and complete model (right), shown to scale.

Previous work [11] in the transverse impedance domain resulted in a simplified model of the kicker that does not include the framework of the kicker, neither its vacuum tank (as is shown in Fig. 8 (left)). This model was used as a starting point to build a more complete geometry required as input for the longitudinal impedance model of the PS (see Fig. 8 (right)), which incorporates the complete geometry of the kicker.

Due to the large amount of modes present in the kicker, eigenmode analysis was impossible and also could even be misleading, since many modes are broadband with frequencies close to one another, such that they would 'stack' upon one another. Consequently, they cannot be analyzed independently. As a result, only wakefield simulations give reasonable results for these types of objects. As an example, the transverse model was simulated for the longitudinal impedance and is compared with the complete model's longitudinal impedance in Fig. 9

Of particular note is the resonance peak at 600 MHz obtained from the simplified model which shifts as low as 60 MHz for the complete model. Further study of the field distributions showed that this shift is the direct result of this mode resonating in the free space around the ferrite-plate sections. The complete kicker model provides for the added

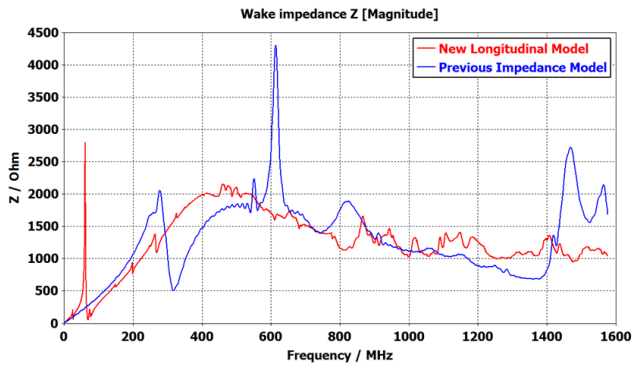


Figure 9: Comparison of calculated wakefields resulting from previous, simplified impedance model and new, complete impedance model of the KFA45.

space in these sections thus pushing this resonance to lower frequency due to its larger overall volume. Note that the overall longitudinal impedance for both models, except for the peak, is very broadband.

Reworking of a Machine Section (Example 4)

In the framework of the ongoing impedance reduction efforts taken for the SPS, each new machine element to be installed into the accelerator has to undergo an impedance evaluation that makes part of an installation approval process. This evaluation includes the calculation of the direct surroundings in the machine to determine if additional elements, like e.g. beam-pipe tapers or other mitigating parts are required. In many cases, impedance shields for the new machine element can be suggested and are implemented. However, in this way, not only individual machine elements could be identified to which a large contribution to beam impedance was attributed, but also some groups of different machine components stood out with a noticeable impedance contribution which resulted from repeated change of beam pipe cross-sections. Further study of these machine sections showed that their overall impedance could not simply be reproduced by adding up the individual contributions of its elements. Instead, wakefield calculations for the entire area had to be carried out as one geometry to obtain a correct impedance contribution, making these simulations heavy and time-consuming. It could be observed that the repetition of a large number of cross-sectional changes from narrow beam-pipe to larger beam-pipe cross-sections results in a cavity-like behaviour of some elements, explicitly in the case of round bellows due to their pill-box shape. This is, however, only the case if the bellow is installed with a narrow beam pipe on both sides. Otherwise, the same bellow does not resonate cavity-like, but contributes with its longitudinal size to the adjacent machine element as a volume extension. Fig. 11 (top) shows the original layout of such an area in the SPS where upstream of a corrector magnet, a large number of cross-sectional changes of the beam pipe could be found. The area consists of different machine elements starting with a beam position monitor (so-called BPCE) with circular aperture that is followed by a small corrector dipole (so-called

MDHA) which is clamped around an elliptical beam pipe of 156 mm width (QFA-type). Three large aperture bellows of two different types are required to allow alignment of the machine elements and to flange the different beam pipe apertures. It should be noted that work in these areas was not foreseen within impedance reduction programmes so far, however, the request of installation of an additional machine element with a race-track shaped aperture upstream of the BPCE led to this investigation of the entire area. Fig. 11 (bottom) also shows the top view and the side view of the original layout as modelled in CST [10]. The location where the new machine element with a race-track shaped aperture is to be inserted into the existing accelerator structure is also indicated. The original layout is with a round beam-pipe at this location.

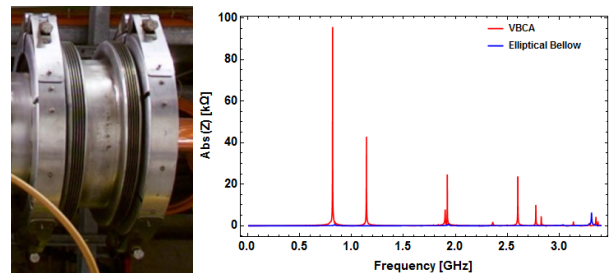


Figure 10: Left: VBCA bellow type consisting of two undulated parts that are connected via a large round opening. Right: Simulated longitudinal beam impedance for the VBCA bellow compared to an elliptical bellow with same horizontal aperture.

The two bellow types are denoted VBDA for the standard bellow and VBCA for the bellow with two separated undulations of which two are used in this area. Fig. 10 (left) shows the VBCA bellow that consists of two undulated parts that are resonating individually and a straight part acting as a large opening that allows full coupling of the resonances which are building up in the bellow undulations. The VBCA bellow has an inner diameter of 340 mm and ends in DN273 flanges, and its main contribution to longitudinal beam impedance could be identified at about 850 MHz, if it is connected on both sides with elliptical beam pipes. This is the case for the bellow position just upstream of the QFA, however, not for the second identical bellow that is located downstream of the BPCE.

It would therefore be incorrect to just calculate the longitudinal beam impedance of the VBCA bellow with elliptical beam pipes on both sides and then double its contribution. Fig. 10 (right) shows the contributing longitudinal impedance of this bellow compared to an elliptical bellow of the same mechanical functionality. From simulation, a contribution of about 90 kΩ is obtained for the VBCA connected to elliptical beam pipes on both sides, in addition to a number of other modes for frequencies above 1 GHz, resulting from the fact that this bellow is shaping an unintended cavity with resonator-behaviour. Note that in this location, mainly elliptical beam-pipes are used, hence aperture re-

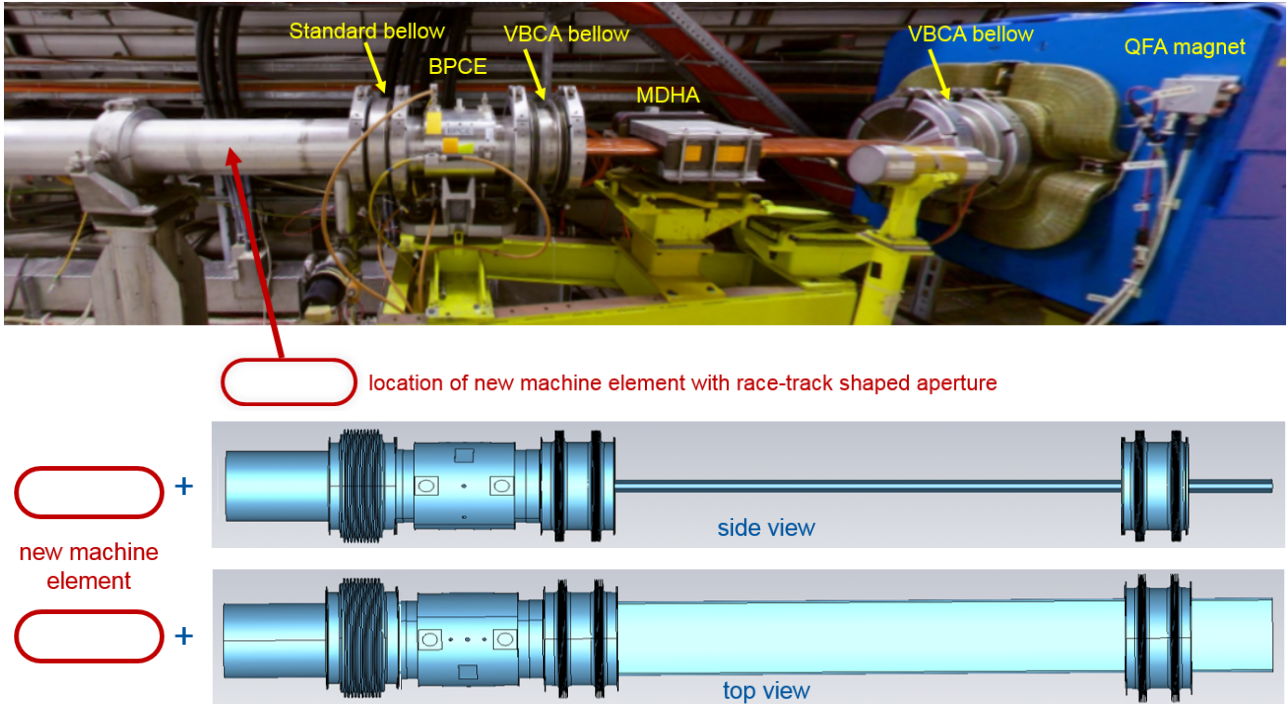


Figure 11: Top: Picture of the original layout of the SPS area for evaluation for impedance improvement due to sorting. Bottom: Top view and side view of the original layout as modelled in CST [10] where the race-track shaped aperture shall be inserted into the existing round beam pipe upstream of the BPCE with its adjacent large aperture standard bellow.

quirements allow for the exchange of VBCA and VBDA bellows with large round apertures with elliptical bellows of the same horizontal aperture. Fig. 12 shows the simulated

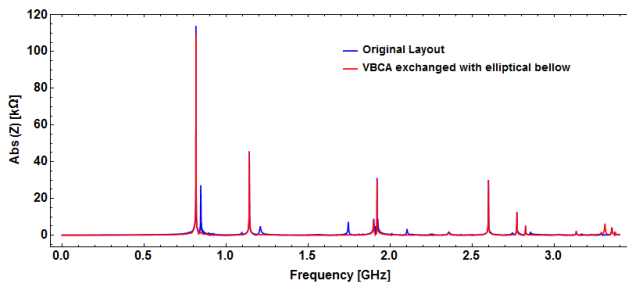


Figure 12: Simulated longitudinal beam impedance obtained from the original layout (blue trace) and after the exchange of the VBCA bellow with an elliptical bellow (red trace).

longitudinal beam impedance obtained from the original layout (blue trace) and after the exchange of the VBCA bellow with an elliptical bellow (red trace). As expected, the peak at approx. 850 MHz vanishes when the VBCA bellow next to the quadrupole is removed. Note that only the VBCA bellow next to the quadrupole magnet was removed, whereas the second VBCA bellow, located downstream of the BPCE is still in the layout. As was mentioned before, the VBCA bellow is contributing differently, depending on how it is flanged on at both sides. In this case, the VBCA bellow downstream of the BPCE is simply acting as a volume extension for the position monitor, and is not acting as an unwanted cavity by creating narrowband resonances.

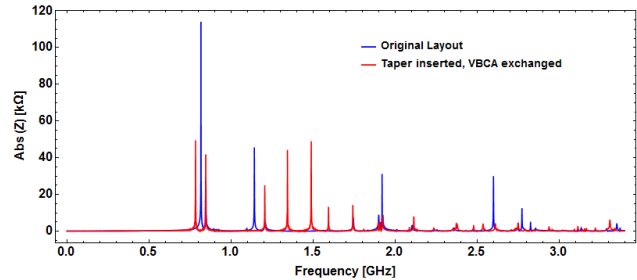


Figure 13: Simulated longitudinal beam impedance obtained from the original layout (blue trace) and after the insertion of an ideal taper to provide transition from the race-track shaped aperture to a round one. In addition, the VBCA bellow was exchanged for an elliptical bellow (red trace).

As a next step, a taper was inserted in the simulations to provide a smooth continuity between the new machine element with its race-track shaped aperture and the existing structure with a round aperture. Today, the use of individualised tapers is standard in most accelerators, following the rule-of-thumb to only keep a minimum number of steps along the vacuum chamber. The taper in our case was calculated as ideal transition from the race-track shaped aperture to round aperture. In addition, one elliptical bellow was placed upstream of the taper, replacing the VBCA. Fig. 13 shows the resulting simulated longitudinal impedance of this study (red trace) compared to the original layout (blue trace). It can be seen that by inserting the taper, resonances at about 1.15 GHz and 1.9 GHz, as well as some higher frequency resonances were suppressed compared to the original layout. However, the largest resonance at about 850 MHz does not

vanish, but is instead reduced by about half and split in two individual resonances. In addition, a number of new resonances shows up in the frequency range between 1 GHz and 2 GHz which diminish the overall improvement. It was then decided to evaluate a possible sorting of the existing machine elements. For this purpose, the VBCA bellow upstream of the quadrupole magnet was exchanged with an elliptical bellow, and the positions of the new machine element and the BPCE with the two connected bellows were swapped. Note that this action moves the BPCE further away from the QF, a change in layout that had first to be agreed by operations to confirm that the functionality of the BPCE is not compromised. Fig. 14 shows the simulated longitudinal beam impedance obtained after sorting the machine elements for best impedance performance (red trace), and compared to the original layout (blue trace). As can be seen from the plots, sorting of the machine elements led to a considerable reduction of the longitudinal beam impedance over the entire frequency range with maximum narrowband contributions of less than 10 k Ω longitudinal beam impedance at about 800 MHz, 1.9 GHz and above 3 GHz which can be considered entirely negligible within the overall impedance budget of the accelerator.

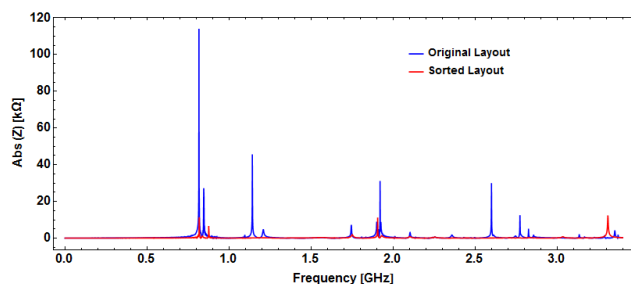


Figure 14: Simulated longitudinal beam impedance obtained from the original layout (blue trace) and after sorting the individual machine elements for best impedance performance (red trace).

CONCLUSION

In this contribution, we investigated the longitudinal beam impedance contribution of various machine elements and possible solutions for their mitigation by means of worked examples. We looked at narrowband and broadband impedances and gave examples of possible mitigations for individual machine elements. One major source of contribution are cross-sectional changes of the beam pipe aperture, hence impedance shields that provide a smooth transition between different beam pipe shapes are an effective way to improve the impedance contribution. It was further shown that considerable care has to be given to the geometrical modeling of individual machine elements in order to correctly reproduce their EM-behaviour. Explicitly elements that appear to be mechanically simple such as flanges, bellows and valves can be electromagnetically complex. It was shown with the example of the PS UHV sector valve, that for machine elements in existing accelerators, where no good mechanical description is available, RF-measurements of

the element are required to benchmark the simulation model. With the example of a kicker magnet, it was demonstrated how over-simplifications of the geometrical model can lead to misinterpretation of the calculated beam impedance contribution. Further, with the example of the VBCA bellows, it was also shown that special care is required in counting the number of machine elements and multiplying the individual contribution without considering the installation situation. Finally, we demonstrated that besides the improvement of individual machine elements, also sorting of their positions in the lattice should be considered if the layout allows for this, since sorting can give an impedance improvement of the overall section without modifying the individual machine elements.

REFERENCES

- [1] E. Shaposhnikova *et al.*, “Removing Known SPS Intensity Limitations for High Luminosity LHC Goals”, in *Proc. of Int. Particle Accelerator Conf. (IPAC’16)*, Busan, Korea, May 2016, paper MOPOY058, pp. 989–991.
- [2] J. E. Varela, “Longitudinal Impedance Characterization of the CERN SPS Vacuum Flanges”, in *Proc. of Int. Particle Accelerator Conf. (IPAC’15)*, Richmond, VA, USA, May 2015, paper MOPJE036, pp. 363–365.
- [3] J. Perez-Espinos, *et al.*, “Analysis and Testing of a New RF Bridge Concept as an Alternative to Conventional Sliding RF-Fingers in the LHC”, in *Proc. of Int. Particle Accelerator Conf. (IPAC’16)*, Busan, Korea, May 2016, paper THPMY006, pp. 3660–3662.
- [4] Ogiwara, *et al.*, “Ultrahigh Vacuum for High Intensity Proton Accelerators: Exemplified by the 3 GeV RCS in the J-Parc”, in *Proc. of Int. Particle Accelerator Conf. (IPAC’11)*, San Sebastian, Spain, May 2011, paper TUZB02, pp. 971–975.
- [5] Ogiwara, *et al.*, “Bellows with a New RF Shield Made of Metal Braid for High Intensity Proton Accelerators”, in *Proc. of Int. Particle Accelerator Conf. (IPAC’13)*, Shanghai, China, May 2013, paper THPF1014.
- [6] T. Kaltenbacher, *et al.*, “Characterization of Shielding for the CERN-SPS Vacuum Flanges With Respect to Beam Coupling Impedance”, in *Proc. of Int. Particle Accelerator Conf. (IPAC’17)*, Copenhagen, Denmark, May 2017, paper WEPIK090, pp. 3143–3146.
- [7] BLD, Beam Longitudinal Dynamics code, <http://blond.web.cern.ch/>.
- [8] J. Repond, *et al.*, “Effect of HOM frequency shift on bunch train stability”, *these proceedings*, Benevento, Italy, September 2017.
- [9] P. Kramer, *et al.*, “Studies for the SPS Travelling Wave Cavities Upgrade”, *these proceedings*, Benevento, Italy, September 2017.
- [10] CST AG, Darmstadt, Germany, <http://www.cst.com/>.
- [11] S. Persichelli *et al.*, “The transverse beam coupling impedance of the CERN Proton Synchrotron” in *Phys. Rev. Accel. Beams*, vol. 19 no. 4, p.041001, April 2016.

ANALYTICAL IMPEDANCE MODELS FOR VERY SHORT BUNCHES

Igor Zagorodnov*, Deutsches Elektronen-Synchrotron, Hamburg, Germany

Abstract

We discuss several analytical models for impedances of very short bunches. The approximate analytical models are compared with direct solution of Maxwell's equations.

INTRODUCTION

We consider only relativistic case where the longitudinal w_{\parallel} and the transverse \vec{w}_{\perp} wake functions for a relativistic point charge q are defined as [1]

$$w_{\parallel}(s) = -\frac{1}{q} \int_{-\infty}^{\infty} E_z(z, t)|_{t=\frac{z+s}{c}} dz, \quad \frac{\partial}{\partial s} \vec{w}_{\perp} = \nabla w_{\parallel}. \quad (1)$$

The coupling impedance is given by the Fourier transform of the wake function

$$\vec{Z}(k) = \frac{1}{c} \int_0^{\infty} \vec{w}(s) e^{iks} ds,$$

where c is a velocity of light.

For very short bunches the difficulty of numerical calculation of wakefields can be associated with a small parameter σ_z/a , where σ_z is the rms bunch length and a is the typical size of the structure. Indeed, for a closed structure of typical size a the calculation time of the wake potential with finite-difference code [2] is proportional to $(a/\sigma_z)^4$. This scaling follows from linear dependence of the calculation time on the number of mesh points, $(a/\sigma_z)^3$, multiplied by the number of time steps, (a/σ_z) .

If the structure is open, f.e. supplied with an outgoing pipe, then the calculation time increases considerably as we have to propagate the field in the outgoing pipe along the formation length a^2/σ_z [3] to reach an accurate estimation of the improper integral in Eq.(1). For the typical parameters of the European FEL linac [4], the rms bunch length $\sigma_z = 25\mu\text{m}$ and the aperture radius $a = 35\text{mm}$, the formation length of the wake potential is approx. 25m. Application of an "indirect integration" method [5] allows to replace the improper integral in Eq.(1) with a proper one in the outgoing pipe cross-section. It returns the calculation time back to $(a/\sigma_z)^4$, but the numerical burden remains huge for very short bunches, $\sigma_z \ll a$.

On the other hand the small parameter σ_z/a allows to develop asymptotic analytical models and to avoid time-consuming numerical simulations. At this paper we will review several analytical models for the impedances of very short relativistic bunches and compare them with direct numerical solution of Maxwell's equations.

OPTICAL MODEL

In order to estimate the high frequency impedance of short transitions an optical model was developed in [6, 7].

In this approximation we assume that the electromagnetic fields carried by a short bunch propagate along straight lines equivalent to rays in the geometric optics. An obstacle inside the beam pipe can intercept the rays and reflect them away from their original direction. The energy in the reflected rays is associated with the energy radiated by the beam, which can then be related to the impedance.

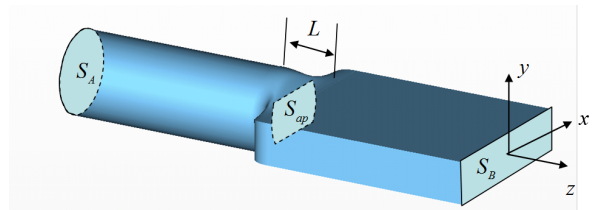


Figure 1: An example of transition geometry.

Consider a short transition with aperture S_{ap} between two pipes with apertures S_A and S_B as shown in Fig. 1. Under aperture area S_{ap} we mean the minimal cross section in the structure if we project it along z -axis. Let a is a characteristic size of the aperture S_{ap} . If the bunch has a short rms length σ_z , $\sigma_z \ll a$, and the transition length L between the ingoing pipe aperture S_A and the outgoing pipe aperture S_B is much shorter than the formation length, $L \ll a^2/\sigma_z$, then the high frequency longitudinal impedance is a constant which can be calculated by relation

$$Z_{\parallel}(\vec{r}_1, \vec{r}_2) = -\frac{2\epsilon_0}{c} \int_{\partial S_{ap}} \phi_B(\vec{r}_2, \vec{r}) \partial_{\vec{n}} \phi_A(\vec{r}_1, \vec{r}) dl, \quad (2)$$

where \vec{n} is the outward pointing unit normal to the line element dl , ϵ_0 is the permittivity of free space, \vec{r}_1 and \vec{r}_2 are offsets of the leading and the trailing particles, correspondingly, and ϕ_A, ϕ_B are the Green's functions for the Laplacian in the ingoing and the outgoing pipe cross-sections (see [6] for details). Let us apply this method to the undulator inter-

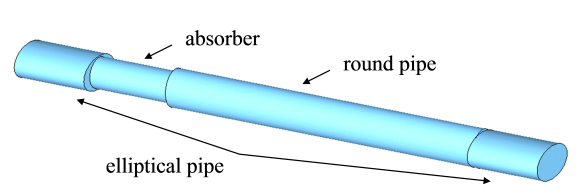


Figure 2: The geometry of the vacuum chamber in the undulator intersections.

section at the European XFEL. Here the vacuum chamber changes from an elliptical pipe to a round one. At the position of the elliptical-to-round transition (E2R) an elliptical absorber of a smaller cross-section is placed as shown in Fig. 2. At the beginning let us consider a simple case without the absorber. In this case we have only an elliptical-to-round

* Igor.Zagorodnov@desy.de

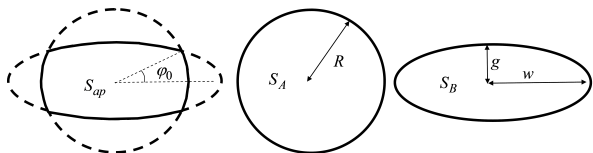


Figure 3: The geometry of transition from round pipe to elliptical one.

(E2R) pipe transition. The geometry of the transition is shown in Fig. 3.

The Green's function for the Laplacian inside the circle of radius R can be written as

$$\phi_R(\vec{r}_1, \vec{r}) = \frac{1}{4\pi\epsilon_0} \Re \left(2 \ln \frac{z^* z_1 - R^2}{R(z - z_1)} \right),$$

$$\vec{r} = (x, y)^T, \quad z = x + iy.$$

The Green's function for the Laplacian inside the ellipse with half axes w and g can be written as [8]

$$\phi_E(\vec{r}_1, \vec{r}) = \phi_E^0(\vec{r}_1, \vec{r}) - \phi_E^0(\vec{r}_1, \vec{r}_0), \quad \vec{r}_0 = (0, g)^T,$$

$$\phi_E^0(\vec{r}_1, \vec{r}) = -\frac{1}{\pi\epsilon_0} \left(\sum_{n=1}^{\infty} \frac{e^{-nu}}{n} F_n - \frac{1}{4} \ln \|\vec{r} - \vec{r}_1\|^2 \right),$$

$$F_n = \frac{\Re T_n\left(\frac{x+iy}{d}\right) \Re T_n\left(\frac{x_1+iy_1}{d}\right)}{\cosh(nu)} + \frac{\Im T_n\left(\frac{x+iy}{d}\right) \Im T_n\left(\frac{x_1+iy_1}{d}\right)}{\sinh(nu)},$$

$$d = \sqrt{w^2 - g^2}, \quad u = \coth^{-1}(w/g),$$

where $T_n(z)$ are the Chebyshev polynomials of the first kind.

For the round-to-elliptical (R2E) pipe transition the Green's functions has to be assigned as $\phi_A = \phi_R$, $\phi_B = \phi_E$. The aperture S_{ap} is shown in Fig. 3.

The longitudinal impedance on the axis can be found as one-dimensional integral

$$Z_{\parallel}^{R2E} = \frac{4}{c\pi} \int_0^{\varphi_0} \phi_E(\varphi, R) d\varphi, \quad (3)$$

$$\varphi_0 = \tan^{-1} \left(\frac{g}{w} \sqrt{\frac{w^2 - R^2}{R^2 - g^2}} \right),$$

where $\phi_E(\varphi, r) \equiv \phi_E(\vec{0}, (r \cos(\varphi), r \sin(\varphi))^T)$.

In order to calculate the longitudinal impedance of the elliptical-to-round (E2R) pipe transition we can use the directional symmetry relation from [5]

$$Z_{\parallel}^{E2R} = Z_{\parallel}^{R2E} - \frac{2}{c} [\phi_E(\vec{0}, \vec{0}) - \phi_R(\vec{0}, \vec{0})].$$

We evaluate the one dimensional integral, Eq. 3, numerically. The right graph in Fig. 4 presents the results for the fixed size of the elliptical pipe ($w = 7.5\text{mm}$, $g = 4.4\text{mm}$) and the Gaussian beam with rms length $\sigma_z = 25\mu\text{m}$. The black dots show the numerical results from CST Particle Studio [9] obtained for the bunch length $\sigma_z = 100\mu\text{m}$ and scaled to the bunch length $\sigma_z = 25\mu\text{m}$ (in the optical model

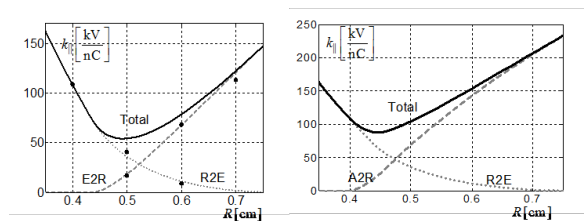


Figure 4: Dependence of the loss factor from the radius of the round pipe. The left graph presents the results without the absorber, the right graph presents the results with the absorber included. The black dots show the numerical results from CST Particle Studio.

the loss factor is inversally proportional to the bunch length, see Eq.(13) in [10]).

Let us now consider the geometry with the absorber included. Here we consider the absorber as a long collimator. The absorber has the half width $w_1 = 4.5\text{mm}$ and the half height $g_1 = 4\text{mm}$. The transition from the elliptical pipe to the absorber (E2A) can be considered as in-step transition and we have $Z_{\parallel}^{E2A} = 0$. The contribution of the absorber to round pipe (A2R) transition can be found from Eq. (2) with w_1 and g_1 . The final result is presented in Fig. 4 in the right graph. We can conclude that the optimal radius of the round pipe in the undulator intersection is 45-50 mm.

In the example considered the longitudinal impedance is written as one-dimensional integral Eq. (3). The transverse impedance dipole and quadrupole terms in the Taylor expansion can be written in closed analytical form [7].

The application of the optical approximation to estimate the high frequency impedances of different transitions in the vacuum chamber of the European XFEL can be found in [10]. The bunch used for the European XFEL operation is very short and the analytical results obtained are quite accurate approximations to the coupling impedances. Most analytical results presented in [10] are new and supplement those already published in [7]. The method of the optical approximation is powerful and allows to study analytically a truly large class of transitions when the analytical form of 2D Green functions of the pipe cross-sections are known.

Usually the vacuum elements in the accelerators are connected with round, elliptical or rectangular pipes, for which the analytical Green functions are well known. For a general case the Green functions can be found through numerical solution of 2D Poisson's equations.

DIFFRACTION MODEL

The optical theory ignores diffraction effects. It predicts zero impedance for the pillbox cavity or periodic array of irises. Indeed, in this case, all the three cross-sections S_A , S_{ap} and S_B are equal and Eq. (2) immediately gives a zero result.

The diffraction theory takes into account the fact that radiated electromagnetic fields do not propagate along straight line. A Fresnel type integral from the diffraction theory

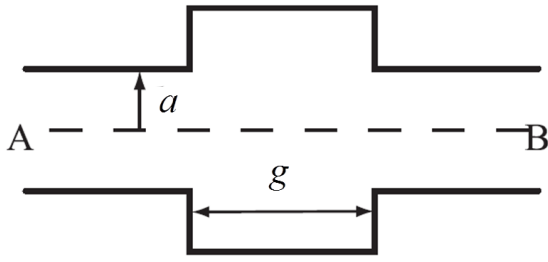


Figure 5: An axisymmetric deep pillbox cavity.

of light is used to evaluate the electromagnetic energy that enters into the cavity region. This energy is associated with the energy lost by the beam and is thus related to the real part of the impedance.

For the deep pillbox cavity shown in Fig. 5 the diffraction theory gives the high-frequency longitudinal (on the axis) impedance as (see, *e.g.* [1])

$$Z_{\parallel}(k) = \frac{Z_0(1+i)}{2\pi^{3/2}a} \sqrt{\frac{g}{k}}, \quad (4)$$

where a is the pipe radius and g is the length of the cavity.

The reason for the optical approximation not reproducing the result of the diffraction theory is that Eq. (4) corresponds to the next order approximation in the small parameter $\sigma_z g/a^2$ [6].

For axisymmetric geometry the transverse impedance near the axis can be approximated as

$$\vec{Z}_{\perp}(k) = (Z_x, Z_y)^T = Z_d(k)(x_0, y_0)^T,$$

where x_0, y_0 are coordinates of source particle. The diffraction model at high-frequencies gives [1]

$$Z_d(k) = \frac{Z_0(1+i)}{2\pi^{3/2}a^3k} \sqrt{\frac{g}{k}}, \quad (5)$$

The corresponding wake functions in the time domain read [11]

$$w_{\parallel}(s) = \frac{Z_0c}{\sqrt{2}\pi^2a} \sqrt{\frac{g}{s}}, \quad w_d(s) = \frac{Z_0c2^{1.5}}{\pi^2a^3} \sqrt{gs}.$$

For the Gaussian bunch with rms length σ_z we can easily to calculate the loss and the kick factors

$$k_{\parallel} = \int w_{\parallel}(s)\lambda(s)ds = \frac{Z_0c}{4\pi^{2.5}a} \Gamma(0.25) \sqrt{\frac{g}{\sigma_z}},$$

$$k_d = \int w_d(s)\lambda(s)ds = \frac{Z_0c2}{\pi^{2.5}a^3} \Gamma(0.75) \sqrt{g\sigma_z},$$

where $\lambda(s)$ is the Gaussian charge density and Γ is a gamma function.

The same estimations for the impedances of pillbox cavity are obtained from parabolic equation method in [12].

The longitudinal impedance of one isolated pillbox cavity, Eq.(4), has $k^{-0.5}$ high frequency behavior. For an array

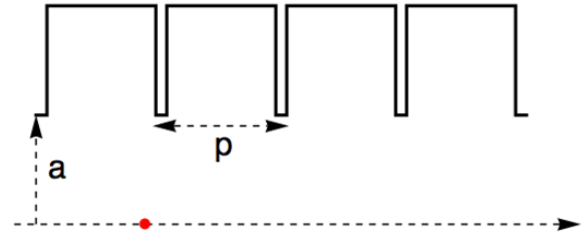


Figure 6: Periodic array of deep cavities.

of cavities with period p (see Fig.6) the high frequency behaviour is quite different. It scales as $k^{-1.5}$. The high frequency impedance of an infinite cavity array was found in [13, 14] and it reads

$$Z_{\parallel}(k) = \frac{Z_0}{2\pi a} \left[\frac{1}{\eta(k)} - ik \frac{a}{2} \right]^{-1}, \quad (6)$$

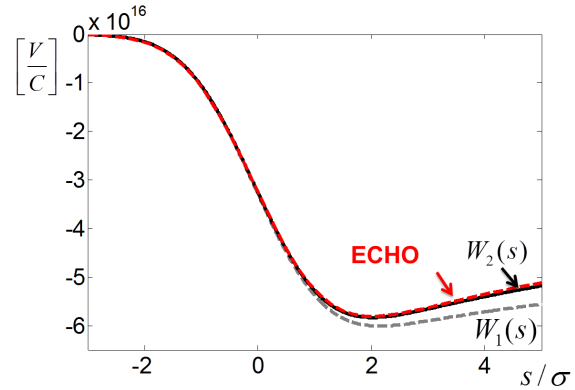
$$\eta(k) = \left[\frac{1-i}{2} \alpha \left(\frac{g}{p} \right) p \sqrt{\frac{k\pi}{g}} \right]^{-1}, \quad (7)$$

$$\alpha(x) = 1 - 0.465\sqrt{x} - 0.070x.$$

Inverse Fourier transforming, one obtains an analytical expression for the wake function:

$$w_{\parallel}^{(1)}(s) = -\frac{Z_0c}{\pi a^2} e^{s/s_0} \operatorname{erfc}(\sqrt{s/s_0}), \quad (8)$$

with the distance scale factor $s_0 = a^2g/(2\pi\alpha^2p^2)$.


 Figure 7: Longitudinal wake of periodic array of thin diaphragms ($g/p=1$).

We have compared this analytical estimation, Eq.(6), with accurate numerical solution of Maxwell's equations by code ECHO [2]. We will refer to the numerical solution as "exact" one.

We consider a chain of pillbox cavities with period $p = 0.5\text{mm}$. The cavities have radius $b = 1.2\text{mm}$ and are joined with a pipe of radius $a = 0.7\text{mm}$. The bunch is Gaussian with rms length $\sigma_z = 10\mu\text{m}$.

Our first example is a structure with periodic array of thin diaphragms, $g/p = 0.98$. Fig. 7 shows the longitudinal wake

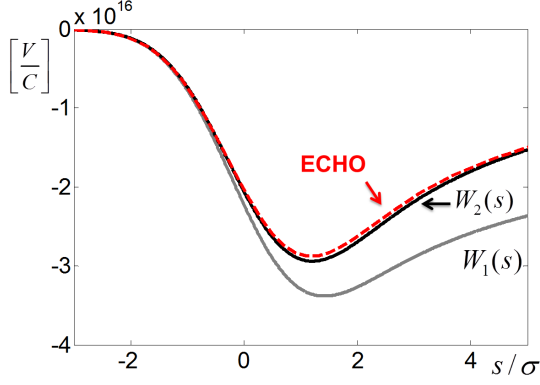


Figure 8: Longitudinal wake of periodic array of short cavities ($g/p=0.1$).

potential

$$W_{\parallel}(s) = \int_{-\infty}^s w_{\parallel}(s') \lambda(s-s') ds'. \quad (9)$$

The dashed curve labeled as "ECHO" is the numerical result, the gray dashed curve labeled as " $W_1(s)$ " is the analytical result, Eq.(6), which disagrees slightly with the "exact" solution. Fig. 8 shows the results for another case where the cavity gap is much smaller than the period, $g/p = 0.1$. In this case the disagreement between the "exact" solution and the approximation, Eq.(6), is large.

For the case of periodic array of infinitely thin diaphragms, $g/p = 1$, an accurate approximation of the impedance was found earlier by G. Stupakov [15]. In the high frequency approximation it gives

$$\eta(k) = \left[\frac{1-i}{2} \alpha(1) \sqrt{pk\pi} + \frac{1}{2} \right]^{-1}. \quad (10)$$

It can be seen that Stupakov's solution contains the additional term, which improves the agreement with the "exact" solution considerably. We would like to have the same order term in the more general case for arbitrary gap $g < p$. We combine Eq.(7) with Eq.(10) and suggest a more general equation

$$\eta(k) = \left[\frac{1-i}{2} \alpha \left(\frac{g}{p} \right) p \sqrt{\frac{k\pi}{g}} + \frac{1}{2} \frac{p}{g} \right]^{-1}. \quad (11)$$

This equation differs from Eq.(7) by additional term $p/(2g)$ and it reduces to Stupakov's result for infinitely thin irises, $g = p$.

There is no exact Fourier transform of this impedance. We introduce here an approximate wake function:

$$w_{\parallel}^{(2)}(s) = -\frac{Z_0 c}{\pi a^2} e^{-\sqrt{s/s_1 - s/s_2}},$$

$$s_1 = s_0 \frac{\pi}{4}, \quad s_2 = s_1 \left(\frac{1}{2} - \frac{\pi}{4} + \frac{s_1 p}{ag} \right)^{-1}.$$

This wake function has the same Taylor expansion up to the third order as the exact Fourier transform of Eq.(11). The

corresponding wake potentials labeled as " W_2 " are shown by black solid lines in Figs. 7- 8. It can be seen a good agreement with the "exact" numerical solution.

The high frequency transverse impedance is related to the longitudinal impedance according to $Z_d = 2Z_{\parallel}/(ka^2)$. Hence the transverse dipole wake function can be found as

$$w_d^{(2)}(s) = \frac{2}{a^2} \int_{-\infty}^s w_{\parallel}^{(2)}(s') ds'.$$

In the next section we will argue that the introduced function $\eta(k)$ can be treated as a surface impedance of corrugated waveguide of arbitrary cross-section.

SURFACE IMPEDANCE

The impedance of a round metallic pipe of radius a with conductivity κ has long been known [1] and is given by Eq. (6) with resistive surface impedance

$$\eta = \eta^c = \frac{1}{Z_0} \sqrt{\frac{i\omega\mu}{\kappa}}, \quad \omega = kc.$$

Let us consider a case when the elements of the vacuum chamber that generate the beam impedance are small and uniformly distributed over the surface of the wall. One example of such an impedance is that due to surface roughness. Another example is a corrugated structure [16]. While exact calculation of the impedance in such cases is difficult the effect on the beam can often be represented by a surface impedance. In the accelerator context the surface impedance was previously employed by Balbekov for the treatment of small obstacles in a vacuum chamber [17]. For a rough surface it was introduced by Dohlus [18].

It was shown in [18, 19] that the effect of the oxide layer and the roughness can be taken into account through the inductive part of the surface impedance

$$\eta = \eta^c + i\omega \frac{L}{Z_0},$$

$$L = \mu_0((1 - \epsilon_r^{-1})d_{oxide} + 0.01d_{rough}),$$

where d_{oxide} , ϵ_r are the thickness of the oxide layer and its relative permittivity, d_{rough} is a rms roughness parameter [18].

If the surface impedance is known then we can consider an arbitrary (smooth enough) cross section of waveguide with the impedance boundary condition.

Let us consider a structure having rectangular cross section, where the material at top and bottom can vary as function of longitudinal coordinate but the width and side walls remain fixed and are perfectly electric conducting. The impedance of such structure of halfwidth w (in x -direction) can be written as [20]

$$Z_{\parallel}(k) = \frac{1}{w} \sum_{m=1}^{\infty} Z(y_0, y, k_x^m, k) \sin(k_x^m x_0) \sin(k_x^m x), \quad (12)$$

$$Z(y_0, y, k_x, k) = Z^c(k_x, k) \cosh(k_x y_0) \cosh(k_x y) + Z^s(k_x, k) \sinh(k_x y_0) \sinh(k_x y),$$

where $k_x^m = (\pi m)(2w)^{-1}$ is a transverse harmonic number.

Using the surface impedance for calculating of high frequency impedance in flat geometry was considered in [21, 22]. It was found that the coefficients in Eq.(12) can be written in the form

$$Z^c(k_x, k) = \frac{Z_0 c}{2a} \operatorname{sech}^2(ak_x) \left[\eta^{-1} - ika \frac{\tanh(ak_x)}{ak_x} \right]^{-1},$$

$$Z^s(k_x, k) = \frac{Z_0 c}{2a} \operatorname{csch}^2(ak_x) \left[\eta^{-1} - ika \frac{\coth(ak_x)}{ak_x} \right]^{-1}.$$

If we use Eq.(7) or Eq.(11) for the surface impedance in the latter expressions then we obtain the high-frequency impedance of the rectangular corrugated structure. Following this approach analytical approximations for the wake functions in flat/rectangular corrugated structures are derived in [22–24].

WAKE ASYMPTOTICS AT THE ORIGIN

The limit of high frequencies corresponds to small distances behind a point charge. For infinitely long cylindrically symmetric disk-loaded accelerator structure, the steady-state wakes at the origin are

$$w_{\parallel}(0^+) = -\frac{Z_0 c}{\pi a^2}, \quad \frac{\partial}{\partial s} w_{\perp}(0^+) = \frac{2Z_0 c}{\pi a^4}.$$

The same is true for a resistive pipe, a pipe with small periodic corrugations, and a dielectric tube within a pipe. It was assumed in [3, 25] that it is generally true. For a non-round structure the constants are different, but again dependent only on transverse dimensions and independent of material properties. This statement for an arbitrary slow down layer was rigorously derived in [26, 27] and it was shown there that for planar, square, and other cross section geometries, one can obtain a corresponding form factor coefficient by using a conformal mapping of these shapes onto the disk.

The asymptotics of the wakes at origin for a short transition and an isolated cavity are different. We summarize the asymptotic behavior at the origin of the considered models in Table 1.

Table 1: Asymptotics of wake functions at the origin

Model	$w_{\parallel}(s)$	$w_{\perp}(s)$
Optical (short transition)	$\sim \delta(s)$	$O(1)$
Diffraction (cavity)	$O(1/\sqrt{s})$	$O(\sqrt{s})$
Diffraction (cavity chain)	$O(1)$	$O(s)$
Slow down layer	$O(1)$	$O(s)$

In Table 1 $\delta()$ is a Dirac delta-function and symbol O is "big O" asymptotic notation.

COMBINING COMPUTATIONS AND ANALYTICS

The real geometry of accelerator vacuum chamber is quite complicated and it is a challenge to give a short range wake

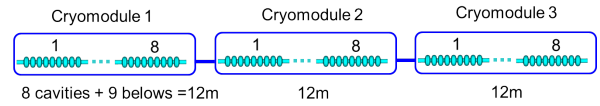


Figure 9: Three TESLA cryomodules.

functions for it. However in many situations it is possible to combine the considered above analytical models with numerical computations.

The first possibility is to take an analytical model for a simple geometry and to assume that the real vacuum chamber can be described by the same model with different coefficients. These coefficients can be found from fitting of the model to results of numerical simulations. Such approach was elaborated in [28, 29] in order to estimate the wake functions in TESLA linac of the European XFEL and FLASH at DESY.

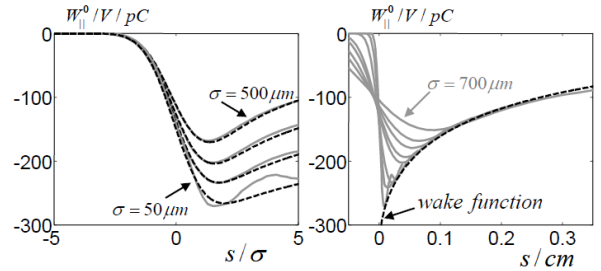


Figure 10: Comparison of analytical and numerical longitudinal wake potentials in the third cryomodule.

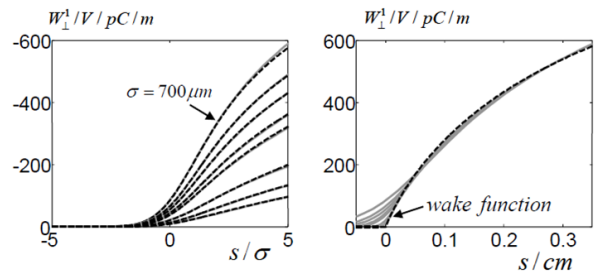


Figure 11: Comparison of analytical and numerical transverse wake potentials in the third cryomodule.

The TESLA linac consists of a long chain of cryomodules. The cryomodule of total length 12m contains 8 cavities and 9 bellows as shown in Fig. 9. The iris radius is 35mm and beam tubes radius is 39mm. The wakefields for Gaussian bunches up to $\sigma_z = 50\mu\text{m}$ have been studied. In order to reach the steady state solution the structure of 3 cryomodules with total length 36m was considered. It was shown that as for periodic structure the loss factor becomes independent from the bunch length and the kick factor decreases linearly with the bunch length (see Table 1).

After fitting of coefficients in Bane's model [31] the following wake functions (for one cryomodule) are obtained

$$w_{\parallel}(s) = -344e^{-\sqrt{s/s_0}} \left[\frac{V}{pC} \right], \quad s_0 = 1.74\text{mm}, s_1 = 0.92\text{mm},$$

$$w_{\perp}(s) = 10^3 \left(1 - \left(1 + \sqrt{\frac{s}{s_1}} \right) e^{-\sqrt{\frac{s}{s_1}}} \right) \left[\frac{V}{pCm} \right].$$

Fig. 10 shows numerical (gray solid lines) and analytical (black dashed lines) wake potentials for bunches with $\sigma_z = 500, 250, 125, 50\mu\text{m}$. The deviation of the curves for the shortest bunch can be explained by insufficiency of the 3 cryomodules to reach the steady state solution. At the right side of Fig. 10 the wakes (gray solid lines) together with the analytical wake function (black dashed line) are shown. The analytical wake function tends to be the envelope function to all wakes. Fig. 11 shows likewise the results for transverse wakes.

It can be seen from Table 1 that the behavior of wake functions for infinite periodic structure and for isolated cavity are different. In [32] we have combined two models in order to obtain wake functions of high harmonic module and transverse deflecting structure used at FLASH facility at DESY.

Recently another method was suggested in [33]. The idea behind the method is to use a combination of computer simulations with an analytical form of the wake function for a given geometry in the high-frequency limit (optical or diffraction model). For example, the longitudinal wake function of round step-out transition can be well approximated as

$$w_{\parallel}(s) = w_{opt}(s) + d(s),$$

$$w_{opt}(s) = -\frac{1}{\pi\epsilon_0} \ln(ba^{-1})\delta(s),$$

$$d(s) = (\alpha + \beta s).$$

The crucial element of the method is that the smooth function $d(s)$ can be obtained from simulations with long bunch by fitting to the formula. This method that combines a (processed) long-bunch wake from an EM solver and a singular analytical wake model allows one to accurately obtain wake fields of short bunches, including that of a point-charge.

IMPEDANCE DATABASE MODEL AND BEAM DYNAMICS SIMULATIONS

The European XFEL contains hundreds of sources of the coupled impedances. In order to obtain the wake functions of different elements we have used analytical and numerical methods. The wake functions of relativistic charge have usually singularities and can be described only in terms of distributions (generalized functions). An approach to tabulate such functions and use them later to obtain wake potentials for different bunch shapes was introduced in [34–36].

The longitudinal wake function near the reference trajectory \vec{r}_a can be presented through the second order Taylor

expansion

$$w_z(\vec{r}, s) = w_z(\vec{r}_a, s) + \langle \nabla w_z(\vec{r}_a, s), \Delta\vec{r} \rangle + \frac{1}{2} \langle \nabla^2 w_z(\vec{r}_a, s) \Delta\vec{r}, \Delta\vec{r} \rangle + O(\Delta\vec{r}^3),$$

where we have incorporated in one vector the transverse coordinates of the source and the witness particles, $\vec{r} = (x_0, y_0, x, y)^T$, $\Delta\vec{r} = \vec{r} - \vec{r}_a$, and s is a distance between these particles.

For arbitrary geometry without any symmetry the Hessian matrix $\nabla^2 w_z(\vec{r}_a, s)$ contains 8 different elements:

$$\nabla^2 w_z(\vec{r}_a, s) = \begin{pmatrix} h_{11} & h_{12} & h_{13} & h_{14} \\ h_{12} & -h_{11} & h_{23} & h_{24} \\ h_{13} & h_{23} & h_{33} & h_{34} \\ h_{14} & h_{24} & h_{34} & -h_{33} \end{pmatrix},$$

where we have taken into account the harmonicity of the wake function in coordinates of the source and the witness particles [20].

Hence in general case we use 13 one-dimensional functions to represent the longitudinal component of the wake function for arbitrary offsets of the source and the witness particles near to the reference axis. Geometric symmetries of vacuum chamber reduce the number of the one-dimensional functions considerably (see, for example, [37]). For each of these coefficients we use the representation [34]

$$h(s) = w_0(s) + \frac{1}{C} + Rc\delta(s) + c \frac{\partial}{\partial s} (Lc\delta(s) + w_1(s)), \quad (13)$$

where w_0, w_1 are non-singular functions, which can be tabulated easily and constants R, L, C have meaning of resistivity, inductance and capacitance, correspondingly. The wake potential for arbitrary bunch shape $\lambda(s)$ can be found by formula

$$W_h(s) = w_0 * \lambda(s) + \frac{1}{C} \int_{-\infty}^s \lambda(s') ds' + Rc\lambda(s) + c^2 L\lambda'(s) + cw_1(s) * \lambda'(s),$$

where λ' is a derivative of λ .

In order to model the beam dynamics in the presence of wakefields we use the open source code OCELOT [38]. We have developed and tested the wakefield module. The implementation follows closely the approach described in [34], [35]. The wakefield impact on the beam is included as series of kicks. In [36] we have studied a possibility to extend the bandwidth of the radiation at the European XFEL with the help of a special compression scenario together with the corrugated structure insertion. We have derived an accurate modal representation of the wake function of corrugated structure and have applied this fully three dimensional wake function in beam dynamics studies with OCELOT in order to estimate the change of the electron beam properties.

CONCLUSION

We have discussed several analytical models for impedances excited by short bunches in accelerators. We

have reviewed some of what has been learned in the last years concerning analytical approaches to the high frequency impedance estimation. The results from analytical models have been compared with direct solution of Maxwell's equation. Several techniques for combining of numerical computations and analytics to obtain wake functions of point charge have been considered. An approach to keeping of these wake functions in database and using them in beam dynamics simulations is presented.

ACKNOWLEDGEMENTS

The author thanks K. Bane, M. Dohlus and G. Stupakov for discussions about short-range wakes.

REFERENCES

- [1] A.W. Chao, *Physics of Collective Beam Instabilities in High Energy Accelerators* (Wiley, New York, 1993).
- [2] I. Zagorodnov, T. Weiland, *TE/TM field solver for particle beam simulations without numerical Cherenkov radiation*, Phys. Rev. ST Accel. Beams **8**, 042001 (2005).
- [3] K.L.F.Bane, *Wakefields of sub-picosecond bunches*, Report No. SLAC-PUB-11829 (2006).
- [4] M. Altarelli et al (Eds), *The European X-Ray Free-Electron Laser. Technical design report*, Report No. DESY 2006-097 (2006).
- [5] I. Zagorodnov, *Indirect methods for wake potential integration*, Phys. Rev. ST Accel. Beams **9**, 102002 (2006).
- [6] G. Stupakov, K.L.F. Bane, I. Zagorodnov, *Optical approximation in the theory of geometric impedance*, Phys. Rev. ST Accel. Beams **10**, 054401 (2007).
- [7] K.L.F. Bane, G. Stupakov, I. Zagorodnov, *Impedance calculations of non-axisymmetric transitions using the optical approximation*, Phys. Rev. ST Accel. Beams **10**, 074401 (2007).
- [8] R. Gluckstern, J. Van Zeijts, and B. Zotter, *Coupling impedance of beam pipes of general cross section*, Phys. Rev. E **47** 656 (1993).
- [9] CST Particle Studio is a trademark of CST AG, Buedinger Strasse 2a, 64289 Darmstadt, Germany (www.cst.de).
- [10] M. Dohlus, I. Zagorodnov, O. Zagorodnova, *High frequency impedances in the European XFEL*, Report No. DESY 10-063 (2011)
- [11] K.L.F. Bane, M. Sands, *Wakefields of very short bunches in an accelerating cavity*, Report No. SLAC-PUB-4441 (1987)
- [12] G. Stupakov, *Using the parabolic equation for calculation of beam impedance*, New Journal of Physics **8**, 280 (2006).
- [13] R. Gluckstern, *Longitudinal impedance of a periodic structure at high frequency*, Phys.Rev. D **39**, 2780 (1989).
- [14] K. Yokoya and K.L.F. Bane, *The longitudinal high-frequency impedance of a periodic accelerating structure*, in Proceedings of the 1999 Particle Accelerator Conference, (IEEE, Piscataway, 1999), p. 1725.
- [15] G. Stupakov, *Coupling impedance of a periodic array of diaphragms*, Proceedings of the 1995 Particle Accelerator Conference, (IEEE, Piscataway, 1995), p. 3303.
- [16] G. Stupakov, K.L.F. Bane, *Surface impedance formalism for a metallic beam pipe with small corrugations*, Phys. Rev. ST Accel. Beams **15**, 124401 (2012).
- [17] V. I. Balbekov, *On using equivalent circuits for calculation of longitudinal beam coupling impedance of a ring accelerator. I. A single insertion*, Report No. IFVE-93-55 (1993).
- [18] M. Dohlus, *Impedance of beam pipes with smooth shallow corrugations*, Report No. TESLA 2001-26 (2001).
- [19] A. Tsakanian, M. Dohlus, I. Zagorodnov, *The effect of the metal oxidation on the vacuum chamber impedance*, Report No. TESLA-FEL 2009-05 (2009).
- [20] I. Zagorodnov, K.L.F. Bane, G. Stupakov, *Calculation of wakefields in 2D rectangular structures*, Phys. Rev. ST Accel. Beams **18**, 104401 (2015).
- [21] K.L.F. Bane and G. Stupakov, *Using surface impedance for calculating wakefields in flat geometry*, Phys. Rev. ST Accel. Beams **18**, 034401 (2015).
- [22] K.L.F. Bane and G. Stupakov, *Dechirper wakefields for short bunches*, Nucl. Inst. Meth. A **820**, 156 (2016).
- [23] K.L.F. Bane, G. Stupakov, I. Zagorodnov, *Analytical formulas for short bunch wakes in a flat dechirper*, Phys. Rev. Accel. Beams **19**, 084401 (2016).
- [24] K.L.F. Bane, G. Stupakov, I. Zagorodnov, *Wakefields of a beam near a single plate in a flat dechirper*, Report No. SLAC-PUB-16881 (2016).
- [25] K.L.F. Bane, G. Stupakov, *Impedance of a rectangular beam tube with small corrugations*, Phys. Rev. ST Accel. Beams **6**, 024401 (2003).
- [26] S.S. Baturin, A.D. Kanareykin, *Cherenkov Radiation from Short Relativistic Bunches: General Approach*, Phys. Rev. Lett. **113**, 214801 (2014).
- [27] S.S. Baturin, A.D. Kanareykin, *New method of calculating the wakefields of a point charge in a waveguide of arbitrary cross section*, Phys. Rev. Accel. Beams **19**, 051001 (2016).
- [28] A. Novokhatski, M. Timm, T. Weiland, *Single bunch energy spread in the TESLA cryomodule*, Report No. TESLA-1999-16 (1999).
- [29] T. Weiland, I.A. Zagorodnov, *The short-range transverse wake function for TESLA accelerating structure*, Report No. TESLA 2003-19 (2003).
- [30] I. Zagorodnov, T. Weiland, M. Dohlus, *Wake fields generated by the LOLA-IV structure and the 3rd harmonic section in TTF-II*, Report No. TESLA 2004-01 (2004).
- [31] K.L.F. Bane, *Short-range dipole wakefields in accelerating structures for the NLC*, Report No. SLAC-PUB-9663, LCC-0116 (2003).
- [32] I. Zagorodnov, T. Weiland, M. Dohlus, *Wake fields generated by the LOLA-IV structure and the 3rd harmonic section in TTF-II*, Report No. TESLA 2004-01 (2004).
- [33] B. Podobedov, G. Stupakov, *Point-charge wakefield calculations from finite length bunch wake potentials*, Phys. Rev. Accel. Beams **16**, 024401 (2013).
- [34] O. Zagorodnova, T. Limberg, *Impedance budget database for the European XFEL*, in Proceedings of 2009 Particle Accelerator Conference, (Vancouver, Canada, 2009).

- [35] M. Dohlus, K. Floettmann, C. Henning, *Fast particle tracking with wake fields*, Report No. DESY 12-012 (2012). (1998).
- [36] I. Zagorodnov, G. Feng, T. Limberg, *Corrugated structure insertion for extending the SASE bandwidth up to 3% at the European XFEL*, Nucl. Instr. Meth. A **837**, 69 (2016).
- [37] S. Heifets, A. Wagner, B. Zotter, *Generalized impedances and wakes in asymmetric structures*, Report No. SLAC-AP-110
- [38] I. Agapov, G. Gelonia, S. Tomin, I. Zagorodnov, *OCELOT: a software framework for synchrotron light source and FEL studies*, Nucl. Instr. Meth. A. **768**, 151 (2014).

MULTIPHYSICS SIMULATIONS OF IMPEDANCE EFFECTS IN ACCELERATORS

C. Zannini, ADAM/AVO, Geneva, Switzerland

Abstract

Multiphysics is a computational discipline that involves multiple physical models. Nowadays commercial 3D simulation codes allow to couple electromagnetic and thermo-mechanical effects. Considering all the induced effects of the electromagnetic fields is fundamental in the development of electromagnetic devices. In this paper, the importance of Multiphysics simulations applied to beam coupling impedance is discussed.

INTRODUCTION

The input power of an electromagnetic device (RF components, accelerator elements etc.) will be partially or almost completely dissipated in the device walls. A good estimation of the power that needs to be dissipated in the device and of its distribution is fundamental to avoid unexpected failures of the component due to thermal and/or structural effects induced by the electromagnetic fields (EM fields). Figure 1 shows the Multiphysics design loop. First, the EM fields and the surface power loss density map are obtained as output of the electromagnetic simulation. Therefore, the power loss density map is used as input of a thermal simulation which will give as main output a thermal map of the device. This map can be used as input of structural simulations to estimate the induced mechanical stress and the structural deformation of the device. Finally, the deformed mesh can be imported in the electromagnetic simulations to study the effect on the EM fields. Performing the design loop illustrated in Fig. 1, EM fields induced thermo-mechanical issues (excessive heating, mechanical stress close to the ultimate tensile strength of the material, unacceptable frequency shift due to wall deformation) could be predicted and corrective actions in the design could be taken at an early stage.

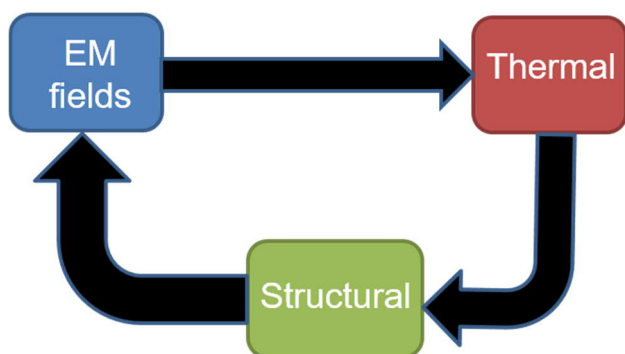


Figure 1: Multiphysics design loop for electromagnetic components

MULTIPHYSICS SIMULATION APPLIED TO IMPEDANCE EFFECTS

The beam coupling impedance characterizes the interaction between the particle beam and the accelerator devices. During the traversal through the accelerator, the particle beam will induce electromagnetic fields which will affect the motion of the beam itself. This mechanism is studied to understand, predict and prevent the beam instability behaviour. However, beam induced EM fields are also responsible of induced effects on the accelerator device itself (heating and structural deformation) which could lead to a modification of the induced EM fields. In order to study also these effects, the Multiphysics design loop has to be applied to beam coupling impedance simulations. Figure 2 shows the Multiphysics design loop detailed for beam coupling impedance studies. In the following, I will describe how to perform the design loop of Fig. 2 by using the commercial simulation package CST Studio Suite [1].

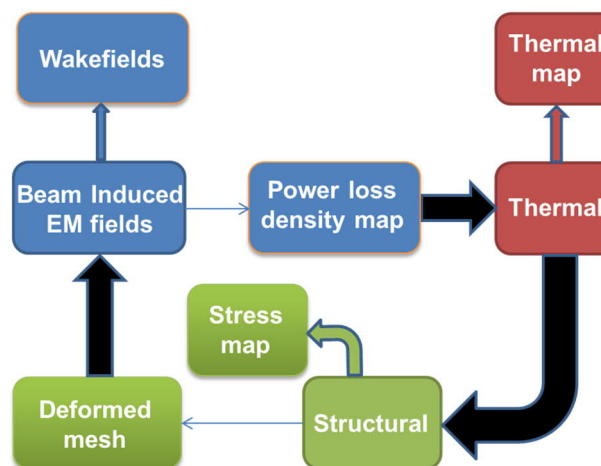


Figure 2: Multiphysics design loop for beam coupling impedance simulations

The first step consists in the computation of the beam induced EM fields. These fields could be calculated performing eigenmode, frequency domain or time domain calculations. The eigenmode would be more appropriate for the simulation of resonating structures (RF cavities and cavity like structures), the frequency domain would fit better for complex devices where the discretization of the domain of calculus requires the use of tetrahedral meshes while time domain simulations (scattering matrix and/or wakefields) could be accurately performed when hexahedral meshes can be used for an accurate representation of the calculus domain. Post-processing eigenmode, frequency domain and time domain results or as direct output of the wakefield

solver is possible to get the wake function and its representation in the frequency domain: the beam coupling impedance.

In the eigenmode simulations, the longitudinal and transverse impedances are reconstructed by using the broadband resonator formulae [2]:

$$Z_{\parallel}(f) = \frac{R}{1 + jQ \left(\frac{f}{f_r} - \frac{f_r}{f} \right)} \quad (1)$$

$$Z_{\perp}(f) = \frac{f_r}{f} \frac{R_{\perp}}{1 + jQ \left(\frac{f}{f_r} - \frac{f_r}{f} \right)} \quad (2)$$

The linear terms of the transverse impedance (dipolar and quadrupolar) can be obtained from the generalized (parabolic) longitudinal impedance using the Panofsky-Wenzel theorem [3].

In the frequency domain simulation, the beam coupling impedance can also be obtained by integrating the electric field at each frequency according to its definition or from the scattering parameters derived by simulating the coaxial wire method setup [4, 5, 6]. In the time domain, the impedance can be obtained from the scattering matrix as for the frequency domain. The time domain wakefield solver gives directly as output result the beam coupling impedance, which is calculated from the wake potential applying the convolution theorem.

A power loss density map can be exported from the EM fields distribution and used as input of thermal simulations. The simulated total power loss can be normalized to the beam induced power loss by using the following normalization factor:

$$Nfactor = \frac{\Delta W}{\Delta W_{sim}} \quad (3)$$

where ΔW is the beam induced power loss obtained considering the actual beam spectrum [7, 8] and ΔW_{sim} is the simulated power loss.

After an accurate definition of the thermal material properties and boundary conditions thermal simulations can be performed. The output of these simulations will give all the information about the thermal behaviour of the device when exposed to the simulated beam induced EM fields. This allows identifying hot spots and driving design modifications and cooling efficiency optimization. The thermal map can be used as input for structural simulations. After an accurate definition of mechanical material properties and boundary conditions structural simulations can be performed. The output of the mechanical simulations will depict the structural behaviour of the device in the presence of the simulated beam induced EM fields. This allows identifying critical points, possible breaking points and modifying design accordingly. Structural simulations also allow exporting the deformed mesh which could be then used to

simulate the deviation of the induced EM fields and therefore of the beam coupling impedance caused by the structural deformation of the accelerator component. The modified beam induced fields could then be used as input for a new loop. Ideally, the Multiphysics design loop should be performed iteratively to find the steady state behaviour of the device under study. However, usually the deviation of the beam induced fields leads to negligible effects on the thermo-mechanical behaviour of the accelerator element.

EXAMPLES OF APPLICATION

In this section some examples of application will be presented to underline the importance of the Multiphysics design loop for beam coupling impedance studies.

CERN-SPS extraction kicker

The CERN-SPS extraction kicker consists of a C-shaped ferrite magnet. After the installation in the machine, it was realized that this accelerator component was suffering of excessive beam induced heating [9]. Therefore, it was needed to introduce a modification to reduce the beam induced heating of this device. Silver paste was used to print by serigraphy finger pattern directly on the ferrite to reduce the beam coupling impedance and consequently the beam induced heating [10] (see Fig. 3).

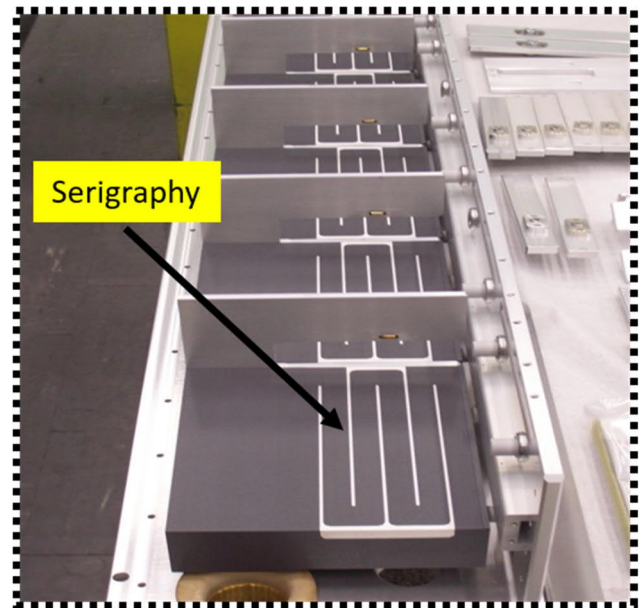


Figure 3: Top view of the serigraphed CERN-SPS extraction kicker ferrite magnet.

Having, the Multiphysics design in place would allow identifying similar issues in the design phase and taking the corrective actions at the design stage. Moreover, the Multiphysics design loop gives an extensive picture of the beam induced EM fields induced effects and therefore, it gives all the elements to the designer to implement the best solution. For example, in the specific case of the SPS extraction kicker the solution implemented gives a significant improvement with respect to the original design but is not optimized in terms of beam induced heating. An additional significant improvement could be obtained optimizing the

serigraphy length. The serigraphy introduces a $\lambda/4$ resonance on the finger length [7] (see Fig. 4). To minimize the impact of this resonance on the beam induced heating the finger length could be optimized to shift the resonance frequency as far as possible from the beam spectrum lines. A resonant frequency of about 50 MHz has been considered an appropriate choice in order to have a workable solution for both 25 ns and 50 ns bunch spacing particle beam (see Fig. 5). This required shortening the serigraphy length by 20 mm. The solution has been implemented and experimentally validated during SPS scrubbing runs [11].

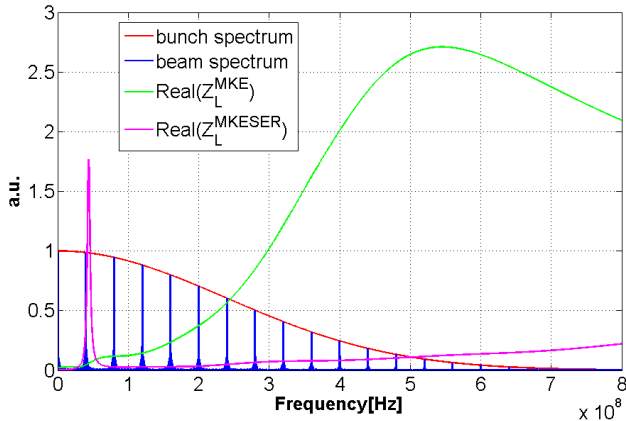


Figure 4: Beam coupling impedance of the CERN-SPS extraction kicker with (magenta curve) and without (green curve) serigraphy. CERN-SPS beam and bunch spectrum are also shown for the beam with 25 ns bunch spacing.

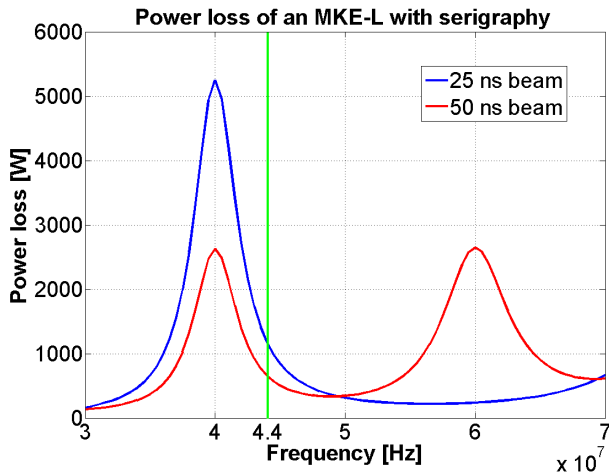


Figure 5: Power loss for the 25ns and 50ns beam as function of the frequency of the resonance introduced by the serigraphy. The green line corresponds to the resonant frequency of the original serigraphy.

The CERN-SPS extraction kicker is just a possible example of application. The Multiphysics design loop should ideally be applied to each accelerator component exposed to the particle beam. The correct implementation of the Multiphysics design loop would allow having more efficient solution and will give us a better understanding of the observed thermal and structural behaviour. For instance, it would allow understanding if wire breaking in the wire scanner could be related to beam induced heating. Finally,

the author would also like to stress the importance of performing the full Multiphysics design loop including the structural simulations. In fact, critical structural deformation which could bring to serious damage and/or rupture does not require having an enormous heating. In particular situations, 5-6 °C of heating could cause serious damage to the accelerator element.

COMPONENT DESIGN FLOW PROCESS

In this last section the author would like to suggest a possible implementation of the Multiphysics design loop for beam coupling impedance in the design of new accelerator elements. A flow chart is displayed in Fig. 6. The design ownership of new devices should be assigned according to the functionality of the accelerator component. Once a functional design is ready, the impedance team could perform a first check looking at all the impedance induced effects. This would require the implementation of the Multiphysics design loop in collaboration with thermal and mechanical engineers for the thermal and structural simulations. If modifications are needed, they will be submitted to the owner of the design for the implementation in the functional design. Once a functional design is approved, the design team can work on the detailed design, which will be checked again by the beam coupling impedance team, which will eventually consider the design impedance compliant or will require additional modifications. Identifying possible impedance issues at an early stage in the design phase will pave the way to have optimized design in terms of beam coupling impedance and its induced effects.

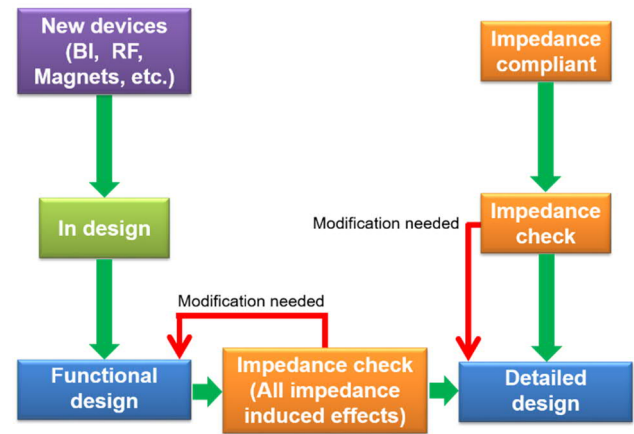


Figure 6: Flow chart for the design of an accelerator component: beam coupling impedance perspective.

SUMMARY

The Multiphysics design loop applied to beam coupling impedance studies has been presented. The implementation of the design loop by using CST Studio Suite has been discussed. The importance of these simulations has been emphasized giving specific examples. Finally, the implementation of the Multiphysics design loop for beam coupling impedance studies in the design of new accelerator elements has been also discussed.

ACKNOWLEDGEMENTS

The author would like to acknowledge ADAM/AVO, M. Barnes, G. De Michele, E. Métral, G. Rumolo, B. Salvant and V.G. Vaccaro.

REFERENCES

- [1] CST, <https://www.cst.com>
- [2] E. Métral, G. Rumolo, W. Herr, "Impedance and collective effects", Landolt-Bornstein 21C (2013) 62-101.
- [3] E. Métral et al, "Kicker impedance measurements for the future multiturn extraction of the CERN Proton Synchrotron", CERN-AB-2006-051, 2006.
- [4] L. Hahn and F. Pedersen, "On a coaxial wire measurements of the Longitudinal Beam Coupling Impedance," BNL-50870, April 1978.
- [5] V. G. Vaccaro, "Coupling impedance measurements: an improved wire method," INFN-94-023, November 1994.
- [6] F. Caspers, C. González, M. Dyachkov, E. Shaposhnikova, and H. Tsutsui, "Impedance measurement of the SPS MKE kicker by means of the coaxial wire method," CERN-PSRF-NOTE-2000-04, February 2000.
- [7] C. Zannini, "Electromagnetic simulation of CERN accelerator components and experimental applications", PhD thesis, Lausanne, EPFL, Switzerland, 2013.
- [8] C. Zannini, G. Iadarola, G. Rumolo, "Power Loss Calculation in Separated and Common Beam Chambers of the LHC", IPAC14, Dresden, Germany (2014).
- [9] J. Uythoven, "Status report on beam induced heating of the MKE magnet," Presented at the CERN Accelerator Performance Committee (APC) meeting (<http://ab-div.web.cern.ch/ab-div/Meetings/APC/>), 24 June 2003.
- [10] T. Kroyer, F. Caspers, and E. Gaxiola, "Longitudinal and Transverse Wire Measurements for the Evaluation of Impedance Reduction Measures on the MKE Extraction Kickers," CERN-AB-Note-2007-028, July 2007.
- [11] M.J. Barnes et al., "Upgrading the SPS Fast Extraction Kicker Systems for HL-LHC", IPAC17, Copenhagen, Denmark (2017).

Acknowledgements

The workshop chairpersons are very thankful to:

- The members of the International Organizing Committee, who enthusiastically responded to the request for input in terms of subjects and speakers. It is thanks to their suggestions that the scientific program of the workshop turned out to be so rich and interesting;
- All the colleagues who accepted to serve as chairpersons and scientific secretaries of the different sessions. Their efforts in organizing well their sessions and their summaries at the end of the workshop were highly appreciated;
- All the speakers and poster presenters for the high quality of their material;
- The young and dynamic local organizing committee, always ready to respond to the needs of the attendees;
- The town of Benevento for welcoming the workshop participants and providing the infrastructure for the workshop to take place. It was a privilege to be able to run the oral sessions at the San Vittorino complex as well as to use the Museum of Sannio for the poster session;
- The CERN library team for their great assistance in setting up these proceedings.

International Advisory Committee

Karl Bane (SLAC, CA, US)
Riccardo Bartolini (DIAMOND, UK)
Mike Blaskiewicz (BNL, NY, US)
Oliver Boine-Frankenheim (GSI, Germany)
Alexey Burov (FNAL, IL, US)
Alexander Wu Chao (SLAC, CA, US)
Yong Ho Chin (KEK, Japan)
In Soo Ko (POSTECH, South Korea)
Elias Métral (CERN, Switzerland)
Mauro Migliorati (La Sapienza University of Rome, Italy)
Ryutaro Nagaoka (SOLEIL, France)
Kazuhito Ohmi (KEK, Japan)
Katsunobu Oide (KEK, Japan, and CERN, Switzerland)
Luigi Palumbo (La Sapienza University of Rome, Italy)
Stefania Petracca (University of Sannio, Italy)
Qin Qing (IHEP, China)
Giovanni Rumolo (CERN, Switzerland)
Elena Shaposhnikova (CERN, Switzerland)
Gennady Stupakov (SLAC, CA, US)
Vittorio Vaccaro (University of Naples Federico II, Italy)
Ursula Van Rienen (University of Rostock, Germany)
Rainer Wanzenberg (DESY, Germany)
Frank Zimmermann (CERN, Switzerland)
Mikhail Zobov (LNF, Italy)

A random collection of
photographs from the Workshop

